Epigenomic Reprogramming and Therapeutics Development in High-Grade Gliomas

by

Stefan R. Sweha

A dissertation submitted in partial fulfillment
of the requirements for the degree of
Doctor of Philosophy
(Neuroscience)
in the University of Michigan
2021

Doctoral Committee:

Associate Professor, Sriram Venneti, Chair
Professor Robert T. Kennedy
Assistant Professor Carl J. Koschmann
Professor Andrew P. Lieberman
Associate Professor Costas A. Lyssiotis

Stefan R. Sweha

ssweha@umich.edu

ORCID iD: 0000-0002-1807-6770

© Stefan R. Sweha 2021

Dedication

To those who positively impacted me.

Acknowledgements

I would like to express gratitude for my advisor, Dr. Sriram Venneti. It has been a privilege to work with a phenomenal scientist and a great person. Committed to helping his trainees, I have appreciated the role Sriram has played in my scientific development, and his witty sense of humor and evenhandedness. As one of his first doctoral trainees, I have been excited to come to the laboratory, knowing that his enthusiasm and scientific prowess are unwavering. I have learned much here – to perform science competently and precisely, and to equally enjoy it. I will cherish the conversations we had and the overall scientific adventure. Thank you!

I would like to thank the members of my dissertation committee, Drs. Carl Koschmann, Costas Lyssiotis, Andrew Lieberman, and Robert Kennedy for their expertise, time, and insights throughout this work. I enjoyed discussing science and learning from you.

To the postdoctoral fellows of the Venneti Laboratory, Drs. Chan Chung and Pooja Panwalkar – thank you for your patience, friendliness, advice, and careful teaching (and laughs). It was great fun working with you and I am excited to see all you will do in your career.

To my fellow colleagues of the University of Michigan, thank you for your words of encouragement, contributions, and the fun experiences throughout my doctoral training. I would like to take this opportunity to thank other members of the Venneti lab who I have the pleasure of working and interacting with over the past several years: Jill Bayliss, Siva Kumar Natarajan, Derek Dang, Adam Banda, Mateus Mota, James Haggerty-Skeans, Matthew Pun, Amer Ghali, and Sushanth Sunil. Much gratitude for making the lab an exciting and enjoyable place to do science

and have productive, thought-provoking conversations. I would also like to thank Dr. Viveka Nand Yadav, Chase Thomas, and Dr. Rodrigo Cartaxo from the Koschmann lab for their support with my animal modeling experiments. Each of you made my experience unique and successes possible.

To Siva Kumar Natarajan, I have enjoyed our conversations over countless lunches at Angelos, dinners at HopCat, drives in the car, or in the cell culture room of the lab. I have admired your tenacity, organization, work ethic, and balance. You truly make an exemplary scientist! I have also enjoyed working alongside you for experiments. Having known you since we began several years ago, I am thankful for the many years of friendship and countless enjoyable times.

To Rudi Starrett, I have enjoyed you telling me about electrophysiology at our Nagomi lunches. Thanks for talking with me when science got challenging or when I needed advice on grant writing. I have enjoyed cruising over to Dairy Queen to get ice cream at all hours and talking about life over beers at Rappourt or a slice at Joe's. Looking forward to more years of friendship!

To Ziheng Xu and Prateek Sharma, thank you for being great friends and showing me around Ann Arbor when I arrived. My first year was fantastic thanks to you. Thanks for staying late in the lab and studying alongside me. I'm excited to see the impact you will make in medicine!

To Amer Ghali, thank you for your friendship! It was an honor to be your mentor. Thank you for your help with experiments and the entertaining rounds of chess to fill our free time. I enjoyed seeing you develop as a thoughtful scientist.

To Haley Grubbs, thank you for being a great person and partner! Thanks for entertaining my conversations about science, helping me balance life, and challenging me to see a new perspective. I have greatly enjoyed exploring the world and seeing new places with you.

To my friends elsewhere, Alex Nauman, Vikram Sivaraja, Jorjit Bhullar, Alfred Zhang, and Kyle Tillinghast – thanks for being there during great, momentous, and difficult times.

To Drs. Fouad Terra, Flora Tassone, and Carolyn Yrigollen – thank you for fostering my scientific interest and teaching me how to be a precise and thoughtful experimentalist. I enjoyed the countless phone calls on the weekend and the inspiration you gave me through your dedication to your research, enthusiasm, and willingness to teach me new things.

To Drs. Maxwell Meng, Joel Piser, and Andrew Pienkny – thanks for your incredible work and the impact it had on my future and for sparking my interest in cancer genetics. Your diligence and support during my senior year at Berkeley made the experience and the work presented here entirely possible. For that, I am grateful.

Finally, thank you to my parents, Sumaya and Sherif. I appreciate you giving me countless opportunities, supporting me, and helping broaden my horizons to appreciate culture, language, music, travel, and art. Thank you for instilling in me the value of hard work and integrity.

Table of Contents

List of Figures

Abstract

Tumors originating in the central nervous system comprise the most common class of childhood malignancy. Approximately 20% of pediatric gliomas are high-grade with an unsatisfactory long-term survival (>5 years) of 10-15%. Trials to develop and refine chemotherapeutic and radiation regimens for these fatal malignancies have seen little progress. Oncogenes classically have been traditionally considered genes, such as *MYC*, *MET*, and *RAS*, that induce malignant transformation via cellular reprogramming. These genes are often mutated, leading to hyperactivity or resistance to degradation, and drive tumorigenesis. Recent work has demonstrated that histones, the building blocks for chromatin, are recurrently mutated in bone cancers and gliomas. Although our knowledge on the role of histone mutations in perturbing epigenetic modifications has expanded from a biochemical perspective, fewer comprehensive studies identifying therapeutic vulnerabilities and oncogenic signaling mechanisms engaged by histone mutants have been completed. This dissertation aims to characterize specific epigenetic mechanisms in H3.3K27M and H3.3G34R/V gliomas and identify therapeutics for each subtype.

In Chapter 1, the introductory chapter, we discuss important aspects of histone biology, seminal discoveries and biochemical studies for histone mutations, and key pathways implicated in disease pathogenesis for histone mutant gliomas. In Chapter 2, this thesis describes the intersection of H3K27M tumor epigenetics with metabolism and how the epigenetic-metabolic axis in these tumors can be targeted for therapeutic benefit. An integrated transcriptomic, metabolomic, proteomic, and epigenetic analysis of tumor cells and tissues revealed enhanced

expression of enzymes involved in glycolysis, glutaminolysis, and the tricarboxylic acid cycle. These upregulated metabolic processes were associated with elevated alpha-ketoglutarate levels in H3.3K27M cells which heterogeneously utilize glutamine and glucose to produce alpha-ketoglutarate. Importantly, we found that depleting sources of alpha-ketoglutarate could raise H3K27me3 and slow tumor cell growth *in vitro.* Data presented in this chapter provides evidence that this metabolic targeting approach is efficacious in slowing *in vivo* tumor growth.

In Chapter 3, this thesis focuses on understanding therapeutic dependencies arising from epigenetic reprogramming by H3.3G34R/V mutations. Comprehensive omics analysis revealed concomitant and cooperative changes in DNA and histone methylation that led to epigenetic activation of the Leukemia Inhibitory Factor/Signal Transducer and Activator of Transcription (LIF/STAT3) signaling pathway. We found that LIF activated STAT3 in an autocrine/paracrine manner to promote H3.3G34R/V glioma cell survival *in vitro.* Further immunohistochemical and single-cell sequencing studies on patient samples confirmed pervasive STAT3 activation and expression, suggesting LIF/STAT3 as a potential therapeutic axis for these tumors. Furthermore, the data presented in this chapter demonstrates that STAT3 may regulate other master forebrain transcription factors that are critical for H3.3G34R/V gliomagenesis. Additional experiments established multiple preclinical animal models of H3.3G34R/V tumors using mouse and patient-derived tumor cells. Genetic and pharmacological targeting of STAT3 using these models provide the first evidence that LIF/STAT3 is a potent target for therapeutic intervention.

Finally, Chapter 4 summarizes and synthesizes the findings of each body of work presented in this dissertation. Critical remaining questions and future directions of study are discussed. Collectively, the work presented sought to uncover epigenetically-driven mechanisms of gliomagenesis for distinct tumor subtypes and to provide much needed therapeutic leads.

Chapter 1

Introduction

1.1 Histones and genome structure

Precise packaging and regulation of DNA structure is a crucial component of eukaryotic cells. Genomic material in the nucleus is packaged into chromatin, a critical highly ordered structure that allows for regulation of DNA compaction and accessibility. Nucleosomes, the building blocks of chromatin, are globular structures around which DNA is wound. Nucleosomes are made up of core components called histones that interact to give rise to an octameric structure. Four types of main canonical histone proteins exist, specifically histones H2A, H2B, H3, and H4 (Venkatesh *et al.,* 2015). These canonical histones each have different amino acid sequences, but include a conserved structure including three alpha helices each separated by loops. Before nucleosome assembly, histones H2A and H2B form a heterodimer. In a similar fashion, histones H3 and H4 form heterodimers. To form nucleosomes, two H3-H4 heterodimers form a tetramer which then subsequently binds with two H2A-H2B heterodimers, forming the octameric structure observed (Marino-Ramirez *et al*., 2005; Zhao *et al.,* 2019).

Histone variants can also be incorporated into nucleosomes, and variants can exhibit replication-dependent or replication-independent expression and deposition patterns. For example, noncanonical variants H3.1 and H3.2 are replication-dependent with high expression observed during S phase. Contrastingly, the H3.3 variant is expressed in a replication-independent manner and its expression is widely observed throughout all phases of the cell cycle (Henikoff *et al.,* 2015).

Noncanonical histone variants can also exhibit specific deposition patterns within chromatin and show tissue-specific expression, as is the case with the germ line-specific H3.5 variant. Interestingly, variant H3.3 varies from H3 at five amino acids (residues 31 and 87-90) which dictate where and how it is deposited into the genome (Goldberg *et al*., 2010; Shi *et al*., 2017). These unique amino acids are recognized by histone chaperones responsible for H3.3 deposition into chromatin. H3.3 is enriched at promoters and actively transcribed gene bodies, suggesting that replacement of canonical H3 in nucleosomes with H3.3 can drive transcriptional activation by increasing the accessibility of a genomic site to promote binding activity of RNA polymerase II and other transcription factors (McKittrick *et al*., 2004; Schwartz *et al*., 2005).

1.2 Histone modulation of gene expression

In addition to their structural importance, histones and nucleosomes play key roles in the complex regulation of gene expression. These proteins have been the focus of intense research with regard to cancer and other diseases, aging, and intellectual disability, since their discovery by Albrecht Kossel over a century ago (Greer *et al*., 2012). The N-terminal tails of each histone can be post-translationally modified at specific residues like lysine, arginine, alanine, and serine. A variety of modifications can occur, including phosphorylation, ubiquitination, acetylation, and methylation, and each residue can be decorated by one or several types of modification (**Figure 1.1**). To date, the most well-studied transcription-activating modifications include H3K27ac, H3K4me3, H3K36me3, and H3K79me2 while H3K9me3, H3K27me3, and H4K20me3 have generally been associated with transcriptional repression (Chi *et al*., 2010; Zhao *et al*., 2019). H3K4me3 is observed at the promoters of actively transcribed genes (Santos-Rosa *et al*., 2002). H3K9me3 is found in heterochromatic regions while H3K9me1 is found near active transcription start sites (Bannister et *al.*, 2001; Vavouri *et al.,* 2012). H3K27me3 is deposited both at promoters

and enhancers (Fang *et al*., 2002; Barski *et al*., 2007). H3K36me3 plays a role in transcriptional elongation and is found through gene bodies. While many histone residues can be acetylated (Zhang *et al*., 2021), we will only discuss H3K27ac throughout this dissertation. H3K27ac localizes to promoters and enhancers (Heintzman *et al*., 2009; Creyghton *et al*., 2010; Rada-Iglesias *et al*., 2011). Importantly, enhancers can harbor different activation states – poised marked by co-occurring H3K27me3 and H3K4me1 and active marked by H3K27ac and H3K4me1 (Creyghton *et al*., 2010; Chen *et al*; 2013).

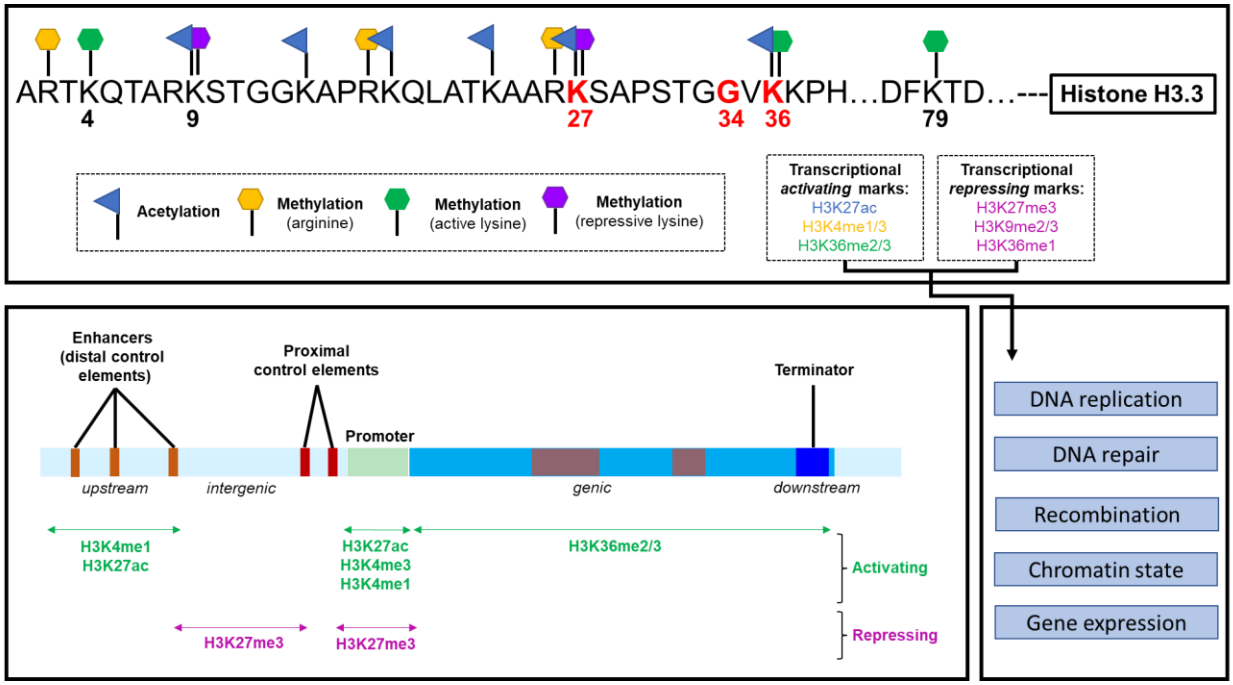

Figure 1.1. Posttranslational modifications of histones and their deposition.
Histones including variant H3.3 can be modified by "writer" and "eraser" enzymes. H3.3 can undergo acetylation and methylation at the various amino acid residues depicted. Red residues indicate locations targeted by recurrent mutations in distinct cancers. Epigenetic modifications can promote or repress transcription and act in a combinatorial manner to dynamically control various nuclear processes such as gene expression, DNA repair, recombination events, chromatin state and accessibility. H3K4me1 is often found at enhancers and upstream control elements while H3K27me3 tends to localize strongly to gene promoters. H3K27ac, H3K4me3, H3K4me1 are abundant at promoters while H3K36me2/3 is often found in gene bodies.

The steady state equilibrium for these modifications is dictated by the relative activity of their enzyme modifiers (methyltransferases and demethylases), and relevant enzymes are briefly described here. CBP/P300 is a histone acetyltransferase catalyzing H3K27ac and can recruit other acetyltransferase complexes (Zhang *et al*., 2021). Importantly, the Polycomb Repressive Complex 2 (PRC2) methyltransferase subunit EZH2 catalyzes H3K27me3 reactions and PRC2 enrichment has been observed at silenced gene promoters (Bernstein *et al*., 2006; Margueron *et al*., 2009). The interplay of the H3K27me3 mark and DNA methylation has been widely studied for its role in development and gene silencing in cancer (Abbosh *et al*., 2006; Boyer *et al*., 2006; Kondo *et al*., 2008; Lee et al., 2006; Reddington *et al*., 2013; Viré *et al*., 2006). Lysine demethylases KDM6A and KDM6B are responsible for H3K27me3 removal. The SET Containing Domain 2 (SETD2) protein plays a role in catalyzing H3K36me3 which marks actively transcribed genomic regions (Kizer *et al*., 2005). Contrastingly, the lysine 36 demethylases KDM4A, KDM4B, and KDM4C are responsible for demethylation reactions occurring at H3K9 and H3K36 residues (Zhao *et al*., 2019).

It is important to realize that one type of histone modification can affect the patterning of other modifications. For example, H3K36me3 marks active genes and acts antagonistically to repressive H3K27me3 (Margueron *et al*., 2009; Yuan *et al.,* 2011). In a similar fashion, H3K27ac, which marks active promoters and enhancers, is observed to antagonize PRC2 (Tie *et al*., 2009).

Modifications are dynamic and can be modulated in tissue- or cell-specific manners where they change the charge of the histone. Thus, these changes in charge state can promote steric interactions between adjacent histones and disrupt histone and underlying DNA interactions. It follows that these modifications play a role in chromatin accessibility, DNA recombination and repair, transcription factor recruitment, and transcription elongation processes. Notably, chromatin

dynamics due to underlying modifications can affect histone turnover, a process by which histones are removed or replaced in nucleosomes (Venkatesh *et al*., 2015). The histone turnover rate can influence local gene accessibility by allowing for replacement with histone variants, discussed earlier, or nucleosome eviction that silence gene expression. Turnover processes are dynamically controlled by histone chaperones (such as HIRA, ATRX, and DAXX) and chromatin readers (Banaszynski *et al*., 2013; Elsässer *et al*., 2010, 2012; Dhayalan *et al*., 2011; Lewis *et al*., 2010; Liu *et al*., 2012;). Importantly, disruptions to the normal modification state can cause inappropriate chromatin compaction or accessibility that is often responsible for impaired cellular differentiation, tumorigenesis, and neurodegeneration. In cancer, epigenetic perturbations often inactivate tumor suppressors, activate oncogenes, or modulate cell cycle dynamics to enable unrestricted growth. These observations strongly implicate histones in drug resistance, metastasis, and tumor progression (Audia *et al*., 2016; Bedi *et al*., 2014; Gomes *et al*., 2019; Tam *et* al*.,* 2013).

1.3 Pediatric and adult brain tumors exhibit unique characteristics

Primary brain tumors are a significant cause of mortality in children (Ostrom *et al.,* 2015; Fontebasso *et al.,* 2013a,b). Different types of tumors can arise in the brain, including astrocytoma, ependymoma, medulloblastoma, and glioblastoma. Up until recently, therapeutic design has been guided by adult glioma treatment paradigms. Despite decades of research and widespread efforts to find viable therapies for pediatric brain cancers, there has been little progress in improving patient survival or outcomes. Mutational differences between adult and childhood central nervous system tumors are likely factors for treatment failures. While adult tumors have been comprehensively classified into molecular and histopathological subgroups, cellular programs distinguishing classes of pediatric glioma are just beginning to be defined. Some important differences between adult glioblastoma (GBM) and childhood glioma have been noted (Jones and

Baker, 2014). Although tumors from each demographic cannot be histologically distinguished, adult primary GBMs tend to undergo a process where low-grade gliomas transform into high-grade malignancy, an event less commonly observed in childhood gliomas. Adult primary GBMs exhibit high frequencies of *IDH1* mutations, inactivating *PTEN* mutations, *CDKN2A* deletion, and EGFR amplification, while these characteristics are not recapitulated in younger patients who often present with *PDGFRA* amplification (Fontebasso *et al*., 2013a; Parsons *et al*., 2008; Yan *et al*., 2009; Zarghooni *et al*., 2010). Pediatric and adult glioma gene expression profiles also have marked differences (Bax *et al*., 2010; Faury *et al*., 2007; Paugh *et al*., 2010, 2011, 2013; Pollack *et al*., 2002; Qu *et al*., 2010). These features emphasize the need to better stratify patients by their gene expression and mutant protein profiles to elucidate therapeutic vulnerabilities.

1.4 Histone mutations in cancer

A breakthrough in pediatric glioma biology occurred with the discovery of recurrent somatic mutations in *H3F3A,* one of two genes encoding histone variant H3.3, and less commonly in *HIST1H3B* encoding the H3.1 isoform (Bender *et al*., 2013; Chan *et al*., 2013; Khuong-Quang *et al*., 2012; Schwartzentruber *et al*., 2012; Sturm *et al*., 2012; Wu *et al*., 2012). By profiling pediatric glioblastoma tumors using whole-exome sequencing, these studies identified lysine-to-methionine mutations at lysine 27 (H3K27M) or glycine-to-arginine/valine mutations at glycine 34 (H3G34R/V) in *H3F3A* (**Figure 1.2**). This seminal discovery was the first identification of a histone mutation in a disease context.

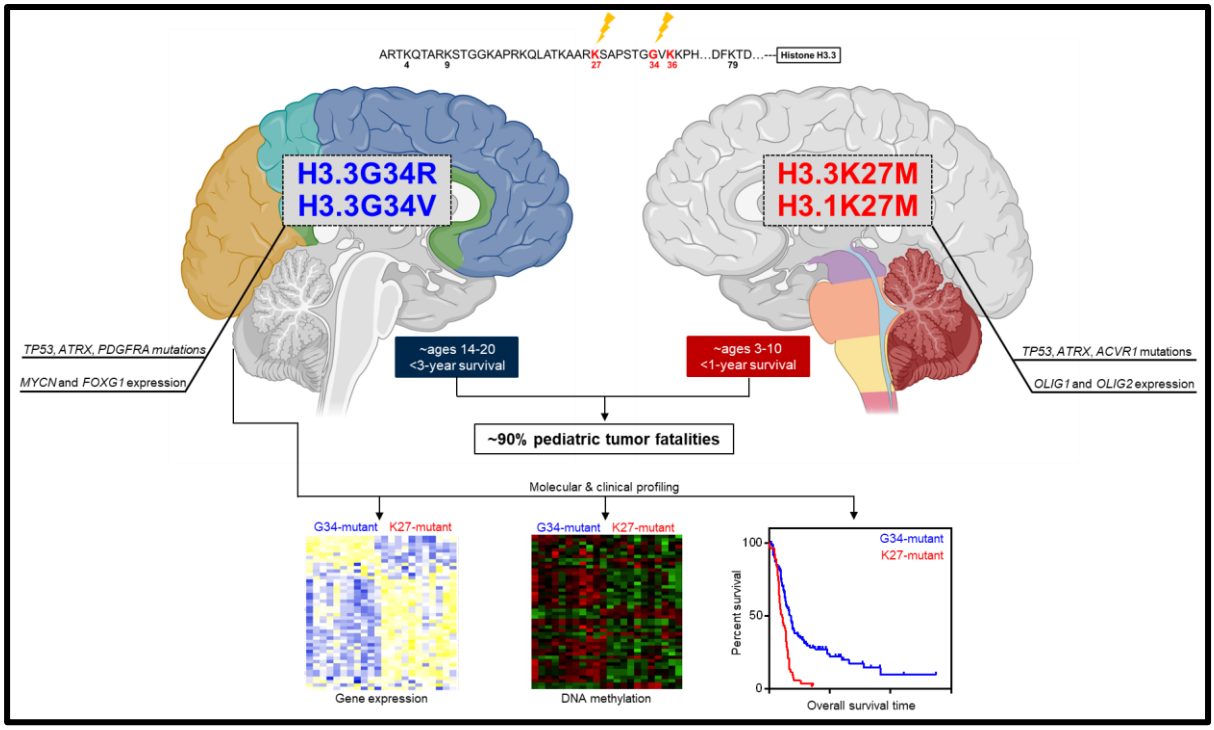

Figure 1.2. Different *H3F3A* mutations occur in distinct brain regions glioma patients. Several types of histone mutations in *H3F3A*, a gene encoding histone variant H3.3, have been identified in pediatric glioma patients. Valine or arginine substitutions of glycine-34, a residue that normally cannot be modified, are observed in tumors localizing to the cerebral hemispheres. However, tumors with methionine substitutions of lysine-27 occur in anatomically distinct regions, often in the brainstem, thalamus, and midline brain structures. Lysine-to-methionine mutations can also occur in *HIST1H3B*, a gene encoding for histone variant H3.1. Collectively, these tumors account for a large fraction of pediatric tumor fatalities. Histone mutations often co-occur with other mutations in *TP53*, *ATRX*, *PDGFRA*, and *ACVR1*. H3G34R/V tumors are characterized by MYCN amplification and FOXG1 expression. Contrastingly, H3K27M tumors exhibit robust OLIG1 and OLIG2 expression. Studies comparing the molecular and clinical characteristics of H3G34R/V and H3K27M tumors have revealed striking differences in activated gene expression programs, DNA methylation patterning, and overall patient survival times. Figure partially constructed with BioRender.com.

Analysis revealed that H3K27M mutations arise in younger populations in midline brain structures, such as the brainstem and thalamus, and are present in nearly 80% of all tumors in these regions (Khuong-Quan *et al.,* 2012; Sturm *et al.,* 2012). H3K27M tumors are marked by aggressive clinical courses and a median survival of 9-14 months (Mackay *et al.,* 2017; Sturm *et al.,* 2012). In contrast, H3G34R/V mutations were observed in older adolescents and young adults in the cerebral cortex and associated with better outcomes compared to H3K27M tumors (Mackay *et al.,*

2017; Sturm *et al*., 2012). These differences in age and anatomic region strongly suggested that each tumor type occurs in a different developmental context and engages distinct molecular programs to drive tumorigenesis (**Figure 1.2**). Co-occurring mutations were also identified in *TP53* and *ATRX*, a chromatin remodeling complex that deposits H3.3 at telomeric regions (Schwartzentruber *et al*., 2012; Sturm *et al*., 2012). Although *TP53* and *ATRX* mutations are commonly observed in adult gliomas, mutations in *H3F3A* have not been observed, further supporting the role of these mutant proteins in driving specific disease histology in the pediatric setting. In addition to H3K27M and H3G34R/V mutations, H3G34W/L mutations have been identified in giant cell tumors of bone (Khazaei *et al*., 2020; Jain *et al.,* 2020; Gong *et al*., 2020; Lutsik *et al*., 2020; Fellenberg *et al*., 2019; Behjati *et al*., 2013). Finally, H3K36M mutations, occurring in *H3F3B* also encoding H3.3, have been reported in chondroblastoma and squamous cell carcinoma of the head and neck (Behjati *et al*., 2013; Lu *et al*., 2016).

1.5 Histone mutations perturb DNA methylation and associate with distinct subgroups

The study by Sturm *et al.* (2012) performed genetic and epigenetic analysis of different glioblastoma types using samples from different anatomic locations and patient age demographics. They first noted that H3G34R/V and H3K27M mutations were mutually exclusive with IDH1 mutations more commonly observed in adult tumors. DNA methylation profiling and clustering analysis of these tumors revealed distinct subgroups, previously described by Verhaak *et al.* (2010, comprised of H3G34R/V, H3K27M, IDH1/2 (Isocitrate dehydrogenase 1 and 2), RTK (Receptor tyrosine kinase), and Mesenchymal tumor samples (Sturm *et al*., 2012). Results indicated that IDH1/2 mutant tumors had a global hypermethylation phenotype while H3G34R/V mutant tumors oppositely exhibited genome-wide hypomethylation, consistent with previous reports on IDH-mutant tumors (Turcan *et al.*, 2012). DNA methylation was significantly reduced in promoter and

non-promoter genomic regions within H3G34-mutants and this also occurred to a lesser extent in H3K27M patients, suggesting that histone mutations can perturb DNA methylation. Unlike mutant-IDH1/2 tumors where hypermethylation is a consequence of oncometabolite D-2HG accumulation (Dang *et al.,* 2009; Lu *et al.*, 2012), DNA methylation perturbations in the H3G34 tumors were especially intriguing since the glycine residue cannot be post-translationally modified and these tumors harbor no recurrent mutations in DNA methylation enzymes. The authors speculated that histone mutations interfere with DNA methylation mechanisms (**Figure 1.2**), and this was supported by later findings that both types of histone mutants alter genomic H3K27me3, H3K27ac, H3K36me3, and H3K4me3, all of which can promote or impede DNA methylation (Cedar and Bergman*,* 2009).

Analysis revealed that H3K27M and H3G34R/V mutations occurred in distinct regions within the brain. Examination of tumors within these groups uncovered unique transcriptomic profiles were also associated with DNA methylation status (**Figure 1.2**; Sturm *et al*., 2012; Mackay *et al*., 2017). Comparison of the gene expression signatures of each group demonstrated that H3G34R and H3K27M were associated with specific gene expression signatures indicative of the anatomic region from which they are derived. For example, thalamic gene signatures were enriched in H3K27M samples arising in midline and infra-tentorial structures while neocortex signatures were enriched in H3G34R/V tissues (Sturm *et al.,* 2012). This suggested that differences in anatomic location might provide cell lineage-specific markers and predictors of the histone mutant status. Indeed, differential gene expression analysis revealed that *OLIG1, OLIG2,* and *FOXG1* were top deregulated transcripts (**Figure 1.2**; Sturm *et al*., 2012). RNA expression of these markers closely associated with DNA methylation. For example, OLIG1/2 are markers of oligodendrocyte lineage, the suggested cell of origin for H3K27M gliomas (Nagaraja *et al.,* 2019),

and H3K27M tumors exhibited higher expression and lower promoter DNA methylation of these genes relative to H3G34R/V tumors. Conversely, FOXG1 is identified as a marker of neuro-progenitor cells thought to give rise to H3G34R/V gliomas and this marker was hypomethylated and upregulated relative to H3K27M tumors (Sturm *et al.*, 2012). Immunohistochemical staining of pediatric glioma tissue microarrays confirmed that these markers related with *H3F3A* and *IDH1* mutation status in samples. Collectively, these results from the Sturm *et al.* (2012) study supported the idea that these two tumor types expressing different *H3F3A* mutants are distinct entities both from a molecular and lineage perspective.

1.6 H3K27M drives tumor mechanisms in Diffuse Midline Glioma (DMG)

1.6.1 Polycomb Repressive Complex 2 (PRC2) and DNA methyltransferase (DNMT3) dysfunction arises in distinct cancer types

The key cellular growth control pathways that are deregulated in cancer are well studied. Research efforts have focused on understanding how activating mutations in oncogenes or inactivating mutations in tumor suppressors drive disease progression. In characterizing this, mutations in the epigenetic machinery – the readers, writers, and erasers of the epigenome were discovered. These enzymes are responsible for DNA methylation, nucleosome remodeling, and histone modifications. Mutations in epigenetic modifiers enzymes like DNA methyltransferases and Polycomb Repressive Complex 2 (PRC2) subunits have been noted (Shen *et al*., 2013). For example, DNMT1 and DNMT3A mutations occur in acute myeloid leukemia and colorectal cancer and have been associated with greater migration and self-renewal capabilities (Kanai *et al*., 2003; Ley *et al*., 2010; Xu *et al*., 2014; Yang *et al*., 2015). Loss of DNA methylation is also an important driver of oncogenes (Hur *et al*., 2014; Ehrlich *et al*., 2013). Interestingly, gain-of-function mutations in the EZH2 catalytic domain (such as Y641) and overexpression of EZH2 have been

reported in melanoma and follicular lymphoma, resulting in H3K27me3 elevation and increased growth rate (Bodor *et al*., 2013; Majer *et al*., 2012; Morin *et al*., 2010; Zhou *et al*., 2015). Other work has revealed loss of EZH2 activity and reduced H3K27me3 in breast and pancreatic tumors, suggesting oncogenic properties of EZH2 are context-dependent (Greer and Shi, 2012). In addition to these, various mutations have been reported in other histone and DNA modifying enzymes including TET1/2, BMI-1, LSD1, KDM6A, KDM5C, CBP/p300, and HDACs (see Baylin *et al.*, 2016 and Shen *et al*., 2013 for a comprehensive review).

Importantly, mutations in epigenetic modifying enzymes can directly disrupt gene expression and affect genome stability. One example of this is the epigenetic silencing of DNA mismatch repair proteins which can promote additional oncogenic mutations. In other cases, mutations in DNA methyltransferases can lead to DNA hypomethylation or hypermethylation, and aberrant transcriptional activation of oncogenes or silencing of tumor suppressors. Several strategies have been used to modulate or restore methylation. Notably, histone deacetylase (HDAC) inhibitors have been used alone or in combination with BRD4 and LSD1 inhibitors to block DNA methylation and rescue expression of repressed tumor suppressors (Fiskus *et al*., 2014a, 2014b).

EZH2 perturbations are widely implicated in cancer progression at both the level of tumors and immune cells. In addition to its role in promoting self-renewal of cancer stem cells, EZH2 overexpression or loss has been noted in cancers of the breast, lung, and prostate and associates with worse prognosis in these patients (Kleer *et al.*, 2003; Gonzalez *et al*., 2009; Matsubara *et al*., 2019; Varambally *et al*., 2002; Wei *et al*., 2008; Wu *et al*., 2019; Yu *et al*., 2007). Interestingly, EZH2 activity can impact adaptive and innate immune responses by modulating antigen presentation and tumor immune recognition via a process termed “immunoediting” within tumor

cells (Burr *et al*., 2019; Garrido *et al*., 2016; Rosenthal *et al*., 2019). For example, EZH2 is implicated in driving immune checkpoint protein PD-L1 expression and silencing of MHC Class I and II molecules within tumor cells through increased H3K27me3 deposition (Zhao *et al.*, 2019). Within T regulatory cells, EZH2 functions to block functions important for CD8+ T cell activation and inhibiting EZH2 within these cells can cause a robust immune response (Wang *et al*., 2018). EZH2 has been found to play a role in activation state and differentiation progression in other immune cells like natural killer cells (Yin *et al*., 2015; Bugide *et al*., 2018). As a result of these discoveries, selective inhibitors targeting DNMT (such as 5-azacytidine and 5-aza-CR) and EZH2 (such as EPZ005687, EPZ-6438, and GSK126) mutants have been the focus of drug development efforts (Han *et al*., 2019; Kang *et al*., 2020; Knutson *et al*., 2014; McCabe *et al*., 2012; Stazi *et al*., 2019; Verma *et al*., 2012; Yin *et al*., 2017). Despite major tumor profiling efforts, histone mutations have not been observed in cancer types with recurrent mutations in epigenetic modifiers like EZH2 and DNMT3A. This suggests that mutant histones like H3K36M, H3G34R/V, and H3K27M not only disrupt modifications at specific histone residues, but likely have other roles in modulating non-histone epigenetic modifiers via aberrant binding or genetic silencing.

1.6.2 H3K27M mutations inhibit Polycomb Repressive Complex 2 (PRC2)-catalyzed H3K27me3 activity

Before the identification of histone mutations, somatic mutations in histone modifying enzymes such as KDM6A and EZH2 had been associated with cancer and tumor progression (Baylin *et al*., 2016; Rotili *et al*., 2011). Not long after the discovery of H3K27M mutations in Diffuse Midline Gliomas (DMG) including Diffuse Intrinsic Pontine Gliomas (DIPG), studies probed the effect of the mutation on histone modifications in patient samples. This work uncovered that H3K27M causes a global loss of H3K27me3 and corresponding robust H3K27ac gains in

DIPG cells and tissues (Lewis *et al*., 2013; Bender *et al*., 2013; Chan *et al*., 2013; Venneti *et al*., 2013). These findings were repeatedly recapitulated in a cell-type independent manner in fibroblasts, astrocytes, neural stem cells, and patient-derived cell lines (Bender *et al.*, 2013; Chan *et al.*, 2013; Lewis *et al.*, 2013). Bender *et al.* (2013) used co-immunoprecipitation assays to extract HA-tagged H3WT or H3K27M histones and probed the effect on H3K27me3 and other histone marks. These experiments demonstrated that H3K27M expression led to reduced H3K27me3 and H3K27me2 both on endogenous and exogenous epitope-tagged histones. Reciprocal immunoprecipitation assays confirmed increasing binding interactions between exogenously expressed H3K27M and endogenous PRC2 components EZH2 and SUZ12, leading to the hypothesis that H3K27M actively disrupts EZH2 enzymatic activity via its aberrant binding. To test this, Bender and colleagues isolated chromatin lysates or immunoprecipitated HA-tagged H3.3WT or H3.3K27M from various cell line pairs and utilized these samples for histone methyltransferase assays. H3K27me3 was stimulated strongly by H3.3WT histones derived from whole chromatin lysate or immunoprecipitation while assays containing H3.3K27M histones had vastly reduced H3K27me3 activity. Using a similar approach, the authors performed demethylase assays and observed no differences in H3K27 demethylase KDM6A/6B activity when incubated under similar conditions with H3.3WT or H3.3K27M histones. Further experiments with H3K27M-containing oligonucleosomes demonstrated strong inhibition of EZH2/PRC2 activity while H3WT oligonucleosomes stimulated activity.

Chan *et al*. (2013) and Bender *et al.* (2013) also made a striking finding that despite global H3K27me3 loss across the genome, some loci retained or even gained H3K27me3 relative to H3WT cells. Using fresh tumor tissues from H3WT and H3K27M pediatric glioma patients, the study by Bender *et al.* made several other important findings regarding H3K27me3 distribution.

ChIP-seq peaks in each tumor sample were localized and analysis revealed that although H3K27me3 gain and loss occurred in promoter and intergenic regions, H3K27me3 retention occurred more often in intergenic regions while loss occurred more frequently at gene promoter elements. This finding about H3K27me3 loss was consistent with the notion that H3.3 and H3.3K27M are preferentially integrated into genic regions with high transcriptional activity. Integrated analysis of differential gene expression with H3K27me3 occupancy demonstrated a relationship between H3K27me3 and the upregulated gene profile. Intriguingly, some genes with differential expression were identified as canonical PRC2 targets. Given this observation, the H3K27me3 status at PRC2 target genes was interrogated in H3WT and H3K27M tumor tissues. These analyses revealed robust H3K27me3 loss associated with elevated gene expression of PRC2 target genes. Bender and colleagues also expanded on initial observation about DNA methylation in pediatric mutant gliomas made by Sturm *et al.* (2012). Here, whole-genome bisulfite sequencing was performed on primary tumor tissues from H3WT and H3K27M gliomas. Results demonstrated distinct DNA methylation patterns and DNA hypomethylation associated with elevated gene expression in H3K27M relative to H3WT samples. The authors then segregated loci with hypo- and hypermethylated promoters and observed inverse patterning with H3K27me3 occupancy at transcription start sites, supporting previous work that link H3K27me3 and DNA methylation processes (Cedar and Bergman, 2009; Schlesinger *et al*., 2007; Viré *et al*., 2006). Notably, informatics analysis demonstrated that a nearly 75% of the upregulated genes in H3K27M samples exhibited H3K27me3 loss, DNA hypomethylation, or both events while suppressed genes showed less perturbations to either modification.

Cell-based models expressing epitope-tagged H3.3K27M, H3.3G3R/V, and other H3K27-substituted histone transgenes confirmed the selective ability of H3.3K27M and H3.3K27I mutants

to reduce H3K27me3/me2 and elevate H3K27ac *in cis* and *in trans* (Lewis *et al*., 2013). In addition, western blotting of H3.3G34R/V constructs demonstrated elevated H3K27me3 and H3K36me3 on exogenous histone, and corresponding H3K36me3 gain on endogenous histone, providing the first evidence that the mutant histone blocks H3K36me3 *in cis* while allowing H3K36me3 gain *in trans.* However, no major effects on global H3K9me3 or H3K4me3 were noted for either mutant (Lewis *et al*., 2013).

The mechanism of how H3K27M causes these effects was further investigated by Lewis *et al.* (2013) using PRC2 methyltransferase assays where wild-type H3.3 or heterotypic H3.3K27M mono- and oligo-nucleosomes were incubated with purified PRC2. Results here indicated that the K27M substitution could effectively block PRC2-mediated methylation while K27R, K27Q, or K27A substitutions failed to elicit similar inhibition. Furthermore, clever experiments were designed to incubate wild-type H3.3 and heterotypic H3.3K27M mono- and oligo-nucleosomes with PRC2 in the presence of H3K27me3 peptide expected to stimulate PRC2 activity. Indeed, results demonstrated that increasing amounts of H3K27me3 were sufficient to elevate H3K27 methylation in a dose-dependent manner on wild-type, but not H2K7M-containing nucleosomes.

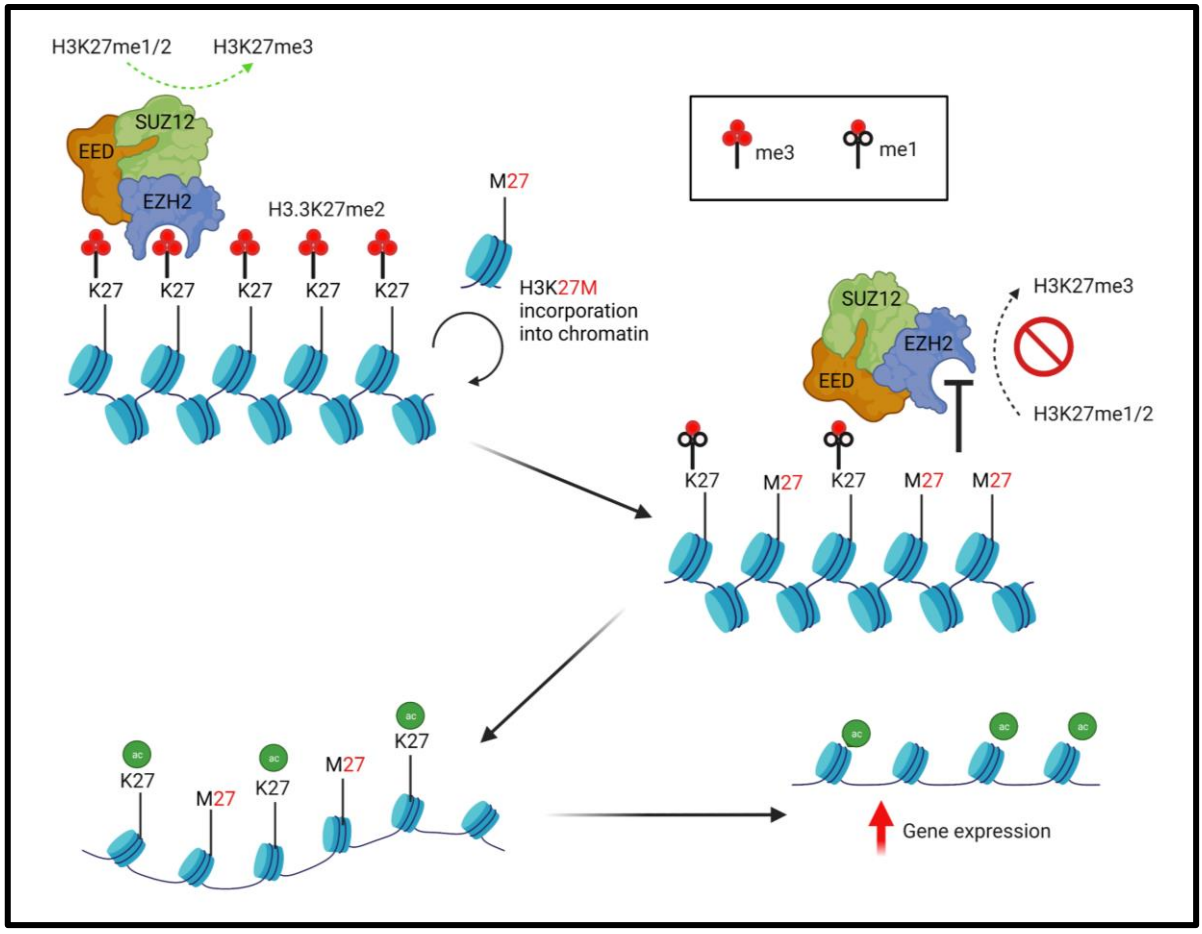

Figure 1.3. Mechanism of EZH2 inhibition by H3K27M oncohistones.
Schematic illustrating the proposed H3K27M-mediated inhibition of EZH2 catalytic activity and spreading on chromatin. As H3K27M histones are incorporated in chromatin, H3K27M binds and inhibits EZH2 activity, leading to H3K27me3 loss and H3K27ac gain.

These results suggested that H3K27M was actively blocking the activity of a component of the PRC2 complex, the Enhancer of Zeste Homolog 2 (EZH2), responsible for H3K27me2 to H3K27me3 conversion (**Figure 1.3**). Lewis and colleagues expressed EZH2 and related EZH2-Y641N constructs in cells expressing H3.3K27M and H3.3K27R to explore this possibility. The co-expression of H3.3K27M and EZH2-Y641N mutant abrogated the ability for H3.3K27M to reduce H3K27me3, supporting the notion that H3.3K27M exerts its inhibition on PRC2 by directly interacting with EZH2. Later studies by Justin *et al.* (2016) and Jiao *et al.* (2015) provided a co-

crystal structure of H3K27M peptide binding with EZH2 that confirmed the initial inhibition hypothesis (**Figure 1.3**). Taken together, these findings set the stage for future work analyzing how H3K27me3 and H3K27ac are perturbed in DMG cells at the genome-wide level and how epigenetic reprogramming might create therapeutic vulnerabilities that can be exploited.

1.6.3 Epigenetic landscapes are remodeled in H3K27M cells

Understanding the chromatin landscape and how it is perturbed by H3K27M "oncohistone" expression has been the focus of recent, international research efforts. Studies have mapped histone modification changes at enhancers and promoters, and expression profiling has been carried out on isogenic H3K27M/H3WT model cells and patient-derived DMG/DIPG cells to elucidate what epigenetic patterns and corresponding changes in gene expression are recapitulated between cell models. Here, we will discuss the most critical and insightful findings.

Piunti *et al.* (2017) performed the first direct profiling of the H3K27M histone distribution in patient-derived DIPG cell lines. Despite a global loss of H3K27me3, this group astutely noticed that H3K27me3 was retained and sometimes even gained at specific genomic regions and these regions excluded PRC2 proteins and H3K27M histones. Similar systematic analysis of genome-wide H3.3K27M and H3K27ac revealed that the ChIP-seq peaks for mutant histone localized with H3K27ac peaks, supporting previous biochemical assays demonstrating the presence of H3K27M-H3K27ac heterotypic nucleosomes from cells stably expressing H3K27M.

The earliest studies on the epigenetic modification landscape in DIPG noted that some regions harbored robust H3K27me3 (Bender *et al*., 2013; Chan *et al*., 2013). To further dissect this, the localization of H3K27me3, RNA polymerase II, and PRC2 components (SUZ12 and EZH2) were analyzed by Piunti *et al.* (2017) to determine relationship with H3K27ac and H3.3K27M. First, it was noted that various genomic regions with concurrent H3K27ac, RNA Pol

II, and H3.3K27M were devoid of PRC2 complex protein binding. However, in regions known to be repressed by PRC2 such as the HOX gene cluster, EZH2, SUZ12, and H3K27me3 colocalization was observed but very low H3.3K27M and H3.3 enrichment was present. One possibility to explain this dichotomy is that strong PRC2 target regions do not undergo histone replacement and thus do not incorporate H3.3 or H3.3K27M. However, this explanation does not account for how H3.1K27M histones, whose deposition occurs in different genomic regions, also exclude the PRC2 complex. Overall, results from the H3.3K27M ChIP assays challenged the hypothesis that H3K27M had an increased binding affinity for EZH2, postulated by the biochemical studies probing the ability of EZH2 to carry out its methylation reaction on tagged H3.3 wild-type or H3K27-mutant nucleosome substrates. These observations argued for an exclusionary model where H3K27M repels PRC2, and consequently H3K27me3, from genomic regions with H3K27ac.

1.6.4 PRC2 activity and CDKN2A silencing are interlinked and implicated in DIPG pathogenesis

Results from the initial ChIP-seq studies brought up two main questions. First, if H3K27me3 is indeed retained as specific loci, what role does it play in disease progression? Second, what is the significance of gained H3K27ac for driving transcription, and could this present an opportunity to target regions with enhanced transcription for therapeutic benefit? Experiments involving knockdown of EZH2 or EED revealed impaired growth in human DIPG cells, suggesting a dependence on remaining PRC2 activity in the context of H3K27M expression for cells to retain proliferative capacity (Piunti *et al.*, 2017). Analysis of canonical PRC2 targets with H3K27me3 retained demonstrated that *CCND2* (coding for Cyclin D2) and *CDKN2A* (coding for p16) genes had robust, concomitant SUZ12, EZH2, and H3K27me3 enrichment in SF8628 and

DIPG-IV patient cells. Early epigenetic silencing of p16 before tumor progression has been noted in lung cancer and breast cancer (Holst *et al*., 2003; Swafford *et al*., 1997). Strikingly, PRC2 proteins have been demonstrated to modulate p16/INK4A gene silencing via a BMI-1 dependent mechanism (Bracken *et al*., 2007). The finding that p16 is epigenetically silenced in DIPG is important because this protein is a critical mediator of cell division by controlling the rate of progression from G1 to S phase. Furthermore, Piunti *et al.* (2017) observed that pharmacological inhibition of EZH2 with EPZ6438 resulted in reduced proliferation and p16 upregulation. RNA-sequencing from cells treated with EPZ6438 showed that genes in regions with strong PRC2 binding were upregulated upon EZH2 inhibition, and further corroborated findings about p16 de-repression.

Given the observation of focal, elevated H3K27me3 at specific genes (Bender *et al.,* 2013; Chan *et al.,* 2013), two other independent studies discovered that remaining EZH2 activity was necessary for DIPG growth in mouse and human DIPG models (Cordero *et al.,* 2017; Mohammad *et al.*, 2017). Cordero *et al.* (2017) established an RCAS mouse model of H3.3WT and H3.3K27M DIPGs. Using their model, they performed RNA-seq analysis on murine tumor tissues and noted upregulated and downregulated PRC2 target genes. ChIP-*q*PCR was performed on murine tumor-derived cell lines at PRC2 target loci, including *Cdkn2a,* which revealed elevated H3K27me3 at the p16 promoter in H3K27M cells. However, reducing global H3K27me3 and p16 promoter-localized H3K27me3 with GSK343 was insufficient to rescue p16 expression. Based on this result, DNA methylation status was investigated at the p16 promoter CpG island and this revealed hypermethylation in H3K27M cells derived from murine tumors. Strikingly, inhibition of DNA methylation with decitabine could elevate p16 expression. Even though this group did not find that H3K27me3 modulation could regulate p16, they did discover that p16 silencing accounts for the

survival difference between H3WT and H3K27M tumor models *in vivo.* Experiments with p16-null mice harboring H3WT and H3K27M tumors showed no survival difference, supporting the idea that H3K27M tumors suppress p16 to drive tumor growth.

Mohammad *et al.* (2017) independently reasoned that the efficacy of EZH2 inhibitors in tumors with EZH2-activating mutations might be translatable to DIPG where aberrant H3K27me3 could silence tumor suppressor genes or negative cell cycle regulators (**Figure 1.4**). First, they determined if Ezh2 inhibitors, GSK-343 and EPZ6438, could reduce cell proliferation in mouse PDGFB-/H3K27M-expressing neural stem cells (NSCs). The importance of Ezh2 for tumor growth *in vivo* was also evaluated using PDGFB-/H3K27M-expressing NSCs generated from a mouse with a conditional Ezh2 allele. Cells were harvested and subjected to 4-hydroxytamoxifen treatment before orthotopic reimplantation where Ezh2 deletion resulted in significantly longer mouse survival compared to vehicle-treated cells. This observation was validated with a second approach where NSCs with the conditional allele were directly implanted into the pons and mice were subsequently treated with tamoxifen which also resulted in significantly increased survival time.

At the time it was known that Polycomb group proteins such as Ezh2 could target and silence the p16, a tumor suppression protein encoded by *Cdkn2a* (Gil *et al.*, 2006). Mohammad and colleagues made the clever observation that p16 was silenced in the H3K27M NSCs as compared with H3WT NSCs, leading them to rationalize that p16 silencing makes H3K27M NSCs sensitive to Ezh2 inhibition. Interestingly, treatment with either EZH2 inhibitor could reduce *Cdkn2a* promoter-localized H3K27me3 and subsequent immunoblot analysis confirmed upregulated p16 expression. Similar treatment of several human H3K27M cells could attenuate

H3K27me3 at the p16 promoter, activate p16 expression, and slow cell growth as determined by cell cycle phase analysis and growth assays.

It had been reported that TP53 inactivation can elevate p16 expression (Verhaak *et al*., 2010). To probe this further, Mohammad *et al.* (2017) performed *Trp53* knockdown or deletion in their H3K27M NSC model and found it could abrogate the growth reduction from EZH2 inhibition. Analysis of a panel of human DIPG cell lines confirmed p16 suppression and robust H3K27me3 at its locus in all models tested, but some cell lines also had *TP53* deletion, suggesting that p16 is suppressed in DIPGs in a TP53-independent manner. Forced p16 expression in human DIPG cells could slow growth, and importantly, p16 knockout rendered the cells insensitive to EZH2 inhibition. In line with this, H3WT cells that robustly expressed p16 showed little sensitivity to EZH2 targeting. These results suggested that DIPG cell sensitivity to EZH2 inhibition is specifically dependent on the p16 induction event and functional p16.

Mohammad *et al.* (2017) also performed further ChIP-seq analysis of H3WT and H3K27M NSC models and analyzed H3K27me3 at CpG islands known to be targeted by PRC2. Comparison of relative H3K27me3 signals in H3WT and H3K27M cells led to identification of loci that fell into unchanged, increased, or reduced categories. Not surprisingly, it was noted that in genes with high H3K27me3 enrichment in H3WT were less susceptible to H3K27me3 loss in H3K27M NSCs. Correspondingly, genes in the unchanged category (i.e. genes in H3K27M NSCs that retained H3K27me3 to extent seen in H3WT NSCs) had the highest H3K27me3, SUZ12, and RING1B occupancy. This relationship between the extent of H3K27me3 retention and the initial H3K27me3 enrichment was demonstrated by experiments where untransduced NSCs were treated with an EZH2 inhibitor and H3K27me3-enriched loci were observed to be most resistant to inhibition. Furthermore, sites with the highest H3K27me3 in both H3WT and H3K27M transduced

NSCs were resistant to H3K27me3 loss upon EPZ6438 treatment, but sites with intermediate enrichment experienced robust losses. Interestingly, comparison of H3K27me3 at orthologous human genes in human DIPG cell lines to those with unchanged H3K27me3 in H3K27M *versus* H3WT NSCs revealed that human cells have robust H3K27me3 at these loci. Genes with reduced H3K27me3 in H3K27M *versus* H3WT NSC had correspondingly less H3K27me3 enrichment levels in human cells.

This key work highlighted the role of residual PRC2 activity in silencing critical cell cycle regulators and cell fate transcription factors. Notably, the experiments by Mohammad and colleagues provided a working model for EZH2 targeting where weak PRC2 targets may be easily deregulated by H3K27M deposition while stronger PRC2 targets can overcome H3K27M-mediated H3K27me3 disruption and maintain gene silencing. Thus, the epigenetic landscape at these regions is relatively unperturbed by H3K27M and provides a unique therapeutic window to de-repress genes important to slow tumor growth. It is important to note, however, that it remains unknown if H3.3K27M is deposited at strong PRC2 targets. Since PRC2 targets are enriched for H3K27me3, there is a possibility that nucleosomes in this genomic region do not undergo high rates of turnover, and consequently do not incorporate high levels of H3.3K27M. Consistent with this hypothesis, brief analysis of ChIP-seq for H3K27M from Wang *et al.* (2021) demonstrates little H3K27M histone incorporation at the *CDKN2A* locus in human DIPG cells. Data from Mohammad *et al.* (2017) showed some level of p16 expression in H3WT NSCs which was suppressed by H3K27M-expressing NSCs. The H3K27M NSCs also exhibited higher H3K27me3 at the *Cdkn2a* promoter. Although *Cdkn2a* is a PRC2 target (discussed earlier), the mechanism by which H3K27M expression causes accumulation of H3K27me3 above the levels seen in H3WT NSCs remains to be determined.

In addition to targeting EZH2, other work has suggested that targeting H3K27 demethylation enzymes to elevate H3K27me3 levels is a potential strategy. Hashizume *et al.* (2014) investigated the efficacy of GSK-J4, an inhibitor of KDM6A and KDM6B lysine 27 demethylases (**Figure 1.4**). Results from cell proliferation and apoptosis assays demonstrated differential and significant cell death in H3K27M cells compared with H3WT cells. Importantly, GSKJ4 could effectively raise H3K27me3 in a time-dependent manner. Genetic targeting of KDM6A and KDM6B suggested that KDM6B loss, but not KDM6A, could slow cell growth of H3K27M-expressing, but not H3WT, cells. Furthermore, treatment of KDM6B-depleted cells failed to elicit cytotoxic effects of GSKJ4, suggesting targeting KDM6B is effective in causing DIPG cell death. Flank and brain models using H3K27M patient-derived cells including SF7761 and SF8628 showed a marked reduction in tumor signal and elevated intratumoral H3K27me3, corresponding with increased survival (Hashizume *et al.,* 2014). Collectively, these results showed that DIPG cells with H3K27me3 loss have a unique vulnerability, not observed in H3WT glioma models, to KDM6B inhibition that might be clinically beneficial.

1.6.5 Bromodomain and BET protein inhibition can therapeutically target aberrant enhancer activation

Given the global gain in H3K27ac observed by western blotting and mass spectrometry on histones extracted from H3.3K27M-expressing cells in several studies (Lewis *et al*., 2013; Chan *et al*., 2013), Piunti and colleagues set out to understand the functional role of this acetylation. To do this, they established an inducible cell model system to express H3.3K27M and performed ChIP-seq for H3K27ac to compare the distribution between control and mutant cells. Strikingly, the H3K27ac peak distribution was similar between the cells, however H3.3K27M and H3.3 localized with H3K27ac (as noted in the human DIPG lines). H3K27ac was gained significantly

in regions with pre-existing peaks in the control cells, suggesting that the mutant histone specifically modulates H3K27ac in areas already decorated with this modification. Moreover, they found that this effect on H3K27ac was reversible upon termination of expression induction.

H3K27ac is a marker of active promoters can be recognized by BET family members (BRD2, BRD3, BRD4, and BRDT) that play a role in transcription initiation and elongation via their recruitment of RNA polymerase II to transcription start sites (Jang *et al*., 2005; Leroy *et al*., 2008). Targeting the core transcription process has been a fundamental approach in cancer biology research (Dawson *et al*., 2011; Delmore *et al*., 2011; Filippakopoulos *et al*., 2014; Loven *et al*., 2013; Sengupta *et al*., 2015). With this in mind, H3.3K27M and H3K27ac enrichment were mapped in relationship to BRD2 and BRD4 occupancy in the same promoter and enhancer regions, demonstrating significant overlap (Piunti *et al*., 2017). Excitingly, treatment of DIPG cells with BET inhibitor, JQ1, slowed cell growth and reduced H3K27ac in a time-dependent manner. Transcriptomic and epigenomic analysis of JQ1-treated cells revealed that genes undergoing downregulation had enrichment of H3K27M, H3K27ac, and BRD2/4 proteins in non-treated cells. Additionally, markers of neuronal differentiation were upregulated upon JQ1 treatment, but no deregulation of *CDKN2A* was seen. Preclinical animal models established with SF7761 and DIPG-IV and treated with JQ1 exhibited a positive response to therapy, highlighting the role H3K27ac and associated bromodomain proteins play in tumor progression and providing a new therapeutic angle (**Figure 1.4**; Piunti *et al.,* 2017).

Work by Nagaraja *et al.* (2017) further investigated BRD4 inhibition via genetic knockdown and with JQ1 in addition to targeting CDK7, a kinase that phosphorylates RNA polymerase II at serine residues, with THZ1, an inhibitor that irreversibly inhibits CDK7 (**Figure 1.4**). Nagaraja and colleagues found that JQ1 and THZ1 treatment decreased the viability of DIPG

cells *in vitro*. Additionally, BRD4 genetic knockdown or THZ1 pharmacologic treatment could slow tumor growth in several human xenograft models *in vivo.* As a result, the group investigated potential synergy of each compound with Panobinostat (used by Grasso *et al.*, 2015). They observed synergy between both inhibitors and Panobinostat, and when JQ1 and THZ1 were combined. Interestingly, treatment of Panobinostat-resistant DIPG cells with THZ1 and JQ1 demonstrated that cells were only sensitive to THZ1, suggesting that JQ1 and Panobinostat modulate similar genetic targets. Indeed, RNA-sequencing studies comparing Panobinostat-, THZ1-, and JQ1-treated cells revealed that Panobinostat/JQ1 deregulated similar targets related to neuron development while THZ1 disrupted a wide range of unique targets including genes associated with transcriptional processes. Profiling of super-enhancers in these DIPG cell lines revealed high H3K27ac enrichment at genes involved in oligodendroglial lineage and highlighted top targets like NOTCH and MAPK signaling pathway that could be targeted for therapy. Importantly, enhancer analysis uncovered novel targets like Ephrin signaling that is important for axon pathfinding, a result that may explain why DIPG cell migrate and form close association with neural synapses. Previous work by Grasso *et al*. (2015) showed that Panobinostat surprisingly raises H3K27me3, leading to the hypothesis that H3K7me3 gain could cause H3K27ac loss specifically at enhancers. Chip-seq results from DIPG cells treated with THZ1 and Panobinostat did in fact reveal a decrease in H3K27ac at super-enhancers and this correlated nicely with downregulated gene expression. Overall, these results suggested that combined Panobinostat and THZ1 treatment is a strong therapeutic strategy to reverse enhancer activation driving key processes in DMG/DIPG tumors.

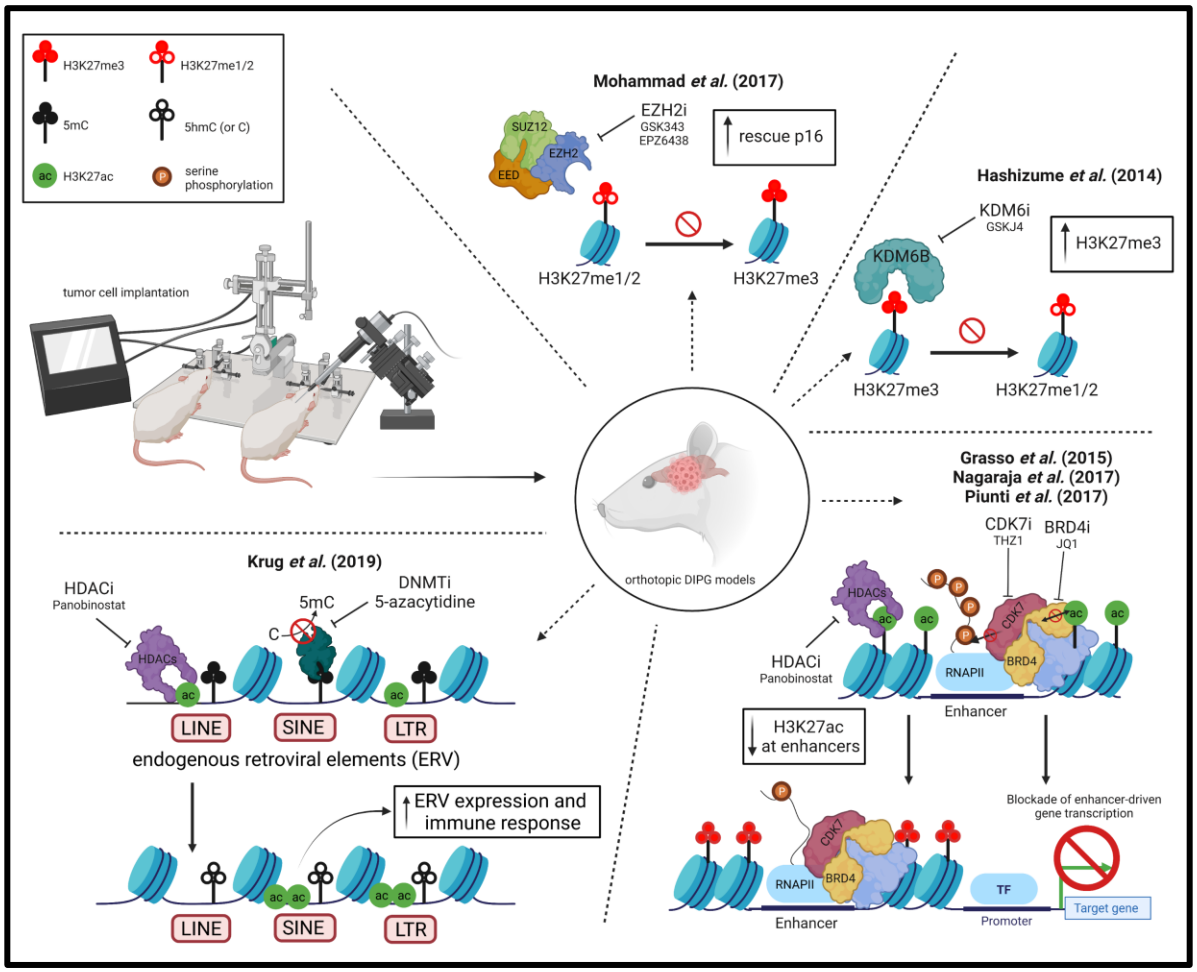

Figure 1.4. Key preclinical therapeutic approaches investigated for H3K27M gliomas. Schematic depicting the overall aims of therapeutic studies for H3K27M tumors. Mohammad *et al.* (2017) utilized EZH2 inhibitors to further lower H3K27me3, de-repress p16 expression, and slow tumor growth. Hashizume *et al.* (2014) investigated the efficacy of lysine demethylase (KDM6) inhibitors in reversing H3K27me3 loss. Grasso *et al.* (2015) performed a study with histone deacetylase (HDAC) inhibitor Panobinostat which surprisingly elevated H3K27me3. Nagaraja *et al.* (2017) followed a similar approach in using Panobinostat and evaluated potential synergy with cyclin dependent kinase 7 (CDK7) inhibitors and bromodomain inhibitor JQ1 in lowering H3K27ac at super enhancers implicated in DIPG. Krug *et al.* (2019) combined HDAC inhibitors with DNA methylase inhibitor, 5-azacytidine, to determine if H3K27ac-enriched endogenous retroviral elements can be exploited to induce viral mimicry and modulate processes for immune cell activation. Figure constructed with BioRender.com.

1.6.6 Dysregulated epigenetics in intergenic regions

Although H3K27M cells exhibit global H3K27ac gain, H3WT and H3K27M glioma cells are found to have roughly equal numbers of active and enhancer promoter regions marked by the H3K27ac modification. Intriguingly, CRISPR-mediated correction of H3K27M-expressing BT245 and DIPG-XIII did not dramatically change H3K27ac levels or distribution (Harutyunyan *et al*., 2019; Krug *et al.,* 2019). Krug *et al.* (2019) undertook an analysis to compare the H3K27ac profile with ATAC-seq data, concluding that H3WT cells had a higher overlap of acetylation peaks in open chromatin. Similar overlap analysis for H3K27M cells showed relatively less overlap which prompted investigation to identify other genomic regions (outside promoters and enhancers) harboring H3K27ac and determine their functional role. Surprisingly, H3K27ac enrichment was observed in intergenic regions, specifically at repetitive elements (LINE, SINE, and LTR) in cell lines and tumor tissue. Normally, these regions are silenced and marked by H3K27me3, H3K9me3, and/or DNA methylation, suggesting that H3K27ac deposition in these regions is an aberrant event that occurs in the disease state (Krug *et al*., 2019). Interestingly, endogenous retroviruses (ERVs) are often expressed from these regions. Comparison of parental and H3.3K27M knockout DIPG cells revealed increased expression of ERVs and H3K27ac occupancy at repeat elements in the presence of H3.3K27M expression. A similar pattern of elevated ERV expression correlated with enhanced H3K27ac in human H3K27M tumors tissues compared with H3WT counterparts, supporting the notion that aberrant acetylation plays a role in promoting ERV expression.

Whereas previously work had revealed that loci are inappropriately silenced (i.e. *CDKN2A* discussed earlier) and rescued expression was favorable, here, the upregulation of ERVs opens a different type of therapeutic opportunity. ERV expression can activate the immune system

(Chiappinelli *et al*., 2015; Rouloi *et al*., 2015). Interferon type I signaling, driven by ERVs, induces expression of interferon stimulated genes (ISGs). ISGs are effectors for the innate immune response (Wong *et al*.; 2016). Thus, one potential therapeutic approach for DIPG is enhancing already-present ERV expression. To test this idea, Krug *et al.* (2020) designed experiments with panobinostat (a histone deacetylase inhibitor) and 5-azacytidine (a DNA demethylating compound). HDAC inhibitors like panobinostat were identified as promising therapeutic compound in work by Grasso *et al.* (2015) who conducted the first large drug screen for DIPG. Results from that study found that shRNA-mediated knockdown of histone deacetylases 1 and 2 (HDAC1/2) could slow DIPG cells growth and recapitulated cytotoxicity seen with panobinostat *in vitro* (**Figure 1.4**). In addition, systemic or convection enhanced delivery of panobinostat in orthotopic DIPG animal models demonstrated survival benefit (Grasso *et al.,* 2015).

Krug and colleagues found that H3K27M cells treated with panobinostat and/or 5-azacytidine enhanced ERV expression and caused ISG elevation (**Figure 1.4**). Importantly, the effect was abrogated upon H3.3K27M knockout, supporting the hypothesis that mutant histones play a role in priming DIPG cells for ERV expression. In contrast to other studies proposing the use of BET inhibitors to eliminate spurious transcription at enhancers (Piunti *et al*., 2017), the study by Krug *et al.* (2020) suggested that BET inhibitors might eliminate a therapeutic window to target and enhance ERVs. Both therapies seem to be effective, however, this highlights the need to characterize tumors in terms of the enhancer-associated expression properties to define an appropriate therapeutic route.

We should note that the efficacy of panobinostat has been controversial, especially in light of a study by Hennika *et al.* (2017). This study found that panobinostat was almost equally effective in reducing cell viability of H3WT and H3K27M cells derived from murine tumors.

Furthermore, *in vivo* panobinostat treatment of H3K27M tumors harboring p53 deletion and PDGFB expression revealed no survival benefit. These results suggest that while Panobinostat is effective *in vitro*, treatment *in vivo* fails to confer survival benefit because drug toxicity limits the therapeutic doses that can be achieved. Overall, Hennika *et al.* (2017) highlights that Panobinostat is a potent inhibitor, but more work is needed to overcome these challenges and design efficacious delivery mechanisms for such compounds.

1.6.7 Overall genome architecture and cells-of-origin for DIPG

Transcriptomic profiling by Harutyunyan *et al.* (2019) revealed that CRISPR-Cas9 mediated knockout (KO) of H3K27M in BT245 and DIPG-XIII cells results in minimal transcriptomic changes. Even with global H3K27me3 loss at many promoters, only a small subset of these genes is upregulated in H3K27M-expressing cells compared to KO counterparts. However, orthotopic implantation of corresponding parental and KO cells *in vivo* demonstrates reduced growth upon H3K27M removal, implicating it is important for tumorgenicity (Harutyunyan *et al*., 2019).

A similar phenotype was found by Silveira *et al.* (2019) who found that *H3F3A* knockdown, but not *H3F3B* targeting, in H3K27M-mutant SJ-DIPGx7, SJ-DIPGx37, and SU-DIPG-VI cells could drastically slow tumor growth and increase survival of intracranial xenograft models. Sequencing analysis of genes upregulated in parental *versus* H3K27M knockout cells demonstrated good overlap with known gene expression changes in primary DIPG samples. However, *H3F3A* knockdown did not shift the relative distribution of H3K27me3 deposition within genic, enhancer, or repeat regions, suggesting that the initial level of H3K27me3 at a subset of genes determines how they are deregulated after H3K27M expression induction. Indeed, some have suggested that the lack of observed loss-of-function mutations for EZH2 in DIPG tumors

suggests that H3K27M itself may have H3K27me3-independent consequences for these tumors. This is supported by findings that H3K27M colocalized in regions with enhanced H3K27ac and low PRC2 complex binding. However, more work is needed to appreciate the significance of the limited transcriptomic changes.

Little work has been carried out to understand the developmental state of DIPG cells. Pioneering work has now characterized the composition of malignant DIPG cells and began to dissect the developmental programs present. Filbin *et al.* (2018) utilized single cell RNA-sequencing to profile the transcriptomes of H3K27M tumors derived from six patients. Cells were categorized into four programs including cell cycle, astrocyte differentiation (AC), oligodendrocyte differentiation (OC), and oligodendrocyte precursor cell (OPC). Interestingly, OPC-like programs were present in a large fraction of cells isolated from each tumor. AC, OC, and OPC-like cells in the normal developing brain were profiled for PRC2 target gene expression. Normal brain OPC-like cells exhibited the highest PRC2 target gene expression, suggesting that DIPG cells in an OPC-like program have de-repression of PRC2 target gene expression due to the PRC2 inhibition exerted by H3K27M mutant histones. Comparison of H3K27M tumors with other non-DIPG tumor types reveals an enrichment for PRC2 target genes, supporting data from scRNA experiments. Several previous studies had suggested that PRC2 target genes remain silences in DIPG to drive tumor progression. Thus, the finding that OPC-like cells are drivers in H3K27M gliomas necessitates future work on how de-repressed PRC2 targets contribute to disease and whether these genes are strong or weak PRC2 targets.

Similarly, few studies have thoroughly investigated how H3K27M remodels the chromatin on a macroscopic level. A recent, three-dimensional characterization of the DIPG genome using high-resolution Hi-C by Wang *et al.* (2021) lends insight here. This study found that DIPGs exhibit

a unique H3K27ac enhancer landscape and that H3K27ac colocalized with H3K27M at enhancer regions and TAD boundaries. Analysis revealed activated enhancers that were specific to DIPG compared to other GBM subtypes, and that these DIPG enhancers were characterized by specific transcription factor motifs associated with *FOXO, ASCL1, SOX, STAT,* and *SMAD*.

Unique loop regions that tended to span longer genomic distances were identified in DIPGs that closely recapitulated some transcriptomic data. For example, a differential loop region was identified between the *OLIG2* promoter region and its associated enhancer (Wang *et al*., 2021). *OLIG2* was also identified as a specific motif enriched in active enhancers for DIPG. This discovery is of pinnacle importance. It suggests that H3K27M may reprogram promoter-enhancer connectivity for transcription factors (TF) to promote their expression and co-enrich enhancer-promoter connectivity for TF downstream targets. In assessing this, it will be critically important to conduct further analysis to determine if looping structures are reversible upon H3K27M knockout or induction in cells to probe the dynamics of loop structure establishment. Importantly, Hi-C experiments on DIPG cells treated with bromodomain inhibitor BRD4i and degrader dBET6 demonstrated reduced enhancer H3K27ac and disrupted enhancer-promoter looping interactions such as that at *OLIG2* (Wang *et al.,* 2021). This puts forward the idea that transcription factor circuits can be impeded by interfering with loop formation (both for the transcription factor itself and their downstream targets) that reinforces a preferred molecular program. Taken together with data suggesting little transcriptomic change occur with H3K27M induction, the field will need to focus on whether chromatin interactions play a more dominant role in fine tuning transcription for key genes rather than major transcriptomic changes being responsible for tumor initiation/growth.

1.6.8 Probing regional specificity and establishing preclinical models of H3K27M glioma

The discovery of histone mutations in pediatric cancers has prompted researchers to establish models to understand how each histone mutation drive oncogenic signaling. Cell modeling for therapeutic and mechanistic discovery has involved the use of patient DIPG cell lines and mouse neuronal stem cells harboring isogenic mutations. Additionally, fetal neural stem cells from different anatomic regions of the human brain have been utilized to parse the effects of histone mutations in cells of different lineage and to understand the regional specificity of each mutation. These types of models are useful because H3K27M gliomas show heterogeneity between samples. The lack of cell lines established from H3WT gliomas arising in the same hindbrain context, necessitating comparisons with H3WT cortical gliomas, also make it difficult to make accurate comparisons within the same developmental context. Another challenge in the field has been the development of *in vivo* models that faithfully reflect tumor initiation and progression processes and provide corresponding *in vitro* systems to isolate different cell populations (cycling *versus* non-cycling, for example) from each tumor. Silveira *et al.* (2019) make a compelling argument here that patient cell lines have differences in the enrichment of astrocyte and oligodendrocyte signatures and may only represent a fraction of the cells present in a primary tumor.

Early studies on H3K27M and H3G34R/V tumors heavily focused on understanding epigenetic reprogramming occurring at the genome level. Comparatively less work has been done to understand why histone mutant occur in cells of specific lineage and the reason for this specificity. Studies have posited that DIPGs originate in neural stem cells or oligodendrocyte precursor cells (Filbin *et al.,* 2018; Funato *et al.,* 2014; Monje *et al.,* 2011). To further study this, Nagaraja *et al.* (2019) investigated the effects of expressing H3K27M oncohistones in neural

precursor cells (NPCs), pre-oligodendrocyte precursor cells (pOPCs), and early oligodendrocyte precursor cells (eOPCs). These three cell types represent progressive differentiation of the pluripotent stem cells from which they are derived. First, intrinsic enhancer landscapes of the NPCs, pOPCs, and eOPCs were compared with DIPG tumor tissues, and this yielded stronger correlations with pOPC and eOPC lineages. This study also profiled superenhancers present in primary DIPG tumor samples (but not normal pons tissue) and profiled associated transcription factors. Strikingly, results suggested that the super enhancers in H3.1K27M and H3.3K27M DIPGs marked oligodendroglial differentiation genes and transcription factors, but not astrocytic lineage-associated genes, lending further support to the hypothesis that these tumors arise in oligodendroglial precursors. Further analysis of differentially activated enhancers in each subtype revealed enhanced PI3K/AKT, p38 MAPK, and EGFR signaling in H3.1K27M tumors while hindbrain morphogenesis, WNT signaling, and Rho GTPase activity were activated in H3.3K27M tumors.

Next, Nagaraja *et al.* (2019) set out to understand if H3.1K27M and H3.3K27M oncohistone expression in eOPCs dysregulates in enhancer and promoter profiles in distinct manners. Results from H3K27ac ChIP-seq experiments paralleled conclusions from enhancer analysis of DIPG tumor tissues, specifically demonstrating Rho GTPase signaling and p38 MAPK signaling activation in H3.3K27M- and H3.1K27M-expressing eOPCs, respectively. Although experiments revealed confined transcriptomic changes induced by H3.1K27M or H3.3K27M in the eOPCs, distinct transcriptional changes occurred for each construct. Most interestingly, H3.1K27M and H3.3K27M-associated enhancer signatures in the eOPCs, but not from NPCs, could be used to accurately segregate human DIPG samples by oncohistone type. Further experiments with the eOPC model probed the hypothesis that H3.1K27M and H3.3K27M

dysregulate PRC2 target genes differently. The rationale for this hypothesis came from observation made from ChIP-seq data that H3.3K27M strongly colocalized with wild-type H3.3 while this behavior did occur for H3.1K27M. PRC2 is reported to target CpG islands (CGIs) which are often enriched for H3.3 (Deaton and Bird, 2011). Significant overlap in H3.3 and H3.3K27M enrichment led Nagaraja and colleagues to test whether the extent of H3K27me3 loss at CGIs was greater in H3.3K27M than H3.1K27M eOPCs, and they found this to be the case. Altogether, these results suggested that H3.1K27M and H3.3K27M expression in specific cell lineages can establish chromatin profiles that resemble the distinct epigenetic landscapes of the two DIPG subtypes.

Recently, neural stem cell cultures derived from various regions of the human fetal brain have been utilized to address questions related to the regional selectivity of H3K27M and H3G34R/V mutations (Bressan *et al*., 2021). These neural stem cells (NSC) retain their region-specific (hindbrain or forebrain) signature present within tissue in cell culture, and not surprisingly signatures representative of each region could stratify human H3K27M and H3G34R (and H3WT) tumors appropriately. Analysis of human tumor samples also demonstrated marked enrichment of hindbrain and forebrain NSC signatures in human H3K27M and H3G34R tumors, respectively, suggesting these models faithfully recapitulate tumor expression profiles. Moreover, expression of H3K27M in cultures of neocortical and striatal origin did not alter their growth rate or properties, while expression in brainstem-derived cultures increased growth (Bressan *et al*., 2021). Expression of the H3G34R transgene in brainstem cultures caused growth rate reduction and senescence, providing evidence for the observed regional selectivity of H3G34-mutants for hemispheric regions. Accordingly, these fetal cultures will be useful in further studying and modeling tumor biology in the proper regional context.

The pediatric glioma field has relied heavily on the establishment of *in vivo* models using patient-derived cells in immunocompromised mice which present inherent difficulties in understanding differences in immune activation and interactions between mutant subtypes. Spontaneous, immune competent models to model H3K27M and H3WT pHGG tumors, of use to address this pitfall, have now been established. Larson *et al.* (2019) successfully created a novel mouse model using conditional knock-in mice to study histone mutant effects in an appropriate development time window. This approach allowed investigators to express H3K27M and H3WT histones in a region-specific manner, specifically in neural stem and progenitor cells. Neural stem cells from the forebrain and hindbrain were extracted from mouse embryos and subjected to RNA-seq and ChIP-seq experiments to profile H3K27me3, H3K27ac, H3K4me3 and assess corresponding transcriptomic changes. Results indicated that no drastic transcriptional changes occur in H3K27M neural stem cells, despite global H3K27me3 loss, as previously reported by others. Furthermore, H3K27M only caused epigenomic and transcriptomic perturbations in a region-specific manner and did not disrupt epigenetic patterning at lineage-specific genes that mark forebrain progenitor cells. Thus, intrinsic expression signatures and patterns of epigenetic marks at specific loci for the forebrain and hindbrain were not disrupted by H3K27M induction, suggesting that H3K27M oncohistones cannot cause similar epigenetic reprogramming of cells in a region-independent manner. These stem cell isogenic models recapitulated findings from the earliest study by Funato *et al*. (2014) which found limited changes in the transcriptome and specific upregulation of key genes like *Lin28b* and *Plag1* in H3.3K27M-expressing neural progenitor cells.

Larson *et al.* (2019) also studied how H3K27M cooperates with other mutations to drive tumor growth. First, they took an approach to study the combined effects of TP53 deletion in the presence of H3.3K27M expression. H3.3WT or H3.3K27M expression alone could not drive

tumor formation in contrast to conditional p53 knock-out which resulted in spontaneous tumors. Interestingly, H3.3K27M expression in the context of p53 knock-out accelerated tumor growth and shortened the latency window. This suggested that H3.3K27M enhances effects of p53 knockout and supported similar findings by Pathania *et al.* (2017) who observed decreased latency when H3K27M expression, but not H3WT expression, was combined with ATRX depletion, TP53 depletion, and PDGFRA overexpression in their *in-utero* electroporation mouse models. A later study using similar techniques observed tumor formation when dominant-negative TP53 was expressed with PDGFRA-D842V and H3.3WT but noticed that H3.3K27M expression in this background decreased latency dramatically (Patel *et al.,* 2020). These studies recapitulated the earliest H3K27M neural stem cell model (NSC) established by Funato *et al.* (2014) who demonstrated synergy of H3K27M with PDGFRA-D842V and p53 depletion. In comparison to H3.3WT expressed in the same NSC background, addition of H3K27M increased the tumorigenic potential of the NSCs. Together these findings suggest that H3K27M synergizes with, and may even require, other mutations to drive tumor progression.

Interestingly, the study by Larson *et al.* (2019) established additional tumor models with combined PDGFRA overexpression and TP53 knockout to study the effect of H3.3WT and H3.3K27M induction on tumor growth. Interestingly, H3.3K27M could further accelerate tumor growth and its expression shifted the relative distribution of anatomic locations towards a larger fraction of tumors occurring in the brainstem region. Notably, ChIP-seq analysis of H3K4me3, H3K27ac, and H3K27me3 in these DIPG models proposed a mechanism of epigenetic release that occurs at bivalent promoters harboring H3K27me3 and H3K4me3 enrichment in H3WT tumor cells. Analysis of the genes upregulated in the H3K27M tumor cells revealed that a large portion of these loci were marked by both H3K27me3 and H3K4me3 in H3WT cells, and that these loci

lose promoter H3K27me3 in the H3K27M cells and their expression rises, like that seen in human DIPG samples. Experiments performed by the same research group to knockdown mutant *H3F3A* in human tumor cells showed the same result where genes marked by H3K27me3 and H3K4me3 co-enrichment, indicating a poised state, in "corrected" cells were those upregulated in corresponding H3K27M-expressing cells.

It is of great interest to understand if these bivalent genes selectively targeted by H3K27M are lineage specific, meaning that H3K4me3 is present at the genes in hindbrain cells, but not in the forebrain. Determining if these genes lack poised promoters in forebrain-derived cells may lend insight into why forced H3K27M expression in these cells has no effect on cell growth and exerts limited reprogramming capacity. Collectively, models discussed here provide information about how H3.3K27M mutations cooperate with other mutations to enhancer tumor growth and give new insight into regional specificity. Additionally, this work has uncovered a mode of epigenetic activation where H3K27M preferentially deregulates expression of genes marked by bivalent promoters.

1.7 H3G34R/V high-grade gliomas are distinct entities from H3K27M tumors.

1.7.1 Background on H3.3G34R/V gliomas

In addition to differences in patient demographics and anatomic location (discussed in Chapter 1.6), the first studies on histone mutants in pediatric glioma observed distinct biochemical properties associated with H3.3K27M and H3.3G34R/V mutant histones. Histone assays performed by Lewis *et al.* (2013) probed the effect of substitution of glycine 34 with arginine or valine on histone modifications such as H3K36me3, H3K27ac, and H3K27me3. Pulldown assays revealed an interesting effect where H3K27me3 increased and H3K36me3 decreased on tagged mononucleosomes (*in cis*) while H3K36me3 increased on endogenous histone H3 (*in trans*).

However, the dominant-negative effect observed with H3K27M and H3K36M oncohistones was not observed with the G34-mutants. This finding might be explained by the lack of post-translational modifications to the glycine 34 residue, and suggests that H3G34 mutants alter the epigenomic landscape through a unique mechanism. Defects in H3K36me3 have previously been implicated in cancer (Papillon-Cavanagh *et al*., 2017). SETD2 mutations have been observed in high-grade gliomas and comparison of SETD2-, G34-, and IDH1/2-mutant tumors revealed distinct DNA methylation profiles that were most similar between H3G34 and SETD2-mutant patients (Fontebasso *et al.,* 2013b). Thus, it is important to localize H3K36me3 changes in the genome to understand the significance of these changes for tumor processes. While knowledge about H3K27M tumors and possible treatment modalities has expanded over time, our understanding of H3G34R/V histone biochemistry and oncogenic mechanism has been limited.

1.7.2 Binding and interactions of mutant histone H3.3G34R and H3.3G34V with lysine 36 readers and modifying enzymes

Early biochemical studies on the H3G34R/V histones attempted to understand how mutations at the glycine 34 position cause the observed effect of H3K36me3 loss *in cis*. Numerous studies on H3K27M mechanisms had suggested that the mutant residue confers a "gain-of-function" to bind specific histone modifiers of that residue and inhibit their activity. In light of this, Fang *et al.* (2018) proposed that arginine and valine residues disrupt the interaction between SETD2 and the lysine 36 residue it methylates (**Figure 1.5**). To probe this, synthetic H3 peptides were created with mutated or nonmutated H3G34 residues and varying H3K36 methylation state (i.e. H3K36me0, H3K36me1,…,H3K36me3) and these constructs were incubated with the purified SETD2 catalytic domain and tritium-labeled S-adenosylmethionine. H3 peptides with non-mutated H3G34 residues and H3K36 methylation state of H3K36me2 or lower could be

successfully methylated while R and V-substituted peptides with any H3K36 state demonstrated little ^{3}H incorporation. Results from the H3 peptide assays could be accurately recapitulated with mutant H3G34 and nonmutant H3-H4 tetramers, suggesting that H3G34 substitutions block SETD2-mediated methylation. The idea that H3G34 mutations impede SETD2 activity directly was further strengthened by co-crystal structures demonstrating that the H3G34 residue is confined to a channel in SETD2 that cannot accommodate larger amino acids which cause steric clash (Fang *et al.,* 2018; Yang *et al.,* 2016).

Interestingly, experiments in HEK293-T cells expressing native and exogenous mutant H3 confirmed previous observations that H3K36me3 is lost on exogenous mutant histone and rises on endogenous H3. Mass spectrometry on immunoprecipitated exogenous histones showed that H3G34R and H3G34V histones had a lesser fraction of histone in the demethylated and trimethylated state compared with WT histone. The study by Fang *et al.* (2018) also discovered that H3G34 mutant peptides exhibit less binding affinity for MutSα, a H3K36me3 interactor and DNA mismatch repair protein. This decreased binding occurred even for H3G34-mutated peptides with H3K36me3 status, suggesting the actual mutation (not the resulting H3K36me3 loss) blocks for MutSα binding. Experiments with H3G34V KNS42 and H3WT SF188 cells, involving immunoprecipitation of MSH6 (a subunit of MutSα), revealed less H3 binding to MSH6 in KNS42 cells. A similar diminished interaction was observed when tagged H3 mutant proteins were expressed in SF188 and HEK293-T cells. After expression, a histone association assay was used to precipitate bulk H3 and assess the amount of bound MSH6 under each construct condition. These assays confirmed that the MSH6 interaction was weaker and less frequent in cells ectopically expressing H3.3G34R and H3.3G34V compared with H3.3WT constructs. Further comparison of MSH6 and H3K36me3 ChIP-seq from KNS42 and SF188 revealed a large overlap

of regions with diminished H3K36me3 and MSH6. Defective mismatch repair mechanisms mediated by MutSα have been implicated both in cancer initiation and therapy resistance. Thus, the finding of disrupted MSH6/MutSα interaction in the context of H3G34 mutations is significant because it may explain the high mutational frequency observed in H3G34 gliomas.

Not surprisingly, the mutant H3G34 histones can bind other histone modifiers. ChIP-seq experiments by Voon *et al.* (2018) on models established with ES cells to express H3.3G34R or H3.3WT histones unexpectedly demonstrated H3K36me3 enrichment at specific genes (**Figure 1.5**). Analysis of H3K36me3-enriched regions in the H3.3G34R cells showed that these regions also were enriched for H3.3, KDM4B, and KDM4C. Conversely, regions relatively depleted for H3K36me3 in H3G34R cells had less KDM4B/C binding. Moreover, the enrichment of H3K36me3 at regions with higher KDM4 binding could be recapitulated by similar cells harboring KDM4A/B/C deletion, and H3K36me3-associated gene expression changes in this model mirrored patterns observed between the H3G34R and H3WT mES cells. These associations strongly implicated H3G34R histones in inhibiting KDM4 family demethylases, causing H3K36me3 elevation. This hypothesis was confirmed by performing co-immunoprecipitation experiments where tagged histones were isolated and probed for their binding behavior with KDM4A, KDM4B, and KDM4C. Additionally, histone demethylase assays were used on H3WT and H3G34R peptides each with different H3K36me3 status (H3K36me0,…,H3K36me2). The results showed stronger binding interaction with KDM4, and corresponding decreased demethylase activity against peptides containing H3K36me3 residue in the presence of H3G34R histone.

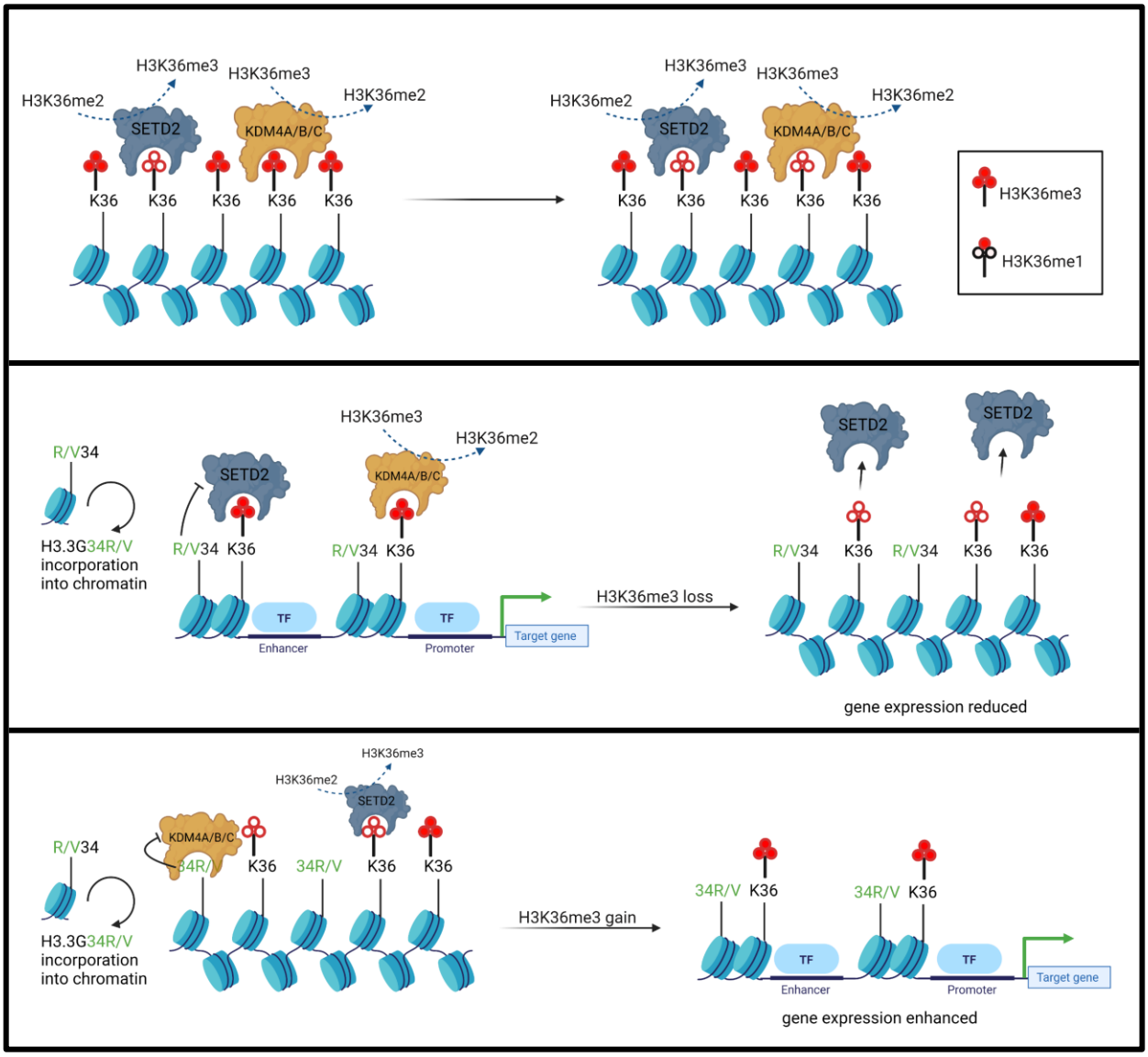

Figure 1.5. Modes of H3G34R/V-mediated inhibition on H3K36-modifying enzymes.
Top panel: The sole H3K36 trimethyltransferase SETD2 catalyzes H3K36me3 while KDM4A/B/C catalyze the removal of H3K36me3. *Middle panel*: *In vitro* methyltransferase assays by Fang *et al*., (2018) suggest that SETD2 is unable to catalyze the reaction converting H3K36me2 to H3K36me3. In the context of chromatin, this suggests that, upon H3G34R/V incorporation, KDM4A/B/C-driven demethylation reactions are dominant at genes where SETD2 is inhibited. H3K36me3 loss is associated with transcriptional repression and formation of heterochromatin. *Bottom panel*: ChIP-seq analysis by Voon *et al*. (2018) demonstrated that focal genomic H3K36me3 occurs in H3G34R/V cells relative to H3.3WT cells. This suggests H3G34R/V differentially inhibits KDM4A/B/C at specific genes and allows for residual SETD2 activity, H3K36me3 gain, and gene activation. Figure constructed with BioRender.com.

The KDM4 demethylases exhibit activity towards H3K9me3 (a repressive histone mark) and H3K36me3, bringing the possibility that H3K9me3 levels as specific genes are perturbed by the presence of H3G34R histones. A similar analysis of H3K9me3 enriched regions also illustrated a relationship with KDM4A/B/C binding. Although the ability of mutant H3G34R to affect H3K36me3 had been established to modulate gene expression, this new discovery of H3K9me3 modulation is exciting because it suggests that H3G34R retention at specific loci might play a role in gene silencing within tumors. Together, these data suggest that H3G34R perturbs both H3K9me3 and H3K36me3 levels at genes that are actively targeted by KDM4 lysine demethylases.

1.7.3 H3.3G34W mutations observed in bone tumors perturb H3K36me3 and H3K27me3

Most giant cell tumors of the bone harbor (~80-90%) harbor mutations in *H3F3A* where the glycine 34 residue is mutated to tryptophan (H3G34W). Two studies have recently characterized the epigenetic features of these malignancies (Khazaei *et al*., 2020; Jain *et al*., 2020). Khazaei et al. edited human H3G34W cells, to establish paired models, with CRISPR-Cas9-mediated correction to WT H3.3 (either via H3F3A knock-in or knockout). Transcriptomic and epigenetic profiling of these cells showed top upregulated and downregulated genes related to extracellular matrix organization and muscle differentiation, respectively. Using mass spectrometry on human H3G34W cells confirmed H3K36me3 decreases and H3K27me3 increases on the mutant H3.3G34W histone (*in cis*). This mechanism was confirmed by Jain *et al.* (2020) who expressed H3G34A/L/R/V/W and H3K36A/E/L/N/Q/R/T mutant histone constructs in HEK293T cells and performed mass spectrometry on tagged histones. Their results demonstrated that H3K36me3 is lost *in cis.* Interestingly, mutant H3G34-residue construct had elevated H3K27me3 *in cis* while H3K36-residue construct did not show similar behavior, highlighting a

potential difference between these two types of mutants that alter H3K36 methylation. Using a sequential methyltransferase reaction paradigm, Jain and colleagues also showed that pre-incubation of H3.3WT nucleosomes with SETD2, followed by incubation with PRC2, could effectively block PRC2-mediated H3K27me3, but that H3.3G34R and H3.3G34W nucleosomes could not replicate this effect, confirming previous notions of mutant-mediated SETD2 inhibition. Not surprisingly, this result further confirmed the antagonistic nature between H3K36me3 and H3K27me3.

Despite this effect, ChIP-seq experiments by Khazaei *et al.* (2020) on H3G34W parental and edited (with WT H3.3 knock-in or H3.3G34W knockout) cells revealed genomic regions with gain and others with loss of H3K36me3. Changes in H3K36me3 were accompanied by a shift in the H3K27me3 distribution. H3K27me3 enrichment was noted at promoters of genes important for muscle differentiation in H3G34W-intact cells. Contrastingly, H3K27me3 was more evident in intergenic regions within the edited cells, suggesting that H3.3G34W causes H3K27me3 redistribution which then has downstream consequences for H3.3 eviction from repressed genic regions. Interestingly, genes with the highest expression showed enrichment of H3.3 and H3.3G34W, suggesting that the effect of the mutant histone on epigenetic modifications is location-dependent and does not always result in gene repression. The results from *H3F3A* knockout or knock-in experiments revealed the reversible nature of H3K36me3, H3K9me3, and H3K27me3 patterning in H3G34W cells. This contrasts data from similar manipulations with H3G34R cells which show minimal perturbation of the established epigenetic landscape. This shows that there is a difference in how H3G34R and H3G34W change epigenetic marks.

Given previous studies reporting of H3.3 as the predominant H3 variant at enhancers, Jain *et al.* (2020) investigated the specific effect of H3.3G34W on the enhancer profiles. Analysis of

enhancers marked by distal H3K27ac peaks demonstrated reduction in both H3.3K36me3 and H3K27ac, colocalized H3.3K27me3 gain, and downregulation of enhancer-associated genes. Treatment of H3.3G34W-expressing cells with EZH2 inhibitor Tazemetostat could lower H3K27me3 and rescue the expression of downregulated genes, some of which are implicated in osteoblast differentiation. Additionally, an experiment was performed to probe the role of this aberrant H3K27me3 in H3.3G34W tumor progression. Mesenchymal stem cells (mMSC) expressing H3WT, H3G34W, or dual H3G34W-K27R mutant histones were used to establish tibial and subcutaneous tumor models. Notably, H3.3G34W cells formed aggressive tumors while the dual mutant delayed tumor progression to a similar profile seen with H3WT mMSCs. This elegantly illustrated that the H3K27R mutant abrogates the effect of H3K27me3 elevation caused by H3.3G34W, strongly implicating a mechanism for tumor progression requiring H3K27me3. Experiments by other groups found that knockout of H3G34W in human bone tumor cells slowed *in vitro* growth and completely prevented tumor growth of tibial and subcutaneous models. This data is consistent with previous ChIP-seq data that shows active and reversible remodeling of epigenetic marks at mesenchymal progenitor differentiation genes by H33G34W. Together, these results suggest a dependence of bone tumors on H3.3G34W directly and its modulation of H3K27me3 to enable tumor growth.

1.7.4 Aberrant molecular mechanisms engaged in H3.3G34R/V tumors

Limited models and information have existed about cancer-driving mechanisms in H3G34-mutant tumors. Only recently have studies attempted to model tumor origins and profile gene signatures. Chen *et al.* (2020) compiled a large cohort of H3G34R/V tumor samples and carried out molecular and genomic profiling. They identified genomic alterations that have already been noted in H3G34 tumors, specifically the high frequency of co-occurring *TP53* and *ATRX*

mutations. Interestingly, only recurrent mutations in PDGFRA were discovered in the H3G34-mutants when comparing with other glioma subtypes such as IDH1, SETD2, and H3K27M mutant tumors. Although amplifications were rarely seen, robust PDGFRA expression was observed with downstream ERK phosphorylation. Stronger MEK/ERK phosphorylation was observed in H3G34-mutant tumors harboring mutations in PDGFRA extracellular immunoglobulin-like domains, suggesting that this subgroup of tumors may be amenable to therapies targeting the MEK/ERK pathway.

Human H3G34R/V tumors were also profiled by Chen *et al.* (2020) with respect to known forebrain and hindbrain signatures. Cortical interneuron and neuronal progenitor signatures were both enriched while cortical excitatory neuron and oligodendrocyte precursor cell signatures were not prominent in H3G34-mutant tumor samples. In addition, single-cell RNA-seq on H3G34R/V glioma samples confirmed a low proportion of oligodendroglial-like cells and relative enrichment of cells with interneuron and astrocytic signatures.

Interestingly, cortical interneurons arise from ganglionic eminences where specific transcription factors are expressed to drive the interneuron phenotype and suppress molecular programs for oligodendrocyte formation. One key transcription factor is GS homeobox 2 (*GSX2*) which was found to be robustly expressed with interneuron markers like *GAD2* and *NPY* in H3G34R/V tumor samples. Surprisingly, the *PDGFRA* and *GSX2* loci are near one another. PDGFRA is not normally expressed in interneuron progenitors, which prompted the hypothesis that PDGFRA expression might be modulated by genomic regulatory regions for genes important for interneuron fate in H3G34R/V cells. Chen *et al.* (2020) performed Hi-C chromosome conformation capture experiments on human H3.3G34R HSJD-GBM-002, H3.3G34V KNS42, and H3WT G477 cells to investigate this. In H3G34R/V cells, enhanced H3K27ac peaks were

noted at the *PDGFRA* promoter and the distal enhancer region for *GSX2*, coincident with a topologically associated domain (TAD) and a larger number of interaction loops within the TAD. GSX2 promoter-localized H3K27ac was enhanced in H3G34R/V tumors with PDGFRA mutations. This heightened activation state of the GSX2 region was suggested as a mechanism for driving higher PDGFRA expression in PDGFRA-mutated tumors. Similar Hi-C experiments conducted with mouse embryonic stem cells (ESCs) and E13.5 ganglionic eminences showed little interaction between the *Pdgfra* promoter and the *Gsx2* regulatory element called *hs687* in ESCs. However, an interaction between bivalent *Gsx2* and *Pdgfra* promoters was observed in the ESCs, but no interactions linked the Gsx2 regulatory region with either promoter at this developmental stage. Strikingly, separate interaction loops linking *hs687* with *Gsx2* and *Pdgfra* are observed in the E13.5 ganglionic eminences. This finding was important because interneurons thought to be the cell of origin for H3G34R/V tumors arise from the ganglionic eminences. Thus, these results show that the co-option of *Gsx2* regulatory machinery to drive aberrant PDGFRA expression is likely a developmentally-regulated event.

Given the ability of H3G34R/V mutant histones to bind and inhibit histone modifying enzymes, studies have also examined the potential for other binding interactions. Notably, Lim *et al.* (2017) performed immunoprecipitations of ectopically expressed H3.3G34W and H3.3G34R histones and found novel interactors such as bromodomain proteins BRD1; SWI/SNF complex protein SMARCA1, SMARCA5, and ARID2; and histone modifiers JMJD1C, HDAC2, and JMJD4. This opens the possibility that H3G34R/V mutations dysregulate chromatin machinery that can be pharmacologically targeted.

A study by Jiao *et al.* (2020) has highlighted the importance of understanding the significance of these interactors in affecting the tumor microenvironment. They discovered that

RACK7, a reader of H3K4me1 marks and transcriptional repressor, exhibits specific binding interaction with H3G34R peptides and oligonucleosomes which does not occur with similar H3G34W/V/L, H3K27M, or H3K36M constructs. Further experimentation involved sequential deletion each reader domain (bromodomain, PWWP, and PHD) from RACK7 where it was ascertained that the PHD domain is a critical component for H3G34R-mutant binding. Having confirmed a H3G34R-RACK7 interaction, ChIP-seq for RACK7 was performed on H3.3G34R native, H3.3G34R-CRISPR corrected, and H3.3WT cell lines to determine its genomic localization under each condition. RACK7 genomic binding was reduced after *H3F3A* correction in H3.3G34R cells, and corresponding RNA-seq analysis of loci with reduced RACK7 binding revealed vesicle pathway and MHC Class II molecule upregulation upon correction. Unexpectedly, little or no RACK7 occupancy was observed at the MHC Class II genes, suggesting an indirect mechanism for gene regulation. RACK7 binding was detected at *CIITA* in H3.3G34R cells, a master transcriptional regulator for these MHC-related genes, suggesting that H3.3G34R binds RACK7 to suppress CIITA expression and consequently, activity required to transcribe MHC Class II genes. To further test if release of MHC gene suppression is caused by disrupting the G34R-RACK7 interaction, Jiao and colleagues performed RACK7 deletion from RACK7 from H3.3G34R cells. Indeed, RACK7 depletion could phenocopy the MHC gene expression patterns observed with CRISPR-mediated WT H3.3 knock-in in G34 mutant cells. Overall, the results from Jiao *et al.* (2020) implicate H3.3G34R in directly modulating MHC class II molecules which play a role in antitumor immunity. Importantly, these experiments on RACK7 revealed that H3G34V and H3G34R differentially interact with RACK7. This underscores the importance of defining interaction-based differences to understand how tumors of each subtype may uniquely interact with the immune microenvironment. It has been demonstrated that MHC class II molecules can

stimulate the immune system and lead to better outcomes in patients with breast carcinoma and melanomas. Thus, targeting RACK7 in H3.3G34R tumors may provide a therapeutic axis for immune activation and much work is needed here.

1.7.5 Establishing and profiling in vitro and in vivo models of H3G34R/V glioma

H3G34R/V models are currently being developed to elucidate signaling mechanisms and therapeutic vulnerabilities in these tumors. One outstanding question for the pediatric glioma field is why tumors harboring distinct histone mutations arise in anatomically distinct brain regions. H3K27M tumors arise in the brainstem and subcortical midline structures in contrast to H3G34R/V mutant tumors exclusively localized to the cerebral hemispheres. Bressan *et al.* (2021) established human fetal neural stem cell (NSC) cultures from cells originating in the neocortex, striatum, midbrain, cerebellum, brainstem, and spinal cord. These cultures broadly recapitulated gene expression and transcription factor signatures present in forebrain- and hindbrain-derived tissues. Clustering analysis demonstrated that these cell-specific signatures could distinguish H3K27M and H3G34R tumor sample, and vice versa, suggesting that the molecular programs in the NSCs closely resemble those of human histone mutant glioma.

Bressan and colleagues hypothesized that the transcriptional programs within forebrain and hindbrain tumors can only be reinforced by a specific mutation (Bressan *et al*., 2021). This meant that forebrain cells might have a lineage-specific transcriptional program permissive to H3G34R but not H3K27M. To test this, they expressed the H3.3G34R and H3.3K27M transgenes in NSCs derived from the various regions. H3.3K27M expression in neocortex, striatum, and brainstem NSCs revealed an enhanced growth phenotype (assessed by colony count or EdU incorporation) only in the brainstem-derived culture. Surprisingly, H3.3G34R expression in forebrain cultures had no effect on growth while expression in brainstem NSC markedly slowed growth which

probably explains the lack of H3.3G34R mutations found in the hindbrain region. Interestingly, H3.3G34R expression combined with Tp53 knockout and PDGFRA overexpression in neocortical NSCs (termed PP5G cells) could enhance growth relative to H3.3WT (termed PP5W) cells with the same background. When compared with PP5W neocortical NSCs, the PP5G neocortical cells demonstrated upregulation of forebrain-specific genes. These changes did not occur in models established with brainstem NSCs where H3.3G34R induction caused p21 upregulation which might explain the stunted growth observed. Consistent with these findings, PP5G neocortical cells robustly formed tumors when implanted *in vivo* while PP5G brainstem cells failed to produce tumors. These results suggested that H3.3G34R could enhance growth in the presence of other oncogenic mutations and retained its oncogenic properties only in forebrain cells.

The role of H3.3G34R in modulating forebrain transcription factor signatures is important to understand. Work has revealed that H3.3G34R genetic deletion from human pGBM002 cells leads to downregulation of established forebrain development and neural progenitor proliferation genes (Bressan *et al*., 2021). Many downregulated progenitor genes such as *SOX1*, *RFX4*, *CDK6*, *ASCL1*, *HES5*, and *EMX2* were observed to be elevated in H3G34R/V patient tissues, suggesting H3.3G34R might enhance their existing expression in forebrain cells. pGBM002 parental cells were subjected to ChIP-seq analysis to determine H3.3G34R, H3K4me3, H3K36me3, and H3K27me3 distribution. H3.3G34R histone colocalized at H3K4me3 and H3K36me3 enriched regions. Interestingly, regions with the highest H3.3G34R incorporation exhibited the largest enrichment magnitude for H3K4me3 and H3K36me3 but showed no relationship with H3K27me3. Similarly, if regions were sub-grouped by H3K4me3 or H3K36me3 enrichment, the regions with the highest ChIP-seq reads demonstrated the highest H3.3G34R enrichment. H3.3G34R enrichment level at promoters also positively correlated with RNA expression of associated genes.

A challenge the pediatric glioma field has faced is the inability to make precise epigenetic comparisons between human tumor cell lines owing to their heterogeneity in other mutations. This barrier makes it difficult to attribute aberrant epigenetic patterns specifically to the histone mutant. Recent work has attempted to solve this issue by creating isogenic paired models of G34R/V cells and corrected cells. Specifically, Bressan *et al.*, (2021) made pGBM002 cells with H3.3G34R-knockout and profiled for them same histone modifications, discussed above, and compared with parental H3.3G34R-expressing cells. The removal of H3.3G34R, especially at promoters, did not decrease promoter-associated H3K4me3 or H3K36me3 levels with the majority of the peaks overlapping between cells. Re-expression of tagged H3.3WT or H3.3G34R transgenes in the knockout cells did not change the distribution for H3.3, H3K4me3, or H3K36me3. Interestingly, forebrain-specific genes that were downregulated upon H3.3G34R-knockout had the highest H3.3G34R enrichment in parental cells. Genes with low H3.3G34R incorporation experienced less transcriptional deregulation upon knockout. This suggested that genomic regions with very high H3.3G34R deposition might undergo changes in transcriptional activity through an unknown pathway. Bressan and colleagues discovered that ZMYND11, a reader of H3K36me3 and transcriptional repressor, had impaired binding with H3.3G34R histones and suggested that diminished binding could allow for gene upregulation at H3.3G34R-enriched loci (Guo *et al.*, 2014; Wen *et al*., 2014). More work is needed in the field to understand the genomic distribution of transcription regulatory proteins (such as repressors) in relation to H3G34R and H3G34V histones. This will help clarify the role H3G34R/V histones play in regulating specific forebrain transcription factors. Although we know forebrain transcription factors are upregulated in H3G34R/V tumors, the complex mechanism re-enforcing these patterns remains unknown. Experiments probing “de-repression” mechanisms such as ZMYND11 also have the potential to

uncover genes important for oncogenic signaling. Recently, H3K27M and H3G34R/V histones have also been demonstrated to interact with pBAF and SWI/SNF complex proteins (Mashtalir *et al*., 2021). Mapping histone interactions with pBAF at a genomic level in H3G34R/V cells and testing the efficacy of protein degraders targeting key complex components (like PBRM1) will lend insight here.

Xenograft models of H3G34R/V tumors have been established by several groups. Experiments have probed the importance of H3.3G34R or H3.3G34V expression on tumor initiation and progression. pGBM002 and KNS42 cells with and without genetic ablation of their mutant histones were implanted into the mouse cortex and monitored (Chen *et al*., 2020). In both cases, H3G34R/V-knockout demonstrated little to no effect on mouse survival. These results contrast observations made from similar experiments where H3.3G34W-knockout cells had reduced growth and tumorigenic capacity *in vitro* and *in vivo* (Fellenberg *et al*., 2019; Jain *et al*., 2020; Khazaei *et al*., 2020). H3G34W is the only recurring mutation in bone tumors unlike H3G34R/V mutations which often present with co-occurring *ATRX* or *TP53* mutation. Although W and R/V mutations occur at the same residue, they are not both required for continued tumor progression. This strongly suggests that the epigenetic changes required for tumor maintenance require the presence of H3.3G34W and similar types of changes do not occur in H3.3G34R/V cells. Instead, H3G34R/V tumors may depend on other mutations and reinforce a transcriptional pattern existing in the cell lineage where tumors arise. It is also likely that W substitutions confer an ability to bind or interact with proteins distinct from those captured or binding with R/V. The role of these protein-histone interactions in shaping the H3K27me3 patterning at enhancers in these tumors still needs to be elucidated. Overall, the experiments to date provide strong evidence that the oncogenic mechanism of action for each histone type are different and cell-specific.

1.7.6 Future directions for study of H3G34R/V glioma

No study to date has probed the relative distributions of H3.3G34W and H3.3G34R/V in their respective tumor cells to determine differences in deposition profiles. It is possible that W and R/V histones are targeted to different genomic regions in different cell types, and this would not be surprising given the finding that H3.3G34R histones have significant enrichment at genes specific for forebrain transcription factors and development. Thus, one possibility is that R/V histones reinforce an already existing transcriptional landscape dictated by the cell lineage while W histones are required to deregulate genes for bone cell differentiation, maintaining an undifferentiated state that is rapidly reversible upon mutant histone depletion. These possibilities are well supported by current experiments in the literature demonstrating the sensitivity of H3G34W cells, and relatively insensitivity of H3G34R/V cells, to EZH2 inhibition (Wiese *et al*., 2016). This underscores the importance of finding therapeutic targets in H3G34R/V cells that can de-stabilize forebrain transcription factors needed for growth. One study has targeted the FOXG1 forebrain-specific transcription factor which is a known negative regulator of p21. Targeted deletion of FOXG1 could rescue p21 levels in H3G34R, but not H3WT cells and completely prevent tumor growth *in vivo* (Bressan *et al*., 2021). Future studies should focus on disrupting these transcriptional networks with pharmacological techniques. H3G34R/V cells are relatively resistant to epigenetic therapies that perturb H3K27me3, suggesting that mutant histones may lock in a transcriptional state that cannot be reversed with epigenetic therapy. To understand this, it could be useful to assess the sensitivity of h3G34R/V parental and corrected isogenic cells to epigenetic therapies to understand how the mutant histones drive resistance. The observation that H3.3G34R deposition directly correlates with H3K36me3 and H3K4me3 enrichment suggests that targeting transcriptional processes with BET/bromodomain inhibitors could be effective.

H3G34R/V/W mutant cells and tissues demonstrate global DNA hypomethylation relative to H3WT bone and glioma cells (Bender *et al*., 2013; Sangatsuda *et al*., 2020). Although deregulated genes have been associated with DNA methylation changes, the mechanism for how H3G34-mutant histones affect methylation processes remains elusive. The lack of recurrent mutations in DNA methylation enzymes in this tumor type, in addition to the observation of global DNA hypomethylation in H3G34W-mutants, indicate that the H3G34 residue plays a role in perturbing the methylation phenotype. One possibility is that DNA methylation might be affected directly by the transcription factors (TF) that are active in the neuroprogenitor cells that give rise to H3G34 tumors. For example, it has been demonstrated that FOXG1, a TF contributing in H3G34R cells discussed earlier, can regulate DNMT3A/3B and TET protein expression and function (Hou *et al*., 2020). Another possibility is that H3G34R-induced changes in H3K36me3 might cause downstream changes in other activating marks like H3K4me3, a modification known to be antagonistic to DNA methylation. Thus, regions with high H3G34R/V histone incorporation might drive DNA hypomethylation through an indirect process. In our study (see Chapter 3) we have observed regions with elevated H3K4me3 in H3G34R cells, suggesting that mutant histones might inhibit lysine 4 demethylases KDM5A-D. Given the literature discussing H3G34R/V binding with histone modifiers like SETD2 and KDM4, it is also possible that mutant histone also binds and/or inhibits DNA methyltransferases (DNMT3A/B) or demethylases (TETs). Colocalization studies of these proteins and H3.3G34R/V/W at the genomic level will allow us to understand interactions and clarify if DNA methylation changes are a consequence of the mutant histone or the intrinsic to an oncogenic cell state. It could be possible that H3G34R/V histones preferentially bind DNMT3A/B proteins whose PWWP domain recognizes H3K36me3, causing elevated TET activity and hypomethylation at G34R/V-enriched regions. Interactions between

H3G34R/V and TETs are not necessarily inhibitory, and aberrant “gain-of-function” interactions might direct TETs to loci with H3G34R/V enrichment to facilitate DNA hypomethylation. In this context, no studies have investigated the effects of pharmacologically reversing DNA hypomethylation with newly available cytosine-based TET inhibitors like Bobcat339. Finally, no comprehensive comparison of biochemical differences has been made between arginine (R) and valine (V) containing histones. Arginine is composed of a polar, charged side chain capable of undergoing methylation while valine is a hydrophobic, uncharged residue. Both R and V substitutions have been demonstrated to inhibit SETD2 catalytic activity. Other studies on mutant histone binding interactions have shown preferential binding of R, but not V, mutants with RACK7. These initial findings support the idea that tumors with R and V mutants probably dysregulate epigenetic patterns in distinct manners, however expansive profiling is needed to find these differences.

1.8 References

Abbosh PH, Montgomery JS, Starkey JA, Novotny M, Zuhowski EG, Egorin MJ, Moseman AP, Golas A, Brannon KM, Balch C, Huang TH, Nephew KP. Dominant-negative histone H3 lysine 27 mutant derepresses silenced tumor suppressor genes and reverses the drug-resistant phenotype in cancer cells. *Cancer Res*. 2006 Jun 1;66(11):5582-91. doi: 10.1158/0008-5472.CAN-05-3575.

Audia JE, Campbell RM. Histone Modifications and Cancer. *Cold Spring Harb Perspect Biol*. 2016 Apr 1;8(4):a019521. doi: 10.1101/cshperspect.a019521.

Banaszynski LA, Wen D, Dewell S, Whitcomb SJ, Lin M, Diaz N, Elsässer SJ, Chapgier A, Goldberg AD, Canaani E, Rafii S, Zheng D, Allis CD. Hira-dependent histone H3.3 deposition facilitates PRC2 recruitment at developmental loci in ES cells. *Cell*. 2013 Sep 26;155(1):107-20. doi: 10.1016/j.cell.2013.08.061.

Bannister AJ, Zegerman P, Partridge JF, Miska EA, Thomas JO, Allshire RC, Kouzarides T. Selective recognition of methylated lysine 9 on histone H3 by the HP1 chromo domain. *Nature*. 2001 Mar 1;410(6824):120-4. doi: 10.1038/35065138.

Barski A, Cuddapah S, Cui K, Roh TY, Schones DE, Wang Z, Wei G, Chepelev I, Zhao K. High-resolution profiling of histone methylations in the human genome. *Cell*. 2007 May 18;129(4):823-37. doi: 10.1016/j.cell.2007.05.009.

Bax DA, Mackay A, Little SE, Carvalho D, Viana-Pereira M, Tamber N, Grigoriadis AE, Ashworth A, Reis RM, Ellison DW, Al-Sarraj S, Hargrave D, Jones C. A distinct spectrum of copy number aberrations in pediatric high-grade gliomas. *Clin Cancer Res*. 2010 Jul 1;16(13):3368-77. doi: 10.1158/1078-0432.CCR-10-0438.

Baylin SB, Jones PA. Epigenetic Determinants of Cancer. *Cold Spring Harb Perspect Biol*. 2016 Sep 1;8(9):a019505. doi: 10.1101/cshperspect.a019505.

Bedi U, Mishra VK, Wasilewski D, Scheel C, Johnsen SA. Epigenetic plasticity: a central regulator of epithelial-to-mesenchymal transition in cancer. *Oncotarget*. 2014 Apr 30;5(8):2016-29. doi: 10.18632/oncotarget.1875.

Behjati S, Tarpey PS, Presneau N, Scheipl S, Pillay N, Van Loo P, Wedge DC, Cooke SL, Gundem G, Davies H, Nik-Zainal S, Martin S, McLaren S, Goodie V, Robinson B, Butler A, Teague JW, Halai D, Khatri B, Myklebost O, Baumhoer D, Jundt G, Hamoudi R, Tirabosco R, Amary MF, Futreal PA, Stratton MR, Campbell PJ, Flanagan AM. Distinct H3F3A and H3F3B driver mutations define chondroblastoma and giant cell tumor of bone. *Nat Genet*. 2013 Dec;45(12):1479-82. doi: 10.1038/ng.2814.

Bender S, Tang Y, Lindroth AM, Hovestadt V, Jones DT, Kool M, Zapatka M, Northcott PA, Sturm D, Wang W, Radlwimmer B, Højfeldt JW, Truffaux N, Castel D, Schubert S, Ryzhova M, Seker-Cin H, Gronych J, Johann PD, Stark S, Meyer J, Milde T, Schuhmann M, Ebinger M, Monoranu CM, Ponnuswami A, Chen S, Jones C, Witt O, Collins VP, von Deimling A, Jabado N,

Puget S, Grill J, Helin K, Korshunov A, Lichter P, Monje M, Plass C, Cho YJ, Pfister SM. Reduced H3K27me3 and DNA hypomethylation are major drivers of gene expression in K27M mutant pediatric high-grade gliomas. *Cancer Cell*. 2013 Nov 11;24(5):660-72. doi: 10.1016/j.ccr.2013.10.006.

Bernstein BE, Mikkelsen TS, Xie X, Kamal M, Huebert DJ, Cuff J, Fry B, Meissner A, Wernig M, Plath K, Jaenisch R, Wagschal A, Feil R, Schreiber SL, Lander ES. A bivalent chromatin structure marks key developmental genes in embryonic stem cells. *Cell*. 2006 Apr 21;125(2):315-26. doi: 10.1016/j.cell.2006.02.041.

Bödör C, Grossmann V, Popov N, Okosun J, O'Riain C, Tan K, Marzec J, Araf S, Wang J, Lee AM, Clear A, Montoto S, Matthews J, Iqbal S, Rajnai H, Rosenwald A, Ott G, Campo E, Rimsza LM, Smeland EB, Chan WC, Braziel RM, Staudt LM, Wright G, Lister TA, Elemento O, Hills R, Gribben JG, Chelala C, Matolcsy A, Kohlmann A, Haferlach T, Gascoyne RD, Fitzgibbon J. EZH2 mutations are frequent and represent an early event in follicular lymphoma. *Blood*. 2013 Oct 31;122(18):3165-8. doi: 10.1182/blood-2013-04-496893.

Boyer LA, Plath K, Zeitlinger J, Brambrink T, Medeiros LA, Lee TI, Levine SS, Wernig M, Tajonar A, Ray MK, Bell GW, Otte AP, Vidal M, Gifford DK, Young RA, Jaenisch R. Polycomb complexes repress developmental regulators in murine embryonic stem cells. *Nature*. 2006 May 18;441(7091):349-53. doi: 10.1038/nature04733.

Bracken AP, Kleine-Kohlbrecher D, Dietrich N, Pasini D, Gargiulo G, Beekman C, Theilgaard-Mönch K, Minucci S, Porse BT, Marine JC, Hansen KH, Helin K. The Polycomb group proteins bind throughout the INK4A-ARF locus and are disassociated in senescent cells. *Genes Dev*. 2007 Mar 1;21(5):525-30. doi: 10.1101/gad.415507.

Bressan RB, Southgate B, Ferguson KM, Blin C, Grant V, Alfazema N, Wills JC, Marques-Torrejon MA, Morrison GM, Ashmore J, Robertson F, Williams CAC, Bradley L, von Kriegsheim A, Anderson RA, Tomlinson SR, Pollard SM. Regional identity of human neural stem cells determines oncogenic responses to histone H3.3 mutants. *Cell Stem Cell*. 2021 May 6;28(5):877-893.e9. doi: 10.1016/j.stem.2021.01.016.

Bugide S, Green MR, Wajapeyee N. Inhibition of Enhancer of zeste homolog 2 (EZH2) induces natural killer cell-mediated eradication of hepatocellular carcinoma cells. *Proc Natl Acad Sci USA*. 2018 Apr 10;115(15):E3509-E3518. doi: 10.1073/pnas.1802691115.

Burr ML, Sparbier CE, Chan KL, Chan YC, Kersbergen A, Lam EYN, Azidis-Yates E, Vassiliadis D, Bell CC, Gilan O, Jackson S, Tan L, Wong SQ, Hollizeck S, Michalak EM, Siddle HV, McCabe MT, Prinjha RK, Guerra GR, Solomon BJ, Sandhu S, Dawson SJ, Beavis PA, Tothill RW, Cullinane C, Lehner PJ, Sutherland KD, Dawson MA. An Evolutionarily Conserved Function of Polycomb Silences the MHC Class I Antigen Presentation Pathway and Enables Immune Evasion in Cancer. *Cancer Cell*. 2019 Oct 14;36(4):385-401.e8. doi: 10.1016/j.ccell.2019.08.008.

Cedar H, Bergman Y. Linking DNA methylation and histone modification: patterns and paradigms. *Nat Rev Genet.* 2009 May;10(5):295-304. doi: 10.1038/nrg2540.

Chan KM, Fang D, Gan H, Hashizume R, Yu C, Schroeder M, Gupta N, Mueller S, James CD, Jenkins R, Sarkaria J, Zhang Z. The histone H3.3K27M mutation in pediatric glioma reprograms H3K27 methylation and gene expression. *Genes Dev*. 2013 May 1;27(9):985-90. doi: 10.1101/gad.217778.113.

Chen CCL, Deshmukh S, Jessa S, Hadjadj D, Lisi V, Andrade AF, Faury D, Jawhar W, Dali R, Suzuki H, Pathania M, A D, Dubois F, Woodward E, Hébert S, Coutelier M, Karamchandani J, Albrecht S, Brandner S, De Jay N, Gayden T, Bajic A, Harutyunyan AS, Marchione DM, Mikael LG, Juretic N, Zeinieh M, Russo C, Maestro N, Bassenden AV, Hauser P, Virga J, Bognar L, Klekner A, Zapotocky M, Vicha A, Krskova L, Vanova K, Zamecnik J, Sumerauer D, Ekert PG, Ziegler DS, Ellezam B, Filbin MG, Blanchette M, Hansford JR, Khuong-Quang DA, Berghuis AM, Weil AG, Garcia BA, Garzia L, Mack SC, Beroukhim R, Ligon KL, Taylor MD, Bandopadhayay P, Kramm C, Pfister SM, Korshunov A, Sturm D, Jones DTW, Salomoni P, Kleinman CL, Jabado N. Histone H3.3G34-Mutant Interneuron Progenitors Co-opt PDGFRA for Gliomagenesis. *Cell*. 2020 Dec 10;183(6):1617-1633.e22. doi: 10.1016/j.cell.2020.11.012.

Chen P, Zhao J, Wang Y, Wang M, Long H, Liang D, Huang L, Wen Z, Li W, Li X, Feng H, Zhao H, Zhu P, Li M, Wang QF, Li G. H3.3 actively marks enhancers and primes gene transcription via opening higher-ordered chromatin. *Genes Dev*. 2013 Oct 1;27(19):2109-24. doi: 10.1101/gad.222174.113.

Chi P, Allis CD, Wang GG. Covalent histone modifications--miswritten, misinterpreted and mis-erased in human cancers. *Nat Rev Cancer*. 2010 Jul;10(7):457-69. doi: 10.1038/nrc2876.

Chiappinelli KB, Strissel PL, Desrichard A, Li H, Henke C, Akman B, Hein A, Rote NS, Cope LM, Snyder A, Makarov V, Budhu S, Slamon DJ, Wolchok JD, Pardoll DM, Beckmann MW, Zahnow CA, Merghoub T, Chan TA, Baylin SB, Strick R. Inhibiting DNA Methylation Causes an Interferon Response in Cancer via dsRNA Including Endogenous Retroviruses. *Cell*. 2015 Aug 27;162(5):974-86. doi: 10.1016/j.cell.2015.07.011.

Cordero FJ, Huang Z, Grenier C, He X, Hu G, McLendon RE, Murphy SK, Hashizume R, Becher OJ. Histone H3.3K27M Represses *p16* to Accelerate Gliomagenesis in a Murine Model of DIPG. *Mol Cancer Res*. 2017 Sep;15(9):1243-1254. doi: 10.1158/1541-7786.MCR-16-0389.

Creyghton MP, Cheng AW, Welstead GG, Kooistra T, Carey BW, Steine EJ, Hanna J, Lodato MA, Frampton GM, Sharp PA, Boyer LA, Young RA, Jaenisch R. Histone H3K27ac separates active from poised enhancers and predicts developmental state. *Proc Natl Acad Sci USA*. 2010 Dec 14;107(50):21931-6. doi: 10.1073/pnas.1016071107.

Dang L, White DW, Gross S, Bennett BD, Bittinger MA, Driggers EM, Fantin VR, Jang HG, Jin S, Keenan MC, Marks KM, Prins RM, Ward PS, Yen KE, Liau LM, Rabinowitz JD, Cantley LC, Thompson CB, Vander Heiden MG, Su SM. Cancer-associated IDH1 mutations produce 2-hydroxyglutarate. *Nature*. 2009 Dec 10;462(7274):739-44. doi: 10.1038/nature08617.

Dawson MA, Prinjha RK, Dittmann A, Giotopoulos G, Bantscheff M, Chan WI, Robson SC, Chung CW, Hopf C, Savitski MM, Huthmacher C, Gudgin E, Lugo D, Beinke S, Chapman TD,

Roberts EJ, Soden PE, Auger KR, Mirguet O, Doehner K, Delwel R, Burnett AK, Jeffrey P, Drewes G, Lee K, Huntly BJ, Kouzarides T. Inhibition of BET recruitment to chromatin as an effective treatment for MLL-fusion leukaemia. *Nature*. 2011 Oct 2;478(7370):529-33. doi: 10.1038/nature10509.

Deaton AM, Bird A. CpG islands and the regulation of transcription. *Genes Dev*. 2011 May 15;25(10):1010-22. doi: 10.1101/gad.2037511.

Delmore JE, Issa GC, Lemieux ME, Rahl PB, Shi J, Jacobs HM, Kastritis E, Gilpatrick T, Paranal RM, Qi J, Chesi M, Schinzel AC, McKeown MR, Heffernan TP, Vakoc CR, Bergsagel PL, Ghobrial IM, Richardson PG, Young RA, Hahn WC, Anderson KC, Kung AL, Bradner JE, Mitsiades CS. BET bromodomain inhibition as a therapeutic strategy to target c-Myc. *Cell*. 2011 Sep 16;146(6):904-17. doi: 10.1016/j.cell.2011.08.017.

Dhayalan A, Tamas R, Bock I, Tattermusch A, Dimitrova E, Kudithipudi S, Ragozin S, Jeltsch A. The ATRX-ADD domain binds to H3 tail peptides and reads the combined methylation state of K4 and K9. *Hum Mol Genet*. 2011 Jun 1;20(11):2195-203. doi: 10.1093/hmg/ddr107.

Ehrlich M, Lacey M. DNA hypomethylation and hemimethylation in cancer. *Adv Exp Med Biol*. 2013;754:31-56. doi: 10.1007/978-1-4419-9967-2_2.

Elsaesser SJ, Allis CD. HIRA and Daxx constitute two independent histone H3.3-containing predeposition complexes. *Cold Spring Harb Symp Quant Biol*. 2010;75:27-34. doi: 10.1101/sqb.2010.75.008.

Elsässer SJ, Huang H, Lewis PW, Chin JW, Allis CD, Patel DJ. DAXX envelops a histone H3.3-H4 dimer for H3.3-specific recognition. *Nature*. 2012 Nov 22;491(7425):560-5. doi: 10.1038/nature11608.

Fang J, Feng Q, Ketel CS, Wang H, Cao R, Xia L, Erdjument-Bromage H, Tempst P, Simon JA, Zhang Y. Purification and functional characterization of SET8, a nucleosomal histone H4-lysine 20-specific methyltransferase. *Curr Biol*. 2002 Jul 9;12(13):1086-99. doi: 10.1016/s0960-9822(02)00924-7.

Fang J, Huang Y, Mao G, Yang S, Rennert G, Gu L, Li H, Li GM. Cancer-driving H3G34V/R/D mutations block H3K36 methylation and H3K36me3-MutSα interaction. *Proc Natl Acad Sci USA*. 2018 Sep 18;115(38):9598-9603. doi: 10.1073/pnas.1806355115.

Faury D, Nantel A, Dunn SE, Guiot MC, Haque T, Hauser P, Garami M, Bognár L, Hanzély Z, Liberski PP, Lopez-Aguilar E, Valera ET, Tone LG, Carret AS, Del Maestro RF, Gleave M, Montes JL, Pietsch T, Albrecht S, Jabado N. Molecular profiling identifies prognostic subgroups of pediatric glioblastoma and shows increased YB-1 expression in tumors. *J Clin Oncol*. 2007 Apr 1;25(10):1196-208. doi: 10.1200/JCO.2006.07.8626.

Fellenberg J, Sähr H, Mancarella D, Plass C, Lindroth AM, Westhauser F, Lehner B, Ewerbeck V. Knock-down of oncohistone H3F3A-G34W counteracts the neoplastic phenotype of giant cell

tumor of bone derived stromal cells. *Cancer Lett*. 2019 Apr 28;448:61-69. doi: 10.1016/j.canlet.2019.02.001.

Filbin MG, Tirosh I, Hovestadt V, Shaw ML, Escalante LE, Mathewson ND, Neftel C, Frank N, Pelton K, Hebert CM, Haberler C, Yizhak K, Gojo J, Egervari K, Mount C, van Galen P, Bonal DM, Nguyen QD, Beck A, Sinai C, Czech T, Dorfer C, Goumnerova L, Lavarino C, Carcaboso AM, Mora J, Mylvaganam R, Luo CC, Peyrl A, Popović M, Azizi A, Batchelor TT, Frosch MP, Martinez-Lage M, Kieran MW, Bandopadhayay P, Beroukhim R, Fritsch G, Getz G, Rozenblatt-Rosen O, Wucherpfennig KW, Louis DN, Monje M, Slavc I, Ligon KL, Golub TR, Regev A, Bernstein BE, Suvà ML. Developmental and oncogenic programs in H3K27M gliomas dissected by single-cell RNA-seq. *Science*. 2018 Apr 20;360(6386):331-335. doi: 10.1126/science.aao4750.

Filippakopoulos P, Knapp S. Targeting bromodomains: epigenetic readers of lysine acetylation. *Nat Rev Drug Discov*. 2014 May;13(5):337-56. doi: 10.1038/nrd4286.

Fiskus W, Sharma S, Qi J, Valenta JA, Schaub LJ, Shah B, Peth K, Portier BP, Rodriguez M, Devaraj SG, Zhan M, Sheng J, Iyer SP, Bradner JE, Bhalla KN. Highly active combination of BRD4 antagonist and histone deacetylase inhibitor against human acute myelogenous leukemia cells. *Mol Cancer Ther*. 2014a May;13(5):1142-54. doi: 10.1158/1535-7163.MCT-13-0770.

Fiskus W, Sharma S, Shah B, Portier BP, Devaraj SG, Liu K, Iyer SP, Bearss D, Bhalla KN. Highly effective combination of LSD1 (KDM1A) antagonist and pan-histone deacetylase inhibitor against human AML cells. *Leukemia*. 2014b Nov;28(11):2155-64. doi: 10.1038/leu.2014.119.

Fontebasso AM, Liu XY, Sturm D, Jabado N. Chromatin remodeling defects in pediatric and young adult glioblastoma: a tale of a variant histone 3 tail. *Brain Pathol*. 2013a Mar;23(2):210-6. doi: 10.1111/bpa.12023.

Fontebasso AM, Schwartzentruber J, Khuong-Quang DA, Liu XY, Sturm D, Korshunov A, Jones DT, Witt H, Kool M, Albrecht S, Fleming A, Hadjadj D, Busche S, Lepage P, Montpetit A, Staffa A, Gerges N, Zakrzewska M, Zakrzewski K, Liberski PP, Hauser P, Garami M, Klekner A, Bognar L, Zadeh G, Faury D, Pfister SM, Jabado N, Majewski J. Mutations in SETD2 and genes affecting histone H3K36 methylation target hemispheric high-grade gliomas. *Acta Neuropathol*. 2013b May;125(5):659-69. doi: 10.1007/s00401-013-1095-8.

Funato K, Major T, Lewis PW, Allis CD, Tabar V. Use of human embryonic stem cells to model pediatric gliomas with H3.3K27M histone mutation. *Science*. 2014 Dec 19;346(6216):1529-33. doi: 10.1126/science.1253799.

Garrido F, Aptsiauri N, Doorduijn EM, Garcia Lora AM, van Hall T. The urgent need to recover MHC class I in cancers for effective immunotherapy. Curr Opin Immunol. 2016 Apr;39:44-51. doi: 10.1016/j.coi.2015.12.007.

Gil J, Peters G. Regulation of the INK4b-ARF-INK4a tumour suppressor locus: all for one or one for all. *Nat Rev Mol Cell Biol*. 2006 Sep;7(9):667-77. doi: 10.1038/nrm1987.

Goldberg AD, Banaszynski LA, Noh KM, Lewis PW, Elsaesser SJ, Stadler S, Dewell S, Law M, Guo X, Li X, Wen D, Chapgier A, DeKelver RC, Miller JC, Lee YL, Boydston EA, Holmes MC, Gregory PD, Greally JM, Rafii S, Yang C, Scambler PJ, Garrick D, Gibbons RJ, Higgs DR, Cristea IM, Urnov FD, Zheng D, Allis CD. Distinct factors control histone variant H3.3 localization at specific genomic regions. *Cell*. 2010 Mar 5;140(5):678-91. doi: 10.1016/j.cell.2010.01.003.

Gomes AP, Ilter D, Low V, Rosenzweig A, Shen ZJ, Schild T, Rivas MA, Er EE, McNally DR, Mutvei AP, Han J, Ou YH, Cavaliere P, Mullarky E, Nagiec M, Shin S, Yoon SO, Dephoure N, Massagué J, Melnick AM, Cantley LC, Tyler JK, Blenis J. Dynamic Incorporation of Histone H3 Variants into Chromatin Is Essential for Acquisition of Aggressive Traits and Metastatic Colonization. *Cancer Cell*. 2019 Oct 14;36(4):402-417.e13. doi: 10.1016/j.ccell.2019.08.006.

Gong L, Bui MM, Zhang W, Sun X, Zhang M, Yi D. H3F3A G34 mutation DNA sequencing and G34W immunohistochemistry analysis in 366 cases of giant cell tumors of bone and other bone tumors. *Histol Histopathol*. 2021 Jan;36(1):61-68. doi: 10.14670/HH-18-264.

Gonzalez ME, Li X, Toy K, DuPrie M, Ventura AC, Banerjee M, Ljungman M, Merajver SD, Kleer CG. Downregulation of EZH2 decreases growth of estrogen receptor-negative invasive breast carcinoma and requires BRCA1. *Oncogene*. 2009 Feb 12;28(6):843-53. doi: 10.1038/onc.2008.433.

Grasso CS, Tang Y, Truffaux N, Berlow NE, Liu L, Debily MA, Quist MJ, Davis LE, Huang EC, Woo PJ, Ponnuswami A, Chen S, Johung TB, Sun W, Kogiso M, Du Y, Qi L, Huang Y, Hütt-Cabezas M, Warren KE, Le Dret L, Meltzer PS, Mao H, Quezado M, van Vuurden DG, Abraham J, Fouladi M, Svalina MN, Wang N, Hawkins C, Nazarian J, Alonso MM, Raabe EH, Hulleman E, Spellman PT, Li XN, Keller C, Pal R, Grill J, Monje M. Functionally defined therapeutic targets in diffuse intrinsic pontine glioma. *Nat Med*. 2015 Jun;21(6):555-9. doi: 10.1038/nm.3855.

Greer EL, Shi Y. Histone methylation: a dynamic mark in health, disease and inheritance. *Nat Rev Genet*. 2012 Apr 3;13(5):343-57. doi: 10.1038/nrg3173.

Guo R, Zheng L, Park JW, Lv R, Chen H, Jiao F, Xu W, Mu S, Wen H, Qiu J, Wang Z, Yang P, Wu F, Hui J, Fu X, Shi X, Shi YG, Xing Y, Lan F, Shi Y. BS69/ZMYND11 reads and connects histone H3.3 lysine 36 trimethylation-decorated chromatin to regulated pre-mRNA processing. *Mol Cell*. 2014 Oct 23;56(2):298-310. doi: 10.1016/j.molcel.2014.08.022.

Han M, Jia L, Lv W, Wang L, Cui W. Epigenetic Enzyme Mutations: Role in Tumorigenesis and Molecular Inhibitors. *Front Oncol*. 2019 Mar 29;9:194. doi: 10.3389/fonc.2019.00194.

Harutyunyan AS, Krug B, Chen H, Papillon-Cavanagh S, Zeinieh M, De Jay N, Deshmukh S, Chen CCL, Belle J, Mikael LG, Marchione DM, Li R, Nikbakht H, Hu B, Cagnone G, Cheung WA, Mohammadnia A, Bechet D, Faury D, McConechy MK, Pathania M, Jain SU, Ellezam B, Weil AG, Montpetit A, Salomoni P, Pastinen T, Lu C, Lewis PW, Garcia BA, Kleinman CL, Jabado N, Majewski J. H3K27M induces defective chromatin spread of PRC2-mediated repressive H3K27me2/me3 and is essential for glioma tumorigenesis. *Nat Commun*. 2019 Mar 19;10(1):1262. doi: 10.1038/s41467-019-09140-x.

Hashizume R, Andor N, Ihara Y, Lerner R, Gan H, Chen X, Fang D, Huang X, Tom MW, Ngo V, Solomon D, Mueller S, Paris PL, Zhang Z, Petritsch C, Gupta N, Waldman TA, James CD. Pharmacologic inhibition of histone demethylation as a therapy for pediatric brainstem glioma. *Nat Med*. 2014 Dec;20(12):1394-6. doi: 10.1038/nm.3716.

Heintzman ND, Hon GC, Hawkins RD, Kheradpour P, Stark A, Harp LF, Ye Z, Lee LK, Stuart RK, Ching CW, Ching KA, Antosiewicz-Bourget JE, Liu H, Zhang X, Green RD, Lobanenkov VV, Stewart R, Thomson JA, Crawford GE, Kellis M, Ren B. Histone modifications at human enhancers reflect global cell-type-specific gene expression. Nature. 2009 May 7;459(7243):108-12. doi: 10.1038/nature07829.

Henikoff S, Smith MM. Histone variants and epigenetics. *Cold Spring Harb Perspect Biol*. 2015 Jan 5;7(1):a019364. doi: 10.1101/cshperspect.a019364.

Hennika T, Hu G, Olaciregui NG, Barton KL, Ehteda A, Chitranjan A, Chang C, Gifford AJ, Tsoli M, Ziegler DS, Carcaboso AM, Becher OJ. Pre-Clinical Study of Panobinostat in Xenograft and Genetically Engineered Murine Diffuse Intrinsic Pontine Glioma Models. *PLoS One*. 2017 Jan 4;12(1):e0169485. doi: 10.1371/journal.pone.0169485.

Holst CR, Nuovo GJ, Esteller M, Chew K, Baylin SB, Herman JG, Tlsty TD. Methylation of p16(INK4a) promoters occurs in vivo in histologically normal human mammary epithelia. *Cancer Res*. 2003 Apr 1;63(7):1596-601.

Hou PS, hAilín DÓ, Vogel T, Hanashima C. Transcription and Beyond: Delineating FOXG1 Function in Cortical Development and Disorders. *Front Cell Neurosci*. 2020;14:35. Published 2020 Feb 25. doi:10.3389/fncel.2020.00035

Hur K, Cejas P, Feliu J, Moreno-Rubio J, Burgos E, Boland CR, Goel A. Hypomethylation of long interspersed nuclear element-1 (LINE-1) leads to activation of proto-oncogenes in human colorectal cancer metastasis. *Gut*. 2014 Apr;63(4):635-46. doi: 10.1136/gutjnl-2012-304219.

Jain SU, Khazaei S, Marchione DM, Lundgren SM, Wang X, Weinberg DN, Deshmukh S, Juretic N, Lu C, Allis CD, Garcia BA, Jabado N, Lewis PW. Histone H3.3 G34 mutations promote aberrant PRC2 activity and drive tumor progression. *Proc Natl Acad Sci USA*. 2020 Nov 3;117(44):27354-27364. doi: 10.1073/pnas.2006076117.

Jang MK, Mochizuki K, Zhou M, Jeong HS, Brady JN, Ozato K. The bromodomain protein Brd4 is a positive regulatory component of P-TEFb and stimulates RNA polymerase II-dependent transcription. *Mol Cell*. 2005 Aug 19;19(4):523-34. doi: 10.1016/j.molcel.2005.06.027.

Jiao F, Li Z, He C, Xu W, Yang G, Liu T, Shen H, Cai J, Anastas JN, Mao Y, Yu Y, Lan F, Shi YG, Jones C, Xu Y, Baker SJ, Shi Y, Guo R. RACK7 recognizes H3.3G34R mutation to suppress expression of MHC class II complex components and their delivery pathway in pediatric glioblastoma. *Sci Adv*. 2020 Jul 17;6(29):eaba2113. doi: 10.1126/sciadv.aba2113.

Jiao L, Liu X. Structural basis of histone H3K27 trimethylation by an active polycomb repressive complex 2. *Science*. 2015 Oct 16;350(6258):aac4383. doi: 10.1126/science.aac4383.

Jones C, Baker SJ. Unique genetic and epigenetic mechanisms driving paediatric diffuse high-grade glioma. *Nat Rev Cancer*. 2014 Oct;14(10):10.1038/nrc3811. doi: 10.1038/nrc3811.

Justin N, Zhang Y, Tarricone C, Martin SR, Chen S, Underwood E, De Marco V, Haire LF, Walker PA, Reinberg D, Wilson JR, Gamblin SJ. Structural basis of oncogenic histone H3K27M inhibition of human polycomb repressive complex 2. *Nat Commun*. 2016 Apr 28;7:11316. doi: 10.1038/ncomms11316.

Kanai Y, Ushijima S, Nakanishi Y, Sakamoto M, Hirohashi S. Mutation of the DNA methyltransferase (DNMT) 1 gene in human colorectal cancers. *Cancer Lett*. 2003 Mar 20;192(1):75-82. doi: 10.1016/s0304-3835(02)00689-4.

Kang N, Eccleston M, Clermont PL, Latarani M, Male DK, Wang Y, Crea F. EZH2 inhibition: a promising strategy to prevent cancer immune editing. *Epigenomics*. 2020 Aug;12(16):1457-1476. doi: 10.2217/epi-2020-0186.

Khazaei S, De Jay N, Deshmukh S, Hendrikse LD, Jawhar W, Chen CCL, Mikael LG, Faury D, Marchione DM, Lanoix J, Bonneil É, Ishii T, Jain SU, Rossokhata K, Sihota TS, Eveleigh R, Lisi V, Harutyunyan AS, Jung S, Karamchandani J, Dickson BC, Turcotte R, Wunder JS, Thibault P, Lewis PW, Garcia BA, Mack SC, Taylor MD, Garzia L, Kleinman CL, Jabado N. H3.3 G34W Promotes Growth and Impedes Differentiation of Osteoblast-Like Mesenchymal Progenitors in Giant Cell Tumor of Bone. *Cancer Discov*. 2020 Dec;10(12):1968-1987. doi: 10.1158/2159-8290.CD-20-0461.

Khuong-Quang DA, Buczkowicz P, Rakopoulos P, Liu XY, Fontebasso AM, Bouffet E, Bartels U, Albrecht S, Schwartzentruber J, Letourneau L, Bourgey M, Bourque G, Montpetit A, Bourret G, Lepage P, Fleming A, Lichter P, Kool M, von Deimling A, Sturm D, Korshunov A, Faury D, Jones DT, Majewski J, Pfister SM, Jabado N, Hawkins C. K27M mutation in histone H3.3 defines clinically and biologically distinct subgroups of pediatric diffuse intrinsic pontine gliomas. *Acta Neuropathol*. 2012 Sep;124(3):439-47. doi: 10.1007/s00401-012-0998-0.

Kizer KO, Phatnani HP, Shibata Y, Hall H, Greenleaf AL, Strahl BD. A novel domain in Set2 mediates RNA polymerase II interaction and couples histone H3 K36 methylation with transcript elongation. Mol *Cell Biol*. 2005 Apr;25(8):3305-16. doi: 10.1128/MCB.25.8.3305-3316.2005.

Kleer CG, Cao Q, Varambally S, Shen R, Ota I, Tomlins SA, Ghosh D, Sewalt RG, Otte AP, Hayes DF, Sabel MS, Livant D, Weiss SJ, Rubin MA, Chinnaiyan AM. EZH2 is a marker of aggressive breast cancer and promotes neoplastic transformation of breast epithelial cells. *Proc Natl Acad Sci USA*. 2003 Sep 30;100(20):11606-11. doi: 10.1073/pnas.1933744100.

Knutson SK, Kawano S, Minoshima Y, Warholic NM, Huang KC, Xiao Y, Kadowaki T, Uesugi M, Kuznetsov G, Kumar N, Wigle TJ, Klaus CR, Allain CJ, Raimondi A, Waters NJ, Smith JJ, Porter-Scott M, Chesworth R, Moyer MP, Copeland RA, Richon VM, Uenaka T, Pollock RM,

Kuntz KW, Yokoi A, Keilhack H. Selective inhibition of EZH2 by EPZ-6438 leads to potent antitumor activity in EZH2-mutant non-Hodgkin lymphoma. *Mol Cancer Ther*. 2014 Apr;13(4):842-54. doi: 10.1158/1535-7163.MCT-13-0773.

Kondo Y, Shen L, Cheng AS, Ahmed S, Boumber Y, Charo C, Yamochi T, Urano T, Furukawa K, Kwabi-Addo B, Gold DL, Sekido Y, Huang TH, Issa JP. Gene silencing in cancer by histone H3 lysine 27 trimethylation independent of promoter DNA methylation. *Nat Genet*. 2008 Jun;40(6):741-50. doi: 10.1038/ng.159.

Krug B, De Jay N, Harutyunyan AS, Deshmukh S, Marchione DM, Guilhamon P, Bertrand KC, Mikael LG, McConechy MK, Chen CCL, Khazaei S, Koncar RF, Agnihotri S, Faury D, Ellezam B, Weil AG, Ursini-Siegel J, De Carvalho DD, Dirks PB, Lewis PW, Salomoni P, Lupien M, Arrowsmith C, Lasko PF, Garcia BA, Kleinman CL, Jabado N, Mack SC. Pervasive H3K27 Acetylation Leads to ERV Expression and a Therapeutic Vulnerability in H3K27M Gliomas. *Cancer Cell*. 2019 May 13;35(5):782-797.e8. doi: 10.1016/j.ccell.2019.04.004.

Larson JD, Kasper LH, Paugh BS, Jin H, Wu G, Kwon CH, Fan Y, Shaw TI, Silveira AB, Qu C, Xu R, Zhu X, Zhang J, Russell HR, Peters JL, Finkelstein D, Xu B, Lin T, Tinkle CL, Patay Z, Onar-Thomas A, Pounds SB, McKinnon PJ, Ellison DW, Zhang J, Baker SJ. Histone H3.3 K27M Accelerates Spontaneous Brainstem Glioma and Drives Restricted Changes in Bivalent Gene Expression. *Cancer Cell*. 2019 Jan 14;35(1):140-155.e7. doi: 10.1016/j.ccell.2018.11.015.

Lee TI, Jenner RG, Boyer LA, Guenther MG, Levine SS, Kumar RM, Chevalier B, Johnstone SE, Cole MF, Isono K, Koseki H, Fuchikami T, Abe K, Murray HL, Zucker JP, Yuan B, Bell GW, Herbolsheimer E, Hannett NM, Sun K, Odom DT, Otte AP, Volkert TL, Bartel DP, Melton DA, Gifford DK, Jaenisch R, Young RA. Control of developmental regulators by Polycomb in human embryonic stem cells. *Cell*. 2006 Apr 21;125(2):301-13. doi: 10.1016/j.cell.2006.02.043.

LeRoy G, Rickards B, Flint SJ. The double bromodomain proteins Brd2 and Brd3 couple histone acetylation to transcription. *Mol Cell*. 2008 Apr 11;30(1):51-60. doi: 10.1016/j.molcel.2008.01.018.

Lewis PW, Elsaesser SJ, Noh KM, Stadler SC, Allis CD. Daxx is an H3.3-specific histone chaperone and cooperates with ATRX in replication-independent chromatin assembly at telomeres. *Proc Natl Acad Sci USA*. 2010 Aug 10;107(32):14075-80. doi: 10.1073/pnas.1008850107.

Lewis PW, Müller MM, Koletsky MS, Cordero F, Lin S, Banaszynski LA, Garcia BA, Muir TW, Becher OJ, Allis CD. Inhibition of PRC2 activity by a gain-of-function H3 mutation found in pediatric glioblastoma. *Science*. 2013 May 17;340(6134):857-61. doi: 10.1126/science.1232245.

Ley TJ, Ding L, Walter MJ, McLellan MD, Lamprecht T, Larson DE, Kandoth C, Payton JE, Baty J, Welch J, Harris CC, Lichti CF, Townsend RR, Fulton RS, Dooling DJ, Koboldt DC, Schmidt H, Zhang Q, Osborne JR, Lin L, O'Laughlin M, McMichael JF, Delehaunty KD, McGrath SD, Fulton LA, Magrini VJ, Vickery TL, Hundal J, Cook LL, Conyers JJ, Swift GW, Reed JP, Alldredge PA, Wylie T, Walker J, Kalicki J, Watson MA, Heath S, Shannon WD, Varghese N,

Nagarajan R, Westervelt P, Tomasson MH, Link DC, Graubert TA, DiPersio JF, Mardis ER, Wilson RK. DNMT3A mutations in acute myeloid leukemia. *N Engl J Med*. 2010 Dec 16;363(25):2424-33. doi: 10.1056/NEJMoa1005143.

Lim J, Park JH, Baude A, Yoo Y, Lee YK, Schmidt CR, Park JB, Fellenberg J, Zustin J, Haller F, Krücken I, Kang HG, Park YJ, Plass C, Lindroth AM. The histone variant H3.3 G34W substitution in giant cell tumor of the bone link chromatin and RNA processing. *Sci Rep*. 2017 Oct 18;7(1):13459. doi: 10.1038/s41598-017-13887-y.

Liu CP, Xiong C, Wang M, Yu Z, Yang N, Chen P, Zhang Z, Li G, Xu RM. Structure of the variant histone H3.3-H4 heterodimer in complex with its chaperone DAXX. *Nat Struct Mol Biol*. 2012 Dec;19(12):1287-92. doi: 10.1038/nsmb.2439.

Lovén J, Hoke HA, Lin CY, Lau A, Orlando DA, Vakoc CR, Bradner JE, Lee TI, Young RA. Selective inhibition of tumor oncogenes by disruption of super-enhancers. *Cell*. 2013 Apr 11;153(2):320-34. doi: 10.1016/j.cell.2013.03.036.

Lu C, Jain SU, Hoelper D, Bechet D, Molden RC, Ran L, Murphy D, Venneti S, Hameed M, Pawel BR, Wunder JS, Dickson BC, Lundgren SM, Jani KS, De Jay N, Papillon-Cavanagh S, Andrulis IL, Sawyer SL, Grynspan D, Turcotte RE, Nadaf J, Fahiminiyah S, Muir TW, Majewski J, Thompson CB, Chi P, Garcia BA, Allis CD, Jabado N, Lewis PW. Histone H3K36 mutations promote sarcomagenesis through altered histone methylation landscape. *Science*. 2016 May 13;352(6287):844-9. doi: 10.1126/science.aac7272.

Lu C, Ward PS, Kapoor GS, Rohle D, Turcan S, Abdel-Wahab O, Edwards CR, Khanin R, Figueroa ME, Melnick A, Wellen KE, O'Rourke DM, Berger SL, Chan TA, Levine RL, Mellinghoff IK, Thompson CB. IDH mutation impairs histone demethylation and results in a block to cell differentiation. *Nature*. 2012 Feb 15;483(7390):474-8. doi: 10.1038/nature10860.

Lutsik P, Baude A, Mancarella D, Öz S, Kühn A, Toth R, Hey J, Toprak UH, Lim J, Nguyen VH, Jiang C, Mayakonda A, Hartmann M, Rosemann F, Breuer K, Vonficht D, Grünschläger F, Lee S, Schuhmacher MK, Kusevic D, Jauch A, Weichenhan D, Zustin J, Schlesner M, Haas S, Park JH, Park YJ, Oppermann U, Jeltsch A, Haller F, Fellenberg J, Lindroth AM, Plass C. Globally altered epigenetic landscape and delayed osteogenic differentiation in H3.3-G34W-mutant giant cell tumor of bone. *Nat Commun*. 2020 Oct 27;11(1):5414. doi: 10.1038/s41467-020-18955-y.

Mackay A, Burford A, Carvalho D, Izquierdo E, Fazal-Salom J, Taylor KR, Bjerke L, Clarke M, Vinci M, Nandhabalan M, Temelso S, Popov S, Molinari V, Raman P, Waanders AJ, Han HJ, Gupta S, Marshall L, Zacharoulis S, Vaidya S, Mandeville HC, Bridges LR, Martin AJ, Al-Sarraj S, Chandler C, Ng HK, Li X, Mu K, Trabelsi S, Brahim DH, Kisljakov AN, Konovalov DM, Moore AS, Carcaboso AM, Sunol M, de Torres C, Cruz O, Mora J, Shats LI, Stavale JN, Bidinotto LT, Reis RM, Entz-Werle N, Farrell M, Cryan J, Crimmins D, Caird J, Pears J, Monje M, Debily MA, Castel D, Grill J, Hawkins C, Nikbakht H, Jabado N, Baker SJ, Pfister SM, Jones DTW, Fouladi M, von Bueren AO, Baudis M, Resnick A, Jones C. Integrated Molecular Meta-Analysis of 1,000 Pediatric High-Grade and Diffuse Intrinsic Pontine Glioma. *Cancer Cell*. 2017 Oct 9;32(4):520-537.e5. doi: 10.1016/j.ccell.2017.08.017.

Majer CR, Jin L, Scott MP, Knutson SK, Kuntz KW, Keilhack H, Smith JJ, Moyer MP, Richon VM, Copeland RA, Wigle TJ. A687V EZH2 is a gain-of-function mutation found in lymphoma patients. *FEBS Lett*. 2012 Sep 21;586(19):3448-51. doi: 10.1016/j.febslet.2012.07.066.

Margueron R, Justin N, Ohno K, Sharpe ML, Son J, Drury WJ 3rd, Voigt P, Martin SR, Taylor WR, De Marco V, Pirrotta V, Reinberg D, Gamblin SJ. Role of the polycomb protein EED in the propagation of repressive histone marks. *Nature*. 2009 Oct 8;461(7265):762-7. doi: 10.1038/nature08398.

Mariño-Ramírez L, Kann MG, Shoemaker BA, Landsman D. Histone structure and nucleosome stability. *Expert Rev Proteomics*. 2005 Oct;2(5):719-29. doi: 10.1586/14789450.2.5.719.

Mashtalir N, Dao HT, Sankar A, Liu H, Corin A, Bagert J, Ge E, D'Avino A, Filipovski M, Michel B, Dann G, Muir T, Kadoch C. Chromatin landscape signals differentially dictate the activities of mSWI/SNF family complexes. *Science*. 2021 Jul 16. doi:10.1126/science.abf8705ss.

Matsubara T, Toyokawa G, Takada K, Kinoshita F, Kozuma Y, Akamine T, Shimokawa M, Haro A, Osoegawa A, Tagawa T, Mori M. The association and prognostic impact of enhancer of zeste homologue 2 expression and epithelial-mesenchymal transition in resected lung adenocarcinoma. *PLoS One*. 2019 May 1;14(5):e0215103. doi: 10.1371/journal.pone.0215103.

McCabe MT, Ott HM, Ganji G, Korenchuk S, Thompson C, Van Aller GS, Liu Y, Graves AP, Della Pietra A 3rd, Diaz E, LaFrance LV, Mellinger M, Duquenne C, Tian X, Kruger RG, McHugh CF, Brandt M, Miller WH, Dhanak D, Verma SK, Tummino PJ, Creasy CL. EZH2 inhibition as a therapeutic strategy for lymphoma with EZH2-activating mutations. *Nature*. 2012 Dec 6;492(7427):108-12. doi: 10.1038/nature11606.

McKittrick E, Gafken PR, Ahmad K, Henikoff S. Histone H3.3 is enriched in covalent modifications associated with active chromatin. *Proc Natl Acad Sci USA*. 2004 Feb 10;101(6):1525-30. doi: 10.1073/pnas.0308092100.

Mohammad F, Weissmann S, Leblanc B, Pandey DP, Højfeldt JW, Comet I, Zheng C, Johansen JV, Rapin N, Porse BT, Tvardovskiy A, Jensen ON, Olaciregui NG, Lavarino C, Suñol M, de Torres C, Mora J, Carcaboso AM, Helin K. EZH2 is a potential therapeutic target for H3K27M-mutant pediatric gliomas. *Nat Med*. 2017 Apr;23(4):483-492. doi: 10.1038/nm.4293.

Monje M, Mitra SS, Freret ME, Raveh TB, Kim J, Masek M, Attema JL, Li G, Haddix T, Edwards MS, Fisher PG, Weissman IL, Rowitch DH, Vogel H, Wong AJ, Beachy PA. Hedgehog-responsive candidate cell of origin for diffuse intrinsic pontine glioma. *Proc Natl Acad Sci USA*. 2011 Mar 15;108(11):4453-8. doi: 10.1073/pnas.1101657108.

Morin RD, Johnson NA, Severson TM, Mungall AJ, An J, Goya R, Paul JE, Boyle M, Woolcock BW, Kuchenbauer F, Yap D, Humphries RK, Griffith OL, Shah S, Zhu H, Kimbara M, Shashkin P, Charlot JF, Tcherpakov M, Corbett R, Tam A, Varhol R, Smailus D, Moksa M, Zhao Y, Delaney A, Qian H, Birol I, Schein J, Moore R, Holt R, Horsman DE, Connors JM, Jones S, Aparicio S,

Hirst M, Gascoyne RD, Marra MA. Somatic mutations altering EZH2 (Tyr641) in follicular and diffuse large B-cell lymphomas of germinal-center origin. *Nat Genet*. 2010 Feb;42(2):181-5. doi: 10.1038/ng.518.

Nagaraja S, Vitanza NA, Woo PJ, Taylor KR, Liu F, Zhang L, Li M, Meng W, Ponnuswami A, Sun W, Ma J, Hulleman E, Swigut T, Wysocka J, Tang Y, Monje M. Transcriptional Dependencies in Diffuse Intrinsic Pontine Glioma. *Cancer Cell*. 2017 May 8;31(5):635-652.e6. doi: 10.1016/j.ccell.2017.03.011.

Nagaraja S, Quezada MA, Gillespie SM, Arzt M, Lennon JJ, Woo PJ, Hovestadt V, Kambhampati M, Filbin MG, Suva ML, Nazarian J, Monje M. Histone Variant and Cell Context Determine H3K27M Reprogramming of the Enhancer Landscape and Oncogenic State. *Mol Cell*. 2019 Dec 19;76(6):965-980.e12. doi: 10.1016/j.molcel.2019.08.030.

Ostrom QT, Gittleman H, Fulop J, Liu M, Blanda R, Kromer C, Wolinsky Y, Kruchko C, Barnholtz-Sloan JS. CBTRUS Statistical Report: Primary Brain and Central Nervous System Tumors Diagnosed in the United States in 2008-2012. *Neuro Oncol*. 2015 Oct;17 Suppl 4(Suppl 4):iv1-iv62. doi: 10.1093/neuonc/nov189.

Papillon-Cavanagh S, Lu C, Gayden T, Mikael LG, Bechet D, Karamboulas C, Ailles L, Karamchandani J, Marchione DM, Garcia BA, Weinreb I, Goldstein D, Lewis PW, Dancu OM, Dhaliwal S, Stecho W, Howlett CJ, Mymryk JS, Barrett JW, Nichols AC, Allis CD, Majewski J, Jabado N. Impaired H3K36 methylation defines a subset of head and neck squamous cell carcinomas. *Nat Genet*. 2017 Feb;49(2):180-185. doi: 10.1038/ng.3757.

Parsons DW, Jones S, Zhang X, Lin JC, Leary RJ, Angenendt P, Mankoo P, Carter H, Siu IM, Gallia GL, Olivi A, McLendon R, Rasheed BA, Keir S, Nikolskaya T, Nikolsky Y, Busam DA, Tekleab H, Diaz LA Jr, Hartigan J, Smith DR, Strausberg RL, Marie SK, Shinjo SM, Yan H, Riggins GJ, Bigner DD, Karchin R, Papadopoulos N, Parmigiani G, Vogelstein B, Velculescu VE, Kinzler KW. An integrated genomic analysis of human glioblastoma multiforme. *Science*. 2008 Sep 26;321(5897):1807-12. doi: 10.1126/science.1164382.

Patel SK, Hartley RM, Wei X, Furnish R, Escobar-Riquelme F, Bear H, Choi K, Fuller C, Phoenix TN. Generation of diffuse intrinsic pontine glioma mouse models by brainstem-targeted in utero electroporation. *Neuro Oncol*. 2020 Mar 5;22(3):381-392. doi: 10.1093/neuonc/noz197.

Pathania M, De Jay N, Maestro N, Harutyunyan AS, Nitarska J, Pahlavan P, Henderson S, Mikael LG, Richard-Londt A, Zhang Y, Costa JR, Hébert S, Khazaei S, Ibrahim NS, Herrero J, Riccio A, Albrecht S, Ketteler R, Brandner S, Kleinman CL, Jabado N, Salomoni P. H3.3^{K27M} Cooperates with Trp53 Loss and PDGFRA Gain in Mouse Embryonic Neural Progenitor Cells to Induce Invasive High-Grade Gliomas. *Cancer Cell*. 2017 Nov 13;32(5):684-700.e9. doi: 10.1016/j.ccell.2017.09.014.

Paugh BS, Broniscer A, Qu C, Miller CP, Zhang J, Tatevossian RG, Olson JM, Geyer JR, Chi SN, da Silva NS, Onar-Thomas A, Baker JN, Gajjar A, Ellison DW, Baker SJ. Genome-wide analyses identify recurrent amplifications of receptor tyrosine kinases and cell-cycle regulatory genes in

diffuse intrinsic pontine glioma. *J Clin Oncol*. 2011 Oct 20;29(30):3999-4006. doi: 10.1200/JCO.2011.35.5677.

Paugh BS, Qu C, Jones C, Liu Z, Adamowicz-Brice M, Zhang J, Bax DA, Coyle B, Barrow J, Hargrave D, Lowe J, Gajjar A, Zhao W, Broniscer A, Ellison DW, Grundy RG, Baker SJ. Integrated molecular genetic profiling of pediatric high-grade gliomas reveals key differences with the adult disease. *J Clin Oncol*. 2010 Jun 20;28(18):3061-8. doi: 10.1200/JCO.2009.26.7252.

Paugh BS, Zhu X, Qu C, Endersby R, Diaz AK, Zhang J, Bax DA, Carvalho D, Reis RM, Onar-Thomas A, Broniscer A, Wetmore C, Zhang J, Jones C, Ellison DW, Baker SJ. Novel oncogenic PDGFRA mutations in pediatric high-grade gliomas. *Cancer Res*. 2013 Oct 15;73(20):6219-29. doi: 10.1158/0008-5472.CAN-13-1491.

Piunti A, Hashizume R, Morgan MA, Bartom ET, Horbinski CM, Marshall SA, Rendleman EJ, Ma Q, Takahashi YH, Woodfin AR, Misharin AV, Abshiru NA, Lulla RR, Saratsis AM, Kelleher NL, James CD, Shilatifard A. Therapeutic targeting of polycomb and BET bromodomain proteins in diffuse intrinsic pontine gliomas. *Nat Med*. 2017 Apr;23(4):493-500. doi: 10.1038/nm.4296.

Pollack IF, Finkelstein SD, Woods J, Burnham J, Holmes EJ, Hamilton RL, Yates AJ, Boyett JM, Finlay JL, Sposto R; Children's Cancer Group. Expression of p53 and prognosis in children with malignant gliomas. *N Engl J Med*. 2002 Feb 7;346(6):420-7. doi: 10.1056/NEJMoa012224..

Qu HQ, Jacob K, Fatet S, Ge B, Barnett D, Delattre O, Faury D, Montpetit A, Solomon L, Hauser P, Garami M, Bognar L, Hansely Z, Mio R, Farmer JP, Albrecht S, Polychronakos C, Hawkins C, Jabado N. Genome-wide profiling using single-nucleotide polymorphism arrays identifies novel chromosomal imbalances in pediatric glioblastomas. *Neuro Oncol*. 2010 Feb;12(2):153-63. doi: 10.1093/neuonc/nop001.

Rada-Iglesias A, Bajpai R, Swigut T, Brugmann SA, Flynn RA, Wysocka J. A unique chromatin signature uncovers early developmental enhancers in humans. *Nature*. 2011 Feb 10;470(7333):279-83. doi: 10.1038/nature09692.

Reddington JP, Perricone SM, Nestor CE, Reichmann J, Youngson NA, Suzuki M, Reinhardt D, Dunican DS, Prendergast JG, Mjoseng H, Ramsahoye BH, Whitelaw E, Greally JM, Adams IR, Bickmore WA, Meehan RR. Redistribution of H3K27me3 upon DNA hypomethylation results in de-repression of Polycomb target genes. *Genome Biol*. 2013 Mar 25;14(3):R25. doi: 10.1186/gb-2013-14-3-r25.

Rosenthal R, Cadieux EL, Salgado R, Bakir MA, Moore DA, Hiley CT, Lund T, Tanić M, Reading JL, Joshi K, Henry JY, Ghorani E, Wilson GA, Birkbak NJ, Jamal-Hanjani M, Veeriah S, Szallasi Z, Loi S, Hellmann MD, Feber A, Chain B, Herrero J, Quezada SA, Demeulemeester J, Van Loo P, Beck S, McGranahan N, Swanton C; TRACERx consortium. Neoantigen-directed immune escape in lung cancer evolution. *Nature*. 2019 Mar;567(7749):479-485. doi: 10.1038/s41586-019-1032-7.

Rotili D, Mai A. Targeting Histone Demethylases: A New Avenue for the Fight against Cancer. *Genes Cancer*. 2011 Jun;2(6):663-79. doi: 10.1177/1947601911417976.

Roulois D, Loo Yau H, Singhania R, Wang Y, Danesh A, Shen SY, Han H, Liang G, Jones PA, Pugh TJ, O'Brien C, De Carvalho DD. DNA-Demethylating Agents Target Colorectal Cancer Cells by Inducing Viral Mimicry by Endogenous Transcripts. *Cell*. 2015 Aug 27;162(5):961-73.

Sangatsuda Y, Miura F, Araki H, Mizoguchi M, Hata N, Kuga D, Hatae R, Akagi Y, Amemiya T, Fujioka Y, Arai Y, Yoshida A, Shibata T, Yoshimoto K, Iihara K, Ito T. Base-resolution methylomes of gliomas bearing histone H3.3 mutations reveal a G34 mutant-specific signature shared with bone tumors. *Sci Rep*. 2020 Sep 30;10(1):16162. doi: 10.1038/s41598-020-73116-x.

Santos-Rosa H, Schneider R, Bannister AJ, Sherriff J, Bernstein BE, Emre NC, Schreiber SL, Mellor J, Kouzarides T. Active genes are tri-methylated at K4 of histone H3. *Nature*. 2002 Sep 26;419(6905):407-11. doi: 10.1038/nature01080.

Schlesinger Y, Straussman R, Keshet I, Farkash S, Hecht M, Zimmerman J, Eden E, Yakhini Z, Ben-Shushan E, Reubinoff BE, Bergman Y, Simon I, Cedar H. Polycomb-mediated methylation on Lys27 of histone H3 pre-marks genes for de novo methylation in cancer. *Nat Genet.* 2007 Feb;39(2):232-6. doi: 10.1038/ng1950.

Schwartz BE, Ahmad K. Transcriptional activation triggers deposition and removal of the histone variant H3.3. *Genes Dev*. 2005 Apr 1;19(7):804-14. doi: 10.1101/gad.1259805.

Schwartzentruber J, Korshunov A, Liu XY, Jones DT, Pfaff E, Jacob K, Sturm D, Fontebasso AM, Quang DA, Tönjes M, Hovestadt V, Albrecht S, Kool M, Nantel A, Konermann C, Lindroth A, Jäger N, Rausch T, Ryzhova M, Korbel JO, Hielscher T, Hauser P, Garami M, Klekner A, Bognar L, Ebinger M, Schuhmann MU, Scheurlen W, Pekrun A, Frühwald MC, Roggendorf W, Kramm C, Dürken M, Atkinson J, Lepage P, Montpetit A, Zakrzewska M, Zakrzewski K, Liberski PP, Dong Z, Siegel P, Kulozik AE, Zapatka M, Guha A, Malkin D, Felsberg J, Reifenberger G, von Deimling A, Ichimura K, Collins VP, Witt H, Milde T, Witt O, Zhang C, Castelo-Branco P, Lichter P, Faury D, Tabori U, Plass C, Majewski J, Pfister SM, Jabado N. Driver mutations in histone H3.3 and chromatin remodelling genes in paediatric glioblastoma. *Nature*. 2012 Jan 29;482(7384):226-31. doi: 10.1038/nature10833.

Sengupta D, Kannan A, Kern M, Moreno MA, Vural E, Stack B Jr, Suen JY, Tackett AJ, Gao L. Disruption of BRD4 at H3K27Ac-enriched enhancer region correlates with decreased c-Myc expression in Merkel cell carcinoma. Epigenetics. 2015;10(6):460-6. doi: 10.1080/15592294.2015.1034416.

Shen H, Laird PW. Interplay between the cancer genome and epigenome. *Cell*. 2013 Mar 28;153(1):38-55. doi: 10.1016/j.cell.2013.03.008.

Shi L, Wen H, Shi X. The Histone Variant H3.3 in Transcriptional Regulation and Human Disease. *J Mol Biol*. 2017 Jun 30;429(13):1934-1945. doi: 10.1016/j.jmb.2016.11.019.

Silveira AB, Kasper LH, Fan Y, Jin H, Wu G, Shaw TI, Zhu X, Larson JD, Easton J, Shao Y, Yergeau DA, Rosencrance C, Boggs K, Rusch MC, Ding L, Zhang J, Finkelstein D, Noyes RM, Russell BL, Xu B, Broniscer A, Wetmore C, Pounds SB, Ellison DW, Zhang J, Baker SJ. H3.3 K27M depletion increases differentiation and extends latency of diffuse intrinsic pontine glioma growth in vivo. *Acta Neuropathol*. 2019 Apr;137(4):637-655. doi: 10.1007/s00401-019-01975-4.

Stazi G, Taglieri L, Nicolai A, Romanelli A, Fioravanti R, Morrone S, Sabatino M, Ragno R, Taurone S, Nebbioso M, Carletti R, Artico M, Valente S, Scarpa S, Mai A. Dissecting the role of novel EZH2 inhibitors in primary glioblastoma cell cultures: effects on proliferation, epithelial-mesenchymal transition, migration, and on the pro-inflammatory phenotype. *Clin Epigenetics*. 2019 Dec 2;11(1):173. doi: 10.1186/s13148-019-0763-5.

Sturm D, Witt H, Hovestadt V, Khuong-Quang DA, Jones DT, Konermann C, Pfaff E, Tönjes M, Sill M, Bender S, Kool M, Zapatka M, Becker N, Zucknick M, Hielscher T, Liu XY, Fontebasso AM, Ryzhova M, Albrecht S, Jacob K, Wolter M, Ebinger M, Schuhmann MU, van Meter T, Frühwald MC, Hauch H, Pekrun A, Radlwimmer B, Niehues T, von Komorowski G, Dürken M, Kulozik AE, Madden J, Donson A, Foreman NK, Drissi R, Fouladi M, Scheurlen W, von Deimling A, Monoranu C, Roggendorf W, Herold-Mende C, Unterberg A, Kramm CM, Felsberg J, Hartmann C, Wiestler B, Wick W, Milde T, Witt O, Lindroth AM, Schwartzentruber J, Faury D, Fleming A, Zakrzewska M, Liberski PP, Zakrzewski K, Hauser P, Garami M, Klekner A, Bognar L, Morrissy S, Cavalli F, Taylor MD, van Sluis P, Koster J, Versteeg R, Volckmann R, Mikkelsen T, Aldape K, Reifenberger G, Collins VP, Majewski J, Korshunov A, Lichter P, Plass C, Jabado N, Pfister SM. Hotspot mutations in H3F3A and IDH1 define distinct epigenetic and biological subgroups of glioblastoma. *Cancer Cell*. 2012 Oct 16;22(4):425-37. doi: 10.1016/j.ccr.2012.08.024.

Swafford DS, Middleton SK, Palmisano WA, Nikula KJ, Tesfaigzi J, Baylin SB, Herman JG, Belinsky SA. Frequent aberrant methylation of p16INK4a in primary rat lung tumors. *Mol Cell Biol*. 1997 Mar;17(3):1366-74. doi: 10.1128/MCB.17.3.1366.

Tam WL, Weinberg RA. The epigenetics of epithelial-mesenchymal plasticity in cancer. *Nat Med*. 2013 Nov;19(11):1438-49. doi: 10.1038/nm.3336.

Tie F, Banerjee R, Stratton CA, Prasad-Sinha J, Stepanik V, Zlobin A, Diaz MO, Scacheri PC, Harte PJ. CBP-mediated acetylation of histone H3 lysine 27 antagonizes Drosophila Polycomb silencing. *Development*. 2009 Sep;136(18):3131-41. doi: 10.1242/dev.037127.

Turcan S, Rohle D, Goenka A, Walsh LA, Fang F, Yilmaz E, Campos C, Fabius AW, Lu C, Ward PS, Thompson CB, Kaufman A, Guryanova O, Levine R, Heguy A, Viale A, Morris LG, Huse JT, Mellinghoff IK, Chan TA. IDH1 mutation is sufficient to establish the glioma hypermethylator phenotype. *Nature*. 2012 Feb 15;483(7390):479-83. doi: 10.1038/nature10866.

Varambally S, Dhanasekaran SM, Zhou M, Barrette TR, Kumar-Sinha C, Sanda MG, Ghosh D, Pienta KJ, Sewalt RG, Otte AP, Rubin MA, Chinnaiyan AM. The polycomb group protein EZH2 is involved in progression of prostate cancer. *Nature*. 2002 Oct 10;419(6907):624-9. doi: 10.1038/nature01075.

Vavouri T, Lehner B. Human genes with CpG island promoters have a distinct transcription-associated chromatin organization. *Genome Biol*. 2012 Nov 27;13(11):R110. doi: 10.1186/gb-2012-13-11-r110.

Venkatesh S, Workman JL. Histone exchange, chromatin structure and the regulation of transcription. *Nat Rev Mol Cell Biol*. 2015 Mar;16(3):178-89. doi: 10.1038/nrm3941.

Venneti S, Garimella MT, Sullivan LM, Martinez D, Huse JT, Heguy A, Santi M, Thompson CB, Judkins AR. Evaluation of histone 3 lysine 27 trimethylation (H3K27me3) and enhancer of Zest 2 (EZH2) in pediatric glial and glioneuronal tumors shows decreased H3K27me3 in H3F3A K27M mutant glioblastomas. *Brain Pathol*. 2013 Sep;23(5):558-64. doi: 10.1111/bpa.12042.

Verhaak RG, Hoadley KA, Purdom E, Wang V, Qi Y, Wilkerson MD, Miller CR, Ding L, Golub T, Mesirov JP, Alexe G, Lawrence M, O'Kelly M, Tamayo P, Weir BA, Gabriel S, Winckler W, Gupta S, Jakkula L, Feiler HS, Hodgson JG, James CD, Sarkaria JN, Brennan C, Kahn A, Spellman PT, Wilson RK, Speed TP, Gray JW, Meyerson M, Getz G, Perou CM, Hayes DN; Cancer Genome Atlas Research Network. Integrated genomic analysis identifies clinically relevant subtypes of glioblastoma characterized by abnormalities in PDGFRA, IDH1, EGFR, and NF1. *Cancer Cell*. 2010 Jan 19;17(1):98-110. doi: 10.1016/j.ccr.2009.12.020.

Verma SK, Tian X, LaFrance LV, Duquenne C, Suarez DP, Newlander KA, Romeril SP, Burgess JL, Grant SW, Brackley JA, Graves AP, Scherzer DA, Shu A, Thompson C, Ott HM, Aller GS, Machutta CA, Diaz E, Jiang Y, Johnson NW, Knight SD, Kruger RG, McCabe MT, Dhanak D, Tummino PJ, Creasy CL, Miller WH. Identification of Potent, Selective, Cell-Active Inhibitors of the Histone Lysine Methyltransferase EZH2. *ACS Med Chem Lett*. 2012 Oct 19;3(12):1091-6. doi: 10.1021/ml3003346.

Viré E, Brenner C, Deplus R, Blanchon L, Fraga M, Didelot C, Morey L, Van Eynde A, Bernard D, Vanderwinden JM, Bollen M, Esteller M, Di Croce L, de Launoit Y, Fuks F. The Polycomb group protein EZH2 directly controls DNA methylation. *Nature*. 2006 Feb 16;439(7078):871-4. doi: 10.1038/nature04431.

Voon HPJ, Udugama M, Lin W, Hii L, Law RHP, Steer DL, Das PP, Mann JR, Wong LH. Inhibition of a K9/K36 demethylase by an H3.3 point mutation found in paediatric glioblastoma. *Nat Commun*. 2018 Aug 7;9(1):3142. doi: 10.1038/s41467-018-05607-5.

Wang D, Quiros J, Mahuron K, Pai CC, Ranzani V, Young A, Silveria S, Harwin T, Abnousian A, Pagani M, Rosenblum MD, Van Gool F, Fong L, Bluestone JA, DuPage M. Targeting EZH2 Reprograms Intratumoral Regulatory T Cells to Enhance Cancer Immunity. *Cell Rep*. 2018 Jun 12;23(11):3262-3274. doi: 10.1016/j.celrep.2018.05.050.

Wang J, Huang TY, Hou Y, Bartom E, Lu X, Shilatifard A, Yue F, Saratsis A. Epigenomic landscape and 3D genome structure in pediatric high-grade glioma. *Sci Adv*. 2021 Jun 2;7(23):eabg4126. doi: 10.1126/sciadv.abg4126.

Wei Y, Xia W, Zhang Z, Liu J, Wang H, Adsay NV, Albarracin C, Yu D, Abbruzzese JL, Mills GB, Bast RC Jr, Hortobagyi GN, Hung MC. Loss of trimethylation at lysine 27 of histone H3 is a predictor of poor outcome in breast, ovarian, and pancreatic cancers. *Mol Carcinog*. 2008 Sep;47(9):701-6. doi: 10.1002/mc.20413..

Wen H, Li Y, Xi Y, Jiang S, Stratton S, Peng D, Tanaka K, Ren Y, Xia Z, Wu J, Li B, Barton MC, Li W, Li H, Shi X. ZMYND11 links histone H3.3K36me3 to transcription elongation and tumour suppression. *Nature*. 2014 Apr 10;508(7495):263-8. doi: 10.1038/nature13045.
Wiese M, Schill F, Sturm D, Pfister S, Hulleman E, Johnsen SA, Kramm CM. No Significant Cytotoxic Effect of the EZH2 Inhibitor Tazemetostat (EPZ-6438) on Pediatric Glioma Cells with Wildtype Histone 3 or Mutated Histone 3.3. *Klin Padiatr*. 2016 Apr;228(3):113-7. doi: 10.1055/s-0042-105292.

Wong MT, Chen SS. Emerging roles of interferon-stimulated genes in the innate immune response to hepatitis C virus infection. *Cell Mol Immunol*. 2016 Jan;13(1):11-35. doi: 10.1038/cmi.2014.127.

Wu G, Broniscer A, McEachron TA, Lu C, Paugh BS, Becksfort J, Qu C, Ding L, Huether R, Parker M, Zhang J, Gajjar A, Dyer MA, Mullighan CG, Gilbertson RJ, Mardis ER, Wilson RK, Downing JR, Ellison DW, Zhang J, Baker SJ; St. Jude Children's Research Hospital–Washington University Pediatric Cancer Genome Project. Somatic histone H3 alterations in pediatric diffuse intrinsic pontine gliomas and non-brainstem glioblastomas. *Nat Genet*. 2012 Jan 29;44(3):251-3. doi: 10.1038/ng.1102.

Wu X, Scott H, Carlsson SV, Sjoberg DD, Cerundolo L, Lilja H, Prevo R, Rieunier G, Macaulay V, Higgins GS, Verrill CL, Lamb AD, Cunliffe VT, Bountra C, Hamdy FC, Bryant RJ. Increased EZH2 expression in prostate cancer is associated with metastatic recurrence following external beam radiotherapy. *Prostate*. 2019 Jul;79(10):1079-1089. doi: 10.1002/pros.23817.

Xu J, Wang YY, Dai YJ, Zhang W, Zhang WN, Xiong SM, Gu ZH, Wang KK, Zeng R, Chen Z, Chen SJ. DNMT3A Arg882 mutation drives chronic myelomonocytic leukemia through disturbing gene expression/DNA methylation in hematopoietic cells. *Proc Natl Acad Sci USA*. 2014 Feb 18;111(7):2620-5. doi: 10.1073/pnas.1400150111.

Xu J, Zhang W, Yan XJ, Lin XQ, Li W, Mi JQ, Li JM, Zhu J, Chen Z, Chen SJ. DNMT3A mutation leads to leukemic extramedullary infiltration mediated by TWIST1. *J Hematol Oncol*. 2016 Oct 10;9(1):106. doi: 10.1186/s13045-016-0337-3.

Yan H, Parsons DW, Jin G, McLendon R, Rasheed BA, Yuan W, Kos I, Batinic-Haberle I, Jones S, Riggins GJ, Friedman H, Friedman A, Reardon D, Herndon J, Kinzler KW, Velculescu VE, Vogelstein B, Bigner DD. IDH1 and IDH2 mutations in gliomas. *N Engl J Med*. 2009 Feb 19;360(8):765-73. doi: 10.1056/NEJMoa0808710.

Yang L, Rau R, Goodell MA. DNMT3A in haematological malignancies. *Nat Rev Cancer*. 2015 Mar;15(3):152-65. doi: 10.1038/nrc3895.

Yang S, Zheng X, Lu C, Li GM, Allis CD, Li H. Molecular basis for oncohistone H3 recognition by SETD2 methyltransferase. *Genes Dev*. 2016 Jul 15;30(14):1611-6. doi: 10.1101/gad.284323.116.

Yin J, Leavenworth JW, Li Y, Luo Q, Xie H, Liu X, Huang S, Yan H, Fu Z, Zhang LY, Zhang L, Hao J, Wu X, Deng X, Roberts CW, Orkin SH, Cantor H, Wang X. Ezh2 regulates differentiation and function of natural killer cells through histone methyltransferase activity. *Proc Natl Acad Sci USA*. 2015 Dec 29;112(52):15988-93. doi: 10.1073/pnas.1521740112.

Yu J, Cao Q, Mehra R, Laxman B, Yu J, Tomlins SA, Creighton CJ, Dhanasekaran SM, Shen R, Chen G, Morris DS, Marquez VE, Shah RB, Ghosh D, Varambally S, Chinnaiyan AM. Integrative genomics analysis reveals silencing of beta-adrenergic signaling by polycomb in prostate cancer. *Cancer Cell*. 2007 Nov;12(5):419-31. doi: 10.1016/j.ccr.2007.10.016.

Yuan W, Xu M, Huang C, Liu N, Chen S, Zhu B. H3K36 methylation antagonizes PRC2-mediated H3K27 methylation. *J Biol Chem*. 2011 Mar 11;286(10):7983-7989. doi: 10.1074/jbc.M110.194027.

Zarghooni M, Bartels U, Lee E, Buczkowicz P, Morrison A, Huang A, Bouffet E, Hawkins C. Whole-genome profiling of pediatric diffuse intrinsic pontine gliomas highlights platelet-derived growth factor receptor alpha and poly (ADP-ribose) polymerase as potential therapeutic targets. *J Clin Oncol*. 2010 Mar 10;28(8):1337-44. doi: 10.1200/JCO.2009.25.5463.

Zhang Y, Sun Z, Jia J, Du T, Zhang N, Tang Y, Fang Y, Fang D. Overview of Histone Modification. *Adv Exp Med Biol*. 2021;1283:1-16. doi: 10.1007/978-981-15-8104-5_1.

Zhao Y, Wang XX, Wu W, Long H, Huang J, Wang Z, Li T, Tang S, Zhu B, Chen D. EZH2 regulates PD-L1 expression via HIF-1α in non-small cell lung cancer cells. *Biochem Biophys Res Commun*. 2019 Sep 17;517(2):201-209. doi: 10.1016/j.bbrc.2019.07.039.

Zhao Z, Shilatifard A. Epigenetic modifications of histones in cancer. *Genome Biol*. 2019 Nov 20;20(1):245. doi: 10.1186/s13059-019-1870-5.

Zhou Z, Gao J, Popovic R, Wolniak K, Parimi V, Winter JN, Licht JD, Chen YH. Strong expression of EZH2 and accumulation of trimethylated H3K27 in diffuse large B-cell lymphoma independent of cell of origin and EZH2 codon 641 mutation. *Leuk Lymphoma*. 2015;56(10):2895-901. doi: 10.3109/10428194.2015.1006220.

Chapter 2

Integrated Metabolic and Epigenomic Axis in Diffuse Intrinsic Pontine Gliomas

2.1 Abstract

H3K27M diffuse intrinsic pontine gliomas (DIPGs) are universally fatal and have lacked adequate treatment modalities. Mutations in histones, the building blocks of nucleosomes which give rise to chromatin, were discovered nearly a decade ago. Recurrent mutations in the genes *H3F3A* and *HIST1H3B*, encoding the replication-independent histone H3.3 and canonical histone H3.1, were described in which amino acid substitutions occur either at the K27 or G34 residues. Although consequences of H3K27M mutations on epigenetic marks such as H3K27me3 and H3K27ac are now well documented, there exists an urgent need to determine therapeutic vulnerabilities in DIPG tumors and develop targeted therapies to overcome resistance to traditional treatment modalities such as radiotherapy. Here, we examined metabolic dependencies in H3K27M pediatric gliomas. Using an integrated analysis of H3.3K27M-mutant cells and tumor tissues, we demonstrate that H3K27M gliomas exhibit enhanced glycolysis, glutaminolysis, and tricarboxylic acid metabolism. Moreover, we found that glucose and glutamine play a significant role in maintaining a lowered H3K27me3 state. Herein we show that glucose and glutamine starvation can reversibly raise H3K27me3, and this effect is recapitulated by targeting of key glycolysis and glutaminolysis enzymes both *in vitro* and *in vivo.* In addition, we show that targeting these metabolic sources of alpha-ketoglutarate, a necessary co-factor for histone demethylases, could prolong survival in

DIPG preclinical animal models. Collectively, this study identified the ability to interrupt a metabolic-epigenetic axis and establish its importance in the treatment of DIPG.

Portions of this work have been published in *Cancer Cell*:

Chung C, Sweha SR…Venneti S. Integrated Metabolic and Epigenomic Reprograming by H3K27M Mutations in Diffuse Intrinsic Pontine Gliomas. *Cancer Cell*. 2020 Sep 14;38(3):334-349. doi: 10.1016/j.ccell.2020.07.008. PMID: 32795401.

2.2 Introduction

Cancer cells often upregulate metabolism through acquisition of oncogenic mutations or epigenetic reprogramming (Daye *et al*., 2012; DeBerardinis *et al*., 2008; Pavlova *et al*., 2016). The upregulation of metabolic activity and metabolite influx has been noted in a variety of cancers compared with non-malignant cells (DeBerardinis *et al*., 2016; Vander Heiden *et al*., 2009; Yang *et al*., 2017). Elevated metabolism plays a key role in cellular fitness and the ability of malignant cells to survive oxidative and environmental stressors. In addition to these roles, changing metabolite levels can further drive changes in gene expression and modulate differentiation and cell cycle processes.

Two key metabolites, glucose and glutamine, play important roles in cell survival and provide necessary fuel for proliferation. Both biomolecules can undergo oxidation to produce NADH, $FADH_2$, or NADPH which are harnessed for ATP production and redox homeostasis, enhancing tumor growth (DeBerardinis *et al*., 2016; Pavlova *et al*., 2016). It has been observed that cells with high proliferation rate uptake glutamine more rapidly than other amino acids from the tumor microenvironment (Eagle *et al*., 1955, 1956). Glutamine serves a source for carbon and nitrogen that are utilized for biosynthetic and redox reactions (Xiang *et al*., 2013). For example, non-essential amino acid and nucleotide synthesis reactions rely on glutamine (Cluntun *et al*.,

2017). Notably, glucose and glutamine can give rise to alpha-ketoglutarate (hereafter alpha-KG or α-KG). Mitochondrial IDH2 converts glucose-derived isocitrate to alpha-KG. Glutamine can be converted by glutaminase (GLS) to glutamate, an alpha-KG precursor. Glutamate is subsequently converted to alpha-KG by glutamate dehydrogenase (GLUD1/2). Many cancers exhibit upregulation of glutamine transporters (such as *SLC1A5*) and glucose transporters (such as *SLC2A3)*. In addition, increased GLS expression has been noted in many cancers, making it an attractive and potent therapeutic target (Altman *et al*., 2016; Chen *et al*., 2015; Choi *et al*., 2018; Marquez *et al*., 2017; Yang *et al*., 2017).

Growth factor signaling and interactions with the extracellular matrix importantly regulate metabolite uptake from the environment by cells. Experiments comparing non-malignant cells cultured with extracellular matrix and detached from the matrix revealed a dependence on extrinsic stimuli that modulate uptake. In cancer, however, cells acquire mutations that allow them to regulate glucose uptake independent of these extraneous signals. Signaling cascades involving PI3K/AKT/mTOR and RAS/MAPK have long been implicated in regulating glucose transporter expression, membrane trafficking, and consequently, glucose uptake and increased glycolytic flux. Similarly, glutamine uptake can be controlled by master regulators like AKT or oncogenes like MYC which has been demonstrated to modulate expression of mitochondrial metabolism and glutaminolysis-related enzymes such as glutaminase (Hao *et al*., 2016; Nagarajan *et al*., 2016; Natarajan *et al*., 2019; Schroff *et al*., 2015). Other malignancies like pancreatic cancer have been found to regulate metabolism with other oncogenes, like KRAS, further demonstrating the role of signaling pathways in metabolic alteration (Bryant *et al*., 2014; Son *et al*., 2013; Wise *et al*., 2008).

Metabolic reprogramming of cancer cells has downstream consequences for gene expression. Notably, specific metabolites can affect the activity of chromatin remodeling and

modifying enzymes. Histone acetylation and methylation mechanisms reflect the metabolic state of a cell. Interestingly, mitochondrial-localized citrate can be transported to the cytosol by the citrate transporter (encoded by *SLC25A1*) where it can be converted to acetyl-CoA by ATP citrate synthase. Increases in this cytosolic acetyl-CoA pool, a key metabolite utilized by histone acetyltransferases, can increase histone acetylation and gene accessibility and consequently, activate gene expression. Cytosolic citrate can also be converted to isocitrate. Importantly, this isocitrate can be converted by Isocitrate Dehydrogenase 1 (IDH1) to alpha-KG which is utilized for DNA and histone demethylation reaction, discussed next.

Research on TET family DNA demethylases and Jumonji C-domain containing (JmjC) histone demethylases revealed their dependence on alpha-ketoglutarate substrates to catalyze demethylation reactions (Xu *et al*., 2011). Termed alpha-ketoglutarate-dependent dioxygenases, these enzymes concurrently convert alpha-ketoglurate and oxygen into succinate and carbon dioxide. Production of succinate leads to feedback inhibition on the demethylases (Pavlova *et al*., 2016). A key role for alpha-ketoglutarate was highlighted by a study using mouse embryonic stem (ES) cells that found that these ES cells had higher alpha-KG levels than cells in a more differentiated state (Carey *et al*., 2015). Glutamine deprivation of the ES cells caused increases in H3K9me3 and H3K27me3, two repressive histone modifications, demonstrating that modulation of the alpha-ketoglutarate:succinate ratio has consequences for histone methylation. Notably, the ratio had implications for cell fate where higher alpha-KG or succinate promoted a pluripotent or differentiated state, respectively. Thus, tumor cells that drive alpha-KG production can self-regulate epigenetic state.

Studies on gliomas have revealed that a large fraction of Grade 2 and 3 gliomas harbor mutations in Isocitrate Dehydrogenase 1 (IDH1) (Dang *et al*., 2009; Parsons *et al.*, 2008; Yan *et*

al., 2009). Mutant IDH1 proteins produce an oncometabolite D-2-hydroxyglutarate (D-2HG) which is structurally similar to alpha-KG (Dang *et al.*, 2009; Lu *et al*., 2012). In contrast to alpha-KG, D-2HG exerts an inhibitory effect on DNA and histone demethylases, raising H3K27me3, H3K9me3, and DNA methylation (Chowdhury *et al*., 2011; Lu *et al*., 2012; Xu *et al*., 2011). This highlights those tumors with distinct metabolic profiles can modulate epigenetic modifications in opposing manners, and precisely accounting for these differences is important for defining metabolically-targeted therapeutics.

Pediatric gliomas are devastating illnesses, surpassing other cancers like leukemia as the leading cause of childhood cancer-related death. Limited therapeutic options currently exist to treat these tumors. Genomic profiling of these tumors has revealed recurrent, somatic mutations that occur in histone proteins. One type of pediatric high-grade glioma localized to the pons, termed Diffuse Intrinsic Pontine Glioma (DIPG), exhibits a lysine-to-methionine substitution at position 27 in histone H3.3 (and less commonly H3.1). This H3K27M mutation results in global loss of H3K27me3, a histone mark associated with transcription repression, despite H3.3/3.1 comprising a small portion of total H3 in cells (Bender *et al*., 2013; Lewis *et al*., 2013). It is believed that H3K27M acts as a major oncogenic driver to reprogram cell cycle processes and transcription to suppress neuroglial differentiation and drive tumor growth. Earlier studies on H3K27M gliomas focused on reversing the epigenetic effects induced by the mutation by inhibiting K27 demethylases (Mohammad *et al*., 2017; Nagaraja *et al*., 2017; Piunti *et al*., 2017). These epigenetic therapies designed to increase H3K27me3 proved to be a key strategy in promoting cell death both *in vitro* and *in vivo* (Grasso *et al*., 2015; Hashizume *et al*., 2014). Surprisingly, inhibiting K27 methyltransferase EZH2 demonstrated efficacy in preclinical DIPG models where therapy rescued

p16 expression by lowering H3K27me3 levels at the *Cdkn2a* locus (Mohammad *et al*., 2017; Piunti *et al*., 2017).

Metabolic reprogramming, a hallmark of cancer cells, is often driven by oncogenic mutations and aberrant extracellular signals, discussed earlier. Although some mechanisms for the progression of DIPG have been established, specific effects of the H3K27M mutation on metabolism and cellular bioenergetics remain unknown.

Here, we probe whether H3K27M mutations rewire glucose and glutamine metabolism using comprehensive whole transcriptomic, proteomic, and metabolomic techniques to define possible metabolic dependencies in these tumors. In addition, we sought to establish if metabolic and epigenetic pathways are integrated in H3.3K27M gliomas, specifically if H3K27me3 is metabolically regulated in mutant cells. We discover that H3.3K27M cells exhibit epigenetic alterations at genes involved in glucose and glutamine transport and catabolism. Furthermore, we demonstrate that upregulation of key metabolic enzymes such as Hexokinase II (HK2), Isocitrate Dehydrogenase 1 (IDH1), and Glutamate Dehydrogenase (GLUD1/2) in DIPG patient tumor tissues and cell lines compared with H3WT tumors. We also establish that H3.3K27M cells have higher alpha-ketoglutarate levels than non-mutant cells using isogenic and patient cell models. Additionally, we demonstrate that H3.3K27M cells exhibit heterogeneity in their utilization of glucose and glutamine to regulate H3K27me3 levels and cell growth. Finally, we probe the preclinical efficacy of an IDH1 inhibitor and glutaminase inhibitor JHU-083 in suppressing tumor growth in orthotopic DIPG animal models.

2.3 Results

2.3.1 H3.3K27M isogenic model cells exhibit enhanced growth in the presence of exogenous amino acids and neurotransmitters in vitro

Prior work has described the ability of cancer cells to upregulate the uptake amino acids such as glutamate and GABA to fuel energetic mechanisms and anabolic processes. This type of metabolic reprogramming often occurs because of potent oncogene expression such as *MYC* or inactivation of tumor suppressors such as *PTEN* (Nagarajan *et al*., 2016; Natarajan *et al*., 2019). Based on this hallmark of altered metabolism in malignancy, we hypothesized that H3K27M mutant histone can also reprogram tumor cells to upregulate glycolysis and/or glutaminolysis. To further investigate the role of H3K27M in cell growth and its relationship with epigenetics, we established an isogenic model system where we expressed HA-tagged H3.3K27M or H3.3WT transgenes in immortalized mouse neuronal stem cells (mNSCs) (**Figure 2.1A**). As observed in patient-derived H3K27M cells, H3.3K27M mNSCs exhibited global decrease of H3K27me3 and an increase in the opposing mark H3K27ac without changes in global H3K36me3 or H3K4me3 levels (**Figure 2.1A**). H3K27me3 ChIP-seq analysis of promoters and gene bodies confirmed global genomic H3K27me3 reduction in H3.3K27M *versus* H3.3WT mNSCs as reported by earlier studies (**Figure 2.1B**) (Bender *et al.*, 2013; Chan *et al.*, 2013; Larson *et al*., 2019; Lewis *et al.*, 2013; Pathania *et al.*, 2017). Next, we treated mNSCs with glutamine, glycine, L-glutamate, dimethyl L-glutamate (cell permeable), and gamma aminobutyric acid (GABA). Cell growth was assessed after incubation for four days. Surprisingly, H3K27M cells exhibited significantly increased growth in the presence of glutamine, glycine, glutamate, and GABA (**Figure 2.2**). However, no significant difference was observed between H3WT and H3K27M cells treated with dimethyl glutamate, suggesting that differential glutamate active transport into H3K27M cells may

explain the difference in response for glutamate and its cell permeable dimethyl analogue. Further analysis of ChIP-seq data from the paired mNSC model revealed differential deposition of transcription-activating epigenetic modifications at glutamate transporters (such as *Slc1a1*, *Slc1a2*, and *Slc1a7*) and glucose transporters (such as *Slc2a1* and *Slc2a3*) (**Figure 2.3A-B**). We also observed enhanced H3K4me3 at promoter regions for these metabolism-related genes in glycolysis and the TCA-cycle such as hexokinase (*Hk2*) and isocitrate dehydrogenase (*Idh1*) (**Figure 2.3C**). This initial data supports the idea that H3.3K27M cells utilize glutamine, glutamate, and GABA to fuel growth. Importantly, all three biomolecules can be converted into TCA-cycle substrates alpha-ketoglutarate or succinate. Alpha-ketoglutarate serves as a critical co-factor for histone demethylases, strongly supporting the hypothesis that H3.3K27M rewires metabolism to maintain a desired low H3K27me3 epigenetic state.

2.3.2 H3.3K27M cells exhibit enhanced glycolysis and TCA cycle metabolism signatures

We used an integrated approach to comprehensively determine metabolic alterations driven by H3.3K27M mutations using the paired isogenic H3WT/H3K27M mNSC, patient-derived tumor cell lines and tumor samples. First, we performed RNA-seq on the isogenic cell lines and characterized pathways engaged in the H3.3K27M mNSCs by gene set enrichment analysis. We noted downregulation of neuronal differentiation pathway genes in H3.3K27M *versus* H3.3WT mNSCs (**Figure 2.4A**). In addition, we observed that the most significantly upregulated pathways in H3.3K27M mNSCs were related to carbohydrate metabolism and the tricarboxylic acid (TCA) cycle (**Figure 2.4A**).

To further investigate whether gene expression changes resulted in increased enzyme expression and metabolite abundance, we utilized an unbiased approach to assess the proteome and metabolome of H3.3K27M and H3.3WT mNSCs. We found differential expression of 1069

proteins (503 upregulated, 566 downregulated) in H3.3K27M mNSCs and targeted analysis of the upregulated gene set demonstrated glycolysis and TCA-cycle as top pathway hits (**Figure 2.4B**). Unbiased analysis of metabolome data revealed 78 deregulated metabolites (48 upregulated, 30 downregulated) in H3.3K27M *versus* H3.3WT mNSCs. Similar targeted pathway analysis of the upregulated metabolites, mirroring the proteomic analysis, showed that TCA-cycle related metabolites (pyruvate, lactate, and alpha-ketoglutarate) were enriched in H3.3K27M cells (**Figure 2.4C**). Glutamine tracing experiments (outlined in **Figure 2.4D**) in the H3.3K27M and H3.3WT mNSCs showed a larger labeled fraction for glutamine, glutamate, and alpha-ketoglutarate in the H3.3K27M mNSCs, confirming that increased glutamine uptake by H3.3K27M cells was indeed occurring (**Figure 2.4E**). We performed a similar tracing experiment in H3.3K27M DIPG-007 and H3.3WT UMPed37 patient-derived high-grade glioma cell lines, noting similar significant enrichment of these metabolites in DIPG-007 cells (**Figure 2.4E**).

Next, we evaluated if elevated metabolic gene expression occurred in patient tumors by querying data from Mackay *et al.* (2017) in the PedCBioPortal repository. This analysis included normalized RNA expression data for midline H3K27M (*n*=83), hemispheric H3WT (*n*=101), and hemispheric H3G34R/V (*n*=19) hemispheric pediatric high-grade gliomas. Results revealed increased expression of glucose transporter SLC2A3/GLUT3; key glycolytic enzymes hexokinase (HK2), phosphofructokinase-P (PFKP), aldolase-C (ALDOC), phosphoglycerate kinase-1 (PGK1), and phosphoglycerate Mutase-1 (PGAM1); glycolysis activators PFKFB2/3/4; and glutaminolysis-related glutamate dehydrogenase (GLUD1/2, GDH) in H3K27M *versus* either H3WT or H3G34R/V tumor samples (**Figure 2.5A**). We corroborated upregulation of glucose transporter SLC2A3/GLUT3, HK2, IDH1, and GDH in H3.3K27M cell lines SF7761, DIPG007,

and DIPG-XIII compared with H3.3WT cell lines UMPed37 and SJGBM2 by immunoblotting (**Figure 2.5B**).

We also analyzed metabolic gene expression in the context of anatomic location and histone mutational status. We sub-grouped the pediatric high-grade gliomas, independent of histone status, into high and low expression categories using the median expression value as a cutoff. Higher expression of *SLC2A3/GLUT3*, *HK2*, *GLUD1*, and *PFKFB2* occurred mainly in the pons/brainstem, consistent with the observation that H3K27M gliomas primarily occur in these regions (**Figure 2.5C**). Additionally, patient survival correlated with HK2 and PFKFB2 expression with higher expression associated with worse outcome for H3K27M patients (**Figure 2.5D**). Interestingly, we also found that when patient tumors are classified into high and low expression categories by each metabolic genes, a larger fraction of both H3.1- and H3.3-K27M patients fell into the high expression category (**Figure 2.5E**). Upregulated protein expression for key TCA-cycle enzymes suggests that DIPG cells enhance metabolism for survival and growth. Taken together, the epigenetic changes observed at these loci (such as *Hk2*, *Idh1*, and *Glud1*), elevated protein expression, enhanced metabolic profile, and patient survival differences demonstrate that H3K27M causes epigenetic perturbations at key genes for glycolysis and TCA-cycle and could present a vulnerability that can be exploited for targeted therapy for these tumors.

2.3.3 Heterogenous regulation of global H3K27me3 levels by glutamine and glucose metabolism in H3.3K27M cells

From our metabolomic studies, we noted that alpha-ketoglutarate (α-KG) levels were higher in H3.3K27M compared to H3.3WT cells. α-KG is a critical cofactor for histone lysine demethylases, including H3K27 demethylases KDM6A and KDM6B. Previous work demonstrated that during demethylation reactions, α-KG is converted to succinate (Loenarz and

Schofield, 2008). Early studies on DIPGs focused on targeting histone deacetylases, histone K27 methyltransferases, and bromodomain proteins to reverse observed epigenetic effects and promote cellular differentiation. Notably, Grasso *et al*. (2015) and Hashizume *et al*. (2014) demonstrated that KDM6A/6B inhibition with GSK-J4 was toxic in preclinical DIPG models and raised H3K27me3 levels robustly in patient cell lines. Research on mouse embryonic stem (ES) cells revealed that these cells can increase glutamine and glucose catabolism, resulting in a higher α-KG:succinate ratio that has direct implications for chromatin modifications like H3K27me3 and DNA methylation (Carey *et al.*, 2015). Interestingly, ES cells deprived of glutamine demonstrated elevated H3K9me3, H3K27me3, H4K20me3, and H3K36me3. Our data demonstrated elevation of the α-KG:succinate ratio in H3.3K27M mNSCs. Thus, we hypothesized that α-KG derived from glucose and glutamine could directly regulate H3K27me3 levels in these cells.

To test if glutamine metabolism could regulate H3K27me3 levels *in vitro*¸ we exposed DIPG-007 and SF7761 to glutamine deprivation by growing cells in media lacking glutamine and assessed changes in H3K27me3. Glutamine deficiency resulted in H3K27me3 elevation in DIPG-007, but this did not occur in SF7761 cells (**Figure 2.6A**). In parallel, we tested whether glucose restriction had a similar effect in elevating H3K27me3 in DIPG-007 and SF7761 cells (**Figure 2.6A**). This result suggested that both DIPG-007 and SF7761 are reliant on glucose, but that only a subset of DIPG cells like DIPG-007 are reliant on glutamine to modulate H3K27me3.

We next tested if glucose and glutamine withdrawal after four days had differential effects on mNSC model cells and human DIPG-007 and SF7761 cells. DIPG-007 cells were more sensitive to glutamine withdrawal compared with SF7761; partial growth defects induced by glutamine withdrawal in DIPG-007 were partially rescued by exogenous α-KG supplementation (**Figure 2.6B**) while no effect was observed in SF7761 (**Figure 2.6C**). In the case of glucose

withdrawal and combined glucose/glutamine withdrawal in both cell lines, cell death could be partially rescued by the addition of α-KG (**Figure 2.6B-C**). These findings were recapitulated in time course experiments of glucose and glutamine withdrawal from cell growth media where cell number was monitored over four days. Full suppression of growth could be achieved in the absence of glucose, but not glutamine, for DIPG-007, suggesting an in-built redundancy in some DIPG cells which could allow them to overcome therapeutic targeting of the glutamine pathway (**Figure 2.6D**). We observed that SF7761 continued to grow in the absence of glutamine while glucose removal induced full suppression of growth (**Figure 2.6E**). These findings in patient cell lines are corroborated by earlier data from the isogenic mNSC model suggesting that H3.3K27M cells treated with glutamine proliferate more than H3.3WT counterparts (**Figure 2.2**). Additionally, glucose withdrawal experiments using mNSC constructs revealed significant differential effects in H3.3K27M compared with H3.3WT mNSCs (**Figure 2.6F**). This heterogeneity in the reliance of DIPG cells on glucose and glutamine highlights the importance of simultaneous targeting of glycolysis and glutaminolysis to achieve maximal tumor growth suppression.

Our previous cell growth experiments with glutamate and GABA neurotransmitters in the isogenic mNSC system revealed a differential growth effect between H3.3K27M and H3.3WT cells grown in the presence of either molecule. Experiments with DIPG-007 and SF7761 confirmed the dependence of these cells on glutamine/glutamate pathway. However, to date the significance of GABA metabolism had not been probed experimentally. Importantly, the GABA shunt is an intracellular mechanism by which glutamate is converted to GABA by glutamate decarboxylase (GAD1), and GABA is subsequently converted to succinic semialdehyde (SSA) by GABA transaminase (GABA-T). In a final step, SSA can be converted to succinate by succinic semialdehyde dehydrogenase (SSADH) and succinate can enter the TCA cycle.

First, we queried the Mackay *et al.* (2017) study for GABA metabolism-related genes to ascertain if any survival or expression differences exist for H3.3K27M tumors in this context. Unexpectedly, we found that H3.1/3.3K27M patients exhibited significantly lower expression of *GAD1* compared to both H3WT and H3G34R/V tumor patients (**Figure 2.7A)**. Based on this result, we wondered whether H3.3K27M patients downregulate GAD1 to minimize the amount of glutamate converted to GABA and ultimately converted to succinate since elevated succinate production might lower the alpha-KG:succinate ratio, promoting H3K27me3 gain. To further assess what effect GABA has in H3.3K27M cells *in vitro,* we treated DIPG-007 cells with increasing doses of GABA and examined cell viability. We observed a small, significant difference in growth, but surprisingly no cell death with GABA (**Figure 2.7B**). Next, we performed glutamine and glucose restriction experiments in DIPG-007 with and without the addition of GABA. Neither glucose, glutamine, nor combined deficiency could be rescued by GABA supplementation (**Figure 2.7C**). Furthermore, we observed that high *GAD1* expression was associated with better survival outcomes when stratifying expression across all H3WT, H3K27M, and H3G34R/V pediatric high-grade gliomas (**Figure 2.7D**). Similarly, H3K27M patients with higher *GAD1* expression had better prognosis than counterparts with lower expression (**Figure 2.7D**). Several key questions come to mind. We wonder why increased GABA does not elicit cell death given its relationship to succinate/H3K27me3. One possibility is that H3.3K27M cells actively downregulate GAD1 and SSADH to decrease succinate production from GABA metabolism to maintain their preferred low H3K27me3 state. Profiling DIPG cell tumor for GAD1 and SSADH protein expression will give insight here. Additionally, experiments involving forced expression of GAD1 and SSADH in DIPG cells could help parse whether engaging GABA metabolism can also regulate H3K27me3. Differential action of GABA on cancer cells is mediated by GABA receptor expression (Young

and Bordley, 2010; Jiang *et al.*, 2012). Given recent work on the role of neuronal activity in stimulating glioma growth *in vitro* and *in vivo*, it remains unknown whether GABA receptors are expressed in DIPG and their functional role in the disease, if any (Venkatesh *et al.*, 2015). Future studies could focus on characterizing the profile of GABA transporters and test whether expression of GABA transporters or GAD1 sensitizes cells to exogenous GABA.

2.3.4 GDH and HK2 inhibition increases H3K27me3 and suppresses proliferation of H3.3K27M cells

Having established that some H3.3K27M cells are reliant on glutamine to maintain low H3K27me3, we next sought to determine whether suppressing glutamine metabolism pharmacologically in these cells could impact cell proliferation. Glutamate dehydrogenase (GDH) generates α-KG from glutamate-derived glutamine and was elevated in H3.3K27M *versus* H3.3WT cells and tumor samples (**Figure 2.5A-B**). We employed the glutamine antagonists/glutaminase (GLS) inhibitors CB-839 and 6-diazo-5-oxo-L-norleucine (DON) and tested their toxicity in DIPG-007 cells. While CB-839 had minimal effect on cell growth at millimolar concentrations, DON exerted high toxicity at low micromolar concentrations in DIPG-007 (**Figure 2.8A-B**). In addition, we assessed the efficacy of DON in an *in vivo* xenograft model established with isogenic H3.3K27M mNSC. DON treatment significantly suppressed xenograft growth in this model, suggesting a targetable therapeutic dependency *in vivo* (**Figure 2.8C**). Next, we targeted glucose metabolism *in vitro* in H3.3K27M/H3.3WT mNSC and DIPG-007 with a glucose analogue, 2-deoxy-D-glucose (2-DG). 2-DG treatment resulted in differential cell death in the mNSC model (**Figure 2.8D**). 2-DG treatment also elicited robust cell death in DIPG-007 and SF7761 cells (**Figure 2.8E**). Because DIPG-007 was reliant on glutamine and glucose, we tested potential synergism of combining 2-DG and DON, however no synergy occurred (**Figure**

2.8F). Since 2-DG exhibits favorable blood-brain barrier penetrability, we sought to determine if *in vitro* growth inhibition could be recapitulated in an orthotopic DIPG-007 *in vivo* model. 2-DG treatment suppressed DIPG-007 tumor growth relative to vehicle-treated mice (**Figure 2.8G-H**). We assessed whether 2-DG treatment targeting glucose metabolism *in vivo* could reverse H3K27me3 loss. After immunohistochemical staining of tumor tissues with mutant-specific H3K27M and H3K27me3 antibodies, we analyzed H3K27me3 levels in H3K27M-positive cells and noted elevated H3K27me3 in 2-DG treated tumors relative to vehicle-treated controls (**Figure 2.8I**).

Our prior experiments demonstrated that inhibition of critical glutamine and glucose pathway enzymes GLS and HK2 can reverse H3K27me3 in H3.3K27M DIPG cells. Alpha-ketoglutarate plays a role in the mechanism mediating cell death using these modes of inhibition. Interestingly, mutant IDH1/2 gliomas are mutually exclusive with H3K27M tumors (Schwartzentruber *et al*., 2012, Sturm *et al.*, 2012). Normally IDH1/2 proteins are responsible for converting isocitrate to alpha-ketoglutarate in the mitochondria or cytosol. Mutant IDH1/2 proteins exhibit a neomorphic property where alpha-ketoglutarate is instead converted to the oncometabolite D-2HG, a competitive inhibitor of H3K27 demethylases (Dang *et al.,* 2009; Lu *et al.,* 2012; Xu *et al.,* 2011). Accordingly, we hypothesized that mIDH1/2 and H3K27M gliomas rely on anabolic pathways that produce alpha-KG but that this metabolite is utilized in opposing manners. Work in our laboratory revealed that mIDH1 R132H and H3.3K27M are synthetic lethal which made us wonder whether H3.3K27M cells would be differentially sensitive to D-2HG and whether exposure to D-2HG could raise H3K27me3. To test this, we treated H3.3K27M DIPG-007 and SF7761 cells, as well as H3.3G34V KNS42 cells as a control, with D-2HG and assessed cell viability and H3K27me3. We found that H3.3K27M cells were indeed differentially sensitive

to D-2HG treatment (**Figure 2.9**). Perturbations in H3K27me3 mirrored cell viability study where H3K27me3 was elevated in DIPG cells but not KNS42 cells (see Chung *et al.* 2020).

2.3.5 Inhibition of IDH1 and glutamine metabolism is therapeutic in vivo

After establishing the efficacy of various metabolic inhibitors using *in vitro* DIPG models, we next determined if these inhibitors exerted therapeutic effects *in vivo.* Efficient delivery of inhibitors to the brainstem or cortex remains a major challenge in the field of pHGG biology and clinical treatment. *In vitro* studies revealed glutaminase inhibition as an effective therapeutic axis which led us to utilize the highly BBB-penetrable DON analogue, JHU-083 (Hanaford *et al*., 2019). JHU-083 has previously been shown to accumulate at millimolar concentrations in brain tissues of mice. We also took advantage of a BBB-penetrable wild-type IDH1 inhibitor, IDH1i compound 13. With knowledge that DIPG cells harbor inbuilt redundancies, we combined both inhibitors to assess their ability to suppress tumor growth in pontine models of DIPG-007. Mice were orthotopically implanted with tumor cells and engraftment was confirmed by serial bioluminescence imaging. Next, we treated mice with WT-IDH1i, JHU-083, or a combination of both inhibitors using a six-week paradigm (**Figure 2.10A**). Single agent treatments significantly increased the overall survival in this animal model (**Figure 2.10B**). Importantly, combined treatment resulted in the maximal therapeutic effect observed (**Figure 2.10B**). Together, this data suggests that specific targeting of enzymes that contribute to alpha-ketoglutarate production is a potential therapeutic axis in DIPG.

2.4 Discussion

Profiling of pediatric tumors has revealed a high frequency of mutations in histone H3. H3K27M mutations often occur in the midline brain structures such as the thalamus and brainstem structures.

A second type of lysine-to-methionine substitution at lysine 36, termed H3K36M, has also been discovered in bone tumors. Both these lysine residues can post-translationally modified with mono-, di-, or trimethylation, as well as acetylation that can modulate gene expression. Within the last decade seminal work has probed epigenetic effects of each mutant histone, associated neural signatures and characteristic tumor markers, aberrant gene activation or silencing, and epigenetically-informed therapeutic approaches.

The finding that H3K27M mutations result in drastic H3K27me3 reduction has invited intense debate about how H3K27M histones interacts with the PRC2 complex to remodel the epigenome. Several theories have emerged, including one that posits that K27M mutant histones sequester EZH2 at poised enhancers, others which suggest EZH2 is excluded from activated enhancers with H3K27ac, and yet other work suggests that H3K27M inhibits the spreading of H3K27me3 (Harutyunyan *et al*., 2019; Piunti *et al*., 2017). Surprisingly, therapies targeting EZH2 to further reduce H3K27me3 have demonstrated rescued p16 expression that slows tumor growth. Contrastingly, targeting histone deacetylases (HDACs) and H3K27 demethylases also show therapeutic promise in DIPG animal models (Grasso *et al*., 2015; Hashizume *et al.*, 2014). This work highlights how therapies that disrupt specific epigenetic features present in DIPG cells are powerful tools. However, this approach requires a strong understanding of how gene-specific epigenetic perturbations play a role in DIPG tumorigenesis.

Some work has been done to understand how the effects of the H3K27M mutation in different tissue contexts using forebrain and hindbrain-derived neural stem cells (NSCs) expressing the H3K27M mutant (Bressan *et al*., 2021; and Larson *et al*., 2019). These models have suggested that H3K27M introduction into forebrain NSCs does not disrupt patterning in region-specific epigenetic modifications or perturb gene expression, but introduction into hindbrain NSCs

causes fine tuning of gene expression. In addition, some mechanistic work has been done to understand H3K27ac-enriched enhancers and specific transcription factors that might be aberrantly recruited to these enhancer loci (Wang *et al.,* 2021). Targeting bromodomain proteins that accumulate at enhancers has shown *in vivo* efficacy and has been suggested to modulate 3D genome structure in DIPG cell lines. Furthermore, extensive compound screening has identified a few promising compounds for the treatment of DIPG, but gaps remain in our knowledge about mechanisms driving these treatment-resistant tumors.

Given what is known about the relationship between epigenetics and metabolism, discussed in the introductory section, we investigated how H3K27M cells may modulate metabolism to regulate their epigenetic state. In our study, we focused on targeting critical metabolic processes to reverse epigenetic disruptions caused by H3K27M. We utilized a comprehensive transcriptomic, proteomic, and metabolomic approach and a parallel analysis of patient tumor data to probe our hypothesis that H3K27M cells upregulate glycolysis, glutaminolysis, and TCA-cycle metabolism. We found that key enzymes involved in these pathways were upregulated both in DIPG patient-derived cell lines and tissues, suggesting a dependence on key metabolites to further maintain a preferred epigenetic state. We hypothesized that increased metabolism could contribute to elevated intracellular alpha-KG pools to drive histone demethylation reactions. Furthermore, we reasoned that targeting this mechanism could raise H3K27me3. Our experiments demonstrated that pharmacologic targeting of enzymes critical for alpha-KG synthesis could suppress tumor cell growth and rescue H3K27me3 loss both *in vitro* and *in vivo.* These findings recapitulate findings that the alpha-ketoglutarate:succinate ratio within cells is a critical determinant of cell-fate and has consequences for H3K27 methylation (Carey *et al*., 2015).

Furthermore, we found that the glutamine and glucose-dependence of H3K27M tumors cell is heterogenous using cell viability experiments. This suggested in-built redundancies in specific tumors that could become resistant to treatment targeting only one carbon source, highlighting the importance of simultaneous targeting of both pathways to achieve optimal response. To test these findings *in vivo*, we established several DIPG models to target glucose and glutamine metabolism, as well as IDH1 activity which is important for cytosolic alpha-KG production. Inhibiting these metabolic nodes *in vivo* increased overall survival of several animal models with maximal effects on survival achieved with combinatorial treatment.

Some important questions remain in light of these results. More genetic analysis and ChIP-sequencing experiments are needed to understand if metabolic manipulations alter the enhancer landscape, described by other studies, to elicit cell death. Additionally, tumors treated with metabolic inhibitors could acquire resistance over the course of therapy. Recent work by Pajovic *et al.* (2020) revealed that RAS/MAPK and MYC target genes are epigenetically activated in mouse and human DIPG cell models. Given the major role of these cascades in regulating metabolism (Dong *et al.*, 2020; Mukhopadhyay *et al.*, 2021; Stine *et al.*, 2015; Yuan *et al.*, 2020), future work in this realm should address how metabolic pathways engaged by H3K27M-activated oncogenic signaling can be alternatively targeted with combination therapies. Although we have established that activating epigenetic modifications accumulate at key metabolic genes, we are still yet to explore if chromatin remodelers, such as the SWI/SNF complex, are recruited by H3K27M and play a role in activating metabolism and whether these present actionable drug targets. Collectively, the results presented here indicate that DIPG cells integrate metabolic and epigenetic pathways and highlight therapeutic opportunities in DIPG tumors.

2.5 Methods

Cell lines and culture conditions

Cells were cultured in a humidified incubator at 37°C and 5% CO_2. HSJD-DIPG-007 (referred to as DIPG-007) and SF7761 were kindly provided by Dr. Rintaro Hashizume (Northwestern University, Chicago, IL, USA). Immortalized mouse NSC ($p16^{Ink4a\,-}/p^{14Arf\,-}$) were obtained from Dr. Richard Gilberton (St. Jude Children's Research Hospital, Memphis, TN, USA). DIPG-007 were cultured as neurospheres in TSM base media [equal parts Neurobasal A and DMEM/F-12, supplemented with HEPES (10 mM), sodium pyruvate (1 mM), Non-Essential Amino Acids (NEAA, 0.1 mM), GlutaMAX (2 mM), antibiotic/antimycotic (1X)] supplemented with B-27 (1X, without Vitamin A), 0.2% heparin (2 μg/mL), human EGF (20 ng/mL), human b-FGF (20 ng/mL), human PDGF-AA (10 ng/mL), and human PDGF-BB (10 ng/mL). Mouse NSCs (mNSCs) and SF7761 cells were cultured as neurospheres in Neurobasal A supplemented with N-2 (1X), B-27 (1X), L-glutamine (2 mM), penicillin/streptomycin (1X), heparin (2 μg/mL), human EGF (20 ng/mL), human b-FGF (20 ng/mL), and bovine serum albumin (45 ng/mL). All cell lines were characterized for histone mutation status by Sanger sequencing, validated by STR profiling, and routinely tested negative for mycoplasma contamination.

Cell counting

For trypan blue exclusion assays, 50,000 cells were plated in 24 well plates. After indicated treatment and time, cells were dissociated using trypsin or Accutase. Cells were counted on a Countess II Cell Counter. For viability experiments using bioluminescent readout, 10,000 cells (stably expressing luciferase) were plated in 100 μl cell media in 96 well plates. After indicated treatment and time, 10 μl of 15 mg/ml D-luciferin (D-LUCK, GoldBio) was added to each well.

Cells were incubated at room temperature for 5-10 minutes. Luminescent signal was captured on a Synergy HTX plate reader. Percent living cells for each condition in each assay was calculated relative to untreated negative or complete media control. The following compounds were utilized for cell culture growth experiments: dimethyl glutamate (Sigma-Aldrich, #49560), L-glutamate (Sigma-Aldrich, #G1626), GABA (Sigma-Alrich, #A2129), glutamine (Gibco, #25030-081), glucose (Gibco, #A2494001), glycine (Gibco, #15527013), 2-DG (2-Deoxy-D-glucose, Cayman Chemical, #14325), 2-HG ((2R)-Octyl-α-hydroxyglutarate, Cayman Chemical, #16366), DON (6-Diazo-5-oxo-L-norleucine, Cayman Chemical, #17580), CB-839 (Cayman Chemical, #22038), and dimethyl α-KG (Sigma-Aldrich, #349631). Neurobasal A without sodium pyruvate and glucose was utilized for cell growth nutrient deprivation experiments (ThermoFisher Scientific, #A2477501).

Immunoblotting

Cells were lysed in 1X RIPA buffer containing appropriate protease and phosphatase inhibitors. Equal amounts of total protein from cell lysate or histone extracts were loaded on 4-15% Mini-Protean TGX precast gels. Proteins were transferred to PVDF membrane using a Bio-Rad Trans-Blot Turbo transfer system. Membranes were blocked with 5% skim milk TBST (TBS buffer containing 0.1% Tween-20) and incubated in primary antibody diluted in 5% skim milk at 4°C overnight. Next, membranes were washed with TBST three times. Membranes were incubated with secondary antibodies conjugated to horseradish peroxidase (HRP) for two hours at room temperature and washed with TBST three times and TBS one time. Immunoreactivity was detected by SuperSignal West Pico PLUS Chemiluminescent Substrate. The following primary antibodies were utilized for immunoblotting: HK2 (Santa Cruz Biotechnology, #sc-374091), IDH1 (Cell

Signaling Technology, #8137), SLC2A3/GLUT3 (abcam, #ab191071), GLUD1 (abcam, #ab166618), ACTB (Sigma-Aldrich, #A5441), H3K27me3 (Active Motif, #39155), total H3 (Cell Signaling Technology #3638S). The following secondary antibodies were utilized for immunoblotting: Goat Anti-Rabbit IgG (H+L)-HRP Conjugate (Bio-Rad, #1706515) and Goat Anti-Mouse IgG (H+L)-HRP Conjugate (Bio-Rad, #1706516).

Histone Extraction

Cells were plated at sub-confluent densities. After indicated treatment, cells were washed with PBS. Cell pellet from centrifugation was suspended in 1.5 ml hypotonic lysis buffer (10 mM Tris HCl pH 8.0, 1 mM KCl, and 1.5 mM $MgCl_2$, protease inhibitor and phosphatase inhibitor) and incubated for 30 min on rotator at 4 °C. The pellet was collected by centrifugation at 10,000g, 4 °C for 10 min. The pellet was suspended in 400 µl of 0.4 N H_2SO_4 and incubated overnight on a rotator at 4 °C. After centrifuging, the supernatant was transferred to a new tube and 132 µl Trichloroacetic acid was added dropwise. The mixed solution was incubated on ice for 30 min. The histone pellet was harvested by centrifuging at 16,000g, 4 °C for 10 min and washed with ice-cold acetone. After centrifuging at 16,000g, 4 °C for 5 min, acetone was removed. The histone pellet was washed using acetone again. Subsequently, the histone pellet was made dry with the caps open at room temperature for 20 minutes to evaporate remaining acetone. The dried histone pellet was suspended in an appropriate volume of ddH_2O water and placed on ice.

ChIP-sequencing

H3.3WT and H3.3K27M mNSC cell lines were fixed with 1% formaldehyde for 15 min and quenched with 0.125 M glycine. Chromatin was isolated by the addition of lysis buffer, followed

by disruption with a Dounce homogenizer. Lysates were sonicated and the DNA sheared to an average length of 300-500 bp. Genomic DNA (Input) was prepared by treating aliquots of chromatin with RNase, proteinase K and heat for de-crosslinking, followed by ethanol precipitation. Pellets were resuspended and the resulting DNA was quantified on a NanoDrop spectrophotometer. Extrapolation to the original chromatin volume allowed quantitation of the total chromatin yield. An aliquot of chromatin (30 μg) was precleared with protein A agarose beads (Invitrogen). Soluble chromatin was spiked-in with soluble *Drosophila* chromatin equivalent to 5-10% of mouse chromatin as previously described (Lu *et al.,* 2016). The mixed soluble chromatin was incubated with 4 μg of antibody against H3K27me3, H3K27ac, H3K4me3 and H3K4me1 (see resources table). Complexes were washed, eluted from the beads with SDS buffer, and subjected to RNase and proteinase K treatment. Crosslinks were reversed by incubation overnight at 65 ^{0}C, and ChIP DNA was purified by phenol-chloroform extraction and ethanol precipitation. Quantitative PCR (qPCR) reactions were carried out in triplicate on specific genomic regions using SYBR Green Supermix (Bio-Rad). The resulting signals were normalized for primer efficiency by carrying out QPCR for each primer pair using Input DNA.

Illumina sequencing libraries were prepared from the ChIP and Input DNAs by the standard consecutive enzymatic steps of end-polishing, dA-addition, and adaptor ligation. Steps were performed on an automated system (Apollo 342, Wafergen Biosystems/Takara). After a final PCR amplification step, the resulting DNA libraries were quantified and sequenced on Illumina's NextSeq 500 (75 nt reads, single end). Reads were aligned to the mouse genome (mm10) using the BWA algorithm (default settings). Duplicate reads were removed and only uniquely mapped reads (mapping quality >= 25) were used for further analysis. The number of test tags were normalized by the same number of spike-in Drosophila tags for each sample. Alignments were

extended in silico at their 3'-ends to a length of 200 bp, which is the average genomic fragment length in the size-selected library, and assigned to 32-nt bins along the genome. The resulting histograms (genomic "signal maps") were stored in bigWig files. For active histone marks (H3K4me3, H3K27Ac, H3K4me1), peak locations were determined using the MACS algorithm (v2.1.0) with a cutoff of *p*-value = 1e-7. For H3K27me3 enriched regions were identified using the SICER algorithm at a cutoff of FDR 1E-10 and a max gap parameter of 600 bp. Peaks that were on the ENCODE blacklist of known false ChIP-Seq peaks were removed. Signal maps and peak locations were used as input data to Active Motifs proprietary analysis program, which creates Excel tables containing detailed information on sample comparison, peak metrics, peak locations and gene annotations. The data was visualized and analyzed using Integrative Genomics Viewer (IGV) genome browser.

RNA-sequencing

RNA-sequencing was performed as previously described (Bayliss *et al.*, 2016). RNA was isolated using Trizol (Invitrogen 15596-026) and treated with DNase (Sigma, 9003-98-9). RNA sequencing libraries were prepared according to the Illumina TruSeq protocol and were sequenced on the HiSeq 2000. RNA-seq data generated were aligned to mouse reference genome using bowtie and analyzed using the RSEM software package with default parameters. Differentially expressed genes were defined using empirical Bayes hierarchical models (EBSeq) that factors for mapping ambiguity variance. Pathway analysis of differentially regulated genes was performed by GSEA (http://software.broadinstitute.org/gsea/index.jsp).

Tandem mass tags proteomics

Cells were rinsed with PBS, 3 times and lysed using RIPA buffer containing 1mM phenylmethylsulfonyl fluoride *(*PMSF*).* Protein concentration was measured using BCA Protein Assay kit (ThermoFisher, #23225). Samples (80 mg/condition) were proteolyzed and labeled with TMT 10-plex essentially by following manufacturer's protocol (ThermoFisher). Briefly, upon reduction and alkylation of cysteines, the proteins were precipitated by adding 6 volumes of ice cold acetone followed by overnight incubation at -20° C. The precipitate was spun down, and the pellet was allowed to air dry. The pellet was resuspended in 0.1M TEAB and overnight digestion with trypsin (1:50; enzyme: protein) at 37° C was performed with constant mixing using a thermomixer. The TMT 10-plex reagents were dissolved in 41 µl of anhydrous acetonitrile and labeling was performed by transferring the entire digest to TMT reagent vial and incubating at room temperature for 1 h. Reaction was quenched by adding 8 µl of 5% hydroxyl amine and further 15 min incubation. Labeled samples were mixed together, and dried using a vacufuge. An offline fractionation of the combined sample (~200 µg) into 10 fractions was performed using high pH reversed-phase peptide fractionation kit according to the manufacturer's protocol (Pierce; Cat #84868). Fractions were dried and reconstituted in 12 µl of 0.1% formic acid/2% acetonitrile in preparation for LC-MS/MS analysis.

Liquid chromatography-mass spectrometry analysis (LC-multinotch MS3):

In order to obtain superior quantitation accuracy, we employed multinotch-MS3 (Ref: McAlister GC) which minimizes the reporter ion ratio distortion resulting from fragmentation of co-isolated peptides during MS analysis. Orbitrap Fusion (ThermoFisher Scientific) and RSLC Ultimate 3000 nano-UPLC (Dionex) was used to acquire the data. 2 µl of sample was resolved on a PepMap RSLC C18 column (Thermo Scientific) at the flow-rate of 300 nl/min using 0.1% formic

acid/acetonitrile gradient system (2-22% acetonitrile in 110 min; 22-40% acetonitrile in 25 min; 6 min wash at 90% followed by 25 min re-equilibration) and directly spray onto the mass spectrometer using EasySpray source (Thermo Fisher Scientific). Mass spectrometer was set to collect one MS1 scan (Orbitrap; 120K resolution; AGC target $2x10^5$; max IT 50 ms) followed by data-dependent, "Top Speed" (3 seconds) MS2 scans (collision induced dissociation; ion trap; NCD 35; AGC $5x10^3$; max IT 100 ms). For multinotch-MS3, top 10 precursors from each MS2 were fragmented by HCD followed by Orbitrap analysis (NCE 55; 60K resolution; AGC $5x10^4$; max IT 120 ms, 100-500 m/z scan range).

Proteome Discoverer (v2.1; Thermo Fisher) was used for data analysis. MS2 spectra were searched against SwissProt mouse protein database (release 2016-04-13; 24861 sequences) using the following search parameters: MS1 and MS2 tolerance were set to 10 ppm and 0.6 Da, respectively; carbamidomethylation of cysteines (57.02146 Da) and TMT labeling of lysine and N-termini of peptides (229.16293 Da) were considered static modifications; oxidation of methionine (15.9949 Da) and deamidation of asparagine and glutamine (0.98401 Da) were considered variable. Identified proteins and peptides were filtered to retain only those that passed ≤1% FDR threshold. Quantitation was performed using high-quality MS3 spectra using the Reporter Ion Quantifier Node of Proteome Discoverer (Average signal-to-noise ratio of 10 and <30% isolation interference). Pathway analysis of differentially regulated proteins was performed by GSEA (http://software.broadinstitute.org/gsea/index.jsp).

^{13}C-isotope tracing

For ^{13}C tracing, 2 million cells were plated in five T25 flasks and cultured using the media containing ^{13}C-U-labeled glucose or glutamine (both from Cambridge Isotope Laboratories, CLM-

1396-1 and CLM-1822-H) for 16 hours. Cells were collected by centrifugation and the medium was completely removed using an aspirator. 1 ml of 80% methanol that was chilled on dry ice was added in the cell pellet. The cell pellet was suspended and placed at -80°C for 10 min. The metabolite was harvested by centrifuging at 700g, 4°C for 10 min and transferring to a chilled tube. Protein concentration was measured in parallel. The aliquot metabolite was normalized to protein concentration and transferred to a new tube. The metabolite pellet was obtained by speedvac at 4 °C. Agilent 1290 UHPLC and 6530 Accurate-Mass Q-TOF LC/MS were used for stable ^{13}C-labeled glucose or glutamine metabolomics tracing experiments. Agilent MassHunter Workstation Software LC/MS Data Acquisition for 6200 series TOF/6500 series Q-TOF (B.06.01) was used for calibration and data acquisition. For chromatography, a Phenomenex Luna NH2 column (5 µm,1.0 x 150mm, 1.7µm) was used with mobile phase (A) consisting of 5 mM ammonium acetate, pH 9.6 in water; mobile phase (B) consisting of acetonitrile with a flow rate of 0.075 ml/min. Gradient program: mobile phase B was started at 80%, decreased to 0% in 15 min and held for 4 min before going to the initial condition with an increased flowrate of 0.09 ml/min and held for 3 min. The column was held at 25 °C and 10 µL of the sample was injected into the LC-MS. Calibration of TOF MS was achieved through Agilent ESI-Low Concentration Tuning Mix. Key parameters were mass range: 100-1400 Da, Gas temp: 285 °C, Fragmentor: 148 V, Skimmer: 80 V, Drying Gas: 8 l/min, Nebulizer: 30 psi, Vcap: 3500 V, and Ref Nebulizer: 10 psi. Negative mode was used, and the reference ions were at 119.0363 and 980.01637 Da.

Immunohistochemistry and quantification

Immunohistochemistry was performed using serial sections from patient tumor sections or mouse brain sections. The sections were deparaffinized using xylene and rehydrated by decreasing

concentrations of ethanol in the order of 100%, 95%, and water. Antigen retrieval was treated using a low-boiled 10mM citrate buffer, pH 6.0. Endogenous peroxidase activity was quenched by 3% hydrogen peroxide. Blocking was performed using 5% goat serum, 1% BSA. Sections were incubated for 5 h with one of the following rabbit polyclonal antibodies: anti-H3K27me3 (07-449, Millipore, 0.1 µg/mL), H3K27ac (D5E4 XP, Cell Signaling, 1:150), H3K27M (anti-H3 K27M, Millipore, #ABE419; 0.5 µg/mL) or rabbit polyclonal anti-SLC1A5 (#HPA035240; SIGMA, 0.5 µg/ml dilution). Tissue sections were then incubated for 60 min with biotinylated goat anti-rabbit IgG (PK6101, Vector Labs) at 1:200 dilution. The stained sections were visualized using 3,3'Diaminobenzidine (DAB) or Fast Red**.** The Slides were then rinsed, dehydrated, mounted and cover slipped.

Stained sections were scanned and quantified in a blinded manner. For automated scoring, each slide was scanned using an AperioScaNSCope Scanner (Aperio Vista) and viewed through AperioImageScope software program. For double staining experiments, the same stained section was visualized through the brown, red or combined channels with all parameters kept constant. An individual blinded to the experimental design captured JPEG images at 10X magnification on the AperioImageScope viewing program. Cells that were positive for H3K27M were counted as H3K27me3 positive or H3K27me3 negative in three non-overlapping high-power fields. Quantification of immunostaining on each JPEG was conducted using an automated analysis program with the MATLAB image processing toolbox, based on previously described methodology (Panwalkar *et al.,* 2017). The algorithm used color segmentation with RGB color differentiation, K-Means Clustering, and background-foreground separation with Otsu's thresholding. To arrive at a score, the numbers of extracted pixels were multiplied by their average

intensity for each core (represented as pixel units). The final score for a given case and marker was calculated by averaging the score of two cores (for each case) for a given marker.

Xenograft and drug administration *in vivo*

For subcutaneous injection into flank, H3.3K27M mNSCs were isolated and counted. 100,000 cells in 50 µl of medium were mixed with 50 µl of Matrigel on incubated on ice. Cells were then injected subcutaneously into the flank region of 8-week-old athymic nude mice (Foxn1^{nu}, Jackson Laboratories, #002019). For pharmacological experiments, mice were randomized into two groups at 8 weeks after implantation. The mice in the treatment group were injected intraperitoneally with DON (1mg/kg) every other day for six weeks. Tumor growth was measured weekly using calipers. Tumor volume (V) was calculated using the formula $V = L \times W \times W / 2$. V is volume ($mm^3$), L is the longest diameter (in mm), and W is the shortest diameter (in mm).

To establish orthotopic xenograft DIPG models, 400,000 cells/2 µl of bioluminescent HSJD-DIPG-007 cells were injected into the pontine tegmentum. NSG (NOD.Cg-*Prkdc*^{scid}*Il2rg*^{tm1Wj1}/SzJ; Jackson Laboratories, #005557) mice were anesthetized with 75mg/kg dexmedetomidine and 0.25mg/kg ketamine by intraperitoneal injection. 5mg/kg carprofen was used for analgesia. Mice were mounted on a stereotaxic device. A sagittal incision was made using a scalpel and a small hole was created using a microdrill at 1.0 mm posterior and 0.8 mm lateral from the lambdoid suture. A sterile Hamilton syringe was utilized for injection. 1 µl containing 200,000 cells was injected at 5 mm depth from the inner base of the skull. The Hamilton syringe was then retracted 0.5 mm, and an additional 1 µl of cells were injected. After the completion of injections, 1mg/kg atipamezole solution was intraperitoneally injected for

anesthesia reversal. Tumor engraftment was confirmed by bioluminescence imaging. For experiments involving 2-DG treatment, mice were randomly divided into two groups at 3-weeks after implantation. Orthotopic xenograft mice received intraperitoneal injection of vehicle or 2-DG (500mg/kg) every other day for three weeks. For experiments involving IDHi compound **13** and/or JHU-083 treatment, orthotopic xenograft mice received IDH1 inhibitor #13 (10mg/kg) by intraperitoneal injection or JHU-083 (20mg/kg) by oral gavage. Tumor size was measured using bioluminescent imaging (IVIS). The following compounds were used for *in vivo* experiments: DON (6-Diazo-5-oxo-L-norleucine, Cayman Chemical, #17580), 2-DG (2-Deoxy-D-glucose, Cayman Chemical, #14325), JHU-083 (MedChemExpress, #HY-122218), and IDH inhibitor **13** (synthesized and obtain from Abbvie).

Statistical analyses

The sample size (*n*) along with the statistical test performed and corresponding *P*-values are indicated in each figure and figure legend. No samples or animals were excluded from data analyses. Because H3K27M-midline gliomas are rare, sample sizes were determined based on number of tumor samples available. Data are represented as the means ± standard deviation. Graphs were plotted and statistical analyses were performed using Prism software (version 7/8, GraphPad, La Jolla, CA). Unpaired, two-sided, Student's *t* test, Chi square test, one-way or two-way analysis of variance (ANOVA) followed by *post hoc* Bonferroni multiple comparison analysis were used to analyze data as indicated. Survival analyses of data obtained from the PedcBioPortal was performed using median cut-off (high and low expression was defined as tumor samples above and below the median expression, respectively). Survival data for animal models were plotted as

Kaplan-Meier curves and the log-rank test was used to examine the association of various factors with overall survival. Data were considered significant if *P*-values were below 0.05.

2.6 Author Contributions & Acknowledgments

This work was performed in collaboration with Dr. Chan Chung. Chan Chung, Stefan Sweha, and Sriram Venneti conceptualized the study. Chan Chung, Stefan Sweha, and Jill Bayliss performed experiments *in vitro* and *in vivo* studies and analyzed data. Stefan Sweha performed bioinformatics and analysis on patient data. Debra Hawes and Fusheng Yang performed immunohistochemistry used for H3K27M and H3K27me3 quantification. J. Brad Shotwell and Zhiguo Bian, of AbbVie, synthesized the small-molecule IDH1 inhibitor utilized for in vivo studies. Ho-Joon Lee, Mengrou Shan, and Costas A. Lyssiotis performed ^{13}C tracing experiments and provided metabolomic results.

2.7 References

Altman BJ, Stine ZE, Dang CV. From Krebs to clinic: glutamine metabolism to cancer therapy. *Nat Rev Cancer*. 2016 Oct;16(10):619-34. doi: 10.1038/nrc.2016.71.

Bayliss J, Mukherjee P, Lu C, Jain SU, Chung C, Martinez D, Sabari B, Margol AS, Panwalkar P, Parolia A, Pekmezci M, McEachin RC, Cieslik M, Tamrazi B, Garcia BA, La Rocca G, Santi M, Lewis PW, Hawkins C, Melnick A, David Allis C, Thompson CB, Chinnaiyan AM, Judkins AR, Venneti S. Lowered H3K27me3 and DNA hypomethylation define poorly prognostic pediatric posterior fossa ependymomas. *Sci Transl Med*. 2016 Nov 23;8(366):366ra161. doi: 10.1126/scitranslmed.aah6904.

Bender S, Tang Y, Lindroth AM, Hovestadt V, Jones DT, Kool M, Zapatka M, Northcott PA, Sturm D, Wang W, Radlwimmer B, Højfeldt JW, Truffaux N, Castel D, Schubert S, Ryzhova M, Seker-Cin H, Gronych J, Johann PD, Stark S, Meyer J, Milde T, Schuhmann M, Ebinger M, Monoranu CM, Ponnuswami A, Chen S, Jones C, Witt O, Collins VP, von Deimling A, Jabado N, Puget S, Grill J, Helin K, Korshunov A, Lichter P, Monje M, Plass C, Cho YJ, Pfister SM. Reduced H3K27me3 and DNA hypomethylation are major drivers of gene expression in K27M mutant

pediatric high-grade gliomas. *Cancer Cell*. 2013 Nov 11;24(5):660-72. doi: 10.1016/j.ccr.2013.10.006.

Bressan RB, Southgate B, Ferguson KM, Blin C, Grant V, Alfazema N, Wills JC, Marques-Torrejon MA, Morrison GM, Ashmore J, Robertson F, Williams CAC, Bradley L, von Kriegsheim A, Anderson RA, Tomlinson SR, Pollard SM. Regional identity of human neural stem cells determines oncogenic responses to histone H3.3 mutants. *Cell Stem Cell*. 2021 May 6;28(5):877-893.e9. doi: 10.1016/j.stem.2021.01.016.

Bryant KL, Mancias JD, Kimmelman AC, Der CJ. KRAS: feeding pancreatic cancer proliferation. *Trends Biochem Sci*. 2014 Feb;39(2):91-100. doi: 10.1016/j.tibs.2013.12.004.

Carey BW, Finley LW, Cross JR, Allis CD, Thompson CB. Intracellular α-ketoglutarate maintains the pluripotency of embryonic stem cells. *Nature*. 2015 Feb 19;518(7539):413-6. doi: 10.1038/nature13981.

Chan KM, Fang D, Gan H, Hashizume R, Yu C, Schroeder M, Gupta N, Mueller S, James CD, Jenkins R, Sarkaria J, Zhang Z. The histone H3.3K27M mutation in pediatric glioma reprograms H3K27 methylation and gene expression. *Genes Dev*. 2013 May 1;27(9):985-90. doi: 10.1101/gad.217778.113.

Chen L, Cui H. Targeting Glutamine Induces Apoptosis: A Cancer Therapy Approach. *Int J Mol Sci*. 2015 Sep 22;16(9):22830-55. doi: 10.3390/ijms160922830.

Choi YK, Park KG. Targeting Glutamine Metabolism for Cancer Treatment. *Biomol Ther* (Seoul). 2018 Jan 1;26(1):19-28. doi: 10.4062/biomolther.2017.178.

Chowdhury R, Yeoh KK, Tian YM, Hillringhaus L, Bagg EA, Rose NR, Leung IK, Li XS, Woon EC, Yang M, McDonough MA, King ON, Clifton IJ, Klose RJ, Claridge TD, Ratcliffe PJ, Schofield CJ, Kawamura A. The oncometabolite 2-hydroxyglutarate inhibits histone lysine demethylases. *EMBO Rep*. 2011 May;12(5):463-9. doi: 10.1038/embor.2011.43.

Chung C, Sweha SR, Pratt D, Tamrazi B, Panwalkar P, Banda A, Bayliss J, Hawes D, Yang F, Lee HJ, Shan M, Cieslik M, Qin T, Werner CK, Wahl DR, Lyssiotis CA, Bian Z, Shotwell JB, Yadav VN, Koschmann C, Chinnaiyan AM, Blüml S, Judkins AR, Venneti S. Integrated Metabolic and Epigenomic Reprograming by H3K27M Mutations in Diffuse Intrinsic Pontine Gliomas. *Cancer Cell*. 2020 Sep 14;38(3):334-349.e9. doi: 10.1016/j.ccell.2020.07.008.

Cluntun AA, Lukey MJ, Cerione RA, Locasale JW. Glutamine Metabolism in Cancer: Understanding the Heterogeneity. *Trends Cancer*. 2017 Mar;3(3):169-180. doi: 10.1016/j.trecan.2017.01.005.

Dang L, White DW, Gross S, Bennett BD, Bittinger MA, Driggers EM, Fantin VR, Jang HG, Jin S, Keenan MC, Marks KM, Prins RM, Ward PS, Yen KE, Liau LM, Rabinowitz JD, Cantley LC, Thompson CB, Vander Heiden MG, Su SM. Cancer-associated IDH1 mutations produce 2-hydroxyglutarate. *Nature*. 2009 Dec 10;462(7274):739-44. doi: 10.1038/nature08617.

Daye D, Wellen KE. Metabolic reprogramming in cancer: unraveling the role of glutamine in tumorigenesis. *Semin Cell Dev Biol*. 2012 Jun;23(4):362-9. doi: 10.1016/j.semcdb.2012.02.002.

DeBerardinis RJ, Chandel NS. Fundamentals of cancer metabolism. *Sci Adv*. 2016 May 27;2(5):e1600200. doi: 10.1126/sciadv.1600200.

DeBerardinis RJ, Lum JJ, Hatzivassiliou G, Thompson CB. The biology of cancer: metabolic reprogramming fuels cell growth and proliferation. *Cell Metab*. 2008 Jan;7(1):11-20. doi: 10.1016/j.cmet.2007.10.002.

Dong Y, Tu R, Liu H, Qing G. Regulation of cancer cell metabolism: oncogenic MYC in the driver's seat. *Signal Transduct Target Ther*. 2020 Jul 10;5(1):124. doi: 10.1038/s41392-020-00235-2.

Eagle H. The minimum vitamin requirements of the L and HeLa cells in tissue culture, the production of specific vitamin deficiencies, and their cure. *J Exp Med*. 1955 Nov 1;102(5):595-600. doi: 10.1084/jem.102.5.595..

Eagle, H., Oyama, V. I., Levy, M., Horton, C. L. & Fleischman, R. The growth response of mammalian cells in tissue culture to L-glutamine and L-glutamic acid. *J. Biol. Chem*. 218, 607–616 (1956).

Grasso CS, Tang Y, Truffaux N, Berlow NE, Liu L, Debily MA, Quist MJ, Davis LE, Huang EC, Woo PJ, Ponnuswami A, Chen S, Johung TB, Sun W, Kogiso M, Du Y, Qi L, Huang Y, Hütt-Cabezas M, Warren KE, Le Dret L, Meltzer PS, Mao H, Quezado M, van Vuurden DG, Abraham J, Fouladi M, Svalina MN, Wang N, Hawkins C, Nazarian J, Alonso MM, Raabe EH, Hulleman E, Spellman PT, Li XN, Keller C, Pal R, Grill J, Monje M. Functionally defined therapeutic targets in diffuse intrinsic pontine glioma. *Nat Med*. 2015 Jun;21(6):555-9. doi: 10.1038/nm.3855.

Hanaford AR, Alt J, Rais R, Wang SZ, Kaur H, Thorek DLJ, Eberhart CG, Slusher BS, Martin AM, Raabe EH. Orally bioavailable glutamine antagonist prodrug JHU-083 penetrates mouse brain and suppresses the growth of MYC-driven medulloblastoma. *Transl Oncol*. 2019 Oct;12(10):1314-1322. doi: 10.1016/j.tranon.2019.05.013.

Hao Y, Samuels Y, Li Q, Krokowski D, Guan BJ, Wang C, Jin Z, Dong B, Cao B, Feng X, Xiang M, Xu C, Fink S, Meropol NJ, Xu Y, Conlon RA, Markowitz S, Kinzler KW, Velculescu VE, Brunengraber H, Willis JE, LaFramboise T, Hatzoglou M, Zhang GF, Vogelstein B, Wang Z. Oncogenic PIK3CA mutations reprogram glutamine metabolism in colorectal cancer. *Nat Commun*. 2016 Jun 20;7:11971. doi: 10.1038/ncomms11971.

Harutyunyan AS, Krug B, Chen H, Papillon-Cavanagh S, Zeinieh M, De Jay N, Deshmukh S, Chen CCL, Belle J, Mikael LG, Marchione DM, Li R, Nikbakht H, Hu B, Cagnone G, Cheung WA, Mohammadnia A, Bechet D, Faury D, McConechy MK, Pathania M, Jain SU, Ellezam B, Weil AG, Montpetit A, Salomoni P, Pastinen T, Lu C, Lewis PW, Garcia BA, Kleinman CL, Jabado N, Majewski J. H3K27M induces defective chromatin spread of PRC2-mediated repressive

H3K27me2/me3 and is essential for glioma tumorigenesis. *Nat Commun*. 2019 Mar 19;10(1):1262. doi: 10.1038/s41467-019-09140-x.

Hashizume R, Andor N, Ihara Y, Lerner R, Gan H, Chen X, Fang D, Huang X, Tom MW, Ngo V, Solomon D, Mueller S, Paris PL, Zhang Z, Petritsch C, Gupta N, Waldman TA, James CD. Pharmacologic inhibition of histone demethylation as a therapy for pediatric brainstem glioma. *Nat Med*. 2014 Dec;20(12):1394-6. doi: 10.1038/nm.3716.

Jiang X, Su L, Zhang Q, He C, Zhang Z, Yi P, Liu J. GABAB receptor complex as a potential target for tumor therapy. *J Histochem Cytochem*. 2012 Apr;60(4):269-79. doi: 10.1369/0022155412438105.

Larson JD, Kasper LH, Paugh BS, Jin H, Wu G, Kwon CH, Fan Y, Shaw TI, Silveira AB, Qu C, Xu R, Zhu X, Zhang J, Russell HR, Peters JL, Finkelstein D, Xu B, Lin T, Tinkle CL, Patay Z, Onar-Thomas A, Pounds SB, McKinnon PJ, Ellison DW, Zhang J, Baker SJ. Histone H3.3 K27M Accelerates Spontaneous Brainstem Glioma and Drives Restricted Changes in Bivalent Gene Expression. *Cancer Cell*. 2019 Jan 14;35(1):140-155.e7. doi: 10.1016/j.ccell.2018.11.015.

Lewis PW, Müller MM, Koletsky MS, Cordero F, Lin S, Banaszynski LA, Garcia BA, Muir TW, Becher OJ, Allis CD. Inhibition of PRC2 activity by a gain-of-function H3 mutation found in pediatric glioblastoma. *Science*. 2013 May 17;340(6134):857-61. doi: 10.1126/science.1232245.

Loenarz C, Schofield CJ. Expanding chemical biology of 2-oxoglutarate oxygenases. *Nat Chem Biol*. 2008 Mar;4(3):152-6. doi: 10.1038/nchembio0308-152.

Lu C, Ward PS, Kapoor GS, Rohle D, Turcan S, Abdel-Wahab O, Edwards CR, Khanin R, Figueroa ME, Melnick A, Wellen KE, O'Rourke DM, Berger SL, Chan TA, Levine RL, Mellinghoff IK, Thompson CB. IDH mutation impairs histone demethylation and results in a block to cell differentiation. *Nature*. 2012 Feb 15;483(7390):474-8. doi: 10.1038/nature10860.

Mackay A, Burford A, Carvalho D, Izquierdo E, Fazal-Salom J, Taylor KR, Bjerke L, Clarke M, Vinci M, Nandhabalan M, Temelso S, Popov S, Molinari V, Raman P, Waanders AJ, Han HJ, Gupta S, Marshall L, Zacharoulis S, Vaidya S, Mandeville HC, Bridges LR, Martin AJ, Al-Sarraj S, Chandler C, Ng HK, Li X, Mu K, Trabelsi S, Brahim DH, Kisljakov AN, Konovalov DM, Moore AS, Carcaboso AM, Sunol M, de Torres C, Cruz O, Mora J, Shats LI, Stavale JN, Bidinotto LT, Reis RM, Entz-Werle N, Farrell M, Cryan J, Crimmins D, Caird J, Pears J, Monje M, Debily MA, Castel D, Grill J, Hawkins C, Nikbakht H, Jabado N, Baker SJ, Pfister SM, Jones DTW, Fouladi M, von Bueren AO, Baudis M, Resnick A, Jones C. Integrated Molecular Meta-Analysis of 1,000 Pediatric High-Grade and Diffuse Intrinsic Pontine Glioma. *Cancer Cell*. 2017 Oct 9;32(4):520-537.e5. doi: 10.1016/j.ccell.2017.08.017.

Márquez J, Alonso FJ, Matés JM, Segura JA, Martín-Rufián M, Campos-Sandoval JA. Glutamine Addiction In Gliomas. *Neurochem Res*. 2017 Jun;42(6):1735-1746. doi: 10.1007/s11064-017-2212-1.

Mohammad F, Weissmann S, Leblanc B, Pandey DP, Højfeldt JW, Comet I, Zheng C, Johansen JV, Rapin N, Porse BT, Tvardovskiy A, Jensen ON, Olaciregui NG, Lavarino C, Suñol M, de Torres C, Mora J, Carcaboso AM, Helin K. EZH2 is a potential therapeutic target for H3K27M-mutant pediatric gliomas. *Nat Med*. 2017 Apr;23(4):483-492. doi: 10.1038/nm.4293.

Mukhopadhyay S, Vander Heiden MG, McCormick F. The Metabolic Landscape of RAS-Driven Cancers from biology to therapy. *Nat Cancer*. 2021 Mar;2(3):271-283. doi: 10.1038/s43018-021-00184-x.

Nagaraja S, Vitanza NA, Woo PJ, Taylor KR, Liu F, Zhang L, Li M, Meng W, Ponnuswami A, Sun W, Ma J, Hulleman E, Swigut T, Wysocka J, Tang Y, Monje M. Transcriptional Dependencies in Diffuse Intrinsic Pontine Glioma. *Cancer Cell*. 2017 May 8;31(5):635-652.e6. doi: 10.1016/j.ccell.2017.03.011.

Nagarajan A, Malvi P, Wajapeyee N. Oncogene-directed alterations in cancer cell metabolism. *Trends Cancer*. 2016 Jul;2(7):365-377. doi: 10.1016/j.trecan.2016.06.002.

Natarajan SK, Venneti S. Glutamine Metabolism in Brain Tumors. *Cancers*. 2019 Oct 24;11(11):1628. doi: 10.3390/cancers11111628.

Pajovic S, Siddaway R, Bridge T, Sheth J, Rakopoulos P, Kim B, Ryall S, Agnihotri S, Phillips L, Yu M, Li C, Milos S, Patel P, Srikanthan D, Huang A, Hawkins C. Epigenetic activation of a RAS/MYC axis in H3.3K27M-driven cancer. *Nat Commun*. 2020 Dec 4;11(1):6216. doi: 10.1038/s41467-020-19972-7.

Parsons DW, Jones S, Zhang X, Lin JC, Leary RJ, Angenendt P, Mankoo P, Carter H, Siu IM, Gallia GL, Olivi A, McLendon R, Rasheed BA, Keir S, Nikolskaya T, Nikolsky Y, Busam DA, Tekleab H, Diaz LA Jr, Hartigan J, Smith DR, Strausberg RL, Marie SK, Shinjo SM, Yan H, Riggins GJ, Bigner DD, Karchin R, Papadopoulos N, Parmigiani G, Vogelstein B, Velculescu VE, Kinzler KW. An integrated genomic analysis of human glioblastoma multiforme. *Science*. 2008 Sep 26;321(5897):1807-12. doi: 10.1126/science.1164382.

Panwalkar P, Clark J, Ramaswamy V, Hawes D, Yang F, Dunham C, Yip S, Hukin J, Sun Y, Schipper MJ, Chavez L, Margol A, Pekmezci M, Chung C, Banda A, Bayliss JM, Curry SJ, Santi M, Rodriguez FJ, Snuderl M, Karajannis MA, Saratsis AM, Horbinski CM, Carret AS, Wilson B, Johnston D, Lafay-Cousin L, Zelcer S, Eisenstat D, Silva M, Scheinemann K, Jabado N, McNeely PD, Kool M, Pfister SM, Taylor MD, Hawkins C, Korshunov A, Judkins AR, Venneti S. Immunohistochemical analysis of H3K27me3 demonstrates global reduction in group-A childhood posterior fossa ependymoma and is a powerful predictor of outcome. *Acta Neuropathol*. 2017 Nov;134(5):705-714. doi: 10.1007/s00401-017-1752-4.

Pavlova NN, Thompson CB. The Emerging Hallmarks of Cancer Metabolism. *Cell Metab*. 2016 Jan 12;23(1):27-47. doi: 10.1016/j.cmet.2015.12.006.

Piunti A, Hashizume R, Morgan MA, Bartom ET, Horbinski CM, Marshall SA, Rendleman EJ, Ma Q, Takahashi YH, Woodfin AR, Misharin AV, Abshiru NA, Lulla RR, Saratsis AM, Kelleher

NL, James CD, Shilatifard A. Therapeutic targeting of polycomb and BET bromodomain proteins in diffuse intrinsic pontine gliomas. *Nat Med*. 2017 Apr;23(4):493-500. doi: 10.1038/nm.4296.

Schwartzentruber J, Korshunov A, Liu XY, Jones DT, Pfaff E, Jacob K, Sturm D, Fontebasso AM, Quang DA, Tönjes M, Hovestadt V, Albrecht S, Kool M, Nantel A, Konermann C, Lindroth A, Jäger N, Rausch T, Ryzhova M, Korbel JO, Hielscher T, Hauser P, Garami M, Klekner A, Bognar L, Ebinger M, Schuhmann MU, Scheurlen W, Pekrun A, Frühwald MC, Roggendorf W, Kramm C, Dürken M, Atkinson J, Lepage P, Montpetit A, Zakrzewska M, Zakrzewski K, Liberski PP, Dong Z, Siegel P, Kulozik AE, Zapatka M, Guha A, Malkin D, Felsberg J, Reifenberger G, von Deimling A, Ichimura K, Collins VP, Witt H, Milde T, Witt O, Zhang C, Castelo-Branco P, Lichter P, Faury D, Tabori U, Plass C, Majewski J, Pfister SM, Jabado N. Driver mutations in histone H3.3 and chromatin remodelling genes in paediatric glioblastoma. *Nature*. 2012 Jan 29;482(7384):226-31. doi: 10.1038/nature10833.

Shroff EH, Eberlin LS, Dang VM, Gouw AM, Gabay M, Adam SJ, Bellovin DI, Tran PT, Philbrick WM, Garcia-Ocana A, Casey SC, Li Y, Dang CV, Zare RN, Felsher DW. MYC oncogene overexpression drives renal cell carcinoma in a mouse model through glutamine metabolism. *Proc Natl Acad Sci USA*. 2015 May 26;112(21):6539-44. doi: 10.1073/pnas.1507228112.

Son J, Lyssiotis CA, Ying H, Wang X, Hua S, Ligorio M, Perera RM, Ferrone CR, Mullarky E, Shyh-Chang N, Kang Y, Fleming JB, Bardeesy N, Asara JM, Haigis MC, DePinho RA, Cantley LC, Kimmelman AC. Glutamine supports pancreatic cancer growth through a KRAS-regulated metabolic pathway. *Nature*. 2013 Apr 4;496(7443):101-5. doi: 10.1038/nature12040.

Stine ZE, Walton ZE, Altman BJ, Hsieh AL, Dang CV. MYC, Metabolism, and Cancer. *Cancer Discov*. 2015 Oct;5(10):1024-39. doi: 10.1158/2159-8290.CD-15-0507.

Sturm D, Witt H, Hovestadt V, Khuong-Quang DA, Jones DT, Konermann C, Pfaff E, Tönjes M, Sill M, Bender S, Kool M, Zapatka M, Becker N, Zucknick M, Hielscher T, Liu XY, Fontebasso AM, Ryzhova M, Albrecht S, Jacob K, Wolter M, Ebinger M, Schuhmann MU, van Meter T, Frühwald MC, Hauch H, Pekrun A, Radlwimmer B, Niehues T, von Komorowski G, Dürken M, Kulozik AE, Madden J, Donson A, Foreman NK, Drissi R, Fouladi M, Scheurlen W, von Deimling A, Monoranu C, Roggendorf W, Herold-Mende C, Unterberg A, Kramm CM, Felsberg J, Hartmann C, Wiestler B, Wick W, Milde T, Witt O, Lindroth AM, Schwartzentruber J, Faury D, Fleming A, Zakrzewska M, Liberski PP, Zakrzewski K, Hauser P, Garami M, Klekner A, Bognar L, Morrissy S, Cavalli F, Taylor MD, van Sluis P, Koster J, Versteeg R, Volckmann R, Mikkelsen T, Aldape K, Reifenberger G, Collins VP, Majewski J, Korshunov A, Lichter P, Plass C, Jabado N, Pfister SM. Hotspot mutations in H3F3A and IDH1 define distinct epigenetic and biological subgroups of glioblastoma. *Cancer Cell*. 2012 Oct 16;22(4):425-37. doi: 10.1016/j.ccr.2012.08.024.

Vander Heiden MG, Cantley LC, Thompson CB. Understanding the Warburg effect: the metabolic requirements of cell proliferation. *Science*. 2009 May 22;324(5930):1029-33. doi: 10.1126/science.1160809.

Venkatesh HS, Johung TB, Caretti V, Noll A, Tang Y, Nagaraja S, Gibson EM, Mount CW, Polepalli J, Mitra SS, Woo PJ, Malenka RC, Vogel H, Bredel M, Mallick P, Monje M. Neuronal Activity Promotes Glioma Growth through Neuroligin-3 Secretion. *Cell*. 2015 May 7;161(4):803-16. doi: 10.1016/j.cell.2015.04.012.

Wang J, Huang TY, Hou Y, Bartom E, Lu X, Shilatifard A, Yue F, Saratsis A. Epigenomic landscape and 3D genome structure in pediatric high-grade glioma. *Sci Adv*. 2021 Jun 2;7(23):eabg4126. doi: 10.1126/sciadv.abg4126.

Wise DR, DeBerardinis RJ, Mancuso A, Sayed N, Zhang XY, Pfeiffer HK, Nissim I, Daikhin E, Yudkoff M, McMahon SB, Thompson CB. Myc regulates a transcriptional program that stimulates mitochondrial glutaminolysis and leads to glutamine addiction. *Proc Natl Acad Sci USA*. 2008 Dec 2;105(48):18782-7. doi: 10.1073/pnas.0810199105.

Xiang L, Xie G, Liu C, Zhou J, Chen J, Yu S, Li J, Pang X, Shi H, Liang H. Knock-down of glutaminase 2 expression decreases glutathione, NADH, and sensitizes cervical cancer to ionizing radiation. *Biochim Biophys Acta*. 2013 Dec;1833(12):2996-3005. doi: 10.1016/j.bbamcr.2013.08.003.

Xu W, Yang H, Liu Y, Yang Y, Wang P, Kim SH, Ito S, Yang C, Wang P, Xiao MT, Liu LX, Jiang WQ, Liu J, Zhang JY, Wang B, Frye S, Zhang Y, Xu YH, Lei QY, Guan KL, Zhao SM, Xiong Y. Oncometabolite 2-hydroxyglutarate is a competitive inhibitor of α-ketoglutarate-dependent dioxygenases. *Cancer Cell*. 2011 Jan 18;19(1):17-30. doi: 10.1016/j.ccr.2010.12.014.

Yan H, Parsons DW, Jin G, McLendon R, Rasheed BA, Yuan W, Kos I, Batinic-Haberle I, Jones S, Riggins GJ, Friedman H, Friedman A, Reardon D, Herndon J, Kinzler KW, Velculescu VE, Vogelstein B, Bigner DD. IDH1 and IDH2 mutations in gliomas. *N Engl J Med*. 2009 Feb 19;360(8):765-73. doi: 10.1056/NEJMoa0808710.

Yang L, Venneti S, Nagrath D. Glutaminolysis: A Hallmark of Cancer Metabolism. *Annu Rev Biomed Eng*. 2017 Jun 21;19:163-194. doi: 10.1146/annurev-bioeng-071516-044546.

Young SZ, Bordey A. GABA's control of stem and cancer cell proliferation in adult neural and peripheral niches. Physiology (Bethesda). 2009 Jun;24:171-85. doi: 10.1152/physiol.00002.2009.

Yuan J, Dong X, Yap J, Hu J. The MAPK and AMPK signalings: interplay and implication in targeted cancer therapy. *J Hematol Oncol*. 2020 Aug 17;13(1):113. doi: 10.1186/s13045-020-00949-4.

2.8 Figures & Figure Legends

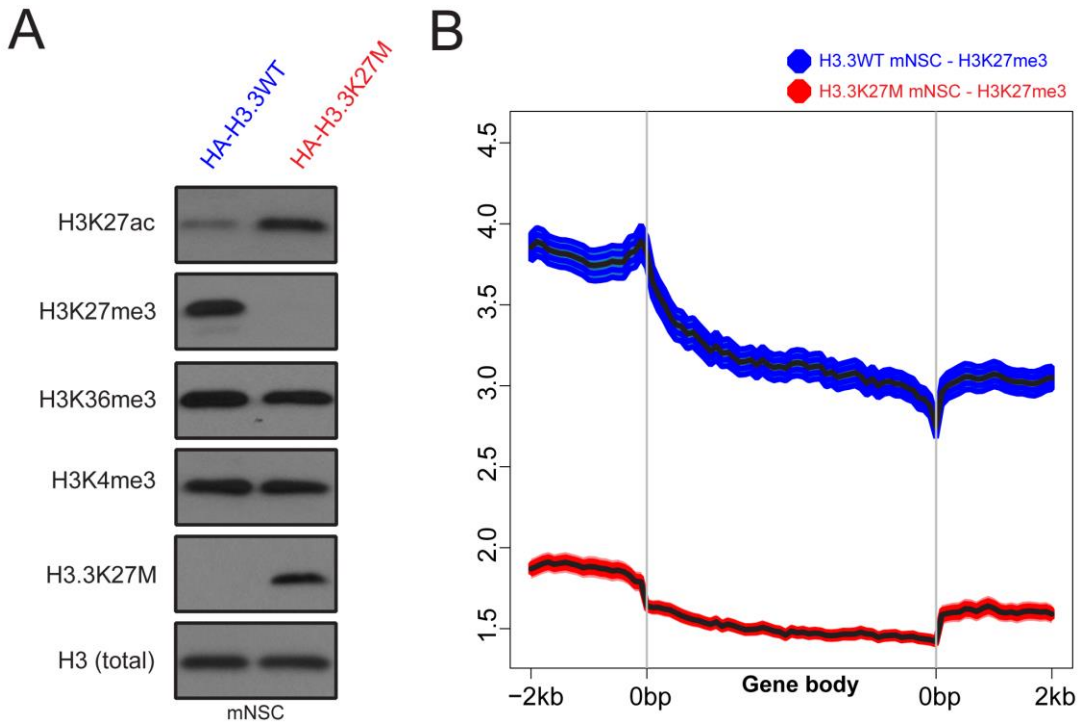

Figure 2.1. Isogenic mouse neuronal stem cell model of H3.3K27M mutant glioma.
(A) Immunoblots of mouse neuronal stem cells (mNSCs) stably transduced with HA-tagged H3.3WT (*blue*) or H3.3K27M (*red*) transgenes for epigenetic modifications H3K27ac, H3K27me3, H3K36me3, H3k4me3, mutant-specific H3.3K27M, and total H3. Representative of *n*=2 independent experiments. **(B)** H3K27me3 occupancy at gene bodies in H3.3WT (*blue*) and H3.3K27M (*red*) mNSCs.

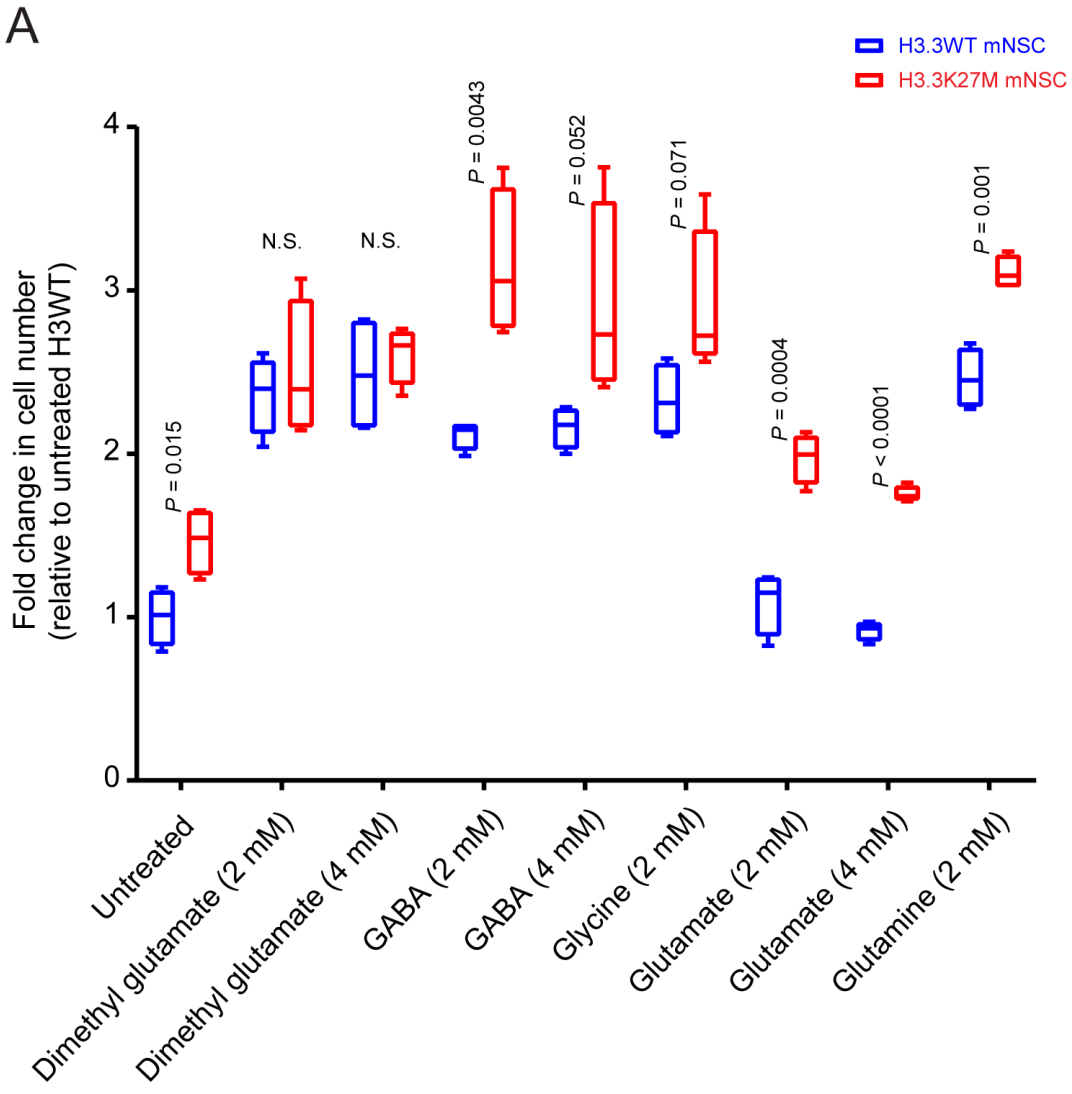

Figure 2.2. Increased growth of H3.3K27M mNSCs with exogenous amino acids or neurotransmitters.

(A) Cell growth experiments using H3.3WT (*blue*) or H3.3K27M (*red*) mNSC grown in complete media supplemented with dimethyl glutamate (2 mM or 4 mM), GABA (2 mM or 4 mM), glycine (2 mM), glutamate (2 or 4 mM), or glutamine (2 mM). Cell growth is reported a fold change in cell number (Y-axis) relative to the untreated H3.3WT mNSC condition. Results representative of *n*=2 independent experiments. *n*=4 biological replicates per treatment condition. Data are plotted as mean ± S.D. and analyzed by nonparametric, two-sided, unpaired, Student's *t* test.

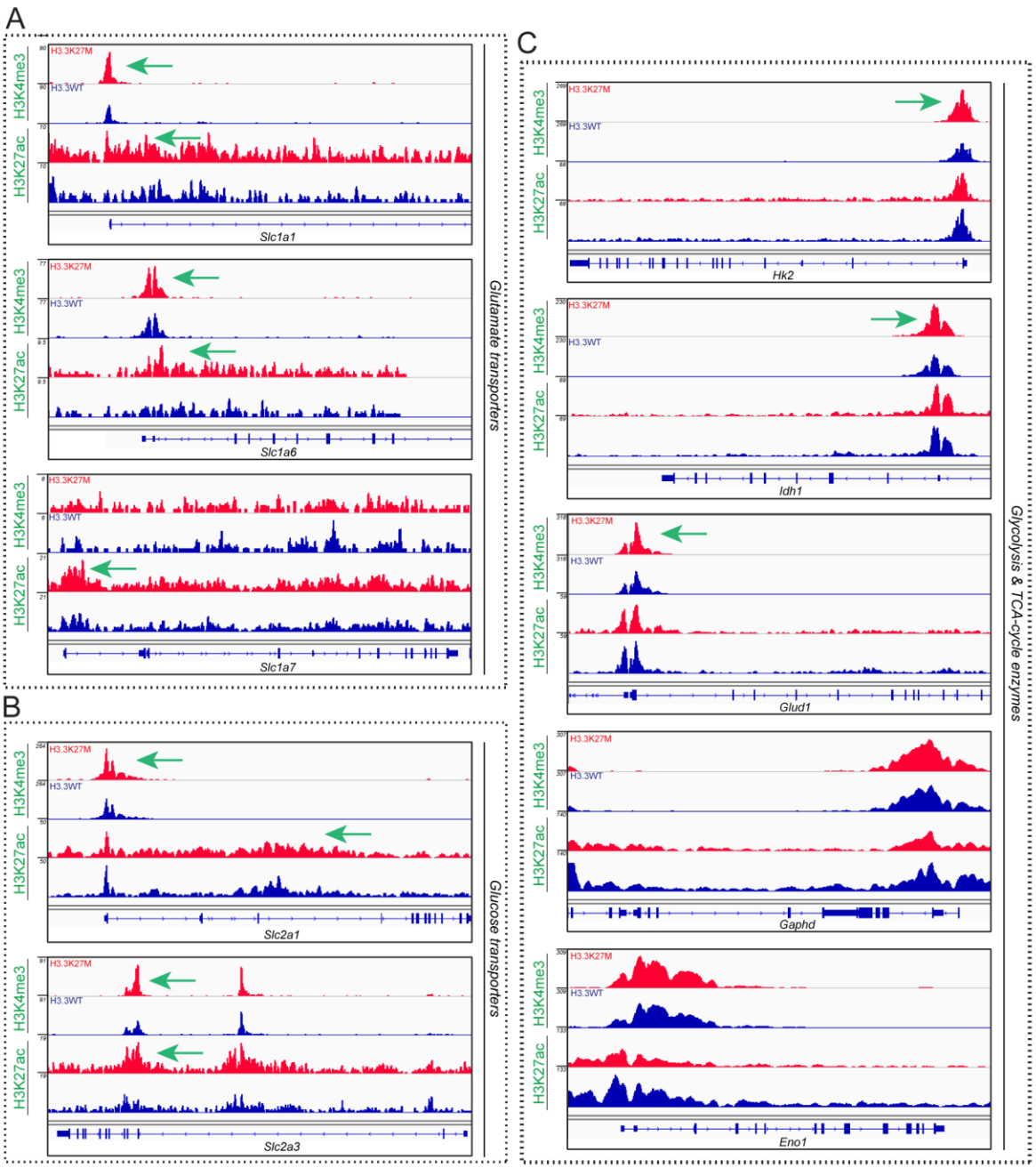

Figure 2.3. Promoter-localized activating epigenetic modifications are enriched in H3.3K27M mNSCs at genes involved in glucose and glutamate transport and metabolism. **(A-C)** Integrated Genomics Viewer snapshot of H3K4me3 and H3K27ac ChIP-seq signals in H3.3WT (*blue*) and H3.3K27M (*red*) mNSCs at loci encoding glutamate transporters (*Slc1a1*, *Slc1a6*, and *Slc1a7;* **A**), glucose transporters (*Slc2a1* and *Slc2a3;* **B**), and glycolysis/TCA-cycle enzymes (*Hk2*, *Idh1*, and *Glud1;* **C**). No changes are observed at loci for other TCA enzymes such as *Gapdh* or *Eno1* **(C)**. Green arrows indicate differential enrichment in H3.3K27M *versus* H3.3WT mNSCs.

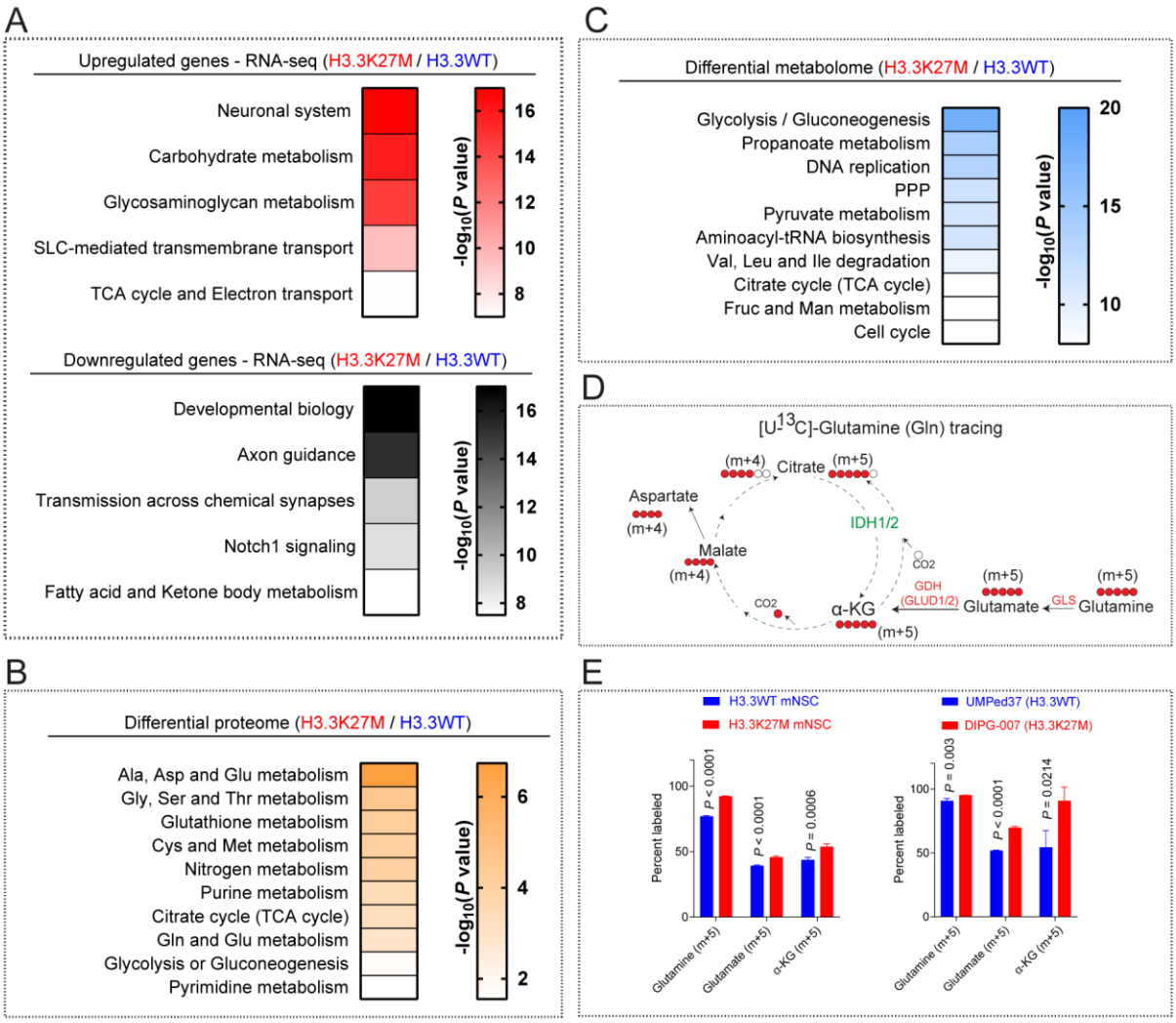

Figure 2.4. H3.3K27M mNSCs exhibit an altered transcriptome, proteome, and metabolome related to energy metabolism processes.

(A) Heatmap depicting gene set enrichment analysis (GSEA) results for upregulated (*red*) and downregulated (*black*) genes in H3.3K27M relative to H3.3WT mNSC as determined by RNA-seq. *n*=3 biological replicates per condition. **(B)** Heatmap depicting GSEA results for differentially expressed proteins as determined by tandem mass tag proteomics. *n*=3 biological replicates per condition. **(C)** Heatmap demonstrating results of enrichment analysis of differential metabolites. *n*=4 biological replicates per condition. **(D)** Schematic for metabolite tracing experiments using uniformly labeled ^{13}C-glutamine ([U-^{13}C]-Gln) and resulting glutamine flux into the TCA cycle. Note that five 13-C labeled carbons derived from glutamine are transferred directly to glutamate and alpha-ketoglutarate. **(E)** Bar plots illustrating percent labeling (Y-axis) as determined by mass spectroscopic analysis of H3.3K27M/H3.3WT mNSC (*left*) and H3.3K27M DIPG-007/H3.3WT UMPed37 (*right*) after cells were incubating with [U-^{13}C]-Gln. Glutamine, glutamate; *n*=4 biological replicates. Alpha-ketoglutarate, *n*=3 biological replicates). Data are plotted as mean ± S.D. and analyzed by nonparametric, two-sided, unpaired, Student's *t* test.

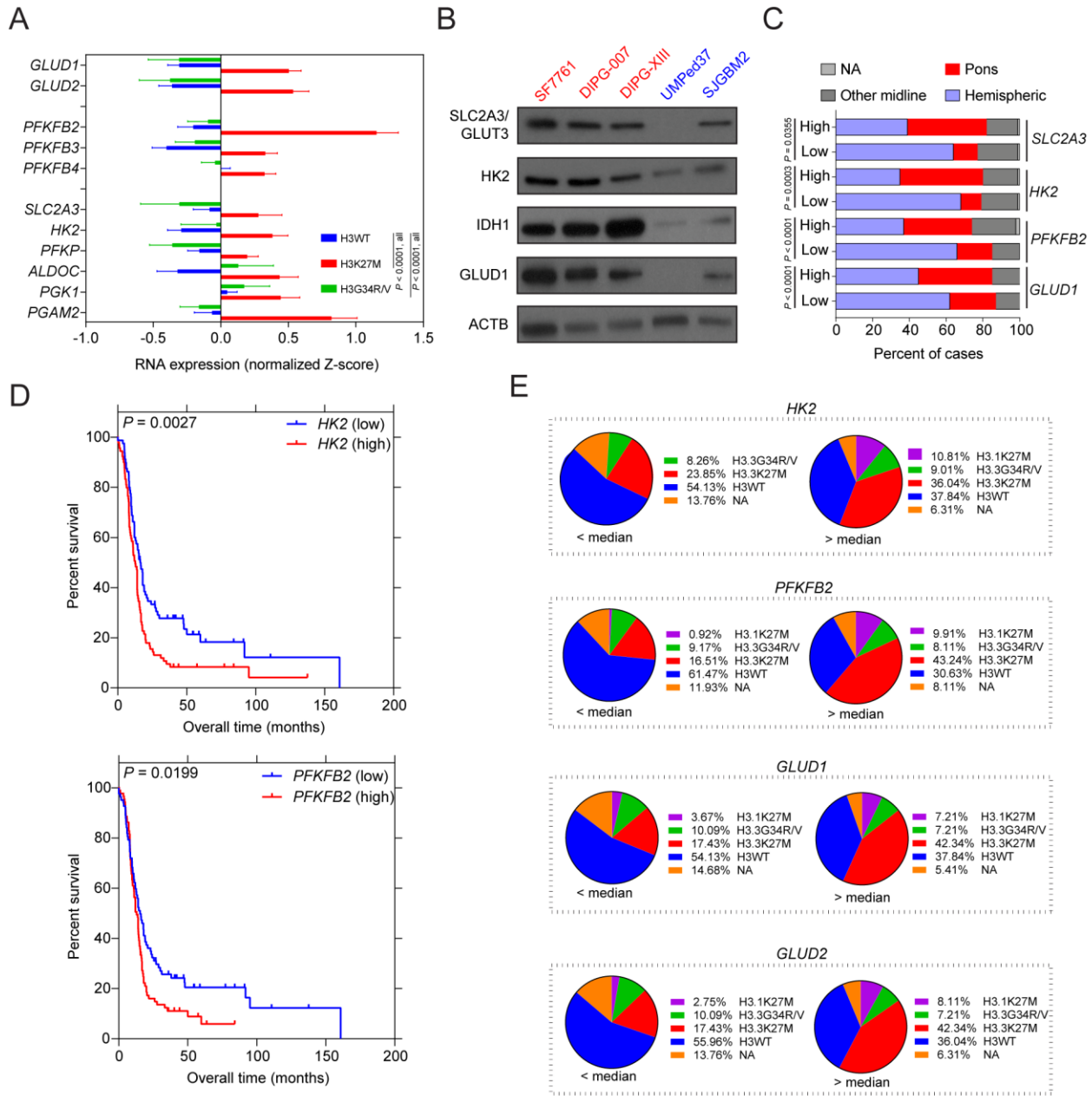

Figure 2.5. Genes involved in glycolysis and glutaminolysis are upregulated in H3.3K27M glioma samples and have prognostic implications.

(A) Bar plot of normalized RNA expression (X-axis) of key genes related to glycolysis and glutaminolysis in H3.1/3.3K27M (*n*=83, *red*), H3.3WT (*n*=101, *blue*), and H3.3G34R/V (*n*=19, *green*) patients from a meta-analysis by Mackay *et al.* (2017). Data are plotted as mean ± SEM and analyzed by one-way ANOVA; all comparisons significant, $P<0.0001$. **(B)** Representative immunoblots of H3.3K27M (SF7761, DIPG-007, DIPG-XIII; *red*) and H3.3WT (UMPed37, SJGBM2; *blue*) pediatric glioma patient-derived cell lines for glucose transporter (GLUT3/SLC2A3), Hexokinase-2 (HK2), Isocitrate Dehydrogenase 1 (IDH1), Glutamate Dehydrogenase 1 (GLUD1), and β-Actin. **(C)** Analysis of patient data from Mackay *et al.* (2017) where gene expression for *SLC2A3*, *HK2*, *PFKFB2*, and *GLUD1* was stratified into low and high

expression categories according to median expression across pediatric high-grade gliomas, independent of histone mutant status. The distribution of anatomical locations within the low and high subgroups was plotted as a percent for the respective subgroup and differences were analyzed. Data analyzed by two-tailed, Chi square test. **(D)** Expression of metabolic enzymes depicted in **(A)** were stratified into high (above median) and low (below median) subgroups and Log-rank analysis performed to determine differences in overall survival of pediatric high-grade glioma patients. Results for *HK2* and *PFKFB2* are illustrated. **(E)** Expression of metabolic enzymes *HK2*, *PFKFB2*, *GLUD1*, and *GLUD2* from **(A)** were stratified into high and low subgroups and the distribution of histone mutations (H3.1K27M, *purple*; H3.3K27M, *red*; H3WT, *blue*; H3.3G34R/V, *green*; unknown status, *orange*) within each subgroup was calculated. Note that H3.1/H3.3K27M mutant tumors are observed more frequently in within tumors with expression above the median for each gene shown.

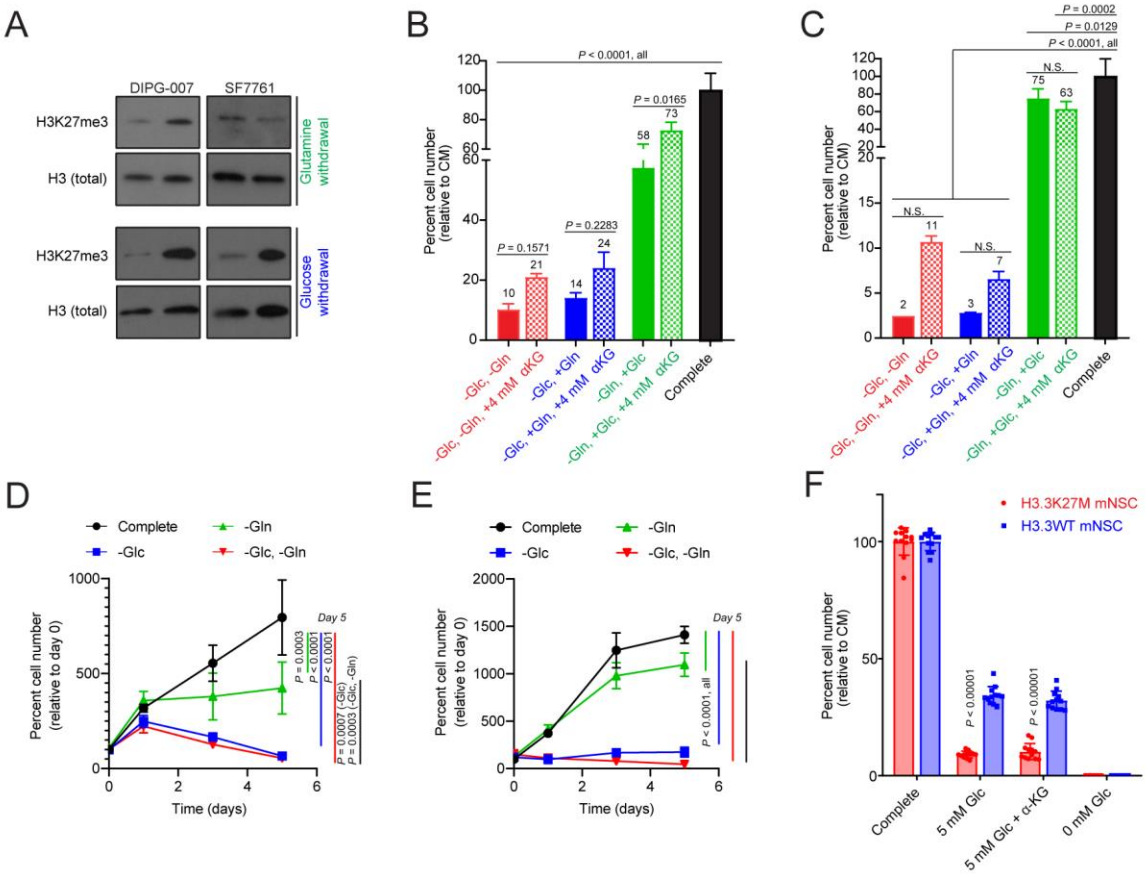

Figure 2.6. H3.3K27M cells heterogeneously utilize glucose and glutamine to regulate H3K27me3 *in vitro.*

(A) Representative immunoblots from H3.3K27M DIPG-007 and SF7761 cells for H3K27me3 and total H3 after glutamine (*top panel*) or glucose (*bottom panel*) deprivation. **(B-C)** Cell growth experiments using H3.3K27M DIPG-007 **(B)** or SF7761 **(C)** cells grown in complete media (*black*), or under glutamine (-Gln, *green*), glucose (-Glc, *blue*), or combined (*red*) deprivation in the presence (*corresponding checkered bars*) and absence (*solid bars*) of cell-permeable α-KG. Percent cell number (Y-axis) is reported after 96 hours in culture relative to complete media (CM)

condition above each bar. *n*=4 technical replicates per condition. **(D-E)** Cell growth experiments using H3.3K27M DIPG-007 **(D)** or SF7761 **(E)** cells grown in complete media (*black*) or under glucose (-Glc, *blue*), glutamine (-Gln, *green*), or combined (*red*) deprivation. Growth was monitored over five days and reported as percent cell number (Y-axis) relative to day 0 for each condition. *n*=6 technical replicates per condition per day. **(F)** Cell growth experiment of H3.3K27M (*red*) and H3.3WT (*blue*) mNSC cultured under partial (5 mM) or full (0 mM) glucose withdrawal in the presence or absence of 4 mM cell-permeable α-KG. Percent cell number (Y-axis) is reported after 96 hours in culture relative to complete media (CM) condition for independent cell lines. *n*=3 biological replicates, *n*=4 technical replicates each. Data plotted as mean ± S.D. Data in **(B)-(E)** analyzed by one-way ANOVA. Data in **(F)** analyzed by two-sided, unpaired Student's *t* test. Experiment in **(A)** performed by Chan Chung; experiments in **(B)-(F)** performed by Stefan Sweha.

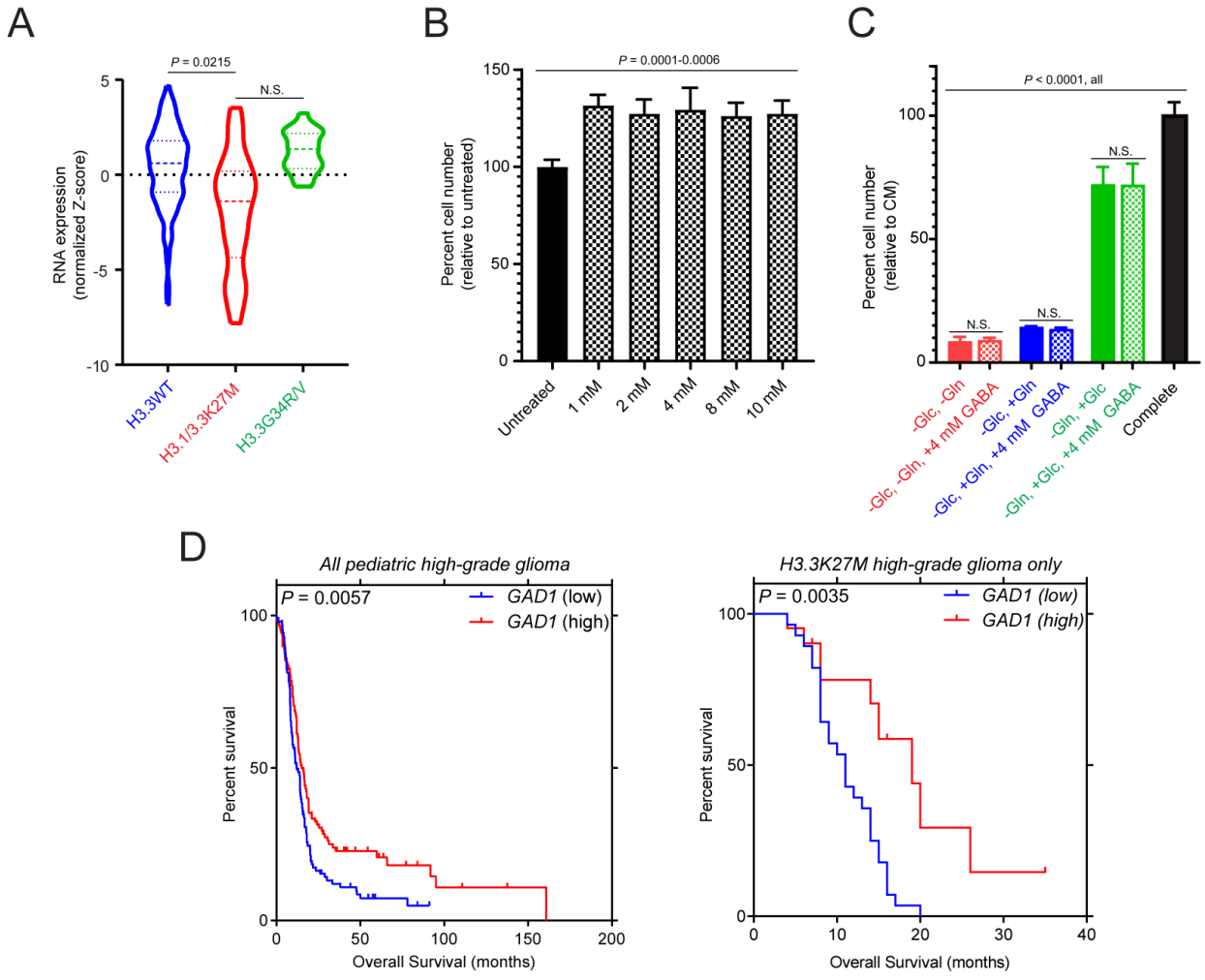

Figure 2.7. Probing the role of GABA in H3.3K27M cell growth and patient survival.
(A) Violin plot comparing Glutamate Decarboxylase 1 (*GAD1*) expression in H3.3WT, H3.1/3.3K27M, and H3.3G34R/V glioma patients from Mackay *et al.* (2017). **(B)** Cell growth experiment of H3.3K27M DIPG-007 cells growth in the presence of exogenous GABA at the indicated concentrations for 96 hours. Percent cell number (Y-axis) is reported relative to untreated

control. *n*=4 technical replicates per condition. **(C)** Cell growth experiment using DIPG-007 grown in complete media (*black*) or under glutamine (*green*), glucose (*blue*), or combined (*red*) deprivation in the presence (*corresponding checkered bars*) or absence of 4 mM GABA. Percent cell number (Y-axis) is reported after 96 hours in culture relative to complete media condition. *n*=4 technical replicates per condition. **(D)** Expression of GABA-metabolism enzyme *GAD1* was stratified into high (> median) and low (<median) subgroups and log-rank analysis performed to determine differences in overall survival for pediatric high-grade glioma patients or only with H3.3K27M patients. Data plotted as mean ± S.D. Data in **(B)** and **(C)** analyzed by one-way ANOVA.

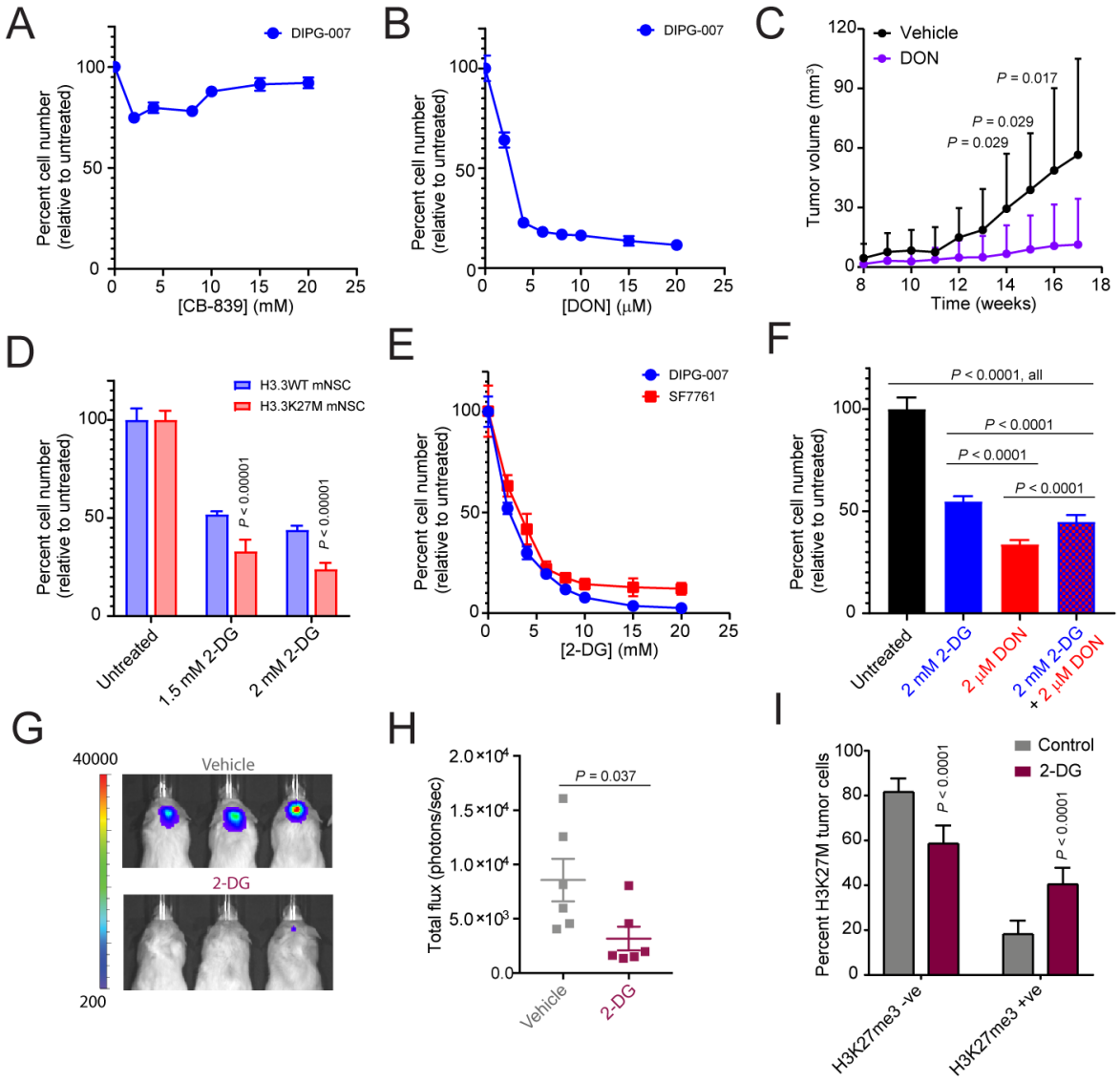

Figure 2.8. Inhibition of glutaminolysis and glycolysis pathways slows tumor cell growth *in vitro* and *in vivo*.

(A-B) Dose response curves for H3.3K27M DIPG-007 cells treated with glutamine antagonists CB-839 and DON. Percent cell number (Y-axis) is reported at 96 hours relative to untreated control. *n*=8 technical replicates per condition. **(C)** X-Y plot illustrating tumor volume (mm^3, Y-

axis) as a function of time for a xenograft DIPG model established with H3.3K27M mNSC in the mouse flank. Mice received 1 mg/kg DON every other day over six weeks and tumor volume was assessed weekly. *n*=10 tumors per condition. **(D)** Bar plot of cell growth experiment using H3.3WT (*blue*) and H3.3K27M (*red*) mNSC treated with hexokinase-2 inhibitor 2-DG. Percent cell number (Y-axis) is reported at 96 hours relative to respective untreated control for each cell type. *n*=4 biological replicates per condition. **(E)** Dose response curves for H3.3K27M DIPG-007 and SF7761 treated with 2-DG for 96 hours. Percent cell number (Y-axis) is reported at 96 hours relative to untreated control for each cell type. *n*=6 technical replicates per condition. **(F)** DIPG-007 cells treated with 2 mM 2-DG, 2 μM DON, or 2 mM 2-DG combined with 2 μM DON to assess potential synergism. Percent cell number (y axis) is reported at 72 hours relative to negative control (*black*). *n*=8 technical replicates per condition. **(G)** Representative scaled bioluminescence images from 2-DG and vehicle-treated mice bearing DIPG-007 pontine tumors. Mice received 500 mg/kg 2-DG every other day over three weeks. **(H)** Bioluminescence signal quantification reported as total flux (Y-axis, photons/sec) of 2-DG and vehicle-treated mice from **(G)**. *n*=6 mice per condition. **(I)** Quantification of H3K27me3 IHC in 2-DG and vehicle-treated cohorts from the DIPG-007 orthotopic tumor model in **(G)** and **(H)**. Data plotted as percent of H3K27M tumor cells that are H3K27me3 negative (*-ve*) and positive (*+ve*) for each treatment condition. *n*=5 control, *n*=5 2-DG-treated animals. Data plotted as mean ± S.D. Data in **(C)**, **(D)**, and **(H)** analyzed by two-sided, unpaired Student's *t* test. Data in **(F)** and **(I)** analyzed by one-way ANOVA. Experiments in **(A)**-**(F)** performed by Stefan Sweha; experiments in **(G)**-**(I)** jointly performed by Chan Chung and Stefan Sweha.

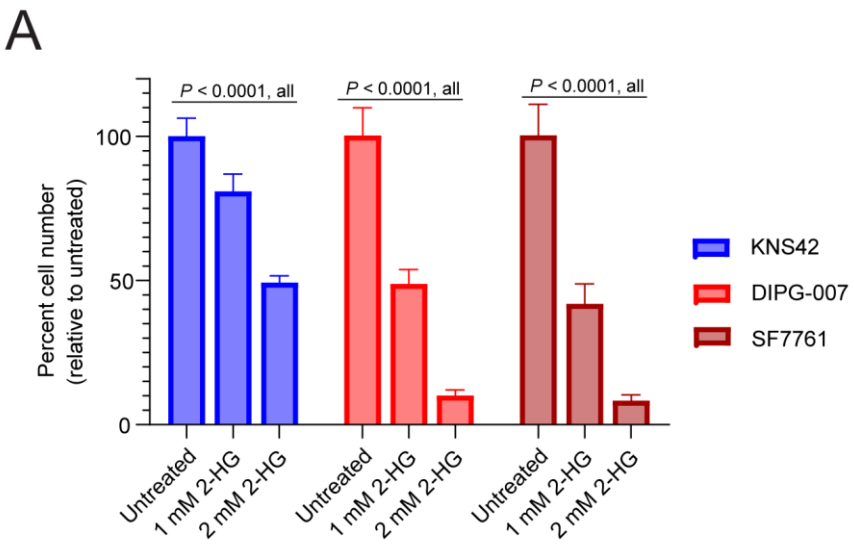

Figure 2.9. D-2HG exerts toxicity in H3.3K27M cells.
(A) Cell viability experiments using H3.3G34V KNS42, H3.3K27M DIPG-007, and H3.3K27M SF7761 cells treated with 1 mM or 2mM D-2HG for 96 hours. Percent cell number is reported relative to respective untreated control. *n*=6 technical replicates per condition. Data plotted as mean ± S.D. and analyzed by two-sided, unpaired Student's *t* test.

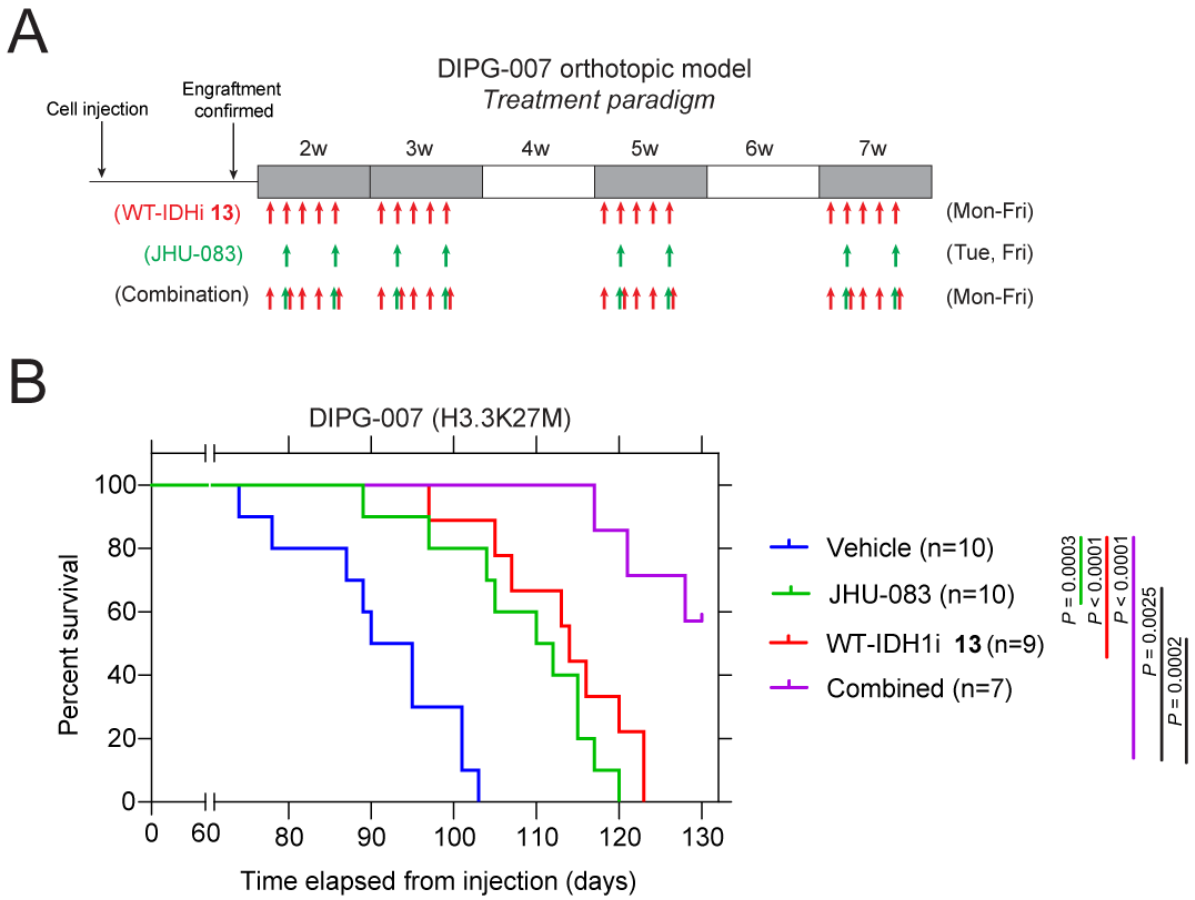

Figure 2.10. *In vivo* inhibition of Isocitrate Dehydrogenase 1 (IDH1) and Glutaminase (GLS) reduces tumor growth and increases survival of a pontine DIPG animal model.
(A) Treatment paradigm for an orthotopic DIPG model established with DIPG-007 cells. Mice received wild-type IDH1 inhibitor (WT-IDH1i compound **13**, *red arrows*), glutaminase inhibitor (JHU-083, *blue arrows*), or a combination regimen over a six-week period. No treatment occurred during weeks 4 and 6. **(B)** Kaplan-Meier analysis of mice harboring H3.3K27M DIPG-007 tumors receiving vehicle (*blue*, *n*=10), JHU-083 (*green*, *n*=10), WT-IDHi **13** (*red*, *n*=9), or combination therapy (*purple*, *n*=7). Percent survival is plotted as a function of time (days) post-injection. Log-rank test was utilized for Kaplan-Meier analysis (*P*-values are indicated for comparison with control animals). Experiments in **(B)** jointly performed by Chan Chung and Stefan Sweha.

Chapter 3

Epigenetically-Defined Therapeutic Targeting in H3G34R/V High-Grade Gliomas

3.1 Abstract

Histone H3.3G34R/V mutant high-grade gliomas carry a dismal prognosis as current treatments, including radio/chemotherapy, are not curative. Because H3.3G34R/V mutations reprogram epigenetic modifications, we undertook a systematic and comprehensive epigenetic approach to define therapeutic dependencies in H3.3G34R/V gliomas. Our analyses revealed a convergence of epigenetic alterations, including: **(a)** activating histone marks H3K36me3, H3K27ac and H3K4me3, **(b)** DNA promoter hypomethylation, and **(c)** redistribution of repressive H3K27me3 to intergenic regions at the Leukemia Inhibitory Factor (*LIF*) locus to drive increased LIF expression and secretion by H3.3G34R/V cells. LIF activated STAT3 signaling in an autocrine/paracrine manner to promote survival of H3.3G34R/V glioma cells. Moreover, immunohistochemistry and single cell RNA sequencing from H3.3G34R/V patient tumors showed high STAT3 expression in tumor cells with both inter- and intra-tumor heterogeneity. We targeted STAT3 using a blood-brain barrier penetrable, small molecule inhibitor, WP1066, currently in clinical trials for adult gliomas. WP1066 treatment resulted in significant toxicity *in vitro* and tumor suppression *in vivo* in H3.3G34R/V in multiple cell lines and preclinical animal models. For the first time, our study identifies the LIF/STAT3 pathway as a key epigenetically-driven and druggable vulnerability in H3.3G34R/V gliomas. This finding could inform

development of targeted, combination therapies designed to target activated oncogenic signaling in these lethal brain tumors.

This work has been published in *Science Translational Medicine* (featured on cover)***:***

Sweha SR, Chung C…Venneti S. Epigenetically defined therapeutic targeting in H3.3G34R/V high-grade gliomas. *Sci Transl Med*. 2021 Oct 13;13(615):eabf7860.
doi: 10.1126/scitranslmed.abf7860. PMID: 34644147.

3.2 Introduction

Brain tumors in children and adolescents are associated with poor outcomes (Kallappagoudar *et al*., 2015; Jones *et al*., 2017). Significant strides have been made in treating childhood cancers like leukemia while incremental progress has been made for pediatric high-grade gliomas (pHGGs) (Madhusoodhan *et al*., 2016; Whitehead *et al*., 2016). The survival rate for pHGG remains dismal with a 5-year patient survival of ~15% (Louis *et al*., 2021). Attempts to translate aggressive chemotherapeutic and radiotherapy regimens utilized for adult high-grade gliomas to younger patients have failed. This treatment void has sparked intense focus to understand the epigenetic and molecular characteristics of pHGG to enable effective treatment discovery.

Research on various pediatric cancers has demonstrated genetic alterations in chromatin remodeling or histone modifying enzymes (Baylin *et al*., 2016; Fontebasso *et al*., 2013). Somatic missense mutations in histone proteins have been identified in pediatric brain tumors, soft tissue sarcomas, and bone tumors (Behjati *et al*., 2013; Bender *et al*., 2013; Lu *et al*., 2016; Schwartzentruber *et al*., 2012; Sturm *et al*., 2012; Wu *et al*., 2012). Approximately 30-50% of high-grade gliomas bear mutations in *H3F3A,* the gene encoding non-canonical histone H3.3 (Sturm *et al*., 2012). These recurrent mutations involve the replacement of the lysine residue at amino acid 27 by methionine (H3.3K27M) or the glycine residue at amino acid 34 by arginine or

valine (H3.3G34R/V). These residues are in the N-terminal tail of H3.3 which undergoes post-translational modification to precisely control transcription. H3.3G34R/V mutations have been observed exclusively in *H3F3A* while H3K27M mutations occur frequently in *H3F3A* and to a lesser extent in *HIST1H3B/C* encoding H3.1. H3K27M tumors are found in midline brain structures and brainstem of young children, while H3G34R/V tumors are found in cortical structures of older adolescents and young adults (Sturm *et al*., 2012; Mackay *et al*., 2017). These temporal, anatomical, and age distinctions suggest that distinct molecular programs enable tumorigenesis in specific cellular contexts.

Histone H3 can undergo many types of post-translational modifications including acetylation, methylation, crotonylation, sumoylation, ubiquitination, and biotinylation. Methylation can be an activator or suppressor of transcription depending on the histone residue modified. For example, H3K27 trimethylation (H3K27me3) is a repressor of transcription, while H3K36me3, H3K27ac, and H3K4me3 are associated with gene activation. Previous studies have revealed striking consequences of H3K27M mutations. This mutant histone has been demonstrated to sequester and allosterically inhibit the methyltransferase activity of EZH2, a subunit of the larger Polycomb Repressive Complex 2 (PRC2), resulting in global H3K27me3 loss (Bender *et al*., 2013; Lewis *et al*., 2013). H3K27M mutant histone is also posited to inhibit the spreading of H3K27me3. Comparatively less is known regarding the molecular mechanisms engaged in H3.3G34R/V tumors. Although the glycine 34 residue cannot be directly modified, its mutation to an arginine or valine residue has been found to inhibit SETD2, a specific lysine 36 (H3K36) trimethyltransferase (Fang *et al*., 2018). Interestingly, SETD2 mutations have been observed in cortical pediatric gliomas, resulting in global H3K36me3 reduction (Fontebasso *et al.*, 2013). H3.3K36M mutations discovered in the second gene encoding H3.3, *H3F3B*, in chondroblastomas

and soft-tissue sarcomas cause similar H3K36me3 loss and corresponding H3K27me3 gain localized to intergenic regions to impair cellular differentiation (Lu *et al*., 2016). However, the dominant-negative effect of SETD2 and histone H3K36M mutations resulting in marked H3K36me3 reduction is not observed in H3G34R/V tumors, suggesting an alternate mechanism for modulating H3K36me3 is engaged. Indeed, studies in recent years on H3G34R/V brain and H3G34W giant cell bone tumors have reported both focal H3K36me3 gain and loss at distinct genomic regions (Bjerke *et al*., 2013; Khazaei *et al*., 2020; Jain *et al*., 2020; Voon *et al*., 2018). While it is now established that H3G34 mutations can reprogram genomic H3K36me3, it remains unknown if these epigenetic alterations create therapeutic vulnerabilities.

Studies on H3.3G34R/V/W mutations have revealed several interesting findings to date. One of the earliest studies profiling H3G34R/V and H3K27M tumors described a global DNA hypomethylation phenotype in H3G34 mutant tumors compared with H3WT and H32K7M tumors (Sturm *et al*., 2012). Perturbation of DNA methylation has been noted as a hallmark in cancers where hypo-methylation can result in genome instability while hypermethylation has been associated with tumor suppressor silencing. A study comparing H3G34R and H3G34W tumors revealed a similar DNA methylome signature, suggesting a tissue-independent effect of the mutation on DNA methylation (Sangatsuda *et al*., 2020). Other work has revealed that H3G34W mutations can decrease H3K36me3 levels, promoting H3K27me3 gain *in cis* (Jain *et al*., 2020). Here, experiments revealed that mutant H3.3G34W histones are deposited at enhancers, resulting in H3K27me3 elevation and silenced gene expression. Cells treated with EZH2 inhibitor Tazemetostat could reverse the gene silencing, and correspondingly H3.3G34W-K27R (abrogating H3K27me3 gain) double mutant cells exhibited reduced growth *in vivo* (Jain *et al*., 2020). Related studies confirmed the ability of H3G34R/V mutated nucleosomes and peptides to

inhibit the catalytic activity of SETD2 and KDM4/B/C which methylate and demethylate the H3K36 residue, respectively (Fang *et al*., 2018; Voon *et al*., 2018). In addition, the mutant H3G34R histone has been found to specifically bind RACK7, a H3K4me1 and H3K14ac reader and transcriptional repressor (Jiao *et al*., 2020).

Gene expression profiling of H3.3G34R/V gliomas has revealed activating *PDGFRA* mutations (or amplification) as well as loss of chromatin remodelers ATRX and DAXX, but relatively low mutational burden compared with other tumors (Chen *et al*., 2020; Mackay *et al*., 2017; Sturm *et al*., 2012). Intriguingly, ablation of the H3G34W mutation by CRISPR-mediated correction slows the growth of bone tumor cells *in vitro* and *in vivo* similar experiments in H3G34R/V mutant cells have failed to elicit a growth defect and still form viable tumors *in vivo* suggesting the mutation is dispensable (Chen *et al*., 2020; Khazaei *et al*., 2020). Furthermore, several studies have suggested that the mutant histones in either tumor type are deposited into actively transcribed regions and promoters (Bressan *et al*., 2021; Jain *et al*., 2020). ChIP sequencing of a H3.3G34R tumor cell line in a recent study revealed that mutant histone deposition positively correlated with increased activating marks (H3K4me3 and H3K36me3) and mRNA expression level, but presence of the H3.3G34R mutation did not significantly alter the H3.3WT distribution across the genome (Bressan *et al*., 2021).

The studies probing the cell-of-origin, co-occurring mutations and mechanisms for epigenetic deregulation in G34R/V and G34W tumors are informative. However, gaps remain in our knowledge about therapeutic vulnerabilities created by epigenetic changes in these tumors, especially in G34 mutant glioma. We hypothesized that epigenetic alteration in H3K6me3 or other histone modifications could identify potential therapeutic targets in these tumors. Here, we investigate if and how H3G34R/V mutations cause aberrant signaling mechanisms that are known

to drive cancer growth and resistance. We undertake an unbiased transcriptomic and epigenomic approach to discover how epigenetic changes correlate with changes in expression of critical signaling cascades.

We demonstrate that H3G34 mutations epigenetically activate LIF/STAT3 signaling which presents an epigenetically-genetically driven therapeutic opportunity. The Janus kinase (JAK)-signal transducer and activator of transcription (STAT) pathway is a well-studied pleiotropic signaling cascade implicated in tumorigenesis, cell proliferative properties, and chemoresistance (Bromberg *et al*., 1999; Johnston *et al.,* 2011). Homodimeric or heterodimeric membrane bound cytokine or growth factor receptors (composed of IL6R, gp130, LIFR, EGFR, PDGFR, VEGFR, etc) can activate the pathway upon ligand binding. Several classes of interleukins and interferons can bind the receptors (Heinrich *et al.,* 1998; Teng *et al.,* 2014). In this chapter, we will focus on the IL-6 family ligands such as IL-6, IL-11, Oncostatin M (OSM), and Leukemia Inhibitory Factor (LIF). Upon binding, tyrosine kinase proteins like the Janus kinases (JAKs) or proto-oncogene tyrosine-protein kinases (Src) are recruited to the receptors (Sen *et al.,* 2009; Silva *et al.,* 2004). JAKs undergo auto-phosphorylation or cross phosphorylate other JAKs, and these activated JAKs phosphorylate the receptor at specific tyrosine residues. This phosphorylation event creates a site for the STAT protein SH2 domain to dock with the receptor. STAT proteins can undergo phosphorylation at the tyrosine 705 residue, allowing for subsequent dimerization via their phosphotyrosine-SH2 linkage (Rane *et al.,* 2000). Activated STATs can translocate to the nucleus to exert transcriptional activity.

STAT3 and STAT5 have been the most well studied for their role in cancer. Persistent activation of these STAT proteins has been demonstrated to directly drive invasion, metastasis, angiogenesis (Teng *et al.,* 2014). In addition, STAT activity plays an important role for immune-

modulatory processes both within tumor cells and immune cells (Hillmer *et al.,* 2016; Lee *et al.,* 2011). Here, we establish several preclinical orthotopic H3.3G34R/V models to test the efficacy of JAK2/STAT3 inhibitor, WP1066, in reducing tumor growth. Our findings highlight the relationship between H3.3G34R/V mutant histones and aberrant STAT3 signaling, a clinically actionable target with clinically approved inhibitors already in use.

3.3 Results

3.3.1 H3.3G34R/V cells exhibit transcriptomic and epigenetic alterations converging on the LIF/JAK/STAT3 axis

We utilized an integrated epigenomic and transcriptomic approach to understand pathways specifically upregulated by the H3.3G34R mutation. We established isogenic cell lines by expressing HA-tagged H3.3G34R or H3.3WT in immortalized mouse neuronal stem cells (mNSCs). We used previously characterized H3.3K27M expressed in the same mNSC background (Chung *et al*., 2020; Johnson *et al*., 2010). Pediatric high-grade gliomas harboring H3.3G34R/V or H3.1/H3.3K27M mutations often occur with other mutations in cancer-associated genes such as *TP53, PDGFRA, EGFR,* and *ATRX/DAXX* (Bender *et al*., 2013; Chen *et al*., 2020; Mackay *et al*., 2017; Paugh *et al*., 2011, 2013; Sturm *et al.,* 2012). Additionally, these tumors exhibit heterogeneity with respect to chromosomal aberrations and specific gene amplification. Since these genes can often independently or collectively alter cellular signaling and metabolism, this presents a difficulty in isolating specific effects of the mutant histone. Single cell-sequencing studies on H3G34R/V tumors have revealed stem-like interneuron progenitors as potential cells of origin (Chen *et al*., 2020). Furthermore, recent studies have utilized forebrain neuronal stem cells or progenitor cells to model H3G34R/V tumors (Bressan *et al*., 2021; Funato *et al*., 2014). Thus,

the *in vitro* isogenic model we developed using cortical neuronal stem cells avoids potential confounding factors from co-occurring mutations and closely models H3.3G34R/V tumor cell origin. We confirmed expression of mutant transgenes in our mNSC model by Western blotting for HA (**Figure 3.1A**). As demonstrated by others, immunoblotting did not exhibit global changes in H3K36me3, H3K4me3, H3K27ac or H3K27me3 between H3.3G34R and H3.3WT or H3.3K27M mNSCs (**Figure 3.1B**) (Lewis *et al*., 2013). As controls, H3.3K27M mNSCs showed a global decrease in H3K27me3 accompanied by an increase in H3K27ac levels (**Figure 3.1B**). In parallel, we assessed H3K36me3, H3K4me3, H3K27me3, H3K27ac, mutant H3.3K27M, and mutant H3.3G34V in H3.3G34R OPGB-GBM-001, H3.3G34V KNS42, H3.3WT SF188, and H3.3K27M DIPG-007 cells (**Figure 3.1C**). We noted no major global changes in H3K36me3 or H3K4me3 in H3.3G34R/V. Both H3.3G34R/V cell lines showed elevated H3K27me3 relative to H3.3WT SF188 while H3.3K27M cells showed marked loss of this epigenetic mark and coincident gain of H3K27ac. Next, we profiled differences in cell proliferation using the isogenic mNSC model. While H3.3K27M increased proliferation, no major differences in proliferation were noted between H3.3G34R and H3.3WT mNSC (**Figure 3.1D**). We performed RNA sequencing in these cells and determined genes specifically altered in H3.3G34R *versus* control H3.3WT and H3.3K27M mNSC, which showed both upregulated (2715) and downregulated (3039) genes (**Figure 3.1E-F**). Some of the top pathways revealed by gene set enrichment analysis (GSEA) of the 2715 upregulated genes in H3.3G34R mNSCs were related to the JAK/STAT pathway, chemokine, and cytokine signaling (**Figure 3.1G**).

We performed comprehensive analyses of epigenetic modifications in H3.3G34R relative to H3.3WT mNSC. H3.3G34R/V mutations are known to reduce local H3K36me3 levels at various genes. However, some genes show a gain of H3K36me3 (Bjerke *et al*., 2013; Voon *et al*.,

2018). Therefore, we performed H3K36me3 chromatin immunoprecipitation followed by deep sequencing (ChIP-seq) in our isogenic cells (**Figure 3.2A**). Because H3K36me3 in gene bodies is associated with active transcription, we focused our efforts on the subset of genes with H3K36me3 enrichment in H3.3G34R *versus* H3.3WT mNSC and compared these data with gene expression in H3.3G34R/H3.3WT mNSC (**Figure 3.2B**). Genes upregulated in H3.3G34R mNSCs exhibited enriched H3K36me3 at gene bodies and H3K27ac/H3K4me3 at promoters relative to H3.3WT (**Figure 3.2C**). These analyses revealed *Lif* as the top upregulated gene associated with increased H3K36me3 enrichment in H3.3G34R compared to H3.3WT mNSC (**Figure 3.2D**). Our finding that the *Lif* locus shows increased H3K36me3 in H3.3G34R mNSC was validated in additional isogenic H3.3G34R/H3.3WT and H3.3G34W/H3.3WT mouse models developed by Voon *et al*. (2018) and Jain *et al.* (2020), respectively (**Figure 3.2E-F**). Additionally, we interrogated H3K36me3 ChIP-seq and RNA-seq data from a study on H3G34W mutations in giant cell tumors of the bone by Khazaei *et al.* (2020). Similar to H3.3G34R mNSCs, Im-GCT-4072 patient-derived cells with H3G34W mutations showed enrichment of H3K36me3 at *LIF* (**Figure 3.2G**). Knockout or correction of mutant H3.3G34W to H3.3WT lowered H3K36me3 enrichment at the *LIF* locus. Importantly, this was associated with decreased *LIF* mRNA compared to controls (**Figure 3.2G**).

H3K36me3 deposition within gene bodies plays an important role in gene activation and has been reported to cause subsequent changes in transcription-activating H3K27ac and H3K4me3 marks (Kizer *et al*., 2005; Morris *et al*., 2005; Venkatesh *et al*., 2012; Xu *et al*., 2011). ChIP-seq analysis for H3K27ac and H3K4me3 demonstrated overall increased enrichment of these activating marks at promoters in H3.3G34R mNSCs compared to H3.3WT mNSCs (**Figure 3.2H**). Moreover, H3.3G34R mNSCs demonstrated increased H3K27ac and H3K4me3 enrichment at the *Lif* promoter relative to H3.3WT and H3.3K27M mNSCs (**Figure 3.2I**). GSEA analysis for genes

exhibiting promoter H3K27ac elevation revealed pathways associated with cellular responses to Lif (**Figure 3.2J**). Similar analysis of H3K27ac enriched loci in H3.3WT mNSCs did not reveal pathways associated with Lif signaling (**Figure 3.2J**). Interestingly, comparison of H3K27ac ChIP-seq signals from Wang *et al.* (2021) in KNS42 cells with various H3K27M pediatric glioma cells and normal human astrocytes revealed marked enrichment this mark at *LIF* in KNS42 cells (**Figure 3.3A)**. Additional analysis of promoter-localized H3K27ac at canonical STAT3 target genes demonstrated robust H3K27ac occupancy in KNS42 cells compared with H3.3K27M DIPG-007, H3.3K27M DIPG-XIII, and H3.3WT NHA cells, confirming the presence of a STAT3 activation signature in H3G34 mutant cells (**Figure 3.3B**). Conversely, H3.3K27M cells showed H3K27me3 retention at these promoters relative to KNS42 (**Figure 3.3B**). Despite the widespread loss of H3K27me3 and global gain in H3K27ac in H.3K27M cells, this finding suggests that H3K27ac enrichment in H3.3K27M is targeted to specific regions and may not upregulate each signaling pathway in a similar fashion. Moreover, differential changes in H3K36me3, H3K27ac, and H3K4me3 levels were not observed between mNSCs at other JAK/STAT loci including *Stat3* (**Figure 3.4A**). Similarly, no enrichment of H3K36me3 was observed at *Stat3* in other isogenic H3.3G34R/W mouse cells (**Figure 3.4B-C**).

Based on findings from previous work on H3.3K27M cell models described in Chapter 2, we profiled H3K36me3, H3K27ac, and H3K4me3 in H3.3G34R mNSC at genes related to glycolysis and glutaminolysis to determine if activation of metabolic pathways occurs in H3.3G34R cells which would present a similar therapeutic vulnerability. Analysis revealed that robust changes that occur at these loci in H3K27M mNSC did not occur in H3.3G34R mNSC when compared with H3.3WT mNSC (data not shown). Furthermore, we profiled H3.3G34R, H3.3WT, and H3.3K27M mNSC for phospho-S6 Ribosomal Protein (pS6-RP) and total S6RP,

downstream targets of AKT/mTOR signaling pathways to determine if H3.3G34R cells exhibit cellular signaling associated with increased metabolism (**Figure 3.5A**). We also conducted a similar experiment on H3.3G34R/V (OPGB-GBM-001, KNS42), H3.3WT (SF188, UMPed37), and H3.3K27M (DIPG-007) human cell lines (**Figure 3.5B**). Although heterogeneity existed in the human cells, results from both the mNSC and human models suggested that phospho-S6RP was not enhanced by presence of H3.3G34R or H3.3G34V mutant histone.

Next, we assessed H3K36me3, H3K27ac, mutant H3.3G34R, mutant H3.3G34V and total H3 at *LIF* in H3.3G34V (KNS42) and H3.3G34R (CHOP-GBM-001 and HSJD-GBM-002) patient-derived cell lines. These results mirrored findings from H3.3G34R mNSC and showed enrichment of both H3K36me3 and H3K27ac at the *LIF* locus (**Figure 3.6A**). We noted heterogeneity in the amount of H3G34R/V histone present at *LIF* in these patient-derived cell lines. KNS42 and CHOP-GBM-001 cells exhibited higher levels of H3.3G34R/V incorporation compared to HSJD-GBM-002 at the *LIF* locus. Interestingly, the level of H3G34R/V histone, but not total H3.3, incorporation paralleled the degree of H3K36me3 deposition in the *LIF* gene body (**Figure 3.6A**).

Because H3.3G34R/V and H3.3K27M mutations occur in *H3F3A,* we used *H3F3A* mRNA expression as a surrogate for mutant H3.3G34R/V or H3.3K27M expression and assessed its relation to *LIF* expression in patient-derived tumor samples deposited in PedCBioportal by Mackay *et al.* (2017). Each type of pediatric glioma was segregated by histone status and patient samples were sorted by *H3F3A* expression. *H3F3A*-high and *H3F3A*-low sample categories were defined as tumors with *H3F3A* expression above or below the median expression value, respectively, within a cohort. *LIF* levels were compared between *H3F3A*-high and *H3F3A*-low subclasses, and Pearson correlation analysis was performed to determine relationships with *H3F3A*

expression. We noted positive correlation between *H3F3A* and *LIF* expression in H3.3G34R/V (*n*=19), but not H3.3K27M (*n*=71) tumors (**Figure 3.7A**). The opposite pattern was observed in H3WT (*n*=101) tumors (**Figure 3.7A**). Additionally, we analyzed *H3F3A* and *H3F3B* correlations with other IL-6 family cytokines and did not note similar trends in any tumor subtype (**Figure 3.7B-C**).

Additionally, we sought to characterize modes of gene regulation by defining chromatin states and their distribution throughout the genome in our isogenic mNSCs. We utilized ChromHMM software (Ernst *et al.*, 2012; Ernst *et al.*, 2017) to locate where combinations of epigenetic modifications including H3K36me3, H3K4me3, H3K27me3, H3K27ac, H3K4me1 and H3K36me2 are differentially enriched in H3.3G34R relative to H3.3WT and H3.3K27M mNSCs (**Figure 3.8A**). States 6 and 7 were only present in the gene body of *Lif* in H3.3G34R compared to H3.3WT and H3.3K27M mNSCs (**Figure 3.8B**). Additionally, state 1 representing activated transcription was enriched at *Lif* in H3.3G34R cells relative to H3.3WT and H3.3K27M mNSCs. State 10 associated with gene repression was only present at *Lif* in H3.3WT cells (**Figure 3.8B**). Epigenetic state analysis also revealed enrichment of states 6 and 7 (representing H3K36me3 deposition) in H3.3G34R mNSC, but not in H3.3WT, at genes related to Jak/Stat signaling and cell cycle regulation (**Figure 3.8C-D**). Together, these data from epigenetic/transcriptomic analysis in isogenic mNSC, confirmed in human patient-derived cell lines and tumor samples, suggest that H3G34R/V mutations epigenetically upregulate LIF.

3.3.2 H3.3G34R/V alters DNA methylation and H3K27me3 at the LIF locus

We evaluated differences in DNA methylation using enhanced reduced representation bisulfite sequencing (ERRBS) in our isogenic mNSC. Differentially methylated regions were assessed between H3.3G34R *versus* H3.3WT and H3.3K27M *versus* H3.3WT cells. We noted a

greater proportion of differentially methylated regions (DMRs) in H3.3G34R/H3.3WT compared to H3.3K27M/H3.3WT mNSCs (**Figure 3.9A**). These findings recapitulate central findings from patient glioma samples studied by Sturm *et al.* (2012) and Sangatsuda *et al.* (2020) who reported robust changes occur in DNA methylation in H3.3G34R/V *versus* H3 wild-type tumors, but to a lesser extent in H3.3K27M tumors. H3.3G34R/H3.3WT mNSC showed greater degrees of hypo- and hyper-methylation of CpG-containing promoter regions compared to H3.3K27M/H3.3WT cells (**Figure 3.9B**). We identified many promoters that were hypo- or hyper-methylated in H3.3G34R/H3.3WT but not in H3.3K27M/H3.3WT mNSC (**Figure 3.9C**). Because hypomethylated promoters are associated with increased gene expression, we compared differential promoter methylation with our RNA-seq data. Genes with hypomethylated promoters were associated with an overall increase in gene expression in H3.3G34R/H3.3WT mNSC (**Figure 3.9D**). While this pattern was similar in H3.3K27M/H3.3WT cells, the degree of difference in gene expression was greater in H3.3G34R/H3.3WT compared to H3.3K27M/H3.3WT mNSC (**Figure 3.9E**). Comparison of hypomethylated promoters with gene expression in H3.3G34R/H3.3WT mNSC revealed *Lif* as one of the top genes associated with both promoter hypomethylation and increased gene expression (**Figure 3.9F**).

We also assessed the relationship between DNA methylation and genomic distribution of histone marks in H3.3G34R *versus* H3.3WT mNSC. Genes with hypomethylated promoters, including *Lif*, exhibited enrichment of activation marks including H3K36me3 at gene bodies and H3K27ac and H3K4me3 at promoters (**Figure 3.10A-C**). In contrast, H3K27me3 was lowered at active promoters and increased in the flanking intergenic regions (**Figure 3.10D**). The top genes that showed promoter hypomethylation, enrichment of H3K36me3, H3K27ac and H3K4me3, and increased flanking H3K27me3 included *Lif* and key development and oncogenic factors such as

Emx2, *Igfbp2*, *Mycn*, *Foxa1*, and *Hoxa1* (**Figure 3.11A**). Our finding of H3K36me3 gain and promoter hypomethylation at *Mycn* mirrors results of Bjerke *et al.* (2013) who reported H3K36me3 gain at *MYCN* in H3.3G34V KNS42 cells, suggesting perturbation of promoter methylation by H3.3G34R/V promotes gene activation (**Figure 3.11A**). Moreover, loci with promoter DNA hypermethylation, such as *Lpl*, *Dedd2*, and *Mical1* exhibited opposite trends where lower H3K36me3 deposition in the gene body was associated with lowered H3K27ac and H3K4me3 at promoters relative to H3.3WT mNSC (**Figure 3.12A**), suggesting these histone marks cooperate with DNA methylation to control transcription. Comparison of H3.3K27M and H3.3WT mNSC did not show similar DNA methylation-associated patterns in H3K36me3, H3K27ac, or H3K4me3 (**Figure 3.13A-C**). Both hypo- and hyper-methylated promoters in H3.3K27M/H3.3WT mNSC showed lower H3K27ac and higher H3K4me3 and H3K36me3. We extended these findings to human tumors where four out of five CpGi in the *LIF* promoter were hypomethylated in H3.3G34R (*n*=73) compared to H3.3WT (*n*=1306) glioma samples (**Figure 3.14A-B**). We expanded the analysis to compare H3.3G34R with each individual H3.3WT glioma subtype and noted similar trends in percent promoter hypomethylation (**Figure 3.14C**). Comparison of raw beta-values for *LIF* promoter CpG sites revealed a similar hypomethylation trend in H3.3G34R glioma patients (**Figure 3.14D**). Overall, these data suggest H3.3G34R drives increased *Lif* gene expression via epigenetically reprogramming at *Lif* including promoter hypomethylation; enrichment of histone activation marks H3K36me3, H3K27ac and H3K4me3; and reduction of repressive H3K27me3.

3.3.3 H3.3G34R/V mutations drive STAT3 signaling

Having established H3.3G34R/V mutations are associated with activating epigenetic modifications at the *Lif* locus, we investigated whether Lif-driven downstream signaling pathways

were upregulated. We noted *Lif*, *Jak2*, *Stat3* and downstream transcriptional target *Pim1* were significantly upregulated in H3.3G34R compared to H3.3K27M and H3.3WT mNSC (**Figure 3.15A**). *Stat5b* was lower in H3.3WT and significantly downregulated in H3.3K27M mNSC (**Figure 3.15A**). We validated these findings in an independent, *in utero* electroporation (IUE)-based mouse tumor model (Patel *et al*., 2020). In this system, plasmids encoding PBase, luciferase, dominant-negative *TP53*, constitutively active mutant PDGFRA-*D842V*, and wild-type (WT) or G34R *H3F3A* were injected into the lateral ventricle of embryonic day 13.5 (E13.5) CD-1 mice to induce H3.3WT or H3.3G34R gliomas. Cultures were established from cells derived from each tumor model. These cell lines termed PPG [mutant TP53, mutant platelet-derived growth factor receptor A (PDGFRA), and mutant G34R H3.3] and PPW [mutant TP53, mutant PDGFRA, and WT H3.3] were subjected to RNA-seq. Similar to the mNSC model, analysis of upregulated genes in PPG relative to PPW cells revealed GO and KEGG pathways related to cytokine responses/interactions and Jak/Stat signaling (**Figure 3.15B-D**). We assessed *LIF* mRNA expression in patient-derived, low passage cell lines, which showed higher levels in H3.3G34V (KNS42) *versus* H3.3WT (TS543 and SJ-HGGx39-c) (**Figure 3.16A-B**) and H3.3G34R (SJ-HGGx6-c and SJ-HGGx42-c) *versus* H3.3WT (SJ-HGGx39-c) cells (**Figure 3.16C**).

Because LIF activates STAT3 via phosphorylation, we performed immunoblotting to compare total and phosphorylated Stat3 (pStat3). We found an increase in pStat3 levels in H3.3G34R compared to both H3.3WT and H3.3K27M mNSC (**Figure 3.17A**). In patient cell lines, pSTAT3 and STAT3 levels were higher in H3.3G34V (KNS42) and H3.3G34R (OPGB-GBM-001 and SJ-HGGx42-c) compared to H3.3WT (SF188, UMPed37, and SJGBM2) and H3.3K27M (HSJD-DIPG-007) cells (**Figure 3.17B-C**). H3.3G34R/V mutant cells also showed higher JAK2 levels compared to H3.3WT and H3.3K27M cells (**Figure 3.17B**). We found no upregulation of

the AKT pathway, an activator of STAT3, in KNS42 compared to SF188 cells (**Figure 3.17D**). We confirmed results from the isogenic mNSC model in **Figure 3.17A** and human cell lines in **Figure 3.17B** by establishing additional paired models of H3.3G34R and H3.3WT using SJGBM2, HEK293T, and immortalized human neural stem cells (hNSC). We observed elevated pSTAT3 levels in these cells expressing the H3.3G34R transgene independent of the cell type utilized to establish the model (**Figure 3.18A-C**).

3.3.4 EZH2 expression is regulated by STAT3 activity but targeting EZH2 expression cannot modulate histone modifications or cell growth in H3.3G34 mutant cells

Earlier work by Lu and colleagues (2016) on epigenetic mechanisms in mutant H3K36M sarcomas had revealed that H3K36M histone causes H3K36me3 loss in a dominant-negative manner via inhibition of the H3K36 trimethyltransferase SETD2. They also noted that H3K27me3 elevation in intergenic regions flanking the genomic regions with prominent H3K36me3 loss. H3.3G34R/V mutant histones were also found to inhibit SETD2 by binding to its catalytic site (Fang *et al*., 2018). Based on these findings, we wondered whether the H3K27me3 elevation we observed in our human cell lines was functionally linked STAT3 activity. Interestingly, EZH2 expression has been found to positively correlate with STAT3 tyrosine 705 phosphorylation in GBM and renal cell carcinoma cell lines. This binding interaction between EZH2 and STAT3 interaction only occurred in cell with stem-like properties (Deng *et al*., 2010; Kim *et al*., 2013; Zhang *et al*., 2018). Work revealed that EZH2 could methylate STAT3 on specific lysine residues which is a critical step for its subsequent phosphorylation and activity (Kim *et al*., 2013). Surprisingly, other studies in gastric cancer discovered the presence of STAT3 binding sites in the EZH2 promoter and demonstrated that patients with elevated STAT3 and EZH2 had worse post-surgery survival than similarly aged patients with either STAT3 or EZH2 elevated (Deng *et al*.,

2010; Pan *et al*., 2016). We hypothesized that EZH2 could be upregulated in H3.3G34R/V cells and that STAT3 could be enhancing its expression. First, we performed immunoblots for Ezh2 in the isogenic mNSCs and noted Ezh2 upregulation specifically in the H3.3G34R construct (**Figure 3.19A**). Furthermore, we probed EZH2 levels in a panel of human cell lines and observed that EZH2 expression failed to correlate with STAT3 expression (**Figure 3.19B**). We confirmed that STAT3 inhibition could attenuate EZH2 expression in KNS42 cells in a dose-dependent manner (**Figure 3.19C**). Prior work on H3.3K27M tumors using orthotopic models surprisingly demonstrated that targeting EZH2 to further lower H3K27me3 in these tumors could prolong survival. These studies demonstrated that H3.3K27M cells actively suppress the *Cdkn2a* locus via increased H3K27me3 retention across its promoter and gene body (Mohammad *et al*., 2017). EZH2 inhibition of these models *in vitro* and *in vivo* revealed that targeting EZH2 could derepress the *Cdkn2a* locus and increase p16 expression, resulting in attenuated cell growth rate. The specific elevation of Ezh2 in the isogenic model and enhanced H3K27me3 in intergenic regions suggested that it might also present a therapeutic vulnerability in the context of H3.3G34R/V gliomas (Mohammad *et al*., 2017). To further probe the role of H3K27me3 and EZH2 in H3.3G34R/V cell survival, we assessed if STAT3 inhibition could modulate H3K27me3 or other epigenetic modifications in these cells. We treated KNS42 cells with Stattic, a small molecule inhibitor of STAT3 that blocks its phosphorylation, performed histone extractions and immunoblotting for H3K27ac, H3K36me3, H3K4me3, H3K9me3, and H3K27me3 (**Figure 3.19D**). Despite abrogation of EZH2 expression after treatment, we did not observe global changes in H3K27me3. However, we noted decreases in H3K27ac upon Stattic treatment. Next, we assessed whether direct EZH2 inhibition could influence cell viability (**Figure 3.19E**). We treated cells with EZH2 inhibitor GSK-343 for four days and failed to observe cell death except at high concentration (20

μM). We also performed immunoblotting for H3K27me3, H3K27ac, and H3K36me3 on KNS42 cells treated with GSK-343 for 48 hours (**Figure 3.19F**). As expected, we observed decreased H3K27me3 in treated cells. Unexpectedly, we saw a decrease in global H3K27ac and H3K36me3, which suggested widespread transcriptional deregulation could be occurring (**Figure 3.19F**). We wondered if LIF expression was perturbed by GSK-343 and immunoblotting revealed no change in LIF expression after treatment (**Figure 3.19F**). This suggested that, despite hypothesized STAT3-EZH2 reciprocal interactions, targeting EZH2 cannot elicit decreases in cell proliferation observed in H3.3K27M cells. Our ChIP-seq data and results from the KNS42 model treated with EZH2 inhibitor suggest that the H3.3G34R/V mutant histone might not drive growth through a similar mechanism where H3K27me3 is elevated to suppress gene expression.

3.3.5 H3.3G34R/V mutations drive STAT3 signaling via elevated LIF secretion

Based on ChIP-seq data for *LIF* and immunoblots of mouse and human cell glioma models, we hypothesized that STAT3 activation observed in H3.3G34R/V cells was driven by LIF secretion in an autocrine/paracrine manner. To probe this mechanism, we performed ELISA experiments on cell media supernatants collected from glioma cells after 96 hours in culture. KNS42 cells also showed increased secretion of LIF into cell culture media compared to H3.3WT (SF188 and UMPed37) cells (**Figure 3.20A**). In parallel, we assessed LIF levels by immunoblotting in additional H3.3G34R (OPGB-GBM-001 and SJ-HGGx42-c) and H3.3WT (SF188, UMPed37, and SJGBM2) cells (**Figure 3.20B**). We noted variation in LIF expression level in H3.3G34R cell lines with lower and higher expression in OPGB-GBM-001 and SJ-HGGx42-c, respectively, suggesting that LIF expression and STAT3 pathway activation may be heterogeneous across H3.3G34R cell lines and patient tissues, similar to ChIP-seq data presented

in **Figure 3.6A**. This result suggested that some cells with STAT3 activation may co-opt LIF-independent, orthogonal mechanisms to drive cell growth.

Elevated LIF expression has been associated with STAT3 activation and worse prognostic outcome in malignancy (Liu *et al*., 2013; Liu *et al*., 2015; McLean *et al*., 2019). We hypothesized that LIF could regulate STAT3 phosphorylation in H3G34 mutant cells. We targeted *LIF* in KNS42 cells with three independent shRNAs, which decreased intracellular (by Western blot, **Figure 3.21A**) and extracellular, supernatant LIF levels (by ELISA, **Figure 3.21B**). Western blotting in these cells revealed decreases in pSTAT3 and total STAT3 on LIF knockdown (**Figure 3.21C**). H3.3G34V KNS42 cells with LIF knockdown exhibited a larger fraction of dead compared to parental cells (**Figure 3.21D**). Cell death was abrogated upon addition of recombinant LIF to the culture media (**Figure 3.21D**). Next, we determined if the effects observed with LIF knockdown could be recapitulated by perturbing mutant *H3F3A* expression. We first targeted *H3F3A* in H3.3G34V KNS42 cells with two independent shRNAs. Both shRNA-expressing cells showed lower levels of H3.3G34V mutant protein (**Figure 3.22A**). H3.3 knockdown did not perturb global H3K36me3, H3K4me3, or H3K27me3 levels (**Figure 3.22B**). shRNA-mediated knockdown of H3.3G34V decreased both intracellular (by Western blot, **Figure 3.22C**) and secreted (by ELISA, **Figure 3.22D**) LIF in KNS42 cells. Similarly, we found shRNA-mediated knockdown of *H3F3A* in H3.3G34R SJ-HGGx42-c cells had a similar effect of decreasing intracellular LIF levels (**Figure 3.22E**). Importantly, KNS42 cells with lowered levels of mutant H3.3G34V protein showed reduced pSTAT3 and total STAT3 (**Figure 3.22F**), and increased cell death (**Figure 3.22G**) compared to controls. This finding was recapitulated in RNA-seq data from parental and *H3F3A*-knockdown KNS42 cells where we observed specific reduction of *H3F3A* relative to *H3F3B* and the downregulated transcription of canonical STAT3 targets, including

SOCS1, SOCS2, and *SOCS3*. *STAT5A* and *STAT5B*, previously shown to be regulated by STAT3, showed downward trends upon *H3F3A* that approached significance (**Figure 3.23A**). Transcriptomic data from our mouse isogenic cell system demonstrated that H3.3G34R cells engage cytokine signaling pathways. This finding has potential important implications for promoting tumor immunity *in vivo.* A recent study on H3.3G34R protein-interactors revealed that H3.3G34R binds RACK7 to suppress transcriptional regulation of MHC class II genes that play a critical role in the immune response to tumors (Jiao *et al.,* 2020). In light of this finding and our mNSC data, we tested the hypothesis that H3.3G34 histone similarly promotes cytokine signaling in human cells. We profiled cytokine expression in parental and sh*H3F3A*-expressing KNS42 cells. Interestingly, we found major significant downregulation of intracellular cytokine levels, supporting the thought that H3.3G34R/V tumors modulate intrinsic and extrinsic factors implicated in immune response (**Figure 3.24A**).

ChIP-seq data discussed earlier demonstrated H3K36me3 and H3K27ac enrichment coincident with H3.3G34R/V mutant histone deposition. Because H3K36me3 is a major regulator of genic transcriptional activity, we wondered if targeting the methyltransferase responsible for catalyzing the conversion of H3K36me2 to H3K36me3 would recapitulate our findings with *H3F3A* knockdown. Previous work revealed H3K36me3 to be antagonistic to H3K27me3. We hypothesized that targeting SETD2, and consequently lowering H3K36me3, could raise H3K27me3 and decrease oncogene expression and signaling. We targeted *SETD2* in H3.3G34V KNS42 cells with independent shRNAs and confirmed H3K36me3 decrease by immunoblotting. Surprisingly, we did not observe a decrease in the genomic distribution of H3K36me3 compared with parental cells (**Figure 3.25A**). Instead, we noted a slight increase in H3K36me3 levels (**Figure 3.25A**). H3.3G34R histones have been found to bind and inhibit H3K36me3 demethylases

KDM4A/B/C, and our result suggests that shSETD2 knockdown in the presence of mutant histone may not be sufficient to lower genomic H3K36me3 levels. We performed immunoblotting for cells with SETD2 knockdown and assessed consequences for LIF expression. The results unexpectedly demonstrated elevated LIF expression upon SETD2 knockdown (**Figure 3.25B**). We previously found that abrogation of H3K27me3 caused concomitant H3K36me3 loss in KNS42 cells. Thus, there is a possibility targeting SETD2 could lower H3K27me3, driving LIF expression. Treatment of sh*SETD2* cells with GSK-343 only enhanced LIF expression further and in a dose-dependent manner, suggesting that specific or combined targeting of H3K27me3 or H3K36me3 is not a therapeutic axis for H3G34R/V glioma (**Figure 3.25C**). However, cytokine profiling of sh*SETD2* cells mirrored results from sh*H3F3A* cells where we observed downregulation of multiple cytokines (**Figure 3.25D**). Thus, an outstanding and very interesting question is how modulation of H3K36me3 is downregulating cytokine expression in these cells since H3K36me3 is not lost from many loci upon SETD2 knockdown.

Seminal work in the H3.3K27M glioma field discovered that targeting both H3K27 methyltransferases and demethylases is therapeutically beneficial. Having investigated EZH2 inhibitor, GSK-343, as a potential therapeutic lead for H3.3G34R/V gliomas, we wondered if utilizing GSK-J4 to inhibit H3K27 demethylase UTX/KDM6A could abrogate cell growth and LIF expression. We performed cell viability experiments with KNS42 cells and observed dose-dependent decrease in growth with GSK-J4 treatment (**Figure 3.26A**). Immunoblotting revealed a decrease in LIF expression and corresponding STAT3 phosphorylation in KNS42 cells (**Figure 3.26B**). This work demonstrates that LIF/STAT3 activation is reversible via KDM6A inhibition. These data from mouse and human tumor cell models suggest that mutant H3.3G34R/V

upregulates LIF expression, which in turn drives STAT3 activity that is important for the survival of H3.3G34R/V cells.

3.3.6 Pervasive STAT3 activation and expression occurs in H3.3G34R/V tumor tissues and patient-derived cell samples

To corroborate *in vitro* findings, we quantified phospho-STAT3 and total STAT3 levels in tumors from H3.3G34R/V (*n*=6) and H3.3WT (*n*=12) high-grade glioma patient tissues (**Figures 3.27A-E**). Results demonstrated significantly higher phospho-STAT3 (**Figures 3.27B-C**) and total STAT3 (**Figures 3.27D-E**) in H3.3G34R/V *versus* H3.3WT samples. We noted both inter- and intra-tumor heterogeneity in these patient tumors, mirroring data from patient-derived cell lines (**Figures 3.6A** and **3.20B**). Next, we queried single cell RNA-seq data from H3.3G34R/V patients presented in Chen *et al.* (2020) and found malignant cells to express *LIFR* (LIF receptor), *JAK2*, and *STAT3* (**Figures 3.27F-H**). This study found that H3G34R/V glioma cells were enriched for both interneuron and astrocytic gene signatures. Our analysis revealed JAK/STAT genes were expressed in cells irrespective of the lineage signature (**Figure 3.27G**). Importantly, we noted variations in gene expression level within malignant cells derived from the same patient and across patients (**Figure 3.28A**).

3.3.7 Genetic and pharmacological STAT3 inhibition show greater toxicity in H3.3G34R/V cells compared to H3.3WT glioma cells in vitro

We investigated whether suppression of STAT3 activity has consequences for cell growth. First, we attempted knockdown of STAT3 using two independent shRNAs in KNS42 cells. The knockdown experiment revealed substantial decrease in total STAT3 levels while tyrosine 705 phosphorylation remained intact (**Figure 3.29A**). Cell growth rate was not affected by STAT3

knockdown using this paradigm (**Figure 3.29B**). This suggested that genetic knockdown of STAT3 was not sufficient to eliminate upstream activation by LIF, other cytokines, or upstream STAT3-effectors.

To further dissect this, we utilized a CRISPR-Cas9-mediated approach to knockout STAT3 in H3.3G34R/V cells. STAT3 knockout in KNS42 and SJ-HGGx42-c cells successfully lowered STAT3 levels (**Figure 3.30A** and **3.30C**) and decreased the percentage of living cells compared to parental controls (**Figure 3.30B** and **3.30D**). We performed RNA-seq to determine pathways altered on STAT3 knockout (**Figure 3.30E**). GSEA of differentially regulated genes showed deregulated pathways related to immune signatures, cell differentiation and motility, apoptosis, cell death, and neuronal differentiation (**Figure 3.30E**).

We probed this further by characterizing the cytokine profile of STAT3 knockout cells and noted similar a similar downregulation as that observed in sh*SETD2* and sh*H3F3A* cells (**Figure 3.30F**). Further RNA-seq analysis of genes downregulated upon STAT3 knockout revealed Achaete-Scute Homolog 1 (*ASCL1*) to be a top, significantly deregulated transcript (**Figure 3.31A**). *ASCL1* is a member of the basic helix-loop-helix family of transcription factors and functions as a major chromatin remodeler and transcription factor (Casey *et al*., 2018; Raposo *et al*., 2015). In addition, *ASCL1* plays a role in regulating chromatin modifying genes (such as *SMARCB1*), cell cycle genes (such as *E2F2, CDK4, POLA2,* and *AURKB*), and neural stem cell transcription factors (such as *OLIG1, OLIG2, NFIA,* and *SOX10*) (Vue *et al*., unpulished data, see https://doi.org/10.1101/2020.02.20.958132). *ASCL1* upregulation has been noted in a variety of CNS and non-CNS cancers (Park *et al*., 2017; Rheinbay *et al*., 2013; Somasundaram *et al*., 2005; Wang *et al*., 2018). Importantly, ASCL1 expression has been observed in neural progenitor cells and H3G34R/V tumor cells (Bressan *et al.*, 2021; Helms *et al*., 2005; Kim *et al*., 2007; Parras *et*

al., 2004). ASCL1 has been implicated in interneuron progenitor development (Alzu'bi *et al.*, 2019; Grimaldi *et al.*, 2009). Thus, we queried the Mackay *et al.* (2017) meta-analysis of pediatric high-grade gliomas to determine differences in *ASCL1* expression across mutant glioma subgroups. We found that *ASCL1* was significantly upregulated in H3.3G34R/V glioma patients relative to H3.3WT patients (**Figure 3.31B)**. Next, we confirmed that STAT3 regulates ASCL1 expression by immunoblotting in KNS42 cells after treatment with STAT3 inhibitors, Stattic and WP1066 (**Figures 3.31C-D**). In addition, we confirmed that GSK-J4 treatment could reduce ASCL1 levels in a dose-dependent manner, similar to that observed with LIF levels on GSK-J4 treatment (**Figure 3.26B**) . Recent work has revealed the role of STAT3 in regulating how ASCL1 binds to chromatin (Jorstad *et al.*, 2020), highlighting the importance of probing whether aberrant STAT3 activity in H3.3G34R/V tumors drives cellular reprogramming via lineage-specific transcription factors (TF) like ASCL1. Given data from Bressan *et al.* (2021) suggesting an interneuron cell-of-origin for H3G34R/V tumors, it is important to delineate core TF networks in order to find upstream effectors like STAT that are suitable drug targets. Overall, these results suggest STAT3 can regulate multiple oncogenic and immune pathways and serve as a major therapeutic target for H3.3G34R/V-mutant gliomas.

Major research efforts and clinical trials have been undertaken to develop pharmacological approaches to inhibit STAT3 signaling in cancer (Avalle *et al*., 2017; Chai *et al*., 2016; Huynh *et al*., 2019; Laudisi *et al*., 2018; Lee *et al*., 2019; Yu *et al*., 2014). Treatment of H3.3G34R mNSCs with Stattic, a selective small-molecular inhibitor of STAT3 phosphorylation and translocation (Schust *et al*., 2006), resulted in significant cell death compared to that observed in H3.3WT mNSCs (**Figure 3.32A**). Similarly, we observed heightened sensitivity to Stattic treatment in H3.3G34V (KNS42) and H3.3G34R (SJ-HGGx6-c and SJ-HGGx42-c) compared to H3.3WT

(SF188, TS543 and SJ-HGGx39-c) and H3.3K27M (HSJD-DIPG-007) (**Figures 3.32B-C**) cells. We confirmed sensitivity to Stattic in OPGB-GBM-001 cells, another H3.3G34R cell model (**Figure 3.32D**). STAT3 phosphorylation in KNS42 and SF188 cells decreased in a dose-dependent manner upon treatment with Stattic (**Figures 3.32E-F**).

Additionally, we assessed therapeutic potential of WP1066, a potent, orally bioavailable STAT3 inhibitor with markedly low toxicity *in vivo* (Hussain *et al*., 2007; Kong *et al*., 2007; Iwamaru *et al*., 2007). Similar to our observations with Stattic, WP1066 showed greater toxicity in H3.3G34R compared to H3.3WT mNSCs (**Figure 3.33A**). WP1066 demonstrated greater therapeutic effects in H3.3G34V (KNS42) and H3.3G34R (SJ-HGGx6-c and SJ-HGGx42-c) cells compared to H3.3WT (SF188, TS543, SJ-HGGx39-c) and H3.3K27M (HSJD-DIPG-007) human cell lines (**Figure 3.33B-C**). We confirmed sensitivity of OPGB-GBM-001 cells to WP1066 (**Figure 3.33D**) and SJ-HGGx42-c to another STAT3 inhibitor, SH-4-54 (**Figure 3.33E**). Finally, we confirmed *IUE*-derived PPG tumor cells grown as explant cultures were sensitive to WP1066 (**Figure 3.33F-G**). Immunoblotting analyses of STAT3 phosphorylation showed dose-dependent decrease in pSTAT3 levels in H3.3G34V KNS42, but not in H3.3WT (TS543 and SF188) cells treated with WP1066 (**Figure 3.33H-I**).

3.3.8 Inhibition of STAT3 activity is therapeutic in flank H3.3G34R/V glioma models

We sought to determine if STAT3 inhibitors have therapeutic potential in preclinical animal models of H3.3G34R/V high-grade gliomas. We began by establishing a xenograft model using KNS42 cells injected in the mouse flank and administered Stattic as a proof-of-principle for STAT3 inhibition. Stattic-treated mice had suppressed tumor volumes and showed decreased expression of proliferation marker Ki-67 as compared to vehicle-treated animals (**Figure 3.34A-C**). Next, we evaluated the effect of LIF knockdown on tumor growth by injecting KNS42 cells

transfected with two independent shRNAs targeting LIF. Significantly smaller tumor volumes were observed for xenografts with LIF knockdown with both shRNAs as compared to xenografts without LIF knockdown (**Figure 3.34D**).

3.3.9 Inhibition of STAT3 activity is therapeutic in orthotopic H3.3G34R/V models

To corroborate initial *in vivo* results, we first tested the effect of STAT3 knockout on tumor growth in an orthotopic model. KNS42 cells with or without STAT3 knockout (KO) were implanted in the cortex. Tumor progression was monitored via measurement of bioluminescence signal by in vivo imaging systems (IVIS) and Kaplan-Meier analyses was performed. Mice with tumors harboring STAT3 KO had significantly increased overall survival (**Figure 3.35A**). KNS42 cells formed aggressive tumors with evidence of tumor invasion into the surrounding skull in control animals. In contrast, a smaller fraction of STAT3 KO mice exhibited skull invasion (**Figure 3.35B**) and demonstrated lower tumor burden compared to controls, assessed as fold change in bioluminescent signal relative to baseline (**Figure 3.35C**). Next, we investigated pharmacological targeting of STAT3 using several orthotopic models. Although various STAT3 inhibitors have been synthesized, the ability to deliver these drugs to the brain remains largely unknown due to lack of in-depth pharmacokinetic and bioavailability studies. To address this difficulty, we utilized the BOILED-Egg (Brain or Intestinal EstimateD permeation) model that considers both lipophilicity and polarity chemical parameters to predict absorption, distribution, metabolism, and excretion (ADME) properties for compounds (Daina *et al*., 2017). We analyzed the predicted blood-brain barrier (BBB) penetrability of 45 small molecule STAT3 inhibitors using this method (**Figure 3.36A**). Towards the goal for rapid translation, we filtered for STAT3 inhibitors currently in clinical trials. From these analyses, WP1066 was the only compound with predicted favorable ADME parameters, including high BBB-penetrability, and also showed

efficacy in preclinical glioblastoma models (Hou *et al*., 2019; Hussain *et al*., 2007; Kong *et al*., 2008; Ott *et al*., 2020) and is currently in clinical trials for malignant gliomas and CNS metastatic melanomas (NCT01904123, NCT04334863) (**Figure 3.36A**). In contrast, Stattic exhibited unfavorable absorption and poor BBB-penetration (**Figure 3.36A**). Based on these results, we tested efficacy of WP1066 in four independent H3G34R/V glioma animal models.

In the first model, we utilized an *in utero* electroporation-based H3.3G34R PPG mouse tumor model (H3.3G34R *IUE*) to study WP1066 efficacy. Successful tumor engraftment was confirmed by capturing bioluminescent signal via IVIS. WP1066 was administered once per day (Monday through Friday) at 40 mg/kg for 6 weeks (based on published doses (Kong *et al*., 2008)) as outlined in **Figure 3.36B.** WP1066-treated mice had significantly increased overall survival compared with vehicle-treated controls (**Figure 3.36C**). Furthermore, mice receiving WP1066 had lower tumor burden compared to vehicle-treated animals, assessed as fold change in bioluminescent signal relative to baseline (**Figure 3.36D-E**). Next, we established a human H3.3G34V tumor model by orthotopically implanting mice with KNS42 cells in the cortex, and confirmed engraftment via IVIS. Using the same treatment paradigm (**Figure 3.36B**), mice receiving WP1066 exhibited prolonged survival and decreased tumor burdens compared to vehicle-treated control animals (**Figure 3.36F-H**). Neuropathological features were assessed in tumors with or without treatment. All mice with KNS42 tumors receiving vehicle exhibited tumor invasion into the surrounding skull while less than 50% of WP1066-treated mice demonstrated this phenotype (**Figure 3.36I**). Moreover, Ki-67 expression was significantly reduced in mice receiving WP1066 (**Figure 3.36J**) compared to vehicle-treated animals. In contrast, WP1066 treatment of a H3.3WT glioma orthotopic model developed with TS543 cells did not result in

decreased tumor burden (**Figure 3.37A-B**). Our results from multiple H3.3G34R/V *in vivo* models demonstrate the therapeutic efficacy of targeting STAT3 genetically and with WP1066.

Finally, we investigated the possibility that H3.3G34R/V tumors may benefit from treatment comprised of current standard radiation therapy (RT) paired with STAT3 inhibitors. Constitutive STAT3 activation has been implicated in tumor radioresistance, and consequently, recent studies have attempted to target STAT proteins to promote radiosensitivity (Gao *et al.*, 2010; Gao *et al.*, 2014; Spitzner *et al*., 2014; Wang *et al*., 2021; Xie *et al*., 2019). We used orthotopic models of H3.3G34R PPG, SJ-HGGx42-c, and KNS42 cells. Potential synergy between radiation therapy and WP1066 was assessed using a modified treatment paradigm (**Figure 3.38A**). Both RT and combination therapy also extended overall survival in PPG animals. Combination therapy significantly extended overall survival compared to radiation therapy alone (**Figure 3.38B**). However, combination therapy provided no additional benefit compared to single agent WP1066 treatment (**Figure 3.38B**). RT alone, or combinatorial treatment significantly lowered tumor burden (as determined by IVIS bioluminescence) in PPG, but not in SJ-HGGx42-c or KNS42 engrafted animals (**Figure 3.38C-F**). Interestingly, the significant decrease in tumor signal was only noted in WP1066-treated SJ-HGGx42 tumor-bearing mice, but not after other treatment modes (**Figures 3.38F**). Studies of irradiation of brain and other solid tumors has revealed that irradiation itself can enhance STAT3 signaling (Gao *et al*., 2014; Wang *et al*., 2021). We therefore hypothesized that this mechanism could account for the resistance of SJ-HGGx42 tumors to RT. SJ-HGGx42-c cells subjected to a single dose of radiation with or without STAT3 inhibitor *in vitro* demonstrated that irradiation enhanced LIF, phospho-STAT3, and total STAT3 levels (**Figure 3.39A**). This enhancement of STAT3 signaling potentially explains why no additive effect of the combination regimen was observed *in vivo*. Similarly, treatment of KNS42 orthotopic tumors did

not result in a significant decrease in tumor signal and, like controls, the skull invasion phenotype was observed in RT-treated mice (**Figure 3.40A-B**). Together our results *in vitro* and *in vivo* serve as proof-of-principle that reducing STAT3 activity with the BBB-penetrable WP1066 is therapeutic in preclinical H3.3G34R/V glioma models.

3.4 Discussion

Discoveries of histone mutations in gliomas have expanded knowledge on how these mutations alter chromatin to impact tumor pathogenesis. Here, we defined therapeutic dependencies arising from specific epigenetic alterations in pHGG driven by H3.3G34R/V mutations. Using comprehensive, cell-based epigenetic and transcriptomic studies, we discovered H3.3G34R/V cells show enhanced LIF/STAT3 signaling compared to H3.3WT cells. This key finding of STAT3 signaling was corroborated by single cell RNA-seq and immunohistochemical analysis in cells and tumor tissues from H3.3G34R/V glioma patients. We noted inter- and intra-tumor heterogeneity in levels of LIF receptor, LIF, and pSTAT3/STAT3 both in patient-derived cell lines and tissues, suggesting that a subset of patients with H3.3G34R/V tumors may benefit from STAT3-targeting therapies.

Mechanistically, H3.3G34 mutant-expressing cells showed enrichment of multiple activating marks, including H3K36me3, at *LIF* to drive LIF expression and knockdown of mutant *H3F3A* lowered LIF expression and secretion. We confirmed these findings in published data from H3G34W cells where correction of mutant H3.3G34W to H3.3WT or *H3F3A* knockout resulted in lowering of both H3K36me3 at *LIF* and LIF expression (Khazaei *et al*., 2020). Recent studies have shown H3.3G34R/V/W mutant cells show both genome-wide gains and losses of H3K36me3 (Bjerke *et al*., 2013; Jain *et al*., 2020; Khazaei *et al*., 2020; Voon *et al*., 2018). Regions with loss of H3K36me3 include genes related to differentiation (Khazaei *et al*., 2020). Our data suggest

regions gaining H3K36me3 involve genes related to the LIF/JAK/STAT pathway. Results demonstrating H3K36me3 enrichment at *Lif* were confirmed in patient-derived, H3.3G34R/V glioma cell lines and multiple independent data sets from Voon *et al.* (2018), Jain *et al.* (2020), and Khazaei *et al*. (2020).

In our study, we discovered H3.3G34R/H3.3WT mNSC exhibit a distinct DNA methylation profile and harbor more differentially methylated regions compared to H3.3K27M/H3.3WT cells. Promoter hypomethylation, reported in H3G34R/V glioma and H3.3G34W bone tumor patient samples (Sturm *et al*., 2012; Sangatsuda *et al*., 2020; Lutsik *et al.*, 2020), was associated with increased gene expression and enrichment of activation marks including H3K36me3, H3K27ac and H3K4me3 in our H3.3G34R mNSC model. We observed significant H3K36me3 gain at DNA hypomethylated loci but did not observe decreases in H3K36me3 to similar extent at hypermethylated loci. Interestingly, DNMT3A has been shown to interact with H3K36me3 via a critical PWWP domain (Dhayalan *et al*., 2010). Our results would suggest that H3G34R/V histones may directly inhibit activity of DNA methyltransferases or block their recognition of H3K36me3, resulting in hypomethylation at promoters with high histone incorporation. To dissect this, more ChIP-seq and histone association assay studies are needed to understand the localization of DNA methylases and demethylases specifically in G34-mutant tumors. Future studies could also use DNA methyltransferase activity assays to probe relative DNMT3 activity level in the presence of H3K36me3-modified H3WT and H3G34R nucleosomes bound with DNA. It is quite possible that H3G34R/V histones do not directly interact or block DNMT3 activity and lack of activity is a secondary effect. In thinking about potential mechanisms, it is also important to realize H3K4me3 enrichment antagonizes DNA methylation by blocking the interaction of DNMT3 proteins with unmodified H3K4 residues (Rose *et al*., 2014; Sharifi-Zarchi

et al., 2017; Ooi *et al*., 2007). As we have noted, G34-mutant histones alter H3K36me3 which may have a secondary effect on H3K4me3 levels, and thus this mechanism may be responsible for reduced DNA methylation observed at promoters. One final possibility is that G34-mutant histones bind lysine 4 demethylases (KDM5A-D). This could cause H4K4me3 accumulation via a similar mechanism observed for KDM4 by Voon *et al.* (2018), and subsequent antagonism of DNA methyltransferases.

We also noted some loci with reduced H3K36me3 accompanied by reduced H3K4me3 and H3K27ac, but this did not occur at many regions. Moreover, H3K27me3 was redistributed with lowered H3K27me3 at promoter regions and increased H3K27me3 in flanking intergenic regions, mirroring findings reported in H3.3G34W bone tumor cells (Jain *et al*., 2020). Cross referencing epigenetic alterations with DNA methylation revealed *Lif* as a top upregulated gene from these analyses. Altogether, our findings of H3.3G34R/V deposition at *LIF* in patient-derived cells, promoter hypomethylation in our isogenic model and patient samples, and epigenetic upregulation of LIF in both G34W and G34R tumors strongly suggest a key role for LIF in pathogenesis of H3.3G34R/V mutant gliomas.

Studies on the closely related H3G34W mutation observed in bone tumors have attempted to probe the role of elevated H3K27me3 at enhancers, which accumulate the H3G34W histone, in driving disease pathology. Jain *et al.* (2020) found that treatment of H3G34W cells with EZH2 inhibitor Tazemetostat could reverse H3K27me3 and de-repress silenced genes. Moreover, introduction of a double mutant H3G34W and H3K27R histone construct into a mesenchymal stem cell *in vivo* tumor model could abrogate tumor growth and aggressiveness, suggesting that targeting EZH2 is a possible therapeutic approach. Given that EZH2 can enhance STAT3 phosphorylation and EZH2 inhibition has a demonstrated benefit in G34W and K27M preclinical

models and, we wondered if similar EZH2 targeting in G34R/V cells could slow growth or reverse gene silencing mediated by the mutant histone. Our experiments revealed that inhibiting EZH2 was ineffective in reducing growth or modulating LIF expression. Unexpectedly, inhibiting H3K27me3 demethylases with GSK-J4 could slow growth and potently reduced LIF expression and STAT3 phosphorylation. This result was surprising since H3G34R/V tumors have slightly elevated H3K27me3 compared to H3.3WT cells, suggesting that elevating H3K27me3 further at actively transcribed genes provides a therapeutic strategy.

Other experiments involving *SETD2* knockdown failed to decrease LIF expression and did not reduce global H3K36me3 levels. One of the earliest biochemical experiments probing the interaction of H3G34R and H3G34V histones revealed their ability to inhibit SETD2 catalytic activity. Although mechanistic experiments are needed, we speculate that mutant histones in cells maintaining H3G34V expression upon SETD2 knockdown can continue to bind and inhibit remaining SETD2 and KDM4. This interaction could potentially block differential K36 demethylase activity on the same histones at highly transcribed regions that maintain high levels of H3G34V incorporation, explaining the slight elevation of H3K36me3 in sh*SETD2* cells compared to parental cells at some genomic regions. If both H3G34V and H3K36me3 are deposited at actively transcribed genes, as described in other studies, it is possible that the differential binding of K36 methylases and demethylases explain the lack of H3K36me3 loss at these genes. An additional possibility is that partial SETD2 knockdown does not affect overall SETD2 catalytic activity at its targets and slows the methylation process rather than reversing it. Since SETD2 is the sole K36 trimethyltransferase, a decrease in H3K36me3 levels across the genome upon SETD2 bi-allelic knockout would confirm this hypothesis. Collectively, our results from these perturbations of H3K36me3 and H3K27me3 levels suggests that targeting the enzymes

that catalyze these methylation reactions have different effects than those observed in H3G34W mutant cells. This result suggests that while H3G34W and H3G34R/V mutations have similar broad effects on H3K36me3 and DNA methylation and parallels can be drawn, the specific genomic regions affected to reprogram cellular signaling and differentiation are likely tissue-dependent and will inform the design of specific therapies to overcome the oncogenic effect mediated by each mutant.

Our functional studies demonstrated that LIF activated STAT3 signaling in an autocrine/paracrine manner and was important for cell survival of H3.3G34R/V mutant cells, suggesting a key epigenetically-driven therapeutic vulnerability. STAT proteins serve as master transcriptional regulators and their dysregulation or overexpression has been noted widely in malignancy (Avalle *et al*., 2017; Chai *et al*., 2016; Laudisi *et al*., 2018; Yu *et al*., 2014). Obstacles in developing STAT3 inhibitors for gliomas include issues of low cell permeability, rapid clearance, and low blood-brain barrier penetrability (Wong *et al*., 2017). We took advantage of low toxicity and high brain penetrability of the small molecule STAT3 inhibitor WP1066 (Iwamaru *et al*., 2007; Kong *et al*., 2008; Ott *et al*., 2020). WP1066 treatment resulted in marked tumor toxicity in H3.3G34R/V models both *in vitro* and *in vivo*. Although radiation was able to decrease tumor burden and increase survival in one H3G34R orthotopic tumor model, combining radiation with WP1066 *in vivo* did not enhance the survival benefit of WP1066 treatment alone. Our results suggest a key epigenetically-driven vulnerability in H3.3G34R/V mutant gliomas that can be leveraged for therapeutic purposes using established STAT3 inhibitors. Moreover, the ability of H3G34R/V/W mutations to modulate epigenetic modifications at *LIF* and its expression provide support to other studies which have suggested G34R and G34W work via similar mechanisms and thus could both benefit from STAT3 inhibition.

Intriguingly, a study profiling the mutational landscape of H3G34R/V tumors noted a large frequency of co-occurring *PDGFRA* mutations (Chen *et al*., 2020). Epigenetic analysis revealed that H3G34R/V gliomas likely originate in interneuron progenitor cells that express the *GSX2* transcription factor. Intriguingly, GSX2 and PDGFRA expression correlated well in H3G34R/V tumors, despite *PDGFRA* expression not normally occurring in the posited interneuron cell-of-origin. This observation of co-expression led to the hypothesis that PDGFRA hijacks the enhancer regulatory element of GSX2 to drive increased expression. The authors found that this aberrant PDGFRA expression also correlated with MEK/ERK pathway activation in patient tumors. In our study, we found that MAPK signaling was a top deregulated pathway in our mNSC isogenic model, suggesting that H3G34R/V tumors not only arise in cells that are poised for PDGFRA activation, but may also independently epigenetically activate other MEK/ERK signaling pathway proteins. Interestingly, studies have demonstrated that platelet derived growth factor (PDGFR) can activate JAK/STAT signaling (Vignais *et al.*, 1996, 1999). Other work has uncovered the role of ERK1/2 in phosphorylating the STAT3 serine 727 residue (Harhous *et al.*, 2019; Lim *et al.*, 2001; Wong *et al.*, 2017). S727 activation has varying roles depending on cell type, but has been associated with enhanced STAT3 DNA binding and radioresistance mechanisms (Masliantsev *et al.*, 2017; Ouedraogo *et al.*, 2016). These findings suggest that MAPK activation in G34-mutant tumors might confer resistance to STAT3 therapies. Because the S727 residue cannot be pharmacologically targeted like Y705, H3G34R/V tumors may benefit from combined MAPK and STAT3 signaling inhibition.

Several key questions remain unanswered in the H3G34R/V glioma biology field. Curiously, reports on H3G34W and H3G34R/V mutant histones effects on the epigenome have made a similar observation that H3K36me3 can either be gained or lost at distinct genomic regions.

Current findings support the notion that H3G34 mutations cause H3K36me3 loss and corresponding H3K27me3 gain *in cis* (i.e. specifically on the same mutant histone). This leaves a question about how H3K36me3 can be gained at genomic regions that harbor the mutant histone. Early work on G34R interactors revealed a stronger binding of lysine 36 demethylases KDM4A/B/C to G34R histone compared with WT histone, and this was suggested to be a mechanism behind focal H3K36me3 gain. Importantly, the localized gain could be accurately phenocopied in cells harboring triple-knockout of the KDM4A/B/C enzymes.

If both the R- and V-substituted histones can inhibit SETD2 and KDM4, it is curious how H3K36me3 gain can be observed in regions harboring these histones. Of note, both mutant and wild-type H3.3 are deposited into actively transcribed promoters and gene bodies and G34 mutants have not been observed to alter the distribution of H3.3 deposition. Indeed, one possibility is that the mutant histone sequesters KDM4 family demethylases and this allows SETD2 to methylate wild-type histone incorporated into the same or nearby nucleosomes. This might occur in regions where KDM4 outcompetes SETD2 for mutant histone binding. One prominent issue arises from the techniques currently used for chromatin immunoprecipitation to study these effects. Many studies perform ChIP-sequencing on chromatin that contains both wild-type and mutant histones, making it difficult to ascertain the relative levels of H3K36me3 on each peptide. Recently, clever experiments using immunoprecipitation specific for tagged mutant histones was able to confirm the loss of H3K36me3 on the same histone but could not explain some of the regional gains. Similar studies might elucidate the relative distribution of SETD2 and KDM4 bound to mutant and wild-type histone by performing re-ChIP experiments with V5- or FLAG-tagged mutant histone.

Critically, the relative affinity for the interaction of SETD2 and KDM4 with mutant R/V histones has not been assessed. Examination of the binding interactions could demonstrate intrinsically different affinity *in vitro* or the binding affinity could be genomic region-dependent. For example, strongly expressed genes with robust H3K36me3 may maintain SETD2 occupancy and deposition of mutant histone into such a gene might inhibit its activity and lead to local H3K36me3 loss, especially if SETD2 outcompetes KDM4 binding to the mutant. However, in loci that are normally weak SETD2 targets or stronger KDM4 targets, incorporation of nucleosomes containing mutant histone might result in KDM4 inhibition and corresponding H3K36me3 elevation. Thus, if we adopt this hypothesis, SETD2 and KDM4 inhibition would be dependent on their normal relative occupancy at each gene region. Additionally, if an intrinsic binding strength difference exists between SETD2 and KDM4 with the mutant histones, this could further exacerbate inhibition in regions targeted by each.

The current literature, albeit limited, suggests that CRISPR-mediated correction of mutant *H3F3A* to wild-type in H3G34R/V cell lines is not able to reverse the H3K36me3, H3K4me3, or H3K27me3 patterning observed in these cells. Furthermore, correction of the mutant allele does not slow tumor growth in several orthotopic models using patient-derived cell lines. This strongly contrasts with results from experiments with H3G34W cells where editing of the mutant *H3F3A* allele can reverse H3K36me3, H3K27me3, and H3K27ac patterns as well as gene expression. Additionally, two studies illustrated that mutant correction or interruption in the presence of concurrent K27R mutation abrogates tumor growth in H3G34W tibial tumor models *in vitro* and *in vivo.* This strongly suggests that the epigenome of H3G34W tumors is plastic while H3G34R/V tumors may undergo “phenotypic lock” that is irreversible after tumor initiation. Indeed, the lack of an effect on growth after deletion or CRISPR-mediated correction in patient cells strongly

supports this hypothesis, highlighting the importance of how we establish models of H3G34R/V tumors. This is also supported by ChIP-seq experiments presented in Bressan *et al.* (2021) where regions with high H3.3G34R incorporation do not undergo significant changes in H3K4me3, H3K36me3, or H3K27me3 occupancy after CRISPR-mediated H3.3G34R knockout compared with parental cells. If H3.3G34R/V is indeed targeted to specific regions with high transcriptional activity, one question that remains is why the H3G34-related mutations only occur in histone H3.3 and not H3.1. Studies have offered explanations for the preferential occurrence of H3K27M mutations in *H3F3A*, namely that a single nucleotide substitution can give rise to the mutation. If K27M were to arise in the other allele encoding H3.3 (*H3F3B*) or H3.1, this would require two such substitutions, making it less likely. This is not the case for codon substitutions involving glycine 34. The codon encoding for G34 is the same in *H3F3A* and *H3F3B.* Moreover, both arginine and valine replacements can be achieved from the glycine 34 codon of H3.3 and H3.1 with a single nucleotide substitution, failing to explain why the mutation preferentially affects H3.3 and specifically *H3F3A.* The same preference for *H3F3A* has been observed in bone tumors with the glycine-to-tryptophan substitution. Interestingly, despite K36 codon similarity in *H3F3A* and *H3F3B*, K36M mutations are observed predominantly in *H3F3B.* The reason for this distinction between H3G34 and H3K36 mutant tumors is still unknown.

One possibility is that G34 tumors prefer H3.3 mutations because H3.3 is targeted to highly transcribed regions and its distribution is different from H3.1. A recent study by Gomes *et al.* (2019) has suggested that the deposition of H3 variants is directly modulated by signaling pathways and can directly affect tumor metastatic and drug resistance traits. This study demonstrated that carcinoma cells treated with TGF-b or TNF-a underwent a shift in histone variant expression where H3.1/3.2 were downregulated and H3.3 expression was upregulated.

They also found that ERK1/2 activity could suppress expression of histone H3.1/3.2 chaperone protein, CHA1FB. Experiments probing the role of CHAF1B *in vitro* and *in vivo* demonstrated that tumors became more aggressive and resistant to therapy. It is tantalizing to think that H3G34R/V tumors might co-opt other mutations in signaling pathways, such as *PDGFRA* discussed earlier, to drive ERK1/2 signaling that causes H3.3 redistribution to drive tumor growth. Although H3G34R knockout (performed by Bressan *et al.*, 2021) and H3G34W expression studies (performed by Jain *et al.,* 2020) did not note a change in the H3.3 distribution with their experiments, this does not rule out the possibility that other factors independent of the mutant histone can change the H3.3 distribution. Future studies should study the relative H3.3 distribution in cells with and without signaling cascade activation (such as ERK1/2) to determine if these oncogenic signals regulate H3.3 genomic patterning.

Collectively, this epigenetic irreversibility suggests the field must investigate what oncogenic factors are already highly expressed in H3G34R/V tumors and assess how they are contributing to tumor growth. This necessitates using appropriate models reflecting the interneuron progenitor cell-of-origin for H3G34R/V tumors and comparing gene expression changes observed in these models to expression patterns present in patient tissues and cells. Interestingly, Bressan *et al.* (2021) established glioma models using neural stem cells derived from the fetal forebrain and hindbrain regions. They noted that cells expressing H3G34R mutations upregulated neuroprogenitor factors such as *EMX2* and *DMRTA2*, and noted similarity with factors highly expressed in mutant patient tissues. They point out that *ASCL1*, a master regulator of neural progenitor fate, is upregulated in patients.

In this realm, our study uncovered that *ASCL1* was a top upregulated gene in H3G34V patient and H3G34R mouse cells. Furthermore, ASCL1 expression could be reduced by treated

cells with STAT3 inhibitors or via STAT3 knockout. Having been noted as highly upregulated in adult gliomas and other cancers, ASCL1 has numerous functions including Acting as a chromatin remodeler and modifying the expression of neural stem cell transcription factors. Of note, STAT3 has been demonstrated to recruit ASCL1 to specific genomic regions in the retinal cells (Jorstad *et al*., 2020). Upregulation of STAT3 and ASCL1 in H3G34R/V cells and tissues suggests that STAT3 might both drive ASCL1 expression and chromatin remodeling. This finding highlights the possibility that H3G34R/V mutations might engage specific oncogenic signaling, such as STAT3, at tumor initiation which then drive other processes like chromatin remodeling that are ultimately irreversible even with mutation knockdown. Here, targeted approaches to disrupt neuroprogenitor factors like ASCL1 and assess their effect chromatin accessibility *in vitro* and on survival in animal models will be informative. Once neuro-progenitor genes that are critical for tumor growth are identified, targeted therapeutic approaches can be designed to inhibit upstream signaling that engage those molecular factors. To address this, other approaches like targeting bromodomain proteins JQ1 (discussed in Chapter 1) might be worth investigating. MYCN-driven transcription is a well-known target of JQ1, and recently JQ1 was shown to downregulate both MYCN and ASCL1 and upregulate p21 in small cell lunger cancer (Kato *et al*., 2016; Shahbazi *et al*., 2016). Importantly, elevated MYCN and ASCL1 and suppresses p21 are all implicated in G34 glioma pathology (Bjerke *et al*., 2013; Bressan *et al*., 2021).

Overall, this study furthers knowledge about H3.3G34R/V biology by uncovering a H3.3G34-driven epigenetic mechanism for LIF/STAT3 activation. Experimentation *in vitro* and *in vivo* revealed a previously undescribed and effective therapeutic axis that can be harnessed to suppress H3.3G34R/V glioma growth in preclinical models. The STAT3 inhibitor utilized for our studies, WP1066, is blood-brain barrier penetrable and is currently in clinical trials for malignant

gliomas and CNS metastatic melanomas (NCT01904123, NCT04334863). Our finding that STAT3 is a targetable dependency in H3G34R/V gliomas is uniquely powerful because it opens the possibility that STAT3 inhibition can allow indirects targeting of other "undruggable" transcription factors. MYCN and ASCL1 upregulation is well-established in these tumors, both of which are direct STAT3 transcriptional targets.

Furthermore, studies have revealed that WP1066 can effectively decrease ERK1/2 phosphorylation (Verstovsek *et al*., 2008). PDGFRA elevation and activated ERK1/2 signaling have recently been described for G34-mutant tumors, and together with our results suggest that WP1066 therapy may deregulate STAT3 and ERK1/2 signaling together. These unique properties make WP1066 an ideal candidate for clinical testing in the mutant glioma context. We hope the work outlined here provides the groundwork for continued design of much-needed therapies for this disease. Most importantly, we hope discoveries such as those presented here will ultimately improve the quality of life for patients.

3.5 Methods

Study Design

This study assessed specific epigenetic, transcriptomic, and proteomic changes in H3.3G34R/V tumors and explored whether signaling mechanisms activated by H3.3G34R/V mutations provide therapeutic vulnerabilities in these tumors. We first used H3.3G34R/V mouse and human tumor model cells to delineate epigenetic patterns and profile signaling pathways. We observed increases in H3K36me3 at the *Lif* locus in these models, which led us to hypothesize that H3K36me3 drives other epigenetic changes at *Lif* that promotes its expression and drives Stat3 signaling in these tumors. Genetic and pharmacological approaches were used to probe STAT3 as a potential therapeutic target in isogenic model cells and patient-derived tumor cells. Last, we demonstrated that STAT3 is a viable, translational therapeutic target in H3.3G34R/V tumors using multiple mouse tumor models.

In vitro pharmacology, quantitative polymerase chain reaction (*q*PCR), immunoblotting, and ELISAs were performed using three independent biologic experiments with technical replicates (n=3-4 or greater) of each condition. DNA methylation and RNA-seq analysis was performed in triplicate for each cell line or assay condition. ChIP-seq analysis was conducted using n=1 biological replicate for each epigenetic modification using isogenic H3.3G34R, H3.3WT or H3.3K27M mutant cells or human pHGG glioma cells. Both mouse histone mutant cells and patient-derived high-grade glioma cell lines were utilized for *in vitro* experiments. No data was excluded from any *in vitro* analysis.

All animal experiments were performed after approval from the University of Michigan Institutional Animal Care and Use Committee (Protocol #PRO00008865 and #PRO00009398) and were conducted as per NIH guidelines for animal welfare. Both male and female mice were equally

used. Flank and orthotopic murine models of H3.3G34R/V tumors were established via either injection of target cells or *in utero* electroporation techniques (Patel *et al.,* 2020). Sample size for *in vivo* animal experiments was based on previously published *in vivo* pHGG models by Grasso *et al.* which showed a minimum group size of three animals to detect a 50% difference in tumor growth between two groups with an α=0.05 and power=0.8 (Grasso *et al.,* 2015). For subcutaneous models, treatment and measurements began at 8 weeks after injection when control tumors measured about 45 mm3. For TS543, SJ-HGGx42-c, and PPG orthotopic models, treatment was commenced 10 to 12 days after tumor cell implantation and tumors were imaged weekly. For the H3.3G34R IUE cortical model, plasmid injection occurred at E13.5 and treatment commenced at about postnatal day 35. For the orthotopic model of KNS42 STAT3 KO tumors, bioluminescence measurements were obtained weekly beginning 10 days after implantation. For the orthotopic model of KNS42 tumors receiving WP1066, treatment was commenced 7 weeks after tumor cell implantation and tumors were imaged weekly. For all studies, engraftment of tumors in the cortex was confirmed by bioluminescence imaging (IVIS). Animals with failed tumor engrafting (absence of bioluminescence signal or bioluminescence did not reach a predefined threshold) were not included. Animals with failed tumor engrafting (absence of bioluminescence signal or bioluminescence did not reach a predefined threshold) were not included for further study. At treatment commencement, total flux exceeded the following predetermined threshold: $>10^6$ photons/s for KNS42, H3.3G34R IUE, H3.3G34R-PPG, and TS543 models; $>10^5$ photons/s for the SJ-HGGx42 model.

After confirmation of appropriate tumor formation, mice were randomized into control and experimental groups before Stattic or WP1066 treatment, radiotherapy, or combinatorial treatment. Tumor progression was evaluated weekly by measuring tumor dimensions or assessing

bioluminescence signal longitudinally by IVIS in a nonblinded manner. Mice were sacrificed at a humane endpoint (onset of neurologic symptoms, lethargy, or lack of ambulation). Immunostaining for in vivo studies and patient samples was performed by capturing and performing quantification analyses by individuals blinded to the experimental design or sample type. All identifiers from cases were removed before analysis. A priori power analysis was not conducted to determine the sample size for methylation or expression data derived from patient samples. Sample size for these analyses was determined on the basis of tumor specimen availability. All studies were conducted in compliance with Reporting Recommendations for Tumor Marker Prognostic Studies (REMARK) and Standards for Reporting of Diagnostic Accuracy Studies (STARD) guidelines.

Statistical Analysis

Statistical analyses were performed in consultation with bioinformaticians. The sample size (*n*) along with the statistical test performed and corresponding *P* values are indicated in each figure and figure legend. Data in all figures is represented as the mean ± standard deviation (S.D.) unless otherwise indicated. Graphs were plotted and statistical analyses were performed using Prism software (Version 8.0.0, Windows 64-bit, GraphPad, La Jolla, CA). Unpaired, two-sided, two-tailed, Student's *t* test or two-sided analysis of variance (ANOVA) followed by multiple comparison analysis were used to analyze data as indicated. Correlational analyses were performed using 95% confidence intervals. Results from correlational analyses are represented by r, Pearson's correlation coefficient. Survival analyses for animal experiments was performed using Kaplan-Meier analyses utilizing the Log-Rank test. Data were considered significant if $P < 0.05$.

Tumor cell lines, growth medium, and culture conditions

Cells were cultured in a humidified incubator at 37°C and 5% CO_2. Parental immortalized mouse NSCs with $p16^{Ink4a-}/p^{14Arf}$ background were gifted by Dr. Richard Gilbertson. KNS42 (H3.3G34V), TS543 (H3.3WT), SJGBM2 (H3.3WT), UMPed37 (H3.3WT), and PPG (H3.3G34R) were a gift from Dr. Carl Koschmann. SF188 (H3.3WT) was obtained from Dr. Craig Thompson. HSJD-DIPG-007 (H3.3K27M) was obtained from Dr. Rintaro Hashizume. SJ-HGGx42-c (H3.3G34R), SJ-HGGx6-c (H3.3G34R), SJ-HGGx39-c (H3.3WT), and SJ-DIPGx37-c (H3.3K27M) were kindly provided by Dr. Suzanne Baker. Immortalized human neural stem cells (hNSC) were provided by Dr. Eric Raabe. Each cell line was authenticated by Sanger sequencing and immunoblotting to confirm *H3F3A* status. All cell lines were routinely tested for *Mycoplasma* contamination.

Mouse NSCs, mouse PPG, and TS543 cells were cultured as neurospheres in Neurobasal A supplemented with N-2 (1X), B-27 (1X), L-glutamine (2 mM), penicillin/streptomycin (1X), heparin (2 μg/mL), human EGF (20 ng/mL), human b-FGF (20 ng/mL), and bovine serum albumin (45 ng/mL).

Human NSCs were cultured in EF media composed of 30 parts Hams F12 and 70 parts DMEM supplemented with antibiotic/antimycotic (1X), L glutamine (2 mM), B-27 without Vitamin A (1X), EGF (20 ng/mL), FGF-2 (20 ng/mL), and heparin (2 ug/mL).

KNS42 and UMPed37 cells were cultured adherently in DMEM/F-12 (with glutamine and HEPES) supplemented with antibiotic/antimycotic (1X), fetal bovine serum (10%), and GlutaMAX (2 mM).

SF188 and HEK293T cells were cultured adherently in DMEM supplemented with fetal bovine serum (10%), sodium pyruvate (1 mM), glutamine (2 mM), and penicillin/streptomycin

(1X). SJGBM2 cells were cultured adherently in IMDM supplemented with 20% FBS, glutamine (2 mM), and antibiotic-antimycotic (1X).

OPGB-GBM-001 and HSJD-DIPG-007 cells were cultured as neurospheres in TSM base media [equal parts Neurobasal A and DMEM/F-12, supplemented with HEPES (10 mM), sodium pyruvate (1 mM), Non-Essential Amino Acids (NEAA, 0.1 mM), GlutaMAX (2 mM), antibiotic/antimycotic (1X)] supplemented with B-27 (1X, without Vitamin A), 0.2% heparin (2 μg/mL), human EGF (20 ng/mL), human b-FGF (20 ng/mL), human PDGF-AA (10 ng/mL), and human PDGF-BB (10 ng/mL).

SJ-HGGx42-c, SJ-HGGx6-c, SJ-HGGx39-c, and SJ-DIPGx37-c cells were maintained in culture flasks pretreated with Geltrex (ThermoFisher, A1413302). Complete media consisted of equal volumes of supplemented NBEFab and StemproEFab medium. NBEFab contained Neurobasal Medium supplemented with B-27 (1X, without Vitamin A), N-2 (1X), human EGF (20 ng/mL), human b-FGF (20 ng/mL), human PDGF-AA (10 ng/mL), human PDGF-BB (10 ng/mL), heparin (2 μg/mL), GlutaMAX (2 mM), and HEPES (10 mM). StemproeFab contained KnockOut DMEM/F-12 supplemented with sodium pyruvate, Gluta-MAX (2 mM), NEAA (0.1 mM), StemPro Neural Supplement (1X), human EGF (20 ng/mL), human FGF (20 ng/mL), human PDGF-AA (10 ng/mL), human PDGF-BB (10 ng/mL), heparin (2 μg/mL), and HEPES (10 mM).

The following reagents were utilized for cell cultures: Neurobasal Medium (Gibco, #21103-049), Neurobasal A Medium (Gibco, #10888-022), KnockOut DMEM/F-12 (Gibco, 12660-012), Opti-MEM I Reduced Serum Medium (Gibco, #31985-070), Ham's F-12 Nutrient Mix (Gibco, #11765-054), Dulbecco's Modified Eagle Medium (DMEM; Gibco, #11960-044), DMEM/F-12 (Gibco, #11330-032), Fetal Bovine Serum (VWR, #89510-186), Iscove's Modified Dulbecco's Medium (IMDM; Gibco, #12440-053), GlutaMAX Supplement (Gibco, #35050-061),

MEM Non-Essential Amino Acid Solution (Gibco, #11140-050), Sodium Pyruvate (Gibco, #11360-070), HEPES (Gibco, #15630-080), L-glutamine (Cytiva, SH30034.01), Antibiotic-Antimycotic (Hyclone, SV30079.01), B-27 Supplement (Gibco, #17504-044), B-27 Supplement minus Vitamin A (Gibco, #12587-010), N2 Supplement (Gibco, #17502-048), Heparin (STEMCELL Technologies, #07980), StemPro Neural Supplement (Gibco, #A10508-01), Geltrex LDEV-Free Reduced Growth Factor Basement Membrane Matrix (Gibco, #14133-02), Penicillin-Streptomycin (Gibco, #15140-122), Human EGF (Shenandoah Biotechnology, #100-26), Human b-FGF (Shenandoah Biotechnology, #100-28), Human PDGF-AA (Shenandoah Biotechnology, #100-16), Human PDGF-BB (Shenandoah Biotechnology, #100-18).

Immunoblotting

Cells were first washed with cold PBS and cell lysis was carried out for 15 minutes in RIPA buffer in the presence of appropriate protease (Sigma-Aldrich, #P8340) and phosphatase (Sigma-Aldrich, #P5726) inhibitor cocktails. Cell pellets were generated after a minimum of 7 day antibiotic selection for knockdown/knockout cells or after treated with a specified inhibitor for durations indicated in each figure legend. All pellets were processed immediately for protein extraction and subsequent electrophoresis. Lysates were centrifuged at 14,000xg for 10 min at 4 °C, and resultant supernatant quantified for protein content using BCA protein assay (Pierce, #23225). Equal amounts of whole cell lysates or histone extracts were electrophoresed on 4-15% Mini-Protean TGX precast gels. A Trans-Blot Turbo transfer system was used to perform transfer to PVDF membrane. Membranes were blocked for 1 hour either in TBST (Tris-Buffered Saline containing 0.05% Tween-20) with either 5% milk or 5% BSA (for phosphorylation-specific antibodies). Membranes were then incubated for 8-12 hours at 4 °C in respective primary antibodies in TBST

with 5% milk or 5% BSA. Next, membranes were incubated in horseradish peroxidase-conjugated secondary antibodies for 2 hours at room temperature. Each membrane was washed three times in TBST for 10 minutes following every primary and secondary antibody incubation period. Immunoreactivity was captured by using Pierce ECL Western Blotting Substrate (Thermo Fisher Scientific, #32106).

The following primary antibodies were utilized for immunoblotting at indicated dilution: HA (Cell Signaling, #3724, 1:1000), H3.3G34R (Millipore Sigma, ABE403, 1:500), H3.3G34V (RevMAb Biosciences, 31-1193-00, 1:1000), H3K36me3 (ActiveMotif, #61021, 1:1000), H3K27ac (Millipore Sigma, #07-360, 1:1000), H3K4me3 (Cell Signaling, # 9751S, 1:1000), H3K27me3 (Millipore Sigma, #077-449, 1:1000), total H3 (Cell Signaling, #3638S, 1:5000), β-Actin (Sigma-Aldrich, #A5441, 1:20,000), LIF (abcam, #ab113262, 1:1000), JAK2 (abcam, #108596, 1:1000), phospho-STAT3(Y705) (Cell Signaling, #9145S, 1:1000), total STAT3 (Cell Signaling, #9139S, 1:5000), phospho-AKT(S473) (Cell Signaling, #9271, 1:1000), total AKT (Cell Signaling, #9272, 1:5000), phospho-S6RP(Ser235/236) (Cell Signaling, #4858, 1:1000), total S6RP (Cell Signaling, #2317, 1:5000), Vinculin (Sigma-Aldrich, #V9264, 1:20,000), Cyclophilin B (Cell Signaling, #43603, 1:1500), and β-Actin (Sigma-Alrich, #A5441, 1:20,000). The following secondary antibodies were utilized for immunoblotting: Goat Anti-Rabbit IgG (H+L)-HRP Conjugate (Bio-Rad, #1706515) and Goat Anti-Mouse IgG (H+L)-HRP Conjugate (Bio-Rad, #1706516).

Proteome Profiler Arrays (R&D Systems, Inc., #ARY005B) were utilized to assess and quantify the relative level of human cytokines in KNS42 parental, sh*H3F3A*-, sh*SETD2*-, and pLenti-CRISPR-STAT3-V2-expressing cells. Cell lysates from each cell type were quantified by BCA assay and equal amounts of cell lysate were incubated with each membrane per the

manufacturer's instructions. All membranes were exposed to the same autoradiographic film for increasing intervals of time to capture signal across each array. Densitometric analysis was carried out use Image Studio Lite software (LI-COR) and normalized Z-scores calculated for each respective cytokine detected.

Histone extraction

Approximately 1.5 x 10^6 culture cells were collected and pelleted. Cells were washed with PBS and suspended in 1.5 mL hypotonic lysis buffer (containing protease/phosphatase inhibitors, 10 mM Tris HCl pH 8, 1 mM KCl, and 1.5 mM $MgCl_2$). Cells were incubated in hypotonic buffer for 30 minutes to promote lysis and pelleted by centrifugation at 10,000xg for 10 minutes at 4 ℃. After discarding supernatants, nuclei were re-suspended in 400 µl sulfuric acid (0.4 N) and incubated overnight at 4 ℃. Samples underwent centrifugation at 16,000xg for 10 minutes at 4 ℃, and resultant supernatant containing histones was transferred to new tubes. 132 µl trichloroacetic acid was added dropwise to each sample, thoroughly mixed, and incubated on ice for 30 minutes. Histones were pelleted by centrifugation at 16,000xg for 10 minutes at 4 ℃. Supernatant was removed and pellets were washed with ice-cold acetone, followed by centrifugation at 16,000xg for 5 minutes at 4 ℃. Acetone wash steps were repeated a total of three times. Histone pellets were then dried at room temperature for 20-30 minutes, re-suspended in 200 µl distilled water, and quantified for downstream application.

Enzyme-Linked Solid-Phase Immunosorbent Assay (ELISA)

To measure LIF content of cell culture supernatants, we utilized a high-sensitivity ELISA for human LIF (ThermoFisher, #BMS242). ELISA experiments were carried out according to the

manufacturer's instructions. Briefly, cells were seeded at a density of 1 x 10^5 into 6 well plates in equal amounts of culture medium and grown in a humidified incubator at 37°C and 5% CO_2 until experimental endpoint. Culture media and cells were isolated separately. Cells counts were conducted to determine cell number. After preparation of microwell strips, standards and culture media were loaded into wells in technical replicate for each condition. Dilution factors for culture media from each cell line were empirically determined before experiments to ensure signal from samples fell within the linear range of the standards. After proper incubation, wash, and development steps, absorbance was measured at 450 nm using a spectrophotometer. Supernatant concentrations of LIF from experimental samples were determined via extrapolation from standard curves and normalized by cell number for each condition.

RT-qPCR

RNA was collected using TRIzol® (ThermoFisher, 15596026). TaqMan® RNA-to-Ct 1-Step Kit was used to carry out reactions (ThermoFisher, #4392938). Quantitative real-time PCR was conducted in technical triplicates using 100 ng total RNA and TaqMan probes (ThermoFisher) for human LIF (Hs01055668_m1) and TBP. RT-qPCR was performed using an ABI 7900HT Sequence Detection System. Relative expression was calculated by the 2^(−ΔΔCt) method using SDS software.

Cell counting and *in vitro* pharmacology

Cell proliferation experiments were carried out using trypan blue exclusion assays or bioluminescence-based reporter assays for 96 hours of treatment. For trypan blue experiments utilizing Stattic, 5.0 x 10^4 cells were plated in 24 well plates. For trypan blue experiments utilizing

WP1066, 2.5 x 10^4 cells were seeded in 24 well plates. Other trypan blue assays to assess cell growth were conducted with cells seeded at a density of 5.0 x 10^4 in 24 well plates. After the indicated treatment (if any) and time, cells were isolated using trypsin or Accutase and re-suspended in constant volume before quantification. For all bioluminescence-based assays, 1.0 x 10^4 cells were seeded in 100 μl total volume in 96 well plates. After indicated treatment and time, 10 μl luciferin (15 mg/mL, GoldBio, LUCK 115144-35-9) was added to each well. Plates were protected from light and incubated at room temperature for 5 minutes. Bioluminescence assays were standardized to ensure a linear relationship between cell number and signal at assay endpoints. A Synergy HTX plate reader was utilized to capture luminescent signal. Multiple independent experiments (*n*=3 or greater) were carried out for all cell growth and cytotoxicity assays. A minimum of four technical replicates were collected for each assay condition. Stattic (Selleckchem, #S7024), SH-4-54 (Cayman Chemical, #25982), WP1066 (Cayman Chemical, #14736), GSK-J4 (Selleckchem, #S7070), and GSK-343 (Cayman Chemical, #14094) were reconstituted in 100% DMSO before further dilution and use.

Extended reduced representation bisulfite sequencing (ERRBS)

ERRBS library preparation and sequencing was performed as previously described (Bayliss *et al.*, 2016). Briefly, DNA was digested with the restriction enzyme MspI (R0106, New England Biolabs) and then phenol extracted, ethanol precipitated, end-repaired, A-tailed and ligated to methylated TruSeq adapters (Illumina Inc). Two size fragment lengths of 150–250 bp and 250–400 bp were then gel isolated and subjected to overnight bisulfite conversion using EZ DNA methylation kit (D5030, Zymo Research), purified and PCR amplified using TruSeq primers (Illumina Inc). The resulting libraries were normalized, pooled, multiplexed and clustered on

single read flow cells and sequenced for 50 cycles on an Illumina HiSeq 2500. Base call files generated from the sequencer were de-multiplexed and converted to FASTQ files using the Illumina CASAVA 1.8.2 pipeline. These were then aligned and post-processed to produce methylation calls at a base pair resolution using a previously described pipeline. CpG sites in the resulting ERRBS data were then interrogated for methylation patterns and differential methylation (q value < 0.01 and methylation percentage difference of at least 25%) using methylKit. The differential methylation data was then queried for differentially methylated regions (DMRs) using eDMR (Li *et al.,* 2013).

ChIP-sequencing

H3.3G34R, H3.3WT, and H3.3K27M mNSCs were fixed with 1% formaldehyde for 15 min and quenched with 0.125 M glycine. Chromatin was isolated by the addition of lysis buffer and lysates were sonicated and the DNA sheared to an average length of 300-500 bp. Genomic DNA was prepared by treating aliquots of chromatin with RNase, proteinase K and heat for de-crosslinking, followed by ethanol precipitation. Pellets were re-suspended and the DNA was quantified on a NanoDrop spectrophotometer. Extrapolation to the original chromatin volume allowed quantitation of the total chromatin yield. An aliquot of chromatin (30 μg) was precleared with protein A agarose beads (Invitrogen), and soluble *Drosophila* chromatin was spiked-in to an amount equivalent to 5-10% of mouse chromatin present. Genomic DNA regions of interest were isolated using 4 μg of antibody against H3K36me3 (ActiveMotif #61021), H3K27me3 (ActiveMotif, #39155), H3K27ac (ActiveMotif, #39133), and H3K4me3 (ActiveMotif, #39159). Complexes were washed, eluted from the beads with SDS buffer, and subjected to RNase and proteinase K treatment. Crosslinks were reversed by overnight incubation at 65 °C. ChIP DNA

was purified by phenol-chloroform extraction and ethanol precipitation. Quantitative PCR reactions were carried out in triplicate on specific genomic regions using SYBR Green Supermix (Bio-Rad). The resulting signals were normalized for primer efficiency by carrying out QPCR for each primer pair using Input DNA.

Illumina sequencing libraries were prepared from the ChIP and Input DNAs by the standard consecutive enzymatic steps of end-polishing, dA-addition, and adaptor ligation. Steps were performed on an automated system (Apollo 342, Wafergen Biosystems/Takara). After a final PCR amplification step, the resulting DNA libraries were quantified and sequenced on Illumina's NextSeq 500 (75 nt reads, single end). Reads were aligned to the mouse genome (mm10) using the BWA algorithm. Duplicate reads were removed and only uniquely mapped reads (mapping quality >= 25) were used for further analysis. Alignments were extended in silico at their 3'-ends to a length of 200 bp, which is the average genomic fragment length in the size-selected library, and assigned to 32-nt bins along the genome. For active histone marks (H3K4me3 and H3K27ac), peak locations were determined using the MACS algorithm (v2.1.0) with a cutoff of *P*-value = 1e-7. For H3K27me3 enriched regions were identified using the SICER algorithm at a cutoff of FDR 1E-10 and a max gap parameter of 600 bp. Spike-in of Drosophila chromatin was performed and the number of test tags were normalized by the same number of spike-in Drosophila tags for each sample. Peaks that were on the ENCODE blacklist of known false ChIP-Seq peaks were removed. The data was visualized using Integrative Genomics Viewer (IGV) genome browser.

RNA-sequencing

RNA-sequencing was performed as previously described (Bayliss *et al.*, 2016). RNA was extracted with Trizol (Invitrogen) and treated with DNase (Sigma-Aldrich). RNA sequencing libraries were

prepared according to the Illumina TruSeq protocol and were sequenced on the HiSeq 2000. RNA-seq data generated were aligned to mouse reference genome using bowtie and analyzed using the RSEM software package with default parameters. Differentially expressed genes were defined using empirical Bayes hierarchical models (EBSeq) that factors for mapping ambiguity variance. Pathway analysis of differentially regulated genes was performed using GSEA (http://software.broadinstitute.org/gsea/).

Single cell RNA-sequencing

To assess JAK/STAT pathway genes in H3G34R/V tumors at the single-cell level, single-cell and single-nuclei RNA-seq data from 16 patient tumor samples was obtained from Chen *et al.* (2020). Cell annotations were used as in the original study, with assignment of each cell to its most similar normal brain cell type, classification of each cell as normal or malignant, and coordinates in two-dimensional Uniform manifold approximation and projection (UMAP) embeddings. Expression levels of JAK/STAT were assessed at two levels: **(1)** across malignant cells from all patient samples, and **(2)** in four individual tumors including both malignant and normal cells. Expression levels shown in UMAP embeddings are normalized values, where for each cell, counts for all genes are scaled to a total of 10,000 unique molecular identifiers (UMIs), and then $\log_2$-transformed.

Immunohistochemistry and quantification for mouse and patient tumors

Immunohistochemistry was performed using serial sections from mouse or human tumor samples. Demographics of human tumor samples used for quantifications in **Figure 3.27C** and **Figure 3.27E** are indicated in **Table 1.1 (**below). Sections were deparaffinized using xylene and

rehydrated by decreasing concentrations of ethanol in the order of 100%, 95%, and water. Antigen retrieval was treated using a low-boiled 10 mM citrate buffer, pH 6.0. Endogenous peroxidase activity was quenched by 3% hydrogen peroxide. Blocking was performed using 5% goat serum, 1% BSA. Sections were incubated for 5 hours with polyclonal antibodies for Ki-67, GFAP (Dako #Z0334), pSTAT3(705) (Cell Signaling #9145), or STAT3 (Cell Signaling #9139). Tissue sections were then incubated with biotinylated goat anti-rabbit IgG (PK6101, Vector Labs) at 1:200 (Ki-67, 60 min, room temp), 1:1000 (GFAP, 1 hour, room temp), 1:50 (pSTAT3, overnight, 4 °C), or 1:800 (STAT3, 1 hour, room temp) dilutions. The stained sections were visualized using 3,3'Diaminobenzidine (DAB) or Fast Red**.** The Slides were then rinsed, dehydrated, mounted and cover slipped.

Stained sections were scanned and quantified in a blinded manner. For automated scoring, each slide was scanned using an AperioScanscope Scanner (Aperio Vista) and viewed through AperioImageScope software program. Quantification of immunostaining on each JPEG was conducted using an automated analysis program with Matlab's image processing toolbox, based on previously described methodology (Bayliss *et al.,* 2016). The algorithm used color segmentation with RGB color differentiation, K-means clustering, and background-foreground separation with Otsu's thresholding. To arrive at a score, the numbers of extracted pixels were multiplied by their average intensity for each image (represented as pixel units).

Table 1.1. Demographics of patient tumor samples used for immunohistochemistry.

Information on the histologic grade, sex, age at diagnosis, tumor site, and *H3F3A* status in glioma patient cases used for quantification.

Case	Histologic grade	Sex	Age at Dx	Site	*H3F3A status*
1	3	Male	7	Right temporal lobe	H3WT
2	3	Male	5	Left occipital	H3WT
3	3	Male	13	Right temporal	H3WT
4	3	Male	13	Left thalamus	H3WT
5	4	Female	18	Left frontal lobe	H3WT
6	4	Female	9	Right parieto-occipital	H3WT
7	4	Male	23	Pineal/third ventricle	H3WT
8	4	Male	16	Right temporal lobe	H3WT
9	4	Female	31	Cerebrum, NOS	H3WT
10	4	Male	3	Right temporal lobe	H3WT
11	4	Female	16	Cerebellum	H3WT
1	4	Female	0.3	Cerebrum, NOS	H3G34R
2	4	Female	17	Right frontal mass	H3G34R
3	4	Female	16	Left parietal lobe	H3G34R
4	4	Male	18	Right frontal lobe	H3G34R
5	4	Male	18	Left precentral gyrus	H3G34R
6	4	Female	13	Right parietal lobe	H3G34R

Lentiviral gene knockdown using shRNA and CRISPR-Cas9 editing

To knockdown genes using shRNA, 2.5 million HEK293T cells were plated on 100 mm dishes 36 hours prior to transfection. A media change was performed the next day to a volume of 5 mL antibiotic-free media. All lentivirus was prepared using the Mirus TransIT Lentivirus System (Mirus Bio, MIR 6650). Briefly, 2.5 μg transfer DNA, 2.5 μg Packaging DNA Premix, and 15 μl TransIT-Lenti Reagent were mixed in 500 μl Opti-MEM media and incubated at room temperature for 10 minutes. The mixture was added dropwise to the HEK293T cell dish and swirled gently to distribute. The transfected cells were incubated at 37 °C and 5% CO_2 to produce virus for 48 hours.

Lentiviral particles were then harvested and filtered using a 0.45 μm PVDF filter. Next, lentiviral particles were evenly distributed onto target cells. Particle-containing media was removed after 24 hours and target cell media was replenished. After 3 days, infected cells were treated with a proper antibiotic for selection. Lentiviral plasmids utilized for shRNA-mediated knockdown are as follows: sh*H3F3A* (Sigma-Aldrich; TRCN0000144550, TRCN0000139066, TRCN0000139180), sh*LIF* (Sigma-Aldrich; TRCN0000308277, TRCN0000290579, TRCN0000058586), sh*SETD2* (TRCN0000237837, TRCN00002373838, TRCN00002373839), and sh*STAT3* (TRCN000329811, TRCN0000329888). Lentiviral CRISPR-mediated knockout of STAT3 was achieved with pLenti-CRISPR-STAT3-V2 (GenScript).

Mice and housing conditions

Animals were housed in pathogen-free conditions using standard guidelines with continuous access to food and water. Orthotopic brain tumor modeling using mouse PPG or human glioma (KNS42, SJ-HGGx42-c, TS543) cells were carried out in NOD-SCID-IL2R gamma chain-deficient (NSG) mice (Jackson Laboratories, NOD.Cg-*Prkdc*^{scid}*Il2rg*^{tm1Wjl}/SzJ, #005557). Xenograft models established in the flank were carried out in nude mice (Jackson Laboratories, Hsd:Athymic Nude-Foxn1^{nu}, #002019). *In-utero* electroporation models utilized immune competent CD-1 mice (Charles River, Crl:CD1(ICR), #022). All experiments were carried out using cohorts equally comprised of male and female animals.

Murine xenograft models and tumor measurement

For subcutaneous injection, viable cells were first isolated and counted. 1.0 x 10^6 KNS42 parental or sh*LIF* (expressing one of two independent shRNAs) cells were suspended in 50 μl complete culture media (not containing FBS), combined with 50 μl Matrigel, and kept on ice until use. Cell

suspensions were subcutaneously injected into the flank of 6-week-old athymic nude mice. Before beginning treatment, mice were randomized at week 8 post-implantation. Stattic (Selleckchem, #S7024) was dissolved in dimethylsulfoxide (DMSO), titered to the desired concentration of 10 mg/kg, and delivered in 100 μl final volume. Mice received intraperitoneal injection of Stattic every three days for 8 total doses. Tumor growth was measured every three days using Vernier calipers. Tumor volumes were calculated with the formula, Volume (in mm^3) = 1/2 x (L x W x W) where L is the longest diameter (in mm) and W is the shorter diameter (in mm). Five control and five experimental mice, receiving injections in both the left and right flank, were utilized for each experiment.

Murine orthotopic models, tumor measurement, and study endpoints/analysis

Tumor engraftment procedures

The orthotopic model of H3.3G34V tumors was established by injecting 1.0 x 10^6 KNS42 cells with or without STAT3 knockout (suspended in 4 μl complete media without FBS) into the cortex. Independent KNS42 models were utilized to study the effect of WP1066 treatment or STAT3 knockout on tumor progression and mouse survival. Additional orthotopic models of H3.3G34R gliomas were established by injecting 0.3 x 10^6 PPG or 1.0 x 10^6 SJ-HGGx42-c cells (suspended in 4 μl media without FBS) into the cortex. An orthotopic model of H3.3WT glioma was established by injecting 0.3 x 10^6 TS543 cells into the cortex. Lentiviral transduction with a firefly luciferase expression vector was carried out on KNS42 and TS543 cells prior to orthotopic injection. All stereotactic injections were performed on 6-8 week old NSG mice.

Prior to implantation, mice were anesthetized via intraperitoneal administration of ketamine (90 mg/kg) and dexmedetomidine (0.6 mg/kg) and each received carprofen (5.5 mg/kg) as an analgesic. Each mouse was mounted onto a stereotaxic apparatus. Using aseptic technique,

a small incision was made using a scalpel along the sagittal axis to reveal sutures. A burr hole was created 3 mm posterior and 2 mm lateral right from the bregma. A sterile Hamilton syringe, loaded with 4 μl cell suspension, was used for each injection. The Hamilton syringe was then aligned and lowered 4 mm into the burr hole relative to the skull surface. At a rate of 1 μl/minute, 2 μl cell suspension was injected a depth of 3 mm, followed by 1 mm retraction, and subsequent injection of the remaining 2 μl cell suspension. Following injection, wounds were clipped with a surgical stapler and each mouse received atipamezol (1.25 mg/kg) via intraperitoneal injection for anesthesia reversal.

In utero electroporation (IUE) tumor modeling

IUE models were generated using immune competent CD-1 mice utilizing previously described methods (Patel *et al.,* 2020). In this system, PPG cells model H3.3G34R tumors by expressing mutant G34R *H3F3A* and PPW cells represent H3.3WT tumors by expressing WT *H3F3A,* both in a dominant-negative *TP53* and constitutively active mutant *PDGFRA*-D842V background (Patel *et al.,* 2020). *In utero* electroporation was performed using sterile technique on isoflurane/oxygen anesthetized pregnant CD-1 females at E13.5. All tumors for this study were generated via lateral ventricle (forebrain) introduction of the following plasmids: **(1)** PB-CAG-DNp53-Ires-Luciferase (dominant-negative TP53), **(2)** PB-CAG-PdgfraD842V-Ires-eGFP (PDGFRA-D842V mutant), and either **(3)** PB-CAG-H3.3G34R-Ires-303 eGFP (H3.3G34R, referred to as PPG) or **(4)** PB-CAG-H3.3WT-Ires-303 eGFP (H3.3WT, referred to as PPW). Plasmids were loaded together into a pulled capillary needle where each plasmid had a final concentration of 1 μg/μl. 1-2 μl plasmid mix was intravesicularly injected into each embryo, followed by electroporation into neural progenitor cells using tweezertrodes at the following conditions: 5 square pulses, 35 V, 50 ms/pulse delivered at 950 ms intervals.

Pharmacological and radiotherapy treatment

Successful tumor engraftment and progression was monitored with weekly bioluminescence imaging using an IVIS Spectrum (PerkinElmer). Experiments were commenced when total flux exceeded a predetermined threshold ($>10^6$ photons/sec for KNS42, H3.3G34R-*IUE*, H3.3G34R-PPG, and TS543 models; $>10^5$ photons/sec for the SJ-HGGx42 model). Mice were randomized into appropriate groups prior to treatment start. WP1066 (obtained from Cayman Chemical, #14736) was prepared using a previous established protocol by Kong *et al*. (2009). Briefly, WP1066 was dissolved in 20 parts dimethylsulfoxide (DMSO) and 80 parts polyethylene glycol 300 (Sigma-Aldrich) to achieve a final concentration of 40 mg/kg. WP1066 treatment was delivered by oral gavage once daily (Monday through Friday) for the duration indicated in treatment paradigms. For experiments involving radiotherapy, whole brain irradiation was performed on mice twice per week (single fraction of 2 Gy/day, Tuesday and Friday) for two consecutive weeks. Ten experimental and ten control mice were utilized for each condition within independent experiments.

Bioluminescence measurements and Kaplan-Meier Analysis Parameters

For bioluminescence imaging, mice received a single intraperitoneal injection of 100 μl D-luciferin (15 mg/mL, GoldBio, LUCK 115144-35-9). Animals were anesthetized using 2% isoflurane while image sequences were captured to enable calculation of peak tumor signal for each mouse at each sampling time point. Total flux was calculated from peak bioluminescent signal from each mouse collected at each time point and normalized to their respective baseline bioluminescent signal before statistical analyses were performed. Kaplan-Meier analyses was performed for H3.3G34R/V orthotopic models using pre-determined endpoints for censoring. H3.3G34V KNS42 (**Figure 3.36F-H**) and H3.3G34R-PPG (**Figure 3.38H**) models testing

WP1066 efficacy used evidence of skull invasion or presence of neurological/physical symptoms, respectively, as the pre-determined endpoint. Survival analysis for KNS42 *STAT3*-KO (**Figure 3.35A-C**) and H3.3G34R-*IUE* (**Figure 3.36C-E**) models was performed by calculating the time elapsed from cell injection or plasmid electroporation, respectively, to observe a three-fold increase in IVIS bioluminescence signal.

Study endpoint and sample preparation

Tumor implantation, IVIS imaging, and euthanasia at study endpoints were performed according to IACUC Guidelines for Animal Use and approved institutional protocols. At the humane endpoint, brains or other xenograft samples were removed, fixed in 4% Paraformaldehyde, and prepared for histological analysis.

DNA methylation analysis of human patient samples

DNA methylation beta values from Illumina HumanMethylation450 BeadChip arrays were obtained from H3.3G34R/V (n=73) and H3.3WT (n=1306) glioma samples from DKFZ (https://www.molecularneuropathology.org/mnp). Following initial filtering of probes (removing X and Y chromosomes, dbSNPs), the resulting 385,184 probes were used for downstream analyses. Differential methylation was performed using limma with an FDR-adjusted P<0.05. Hypergeometric adjusted P-values for gene set overlaps were obtained for hypermethylated ($\log_2$FC>0.3, P_{adj}<0.05) and hypomethylated ($\log_2$FC<-0.3, P_{adj}<0.05) genes and CpGi with differential methylation at *LIF* were identified.

ChromHMM Differential Epigenetic State Analysis

ChromHMM was applied to CHIP-seq maps of various histone modifications (H3K36me3, H3K4me1, H3K27ac, H3K4me3, H3K36me2, and H3K27me3) associated with H3.3G34R, H3.3WT, and H3.3K27M mNSCs to learn and characterize chromatin states using a multivariate Hidden Markov Model. Briefly, ChromHMM models spatial and combinatorial patterns in the data across multiple histone marks to annotate different chromatin states. The *BinarizeBed* function was used to convert bed files of aligned reads into binarized data files for model learning. The *LearnModel* function was used to learn the chromatin state model. A shared, 10-state chromatin model in addition to cell-type-specific annotations were learnt for all the cell types.

Differential histone modification ChIP-seq enrichment and pathway analysis

From the called ChIP-seq peaks, differential regions were identified using MACS2 *bdgdiff*, and the unique regions associated with each cell type were obtained. Peak annotation was performed with respect to the mm10 mouse genome using CHIPseeker's *annotatePeak* function (Yu *et al.*, 2015), with the TSS defined from -5kb to +5kb. Differential peaks falling within promoter regions (5kb upstream of TSS) were mapped to the corresponding genes and enrichment analysis was performed using PANTHER-GO (Mi *et al.*, 2019) for genes that were uniquely enriched across each cell type. Only enriched pathways with a gene count of >10 were considered.

Re-analysis of published data

Previously published H3K36me3 ChIP-seq and RNA-seq data in H3.3G34R and H3.3G34W models were downloaded from the NCBI GEO database with accession numbers GSE106203, GSE149198, GSE149211, and GSE162976 (**Figures 3.2E-G, 3.3A-B, and 3.4B-C**). Published normalized expression Z-score data from PedCBioportal (https://d3b.center/our-

research/pedcbioportal/) was utilized for *in silico* analysis of gene correlations with *H3F3A* expression levels (**Figure 3.7A-C**).

Data and Materials Availability

OPGB-GBM-001 cells were obtained from Dr. Maria Vinci (Department of Hematology/Oncology, Bambino Gesu Children's Hospital-IRCCS, Rome, Italy). SJ-HGGx6-c, SJ-HGGx42-c, SJ-HGGx37-c, and SJ-HGGx39-c were obtained after a material transfer agreement (MTA) from Dr. Suzanne Baker (Department of Developmental Neurobiology, St. Jude Children's Research Hospital, Memphis, TN, USA). mNSCs were obtained after MTA from Dr. Richard J. Gilbertson (St. Jude Children's Research Hospital, Memphis, TN, USA). HA-tagged H3.3G34R, H3.3K27M, and H3.3WT expression plasmids were obtained from C. D. Allis. Human neural stem cells (hNSCs) were obtained from Dr. Eric Raabe (Johns Hopkins University School of Medicine, Baltimore, MD, USA). H3K36me3, H3K4me3, H3K27ac, and H3K27me3 ChIP-seq raw data, RNA-sequencing, and DNA methylation data have been deposited in the National Center for Biotechnology Information (NCBI) Gene Expression Omnibus (GSE161287, GSE161288, and GSE161289).

3.6 Author Contributions & Acknowledgments

Stefan Sweha and Dr. Sriram Venneti conceived the project, analyzed data, constructed figures, and wrote the published manuscript. Dr. Chan Chung and Jill Bayliss prepared samples for ChIP-sequencing and DNA methylation analysis. Stefan Sweha performed transfections/viral transductions, immunoblotting, cell viability studies, and bioinformatic analysis throughout. Stefan Sweha established orthotopic tumor animal models with additional support from Dr. Chan

Chung and Siva Kumar Natarajan. Drs. Pooja Panwalkar and Chan Chung provided tumor implantation protocols and methodological advice for animal procedures. Dr. Timothy Phoenix provided *IUE* model plasmids and Dr. Viveka Nand Yadav optimized *in utero* electroporation techniques and provided mice with H3.3G34R cranial tumors. Dr. Andrew J. Scott, Kari Wilder-Romans, and Dr. Daniel R. Wahl provided guidance and support for *in vivo* studies involving radiation treatment. Drs. Carl J. Koschmann and Suzanne J. Baker gave valuable input regarding *in vivo* models and provided cell lines.

Dr. Drew Pratt provided processed DNA methylation data from human glioma patients. Dr. Tingting Qin provided raw RNA-sequencing data from PPG/PPW cell culture explant models for further analysis. Drs. Alan Mackay and Chris Jones kindly provided ChIP-seq data from H3.3G34R/V human cells. Selin Jessa, Dr. Claudia L. Kleinman, and Dr. Nada Jabado provided single-cell data and interpretation.

Anand Shankar and Visweswaran Ravikumar collaborated for the ChromHMM analyses and worked closely with Stefan Sweha to refine the analysis. Finally, we would also like to acknowledge Piali Mukherjee from the Epigenetics Core Facility at Weill Medical College of Cornell University for assistance with processing of the DNA methylation experiments.

3.7 References

Alzu'bi A, Clowry GJ. Expression of ventral telencephalon transcription factors ASCL1 and DLX2 in the early fetal human cerebral cortex. J Anat. 2019 Sep;235(3):555-568. doi: 10.1111/joa.12971.

Avalle L, Camporeale A, Camperi A, Poli V. STAT3 in cancer: A double edged sword. *Cytokine*. 2017 Oct;98:42-50. doi: 10.1016/j.cyto.2017.03.018.

Baylin SB, Jones PA. Epigenetic Determinants of Cancer. *Cold Spring Harb Perspect Biol*. 2016 Sep 1;8(9):a019505. doi: 10.1101/cshperspect.a019505.

Bayliss J, Mukherjee P, Lu C, Jain SU, Chung C, Martinez D, Sabari B, Margol AS, Panwalkar P, Parolia A, Pekmezci M, McEachin RC, Cieslik M, Tamrazi B, Garcia BA, La Rocca G, Santi M, Lewis PW, Hawkins C, Melnick A, David Allis C, Thompson CB, Chinnaiyan AM, Judkins AR, Venneti S. Lowered H3K27me3 and DNA hypomethylation define poorly prognostic pediatric posterior fossa ependymomas. *Sci Transl Med*. 2016 Nov 23;8(366):366ra161. doi: 10.1126/scitranslmed.aah6904.

Behjati S, Tarpey PS, Presneau N, Scheipl S, Pillay N, Van Loo P, Wedge DC, Cooke SL, Gundem G, Davies H, Nik-Zainal S, Martin S, McLaren S, Goodie V, Robinson B, Butler A, Teague JW, Halai D, Khatri B, Myklebost O, Baumhoer D, Jundt G, Hamoudi R, Tirabosco R, Amary MF, Futreal PA, Stratton MR, Campbell PJ, Flanagan AM. Distinct H3F3A and H3F3B driver mutations define chondroblastoma and giant cell tumor of bone. *Nat Genet*. 2013 Dec;45(12):1479-82. doi: 10.1038/ng.2814.

Bender S, Tang Y, Lindroth AM, Hovestadt V, Jones DT, Kool M, Zapatka M, Northcott PA, Sturm D, Wang W, Radlwimmer B, Højfeldt JW, Truffaux N, Castel D, Schubert S, Ryzhova M, Seker-Cin H, Gronych J, Johann PD, Stark S, Meyer J, Milde T, Schuhmann M, Ebinger M, Monoranu CM, Ponnuswami A, Chen S, Jones C, Witt O, Collins VP, von Deimling A, Jabado N, Puget S, Grill J, Helin K, Korshunov A, Lichter P, Monje M, Plass C, Cho YJ, Pfister SM. Reduced H3K27me3 and DNA hypomethylation are major drivers of gene expression in K27M mutant pediatric high-grade gliomas. *Cancer Cell*. 2013 Nov 11;24(5):660-72. doi: 10.1016/j.ccr.2013.10.006.

Bjerke L, Mackay A, Nandhabalan M, Burford A, Jury A, Popov S, Bax DA, Carvalho D, Taylor KR, Vinci M, Bajrami I, McGonnell IM, Lord CJ, Reis RM, Hargrave D, Ashworth A, Workman P, Jones C. Histone H3.3. mutations drive pediatric glioblastoma through upregulation of MYCN. *Cancer Discov*. 2013 May;3(5):512-9. doi: 10.1158/2159-8290.CD-12-0426.

Bressan RB, Southgate B, Ferguson KM, Blin C, Grant V, Alfazema N, Wills JC, Marques-Torrejon MA, Morrison GM, Ashmore J, Robertson F, Williams CAC, Bradley L, von Kriegsheim A, Anderson RA, Tomlinson SR, Pollard SM. Regional identity of human neural stem cells determines oncogenic responses to histone H3.3 mutants. *Cell Stem Cell*. 2021 May 6;28(5):877-893.e9. doi: 10.1016/j.stem.2021.01.016.

Bromberg JF, Wrzeszczynska MH, Devgan G, Zhao Y, Pestell RG, Albanese C, Darnell JE Jr. Stat3 as an oncogene. *Cell*. 1999 Aug 6;98(3):295-303. doi: 10.1016/s0092-8674(00)81959-5.

Casey BH, Kollipara RK, Pozo K, Johnson JE. Intrinsic DNA binding properties demonstrated for lineage-specifying basic helix-loop-helix transcription factors. *Genome Res*. 2018 Apr;28(4):484-496. doi: 10.1101/gr.224360.117.

Chai EZ, Shanmugam MK, Arfuso F, Dharmarajan A, Wang C, Kumar AP, Samy RP, Lim LH, Wang L, Goh BC, Ahn KS, Hui KM, Sethi G. Targeting transcription factor STAT3 for cancer prevention and therapy. *Pharmacol Ther*. 2016 Jun;162:86-97. doi: 10.1016/j.pharmthera.2015.10.004.

Chan KM, Fang D, Gan H, Hashizume R, Yu C, Schroeder M, Gupta N, Mueller S, James CD, Jenkins R, Sarkaria J, Zhang Z. The histone H3.3K27M mutation in pediatric glioma reprograms H3K27 methylation and gene expression. *Genes Dev*. 2013 May 1;27(9):985-90. doi: 10.1101/gad.217778.113.

Chen CCL, Deshmukh S, Jessa S, Hadjadj D, Lisi V, Andrade AF, Faury D, Jawhar W, Dali R, Suzuki H, Pathania M, A D, Dubois F, Woodward E, Hébert S, Coutelier M, Karamchandani J, Albrecht S, Brandner S, De Jay N, Gayden T, Bajic A, Harutyunyan AS, Marchione DM, Mikael LG, Juretic N, Zeinieh M, Russo C, Maestro N, Bassenden AV, Hauser P, Virga J, Bognar L, Klekner A, Zapotocky M, Vicha A, Krskova L, Vanova K, Zamecnik J, Sumerauer D, Ekert PG, Ziegler DS, Ellezam B, Filbin MG, Blanchette M, Hansford JR, Khuong-Quang DA, Berghuis AM, Weil AG, Garcia BA, Garzia L, Mack SC, Beroukhim R, Ligon KL, Taylor MD, Bandopadhayay P, Kramm C, Pfister SM, Korshunov A, Sturm D, Jones DTW, Salomoni P, Kleinman CL, Jabado N. Histone H3.3G34-Mutant Interneuron Progenitors Co-opt PDGFRA for Gliomagenesis. *Cell*. 2020 Dec 10;183(6):1617-1633.e22. doi: 10.1016/j.cell.2020.11.012.

Chung C, Sweha SR, Pratt D, Tamrazi B, Panwalkar P, Banda A, Bayliss J, Hawes D, Yang F, Lee HJ, Shan M, Cieslik M, Qin T, Werner CK, Wahl DR, Lyssiotis CA, Bian Z, Shotwell JB, Yadav VN, Koschmann C, Chinnaiyan AM, Blüml S, Judkins AR, Venneti S. Integrated Metabolic and Epigenomic Reprograming by H3K27M Mutations in Diffuse Intrinsic Pontine Gliomas. *Cancer Cell*. 2020 Sep 14;38(3):334-349.e9. doi: 10.1016/j.ccell.2020.07.008.

Daina A, Michielin O, Zoete V. SwissADME: a free web tool to evaluate pharmacokinetics, drug-likeness and medicinal chemistry friendliness of small molecules. *Sci Rep*. 2017 Mar 3;7:42717. doi: 10.1038/srep42717.

Deng JY, Sun D, Liu XY, Pan Y, Liang H. STAT-3 correlates with lymph node metastasis and cell survival in gastric cancer. *World J Gastroenterol*. 2010 Nov 14;16(42):5380-7. doi: 10.3748/wjg.v16.i42.5380.

Dhayalan A, Rajavelu A, Rathert P, Tamas R, Jurkowska RZ, Ragozin S, Jeltsch A. The Dnmt3a PWWP domain reads histone 3 lysine 36 trimethylation and guides DNA methylation. *J Biol Chem*. 2010 Aug 20;285(34):26114-20. doi: 10.1074/jbc.M109.089433.

Ernst J, Kellis M. Chromatin-state discovery and genome annotation with ChromHMM. *Nat Protoc*. 2017 Dec;12(12):2478-2492. doi: 10.1038/nprot.2017.124.

Fang D, Gan H, Lee JH, Han J, Wang Z, Riester SM, Jin L, Chen J, Zhou H, Wang J, Zhang H, Yang N, Bradley EW, Ho TH, Rubin BP, Bridge JA, Thibodeau SN, Ordog T, Chen Y, van Wijnen AJ, Oliveira AM, Xu RM, Westendorf JJ, Zhang Z. The histone H3.3K36M mutation reprograms the epigenome of chondroblastomas. *Science*. 2016 Jun 10;352(6291):1344-8. doi: 10.1126/science.aae0065.

Fang J, Huang Y, Mao G, Yang S, Rennert G, Gu L, Li H, Li GM. Cancer-driving H3G34V/R/D mutations block H3K36 methylation and H3K36me3-MutSα interaction. *Proc Natl Acad Sci USA*. 2018 Sep 18;115(38):9598-9603. doi: 10.1073/pnas.1806355115.

Fontebasso AM, Liu XY, Sturm D, Jabado N. Chromatin remodeling defects in pediatric and young adult glioblastoma: a tale of a variant histone 3 tail. *Brain Pathol*. 2013a Mar;23(2):210-6. doi: 10.1111/bpa.12023.

Fontebasso AM, Schwartzentruber J, Khuong-Quang DA, Liu XY, Sturm D, Korshunov A, Jones DT, Witt H, Kool M, Albrecht S, Fleming A, Hadjadj D, Busche S, Lepage P, Montpetit A, Staffa A, Gerges N, Zakrzewska M, Zakrzewski K, Liberski PP, Hauser P, Garami M, Klekner A, Bognar L, Zadeh G, Faury D, Pfister SM, Jabado N, Majewski J. Mutations in SETD2 and genes affecting histone H3K36 methylation target hemispheric high-grade gliomas. *Acta Neuropathol*. 2013b May;125(5):659-69. doi: 10.1007/s00401-013-1095-8.

Gao L, Li F, Dong B, Zhang J, Rao Y, Cong Y, Mao B, Chen X. Inhibition of STAT3 and ErbB2 suppresses tumor growth, enhances radiosensitivity, and induces mitochondria-dependent apoptosis in glioma cells. *Int J Radiat Oncol Biol Phys*. 2010 Jul 15;77(4):1223-31. doi: 10.1016/j.ijrobp.2009.12.036.

Gao L, Li FS, Chen XH, Liu QW, Feng JB, Liu QJ, Su X. Radiation induces phosphorylation of STAT3 in a dose- and time-dependent manner. *Asian Pac J Cancer Prev*. 2014;15(15):6161-4. doi: 10.7314/apjcp.2014.15.15.6161.

Gomes AP, Ilter D, Low V, Rosenzweig A, Shen ZJ, Schild T, Rivas MA, Er EE, McNally DR, Mutvei AP, Han J, Ou YH, Cavaliere P, Mullarky E, Nagiec M, Shin S, Yoon SO, Dephoure N, Massagué J, Melnick AM, Cantley LC, Tyler JK, Blenis J. Dynamic Incorporation of Histone H3 Variants into Chromatin Is Essential for Acquisition of Aggressive Traits and Metastatic Colonization. *Cancer Cell*. 2019 Oct 14;36(4):402-417.e13. doi: 10.1016/j.ccell.2019.08.006.

Grasso CS, Tang Y, Truffaux N, Berlow NE, Liu L, Debily MA, Quist MJ, Davis LE, Huang EC, Woo PJ, Ponnuswami A, Chen S, Johung TB, Sun W, Kogiso M, Du Y, Qi L, Huang Y, Hütt-Cabezas M, Warren KE, Le Dret L, Meltzer PS, Mao H, Quezado M, van Vuurden DG, Abraham J, Fouladi M, Svalina MN, Wang N, Hawkins C, Nazarian J, Alonso MM, Raabe EH, Hulleman E, Spellman PT, Li XN, Keller C, Pal R, Grill J, Monje M. Functionally defined therapeutic targets in diffuse intrinsic pontine glioma. *Nat Med*. 2015 Jun;21(6):555-9. doi: 10.1038/nm.3855.

Grimaldi P, Parras C, Guillemot F, Rossi F, Wassef M. Origins and control of the differentiation of inhibitory interneurons and glia in the cerebellum. Dev Biol. 2009 Apr 15;328(2):422-33. doi: 10.1016/j.ydbio.2009.02.008.

Harhous Z, Booz GW, Ovize M, Bidaux G, Kurdi M. An Update on the Multifaceted Roles of STAT3 in the Heart. *Front Cardiovasc Med*. 2019 Oct 25;6:150. doi: 10.3389/fcvm.2019.00150.

Heinrich PC, Behrmann I, Müller-Newen G, Schaper F, Graeve L. Interleukin-6-type cytokine signalling through the gp130/Jak/STAT pathway. *Biochem J*. 1998 Sep 1;334 (Pt 2)(Pt 2):297-314. doi: 10.1042/bj3340297.

Helms AW, Battiste J, Henke RM, Nakada Y, Simplicio N, Guillemot F, Johnson JE. Sequential roles for Mash1 and Ngn2 in the generation of dorsal spinal cord interneurons. *Development*. 2005 Jun;132(12):2709-19. doi: 10.1242/dev.01859.

Hillmer EJ, Zhang H, Li HS, Watowich SS. STAT3 signaling in immunity. *Cytokine Growth Factor Rev*. 2016 Oct;31:1-15. doi: 10.1016/j.cytogfr.2016.05.001.

Hou J, Lv A, Deng Q, Zhang G, Hu X, Cui H. TROP2 promotes the proliferation and metastasis of glioblastoma cells by activating the JAK2/STAT3 signaling pathway. *Oncol Rep*. 2019 Feb;41(2):753-764. doi: 10.3892/or.2018.6859.

Hussain SF, Kong LY, Jordan J, Conrad C, Madden T, Fokt I, Priebe W, Heimberger AB. A novel small molecule inhibitor of signal transducers and activators of transcription 3 reverses immune tolerance in malignant glioma patients. *Cancer Res*. 2007 Oct 15;67(20):9630-6. doi: 10.1158/0008-5472.CAN-07-1243..

Huynh J, Chand A, Gough D, Ernst M. Therapeutically exploiting STAT3 activity in cancer - using tissue repair as a road map. *Nat Rev Cancer*. 2019 Feb;19(2):82-96. doi: 10.1038/s41568-018-0090-8.

Iwamaru A, Szymanski S, Iwado E, Aoki H, Yokoyama T, Fokt I, Hess K, Conrad C, Madden T, Sawaya R, Kondo S, Priebe W, Kondo Y. A novel inhibitor of the STAT3 pathway induces apoptosis in malignant glioma cells both in vitro and in vivo. *Oncogene*. 2007 Apr 12;26(17):2435-44. doi: 10.1038/sj.onc.1210031.

Jain SU, Khazaei S, Marchione DM, Lundgren SM, Wang X, Weinberg DN, Deshmukh S, Juretic N, Lu C, Allis CD, Garcia BA, Jabado N, Lewis PW. Histone H3.3 G34 mutations promote aberrant PRC2 activity and drive tumor progression. *Proc Natl Acad Sci USA*. 2020 Nov 3;117(44):27354-27364. doi: 10.1073/pnas.2006076117.

Jiao F, Li Z, He C, Xu W, Yang G, Liu T, Shen H, Cai J, Anastas JN, Mao Y, Yu Y, Lan F, Shi YG, Jones C, Xu Y, Baker SJ, Shi Y, Guo R. RACK7 recognizes H3.3G34R mutation to suppress expression of MHC class II complex components and their delivery pathway in pediatric glioblastoma. *Sci Adv*. 2020 Jul 17;6(29):eaba2113. doi: 10.1126/sciadv.aba2113.

Johnson RA, Wright KD, Poppleton H, Mohankumar KM, Finkelstein D, Pounds SB, Rand V, Leary SE, White E, Eden C, Hogg T, Northcott P, Mack S, Neale G, Wang YD, Coyle B, Atkinson J, DeWire M, Kranenburg TA, Gillespie Y, Allen JC, Merchant T, Boop FA, Sanford RA, Gajjar A, Ellison DW, Taylor MD, Grundy RG, Gilbertson RJ. Cross-species genomics matches driver mutations and cell compartments to model ependymoma. *Nature*. 2010 Jul 29;466(7306):632-6. doi: 10.1038/nature09173.

Johnston PA, Grandis JR. STAT3 signaling: anticancer strategies and challenges. *Mol Interv*. 2011 Feb;11(1):18-26. doi: 10.1124/mi.11.1.4.

Jones C, Karajannis MA, Jones DTW, Kieran MW, Monje M, Baker SJ, Becher OJ, Cho YJ, Gupta N, Hawkins C, Hargrave D, Haas-Kogan DA, Jabado N, Li XN, Mueller S, Nicolaides T, Packer RJ, Persson AI, Phillips JJ, Simonds EF, Stafford JM, Tang Y, Pfister SM, Weiss WA. Pediatric high-grade glioma: biologically and clinically in need of new thinking. *Neuro Oncol*. 2017 Feb 1;19(2):153-161. doi: 10.1093/neuonc/now101.

Jorstad NL, Wilken MS, Todd L, Finkbeiner C, Nakamura P, Radulovich N, Hooper MJ, Chitsazan A, Wilkerson BA, Rieke F, Reh TA. STAT Signaling Modifies Ascl1 Chromatin Binding and Limits Neural Regeneration from Muller Glia in Adult Mouse Retina. *Cell Rep*. 2020 Feb 18;30(7):2195-2208.e5. doi: 10.1016/j.celrep.2020.01.075.

Kallappagoudar S, Yadav RK, Lowe BR, Partridge JF. Histone H3 mutations--a special role for H3.3 in tumorigenesis? *Chromosoma*. 2015 Jun;124(2):177-89.
doi: 10.1007/s00412-015-0510-4.

Kato F, Fiorentino FP, Alibés A, Perucho M, Sánchez-Céspedes M, Kohno T, Yokota J. MYCL is a target of a BET bromodomain inhibitor, JQ1, on growth suppression efficacy in small cell lung cancer cells. *Oncotarget*. 2016 Nov 22;7(47):77378-77388.
doi: 10.18632/oncotarget.12671.

Khazaei S, De Jay N, Deshmukh S, Hendrikse LD, Jawhar W, Chen CCL, Mikael LG, Faury D, Marchione DM, Lanoix J, Bonneil É, Ishii T, Jain SU, Rossokhata K, Sihota TS, Eveleigh R, Lisi V, Harutyunyan AS, Jung S, Karamchandani J, Dickson BC, Turcotte R, Wunder JS, Thibault P, Lewis PW, Garcia BA, Mack SC, Taylor MD, Garzia L, Kleinman CL, Jabado N. H3.3 G34W Promotes Growth and Impedes Differentiation of Osteoblast-Like Mesenchymal Progenitors in Giant Cell Tumor of Bone. *Cancer Discov*. 2020 Dec;10(12):1968-1987. doi: 10.1158/2159-8290.CD-20-0461.

Kim E, Kim M, Woo DH, Shin Y, Shin J, Chang N, Oh YT, Kim H, Rheey J, Nakano I, Lee C, Joo KM, Rich JN, Nam DH, Lee J. Phosphorylation of EZH2 activates STAT3 signaling via STAT3 methylation and promotes tumorigenicity of glioblastoma stem-like cells. *Cancer Cell*. 2013 Jun 10;23(6):839-52. doi: 10.1016/j.ccr.2013.04.008.

Kim EJ, Leung CT, Reed RR, Johnson JE. In vivo analysis of Ascl1 defined progenitors reveals distinct developmental dynamics during adult neurogenesis and gliogenesis. *J Neurosci*. 2007 Nov 21;27(47):12764-74. doi: 10.1523/JNEUROSCI.3178-07.2007.

Kizer KO, Phatnani HP, Shibata Y, Hall H, Greenleaf AL, Strahl BD. A novel domain in Set2 mediates RNA polymerase II interaction and couples histone H3 K36 methylation with transcript elongation. *Mol Cell Biol*. 2005 Apr;25(8):3305-16. doi: 10.1128/MCB.25.8.3305-3316.2005.

Kong LY, Abou-Ghazal MK, Wei J, Chakraborty A, Sun W, Qiao W, Fuller GN, Fokt I, Grimm EA, Schmittling RJ, Archer GE Jr, Sampson JH, Priebe W, Heimberger AB. A novel inhibitor of signal transducers and activators of transcription 3 activation is efficacious against established central nervous system melanoma and inhibits regulatory T cells. *Clin Cancer Res*. 2008 Sep 15;14(18):5759-68. doi: 10.1158/1078-0432.CCR-08-0377.

Laudisi F, Cherubini F, Monteleone G, Stolfi C. STAT3 Interactors as Potential Therapeutic Targets for Cancer Treatment. *Int J Mol Sci*. 2018 Jun 16;19(6):1787. doi: 10.3390/ijms19061787.

Lee H, Jeong AJ, Ye SK. Highlighted STAT3 as a potential drug target for cancer therapy. *BMB Rep*. 2019 Jul;52(7):415-423. doi: 10.5483/BMBRep.2019.52.7.152.

Lee H, Pal SK, Reckamp K, Figlin RA, Yu H. STAT3: a target to enhance antitumor immune response. *Curr Top Microbiol Immunol*. 2011;344:41-59. doi: 10.1007/82_2010_51.

Lewis PW, Müller MM, Koletsky MS, Cordero F, Lin S, Banaszynski LA, Garcia BA, Muir TW, Becher OJ, Allis CD. Inhibition of PRC2 activity by a gain-of-function H3 mutation found in pediatric glioblastoma. *Science*. 2013 May 17;340(6134):857-61. doi: 10.1126/science.1232245.

Li S, Garrett-Bakelman FE, Akalin A, Zumbo P, Levine R, To BL, Lewis ID, Brown AL, D'Andrea RJ, Melnick A, Mason CE. An optimized algorithm for detecting and annotating regional differential methylation. *BMC Bioinformatics*. 2013;14 Suppl 5(Suppl 5):S10. doi: 10.1186/1471-2105-14-S5-S10.

Lim CP, Cao X. Regulation of Stat3 activation by MEK kinase 1. *J Biol Chem*. 2001 Jun 15;276(24):21004-11. doi: 10.1074/jbc.M007592200.

Liu B, Lu Y, Li J, Liu Y, Liu J, Wang W. Leukemia inhibitory factor promotes tumor growth and metastasis in human osteosarcoma via activating STAT3. *APMIS*. 2015 Oct;123(10):837-46. doi: 10.1111/apm.12427.

Liu SC, Tsang NM, Chiang WC, Chang KP, Hsueh C, Liang Y, Juang JL, Chow KP, Chang YS. Leukemia inhibitory factor promotes nasopharyngeal carcinoma progression and radioresistance. *J Clin Invest*. 2013 Dec;123(12):5269-83. doi: 10.1172/JCI63428.

Louis DN, Perry A, Wesseling P, Brat DJ, Cree IA, Figarella-Branger D, Hawkins C, Ng HK, Pfister SM, Reifenberger G, Soffietti R, von Deimling A, Ellison DW. The 2021 WHO Classification of Tumors of the Central Nervous System: a summary. *Neuro Oncol*. 2021 Aug 2;23(8):1231-1251. doi: 10.1093/neuonc/noab106.

Lu C, Jain SU, Hoelper D, Bechet D, Molden RC, Ran L, Murphy D, Venneti S, Hameed M, Pawel BR, Wunder JS, Dickson BC, Lundgren SM, Jani KS, De Jay N, Papillon-Cavanagh S, Andrulis IL, Sawyer SL, Grynspan D, Turcotte RE, Nadaf J, Fahiminiyah S, Muir TW, Majewski J, Thompson CB, Chi P, Garcia BA, Allis CD, Jabado N, Lewis PW. Histone H3K36 mutations promote sarcomagenesis through altered histone methylation landscape. *Science*. 2016 May 13;352(6287):844-9. doi: 10.1126/science.aac7272.

Mackay A, Burford A, Carvalho D, Izquierdo E, Fazal-Salom J, Taylor KR, Bjerke L, Clarke M, Vinci M, Nandhabalan M, Temelso S, Popov S, Molinari V, Raman P, Waanders AJ, Han HJ, Gupta S, Marshall L, Zacharoulis S, Vaidya S, Mandeville HC, Bridges LR, Martin AJ, Al-Sarraj

S, Chandler C, Ng HK, Li X, Mu K, Trabelsi S, Brahim DH, Kisljakov AN, Konovalov DM, Moore AS, Carcaboso AM, Sunol M, de Torres C, Cruz O, Mora J, Shats LI, Stavale JN, Bidinotto LT, Reis RM, Entz-Werle N, Farrell M, Cryan J, Crimmins D, Caird J, Pears J, Monje M, Debily MA, Castel D, Grill J, Hawkins C, Nikbakht H, Jabado N, Baker SJ, Pfister SM, Jones DTW, Fouladi M, von Bueren AO, Baudis M, Resnick A, Jones C. Integrated Molecular Meta-Analysis of 1,000 Pediatric High-Grade and Diffuse Intrinsic Pontine Glioma. *Cancer Cell*. 2017 Oct 9;32(4):520-537.e5. doi: 10.1016/j.ccell.2017.08.017.

Madhusoodhan PP, Carroll WL, Bhatla T. Progress and Prospects in Pediatric Leukemia. *Curr Probl Pediatr Adolesc Health Care*. 2016 Jul;46(7):229-241. doi: 10.1016/j.cppeds.2016.04.003.

Masliantsev K, Pinel B, Balbous A, Guichet PO, Tachon G, Milin S, Godet J, Duchesne M, Berger A, Petropoulos C, Wager M, Karayan-Tapon L. Impact of STAT3 phosphorylation in glioblastoma stem cells radiosensitization and patient outcome. *Oncotarget*. 2017 Dec 16;9(3):3968-3979. doi: 10.18632/oncotarget.23374.

McLean K, Tan L, Bolland DE, Coffman LG, Peterson LF, Talpaz M, Neamati N, Buckanovich RJ. Leukemia inhibitory factor functions in parallel with interleukin-6 to promote ovarian cancer growth. *Oncogene*. 2019 Feb;38(9):1576-1584. doi: 10.1038/s41388-018-0523-6.

Mi H, Muruganujan A, Ebert D, Huang X, Thomas PD. PANTHER version 14: more genomes, a new PANTHER GO-slim and improvements in enrichment analysis tools. *Nucleic Acids Res*. 2019 Jan 8;47(D1):D419-D426. doi: 10.1093/nar/gky1038.

Morris SA, Shibata Y, Noma K, Tsukamoto Y, Warren E, Temple B, Grewal SI, Strahl BD. Histone H3 K36 methylation is associated with transcription elongation in Schizosaccharomyces pombe. *Eukaryot Cell*. 2005 Aug;4(8):1446-54. doi: 10.1128/EC.4.8.1446-1454.2005.

Ooi SK, Qiu C, Bernstein E, Li K, Jia D, Yang Z, Erdjument-Bromage H, Tempst P, Lin SP, Allis CD, Cheng X, Bestor TH. DNMT3L connects unmethylated lysine 4 of histone H3 to de novo methylation of DNA. *Nature*. 2007 Aug 9;448(7154):714-7. doi: 10.1038/nature05987.

Ott M, Kassab C, Marisetty A, Hashimoto Y, Wei J, Zamler D, Leu JS, Tomaszowski KH, Sabbagh A, Fang D, Gupta P, Priebe W, Zielinski RJ, Burks JK, Long JP, Kong LY, Fuller GN, DeGroot J, Sulman EP, Heimberger AB. Radiation with STAT3 Blockade Triggers Dendritic Cell-T cell Interactions in the Glioma Microenvironment and Therapeutic Efficacy. *Clin Cancer Res*. 2020 Sep 15;26(18):4983-4994. doi: 10.1158/1078-0432.CCR-19-4092.

Ouédraogo ZG, Müller-Barthélémy M, Kemeny JL, Dedieu V, Biau J, Khalil T, Raoelfils LI, Granzotto A, Pereira B, Beaudoin C, Guissou IP, Berger M, Morel L, Chautard E, Verrelle P. STAT3 Serine 727 Phosphorylation: A Relevant Target to Radiosensitize Human Glioblastoma. *Brain Pathol*. 2016 Jan;26(1):18-30. doi: 10.1111/bpa.12254.

Pan YM, Wang CG, Zhu M, Xing R, Cui JT, Li WM, Yu DD, Wang SB, Zhu W, Ye YJ, Wu Y, Wang S, Lu YY. STAT3 signaling drives EZH2 transcriptional activation and mediates poor prognosis in gastric cancer. *Mol Cancer*. 2016 Dec 9;15(1):79. doi: 10.1186/s12943-016-0561-z.

Panwalkar P, Clark J, Ramaswamy V, Hawes D, Yang F, Dunham C, Yip S, Hukin J, Sun Y, Schipper MJ, Chavez L, Margol A, Pekmezci M, Chung C, Banda A, Bayliss JM, Curry SJ, Santi M, Rodriguez FJ, Snuderl M, Karajannis MA, Saratsis AM, Horbinski CM, Carret AS, Wilson B, Johnston D, Lafay-Cousin L, Zelcer S, Eisenstat D, Silva M, Scheinemann K, Jabado N, McNeely PD, Kool M, Pfister SM, Taylor MD, Hawkins C, Korshunov A, Judkins AR, Venneti S. Immunohistochemical analysis of H3K27me3 demonstrates global reduction in group-A childhood posterior fossa ependymoma and is a powerful predictor of outcome. *Acta Neuropathol*. 2017 Nov;134(5):705-714. doi: 10.1007/s00401-017-1752-4.

Park NI, Guilhamon P, Desai K, McAdam RF, Langille E, O'Connor M, Lan X, Whetstone H, Coutinho FJ, Vanner RJ, Ling E, Prinos P, Lee L, Selvadurai H, Atwal G, Kushida M, Clarke ID, Voisin V, Cusimano MD, Bernstein M, Das S, Bader G, Arrowsmith CH, Angers S, Huang X, Lupien M, Dirks PB. ASCL1 Reorganizes Chromatin to Direct Neuronal Fate and Suppress Tumorigenicity of Glioblastoma Stem Cells. *Cell Stem Cell*. 2017 Aug 3;21(2):209-224.e7. doi: 10.1016/j.stem.2017.06.004.

Parras CM, Galli R, Britz O, Soares S, Galichet C, Battiste J, Johnson JE, Nakafuku M, Vescovi A, Guillemot F. Mash1 specifies neurons and oligodendrocytes in the postnatal brain. *EMBO J*. 2004 Nov 10;23(22):4495-505. doi: 10.1038/sj.emboj.7600447.

Patel SK, Hartley RM, Wei X, Furnish R, Escobar-Riquelme F, Bear H, Choi K, Fuller C, Phoenix TN. Generation of diffuse intrinsic pontine glioma mouse models by brainstem-targeted in utero electroporation. *Neuro Oncol*. 2020 Mar 5;22(3):381-392. doi: 10.1093/neuonc/noz197.

Paugh BS, Broniscer A, Qu C, Miller CP, Zhang J, Tatevossian RG, Olson JM, Geyer JR, Chi SN, da Silva NS, Onar-Thomas A, Baker JN, Gajjar A, Ellison DW, Baker SJ. Genome-wide analyses identify recurrent amplifications of receptor tyrosine kinases and cell-cycle regulatory genes in diffuse intrinsic pontine glioma. *J Clin Oncol*. 2011 Oct 20;29(30):3999-4006. doi: 10.1200/JCO.2011.35.5677.

Paugh BS, Zhu X, Qu C, Endersby R, Diaz AK, Zhang J, Bax DA, Carvalho D, Reis RM, Onar-Thomas A, Broniscer A, Wetmore C, Zhang J, Jones C, Ellison DW, Baker SJ. Novel oncogenic PDGFRA mutations in pediatric high-grade gliomas. *Cancer Res*. 2013 Oct 15;73(20):6219-29. doi: 10.1158/0008-5472.CAN-13-1491.

Rane SG, Reddy EP. Janus kinases: components of multiple signaling pathways. *Oncogene*. 2000 Nov 20;19(49):5662-79. doi: 10.1038/sj.onc.1203925.

Raposo AASF, Vasconcelos FF, Drechsel D, Marie C, Johnston C, Dolle D, Bithell A, Gillotin S, van den Berg DLC, Ettwiller L, Flicek P, Crawford GE, Parras CM, Berninger B, Buckley NJ, Guillemot F, Castro DS. Ascl1 Coordinately Regulates Gene Expression and the Chromatin Landscape during Neurogenesis. *Cell Rep*. 2015 Mar 10;10(9):1544-1556. doi: 10.1016/j.celrep.2015.02.025.

Rheinbay E, Suvà ML, Gillespie SM, Wakimoto H, Patel AP, Shahid M, Oksuz O, Rabkin SD, Martuza RL, Rivera MN, Louis DN, Kasif S, Chi AS, Bernstein BE. An aberrant transcription factor network essential for Wnt signaling and stem cell maintenance in glioblastoma. *Cell Rep*. 2013 May 30;3(5):1567-79. doi: 10.1016/j.celrep.2013.04.021.

Rose NR, Klose RJ. Understanding the relationship between DNA methylation and histone lysine methylation. *Biochim Biophys Acta*. 2014 Dec;1839(12):1362-72. doi: 10.1016/j.bbagrm.2014.02.007.

Sangatsuda Y, Miura F, Araki H, Mizoguchi M, Hata N, Kuga D, Hatae R, Akagi Y, Amemiya T, Fujioka Y, Arai Y, Yoshida A, Shibata T, Yoshimoto K, Iihara K, Ito T. Base-resolution methylomes of gliomas bearing histone H3.3 mutations reveal a G34 mutant-specific signature shared with bone tumors. *Sci Rep*. 2020 Sep 30;10(1):16162. doi: 10.1038/s41598-020-73116-x.

Schust J, Sperl B, Hollis A, Mayer TU, Berg T. Stattic: a small-molecule inhibitor of STAT3 activation and dimerization. *Chem Biol*. 2006 Nov;13(11):1235-42. doi: 10.1016/j.chembiol.2006.09.018.

Schwartzentruber J, Korshunov A, Liu XY, Jones DT, Pfaff E, Jacob K, Sturm D, Fontebasso AM, Quang DA, Tönjes M, Hovestadt V, Albrecht S, Kool M, Nantel A, Konermann C, Lindroth A, Jäger N, Rausch T, Ryzhova M, Korbel JO, Hielscher T, Hauser P, Garami M, Klekner A, Bognar L, Ebinger M, Schuhmann MU, Scheurlen W, Pekrun A, Frühwald MC, Roggendorf W, Kramm C, Dürken M, Atkinson J, Lepage P, Montpetit A, Zakrzewska M, Zakrzewski K, Liberski PP, Dong Z, Siegel P, Kulozik AE, Zapatka M, Guha A, Malkin D, Felsberg J, Reifenberger G, von Deimling A, Ichimura K, Collins VP, Witt H, Milde T, Witt O, Zhang C, Castelo-Branco P, Lichter P, Faury D, Tabori U, Plass C, Majewski J, Pfister SM, Jabado N. Driver mutations in histone H3.3 and chromatin remodelling genes in paediatric glioblastoma. *Nature*. 2012 Jan 29;482(7384):226-31. doi: 10.1038/nature10833.

Sen B, Saigal B, Parikh N, Gallick G, Johnson FM. Sustained Src inhibition results in signal transducer and activator of transcription 3 (STAT3) activation and cancer cell survival via altered Janus-activated kinase-STAT3 binding. *Cancer Res*. 2009 Mar 1;69(5):1958-65. doi: 10.1158/0008-5472.CAN-08-2944.

Silva CM. Role of STATs as downstream signal transducers in Src family kinase-mediated tumorigenesis. *Oncogene*. 2004 Oct 18;23(48):8017-23. doi: 10.1038/sj.onc.1208159.

Shahbazi J, Liu PY, Atmadibrata B, Bradner JE, Marshall GM, Lock RB, Liu T. The Bromodomain Inhibitor JQ1 and the Histone Deacetylase Inhibitor Panobinostat Synergistically Reduce N-Myc Expression and Induce Anticancer Effects. *Clin Cancer Res*. 2016 May 15;22(10):2534-44. doi: 10.1158/1078-0432.CCR-15-1666.

Sharifi-Zarchi A, Gerovska D, Adachi K, Totonchi M, Pezeshk H, Taft RJ, Schöler HR, Chitsaz H, Sadeghi M, Baharvand H, Araúzo-Bravo MJ. DNA methylation regulates discrimination of enhancers from promoters through a H3K4me1-H3K4me3 seesaw mechanism. *BMC Genomics*. 2017 Dec 12;18(1):964. doi: 10.1186/s12864-017-4353-7.

Somasundaram K, Reddy SP, Vinnakota K, Britto R, Subbarayan M, Nambiar S, Hebbar A, Samuel C, Shetty M, Sreepathi HK, Santosh V, Hegde AS, Hegde S, Kondaiah P, Rao MR. Upregulation of ASCL1 and inhibition of Notch signaling pathway characterize progressive astrocytoma. *Oncogene*. 2005 Oct 27;24(47):7073-83. doi: 10.1038/sj.onc.1208865.

Spitzner M, Ebner R, Wolff HA, Ghadimi BM, Wienands J, Grade M. STAT3: A Novel Molecular Mediator of Resistance to Chemoradiotherapy. *Cancers*. 2014 Sep 29;6(4):1986-2011. doi: 10.3390/cancers6041986.

Sturm D, Witt H, Hovestadt V, Khuong-Quang DA, Jones DT, Konermann C, Pfaff E, Tönjes M, Sill M, Bender S, Kool M, Zapatka M, Becker N, Zucknick M, Hielscher T, Liu XY, Fontebasso AM, Ryzhova M, Albrecht S, Jacob K, Wolter M, Ebinger M, Schuhmann MU, van Meter T, Frühwald MC, Hauch H, Pekrun A, Radlwimmer B, Niehues T, von Komorowski G, Dürken M, Kulozik AE, Madden J, Donson A, Foreman NK, Drissi R, Fouladi M, Scheurlen W, von Deimling A, Monoranu C, Roggendorf W, Herold-Mende C, Unterberg A, Kramm CM, Felsberg J, Hartmann C, Wiestler B, Wick W, Milde T, Witt O, Lindroth AM, Schwartzentruber J, Faury D, Fleming A, Zakrzewska M, Liberski PP, Zakrzewski K, Hauser P, Garami M, Klekner A, Bognar L, Morrissy S, Cavalli F, Taylor MD, van Sluis P, Koster J, Versteeg R, Volckmann R, Mikkelsen T, Aldape K, Reifenberger G, Collins VP, Majewski J, Korshunov A, Lichter P, Plass C, Jabado N, Pfister SM. Hotspot mutations in H3F3A and IDH1 define distinct epigenetic and biological subgroups of glioblastoma. *Cancer Cell*. 2012 Oct 16;22(4):425-37. doi: 10.1016/j.ccr.2012.08.024.

Teng Y, Ross JL, Cowell JK. The involvement of JAK-STAT3 in cell motility, invasion, and metastasis. *JAKSTAT*. 2014 Jan 1;3(1):e28086. doi: 10.4161/jkst.28086.

Venkatesh S, Smolle M, Li H, Gogol MM, Saint M, Kumar S, Natarajan K, Workman JL. Set2 methylation of histone H3 lysine 36 suppresses histone exchange on transcribed genes. *Nature*. 2012 Sep 20;489(7416):452-5. doi: 10.1038/nature11326.

Verstovsek S, Manshouri T, Quintás-Cardama A, Harris D, Cortes J, Giles FJ, Kantarjian H, Priebe W, Estrov Z. WP1066, a novel JAK2 inhibitor, suppresses proliferation and induces apoptosis in erythroid human cells carrying the JAK2 V617F mutation. *Clin. Cancer Res*. 2008 Feb 1;14(3):788-96. doi: 10.1158/1078-0432.CCR-07-0524.

Voon HPJ, Udugama M, Lin W, Hii L, Law RHP, Steer DL, Das PP, Mann JR, Wong LH. Inhibition of a K9/K36 demethylase by an H3.3 point mutation found in paediatric glioblastoma. *Nat Commun*. 2018 Aug 7;9(1):3142. doi: 10.1038/s41467-018-05607-5.

Vignais ML, Gilman M. Distinct mechanisms of activation of Stat1 and Stat3 by platelet-derived growth factor receptor in a cell-free system. *Mol Cell Biol*. 1999 May;19(5):3727-35. doi: 10.1128/MCB.19.5.3727.

Vignais ML, Sadowski HB, Watling D, Rogers NC, Gilman M. Platelet-derived growth factor induces phosphorylation of multiple JAK family kinases and STAT proteins. *Mol Cell Biol*. 1996 Apr;16(4):1759-69. doi: 10.1128/MCB.16.4.1759.

Wang CY, Shahi P, Huang JT, Phan NN, Sun Z, Lin YC, Lai MD, Werb Z. Systematic analysis of the achaete-scute complex-like gene signature in clinical cancer patients. *Mol Clin Oncol*. 2017 Jan;6(1):7-18. doi: 10.3892/mco.2016.1094.

Wang F, Ma X, Mao G, Zhang X, Kong Z. STAT3 enhances radiation-induced tumor migration, invasion and stem-like properties of bladder cancer. Mol Med Rep. 2021 Jan;23(1):87. doi: 10.3892/mmr.2020.11728.

Wang J, Huang TY, Hou Y, Bartom E, Lu X, Shilatifard A, Yue F, Saratsis A. Epigenomic landscape and 3D genome structure in pediatric high-grade glioma. *Sci Adv*. 2021 Jun 2;7(23):eabg4126. doi: 10.1126/sciadv.abg4126.

Whitehead TP, Metayer C, Wiemels JL, Singer AW, Miller MD. Childhood Leukemia and Primary Prevention. *Curr Probl Pediatr Adolesc Health Care*. 2016 Oct;46(10):317-352. doi: 10.1016/j.cppeds.2016.08.004.

Wong ALA, Hirpara JL, Pervaiz S, Eu JQ, Sethi G, Goh BC. Do STAT3 inhibitors have potential in the future for cancer therapy? *Expert Opin Investig Drugs*. 2017 Aug;26(8):883-887. doi: 10.1080/13543784.2017.1351941.

Wu G, Broniscer A, McEachron TA, Lu C, Paugh BS, Becksfort J, Qu C, Ding L, Huether R, Parker M, Zhang J, Gajjar A, Dyer MA, Mullighan CG, Gilbertson RJ, Mardis ER, Wilson RK, Downing JR, Ellison DW, Zhang J, Baker SJ; St. Jude Children's Research Hospital–Washington University Pediatric Cancer Genome Project. Somatic histone H3 alterations in pediatric diffuse intrinsic pontine gliomas and non-brainstem glioblastomas. *Nat Genet*. 2012 Jan 29;44(3):251-3. doi: 10.1038/ng.1102.

Xie B, Zhang L, Hu W, Fan M, Jiang N, Duan Y, Jing D, Xiao W, Fragoso RC, Lam KS, Sun LQ, Li JJ. Dual blockage of STAT3 and ERK1/2 eliminates radioresistant GBM cells. *Redox Biol*. 2019 Jun;24:101189. doi: 10.1016/j.redox.2019.101189.

Yu G, Wang LG, He QY. ChIPseeker: an R/Bioconductor package for ChIP peak annotation, comparison and visualization. *Bioinformatics*. 2015 Jul 15;31(14):2382-3. doi: 10.1093/bioinformatics/btv145.

Yu H, Lee H, Herrmann A, Buettner R, Jove R. Revisiting STAT3 signalling in cancer: new and unexpected biological functions. *Nat Rev Cancer*. 2014 Nov;14(11):736-46. doi: 10.1038/nrc3818.

Yuan W, Xu M, Huang C, Liu N, Chen S, Zhu B. H3K36 methylation antagonizes PRC2-mediated H3K27 methylation. *J Biol Chem*. 2011 Mar 11;286(10):7983-7989. doi: 10.1074/jbc.M110.194027.

Zhang D, Yang XJ, Luo QD, Fu DL, Li HL, Li HC, Zhang P, Chong T. EZH2 enhances the invasive capability of renal cell carcinoma cells via activation of STAT3. *Mol Med Rep*. 2018 Mar;17(3):3621-3626. doi: 10.3892/mmr.2017.8363.

3.8 Figures & Figure Legends

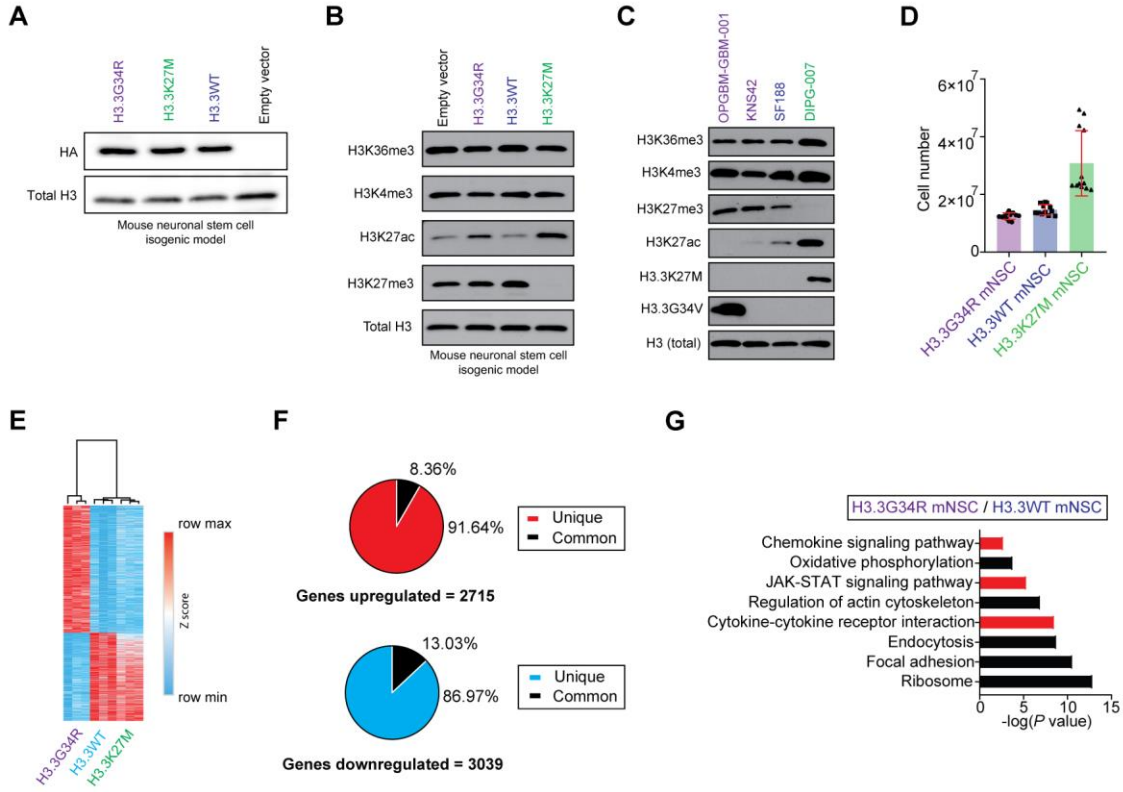

Figure 3.1. Establishment of H3.3G34R, H3.3WT, and H3.3K27M murine cell models.
(A) Representative Western blots for Hemagglutinin (HA) and total H3 in mNSCs stably transduced with HA-tagged H3.3G34R, H3.3K27M, H3.3WT, or empty vector expression plasmids. **(B)** Western blots of parental mNSCs stably transduced with HA-tagged H3.3G34R, H3.3WT, and H3.3K27M expression plasmids for H3K36me3, H3K4me3, H3K27ac, H3K27me3, and total H3. **(C)** Western blots of H3.3G34R OPGB-GBM-001, H3.3G34V KNS42, H3.3WT SF188, and H3.3K27M DIPG-007 for H3K36me3, H3K4me3, H3K27me3, H3K27ac, mutant H3.3K27M, mutant H3.3G34V, and total H3. **(D)** Cell counts (Y-axis) in isogenic mNSCs after 4 days in culture. Note that H3.3K27M (*green*), but not H3.3G34R (*purple*) showed an increase in proliferation relative to H3.3WT (*blue*) mNSC. *n*=3 biological replicates; *n*=4 technical replicates. **(E)** Heatmap of differentially expressed genes determined by RNA-seq in H3.3G34R, H3.3WT, and H3.3K27M mNSCs. **(F)** RNA-seq analysis comparing H3.3G34R/H3.3WT and H3.3K27M/H3.3WT mNSCs demonstrating upregulated/downregulated genes unique to H3.3G34R and shared with H3.3K27M mNSCs. **(G)** Gene set enrichment analysis (GSEA) for genes upregulated in H3.3G34R mNSC compared to H3.3WT mNSC. Data are plotted as mean ± S.D.

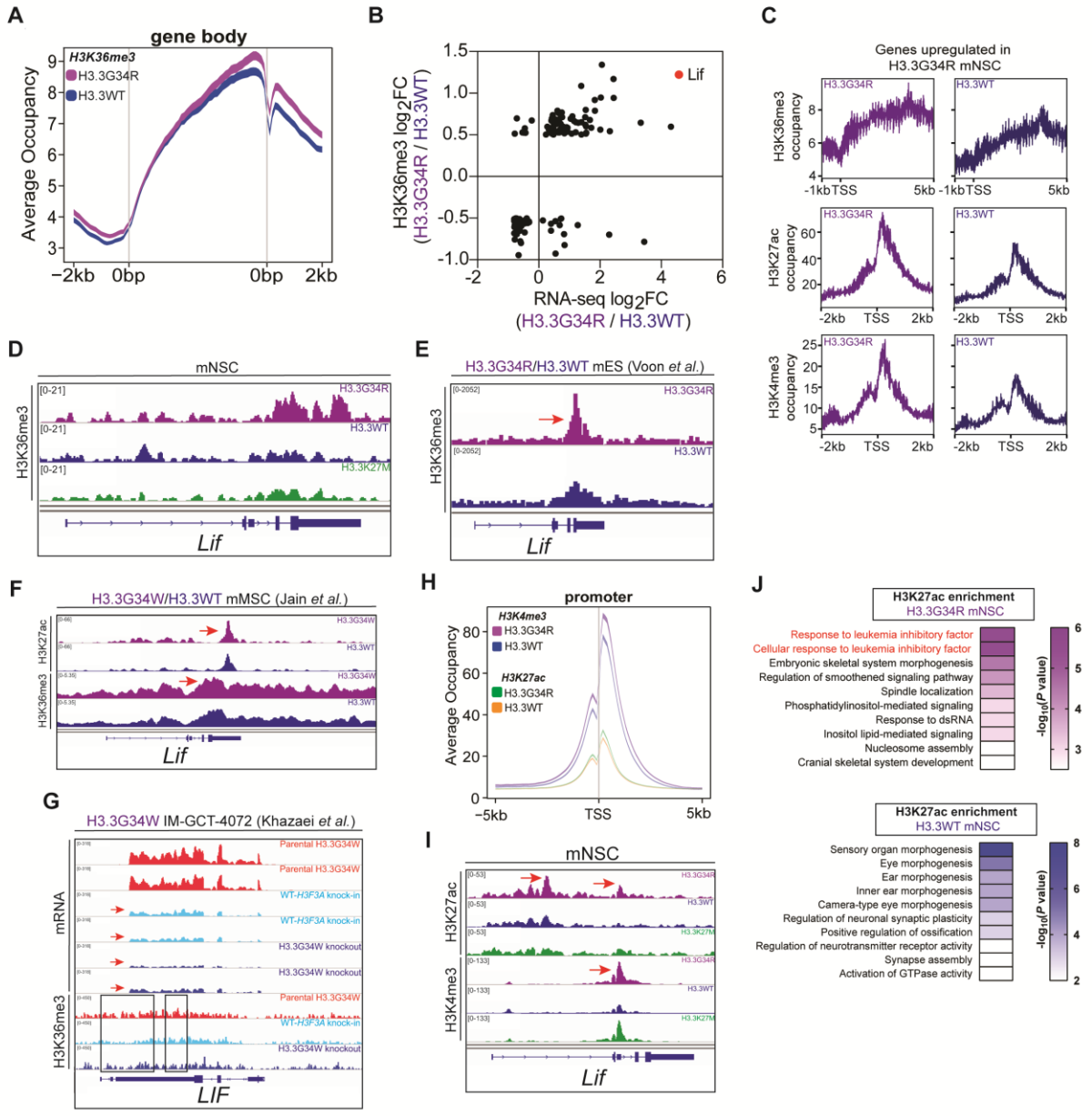

Figure 3.2. H3K36me3, H3K27ac, and H3K4me3 are enriched in H3.3G34R-expressing cells at upregulated genes including *Lif*.

(A) Average H3K36me3 occupancy (Y-axis) at gene bodies in H3.3G34R and H3.3WT mNSCs. **(B)** H3K36me3 enrichment in H3.3G34R/H3.3WT mNSC (log_2 fold-change, Y-axis plotted against H3.3G34R/H3.3WT gene expression (log_2 fold-change, X-axis) for genes with differential H3K36me3. **(C)** Average H3K36me3 occupancy at gene bodies (*top*); H3K27ac (*center*) and H3K4me3 (*bottom*) enrichment at promoter regions (±2kb) plotted for upregulated genes in H3.3G34R (*purple*) *versus* H3.3WT (*blue*) mNSC. **(D)** Integrated Genomics Viewer (IGV) snapshot of H3K36me3 enrichment at the *Lif* gene body in H3.3G34R (*purple*), H3.3WT (*blue*), and H3.3K27M (*green*) mNSC. Red arrow demonstrates enrichment in H3.3G34R mNSC. **(E)** IGV snapshot of H3K36me3 enrichment at *Lif* in an endogenous H3.3G34R and H3.3WT mouse cell model established by Voon *et al.* (2018). **(F)** IGV snapshot of H3K36me3 enrichment at *Lif*

from an endogenous H3.3G34W and H3.3WT mouse cell model established by Jain *et al.* (2020). **(G)** IGV snapshot illustrating decreases in H3K36me3 and RNA-seq signals at *LIF* in a human H3.3G34W bone tumor cell model (Im-GCT-4072; *red*) with CRISPR-Cas9 mediated correction to WT-H3.3 (*light blue*) or knock-out (*dark blue*) of H3.3G34W histone. Red arrows indicate reduced *LIF* expression upon WT-H3F3A knock-in or H3.3G34W knockout compared to controls (*red*); *n*=2 biological replicates per RNA-*seq* condition; *n*=1 biological replicate for ChIP-*seq*. Data derived from Khazaei *et al.* (2020). **(H)** Average H3K27ac and H3K4me3 occupancy (Y-axis) at gene promoters (defined as ±5kb from TSS, X-axis) in H3.3G34R and H3.3WT mNSCs. **(I)** IGV snapshot of H3K27ac and H3K4me3 enrichment at the *Lif* promoter in H3.3G34R (*purple*), H3.3WT (*blue*), and H3.3K27M (*green*) mNSC. Red arrow demonstrates enrichment in H3.3G34R mNSC. **(J)** Pathway analysis for genes with significant, differential deposition of H3K27ac in H3.3G34R mNSC *versus* H3.3WT mNSC (*top panel*) and H3.3WT mNSC *versus* H3.3G34R mNSC (*bottom panel*).

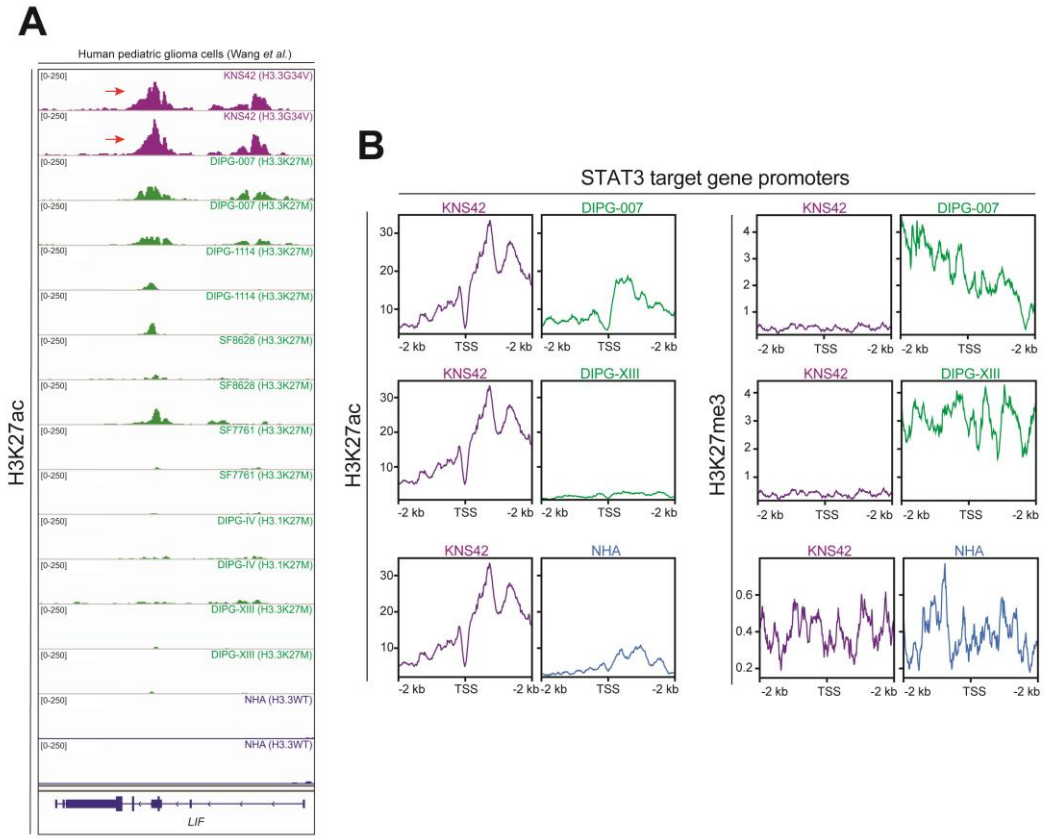

Figure 3.3. H3K27ac is enriched at *LIF* and downstream targets of the STAT3 pathway in KNS42 cells.

(A) IGV snapshot of H3K27ac enrichment at *LIF* in H3.3G34V KNS42 (*purple*) relative to H3K27M-positive cells (DIPG-007, DIPG-1114, SF8628, SF7761, DIPG-IV, DIPG-XIII; *green*) and normal human astrocytes (NHA; *blue*); *n*=2 biological replicates for ChIP-*seq*. Data derived from Wang *et al.* (2021). **(B)** Average H3K27ac (*left panel*) or H3K27me3 (*right panel*) occupancy at promoter region of known STAT3 target genes (±2kb from transcription start site, TSS) in KNS42 (*purple*), DIPG-007 (*green*), DIPG-XIII (*green*), and NHA (*blue*). Red arrows indicate enrichment of the histone modification.

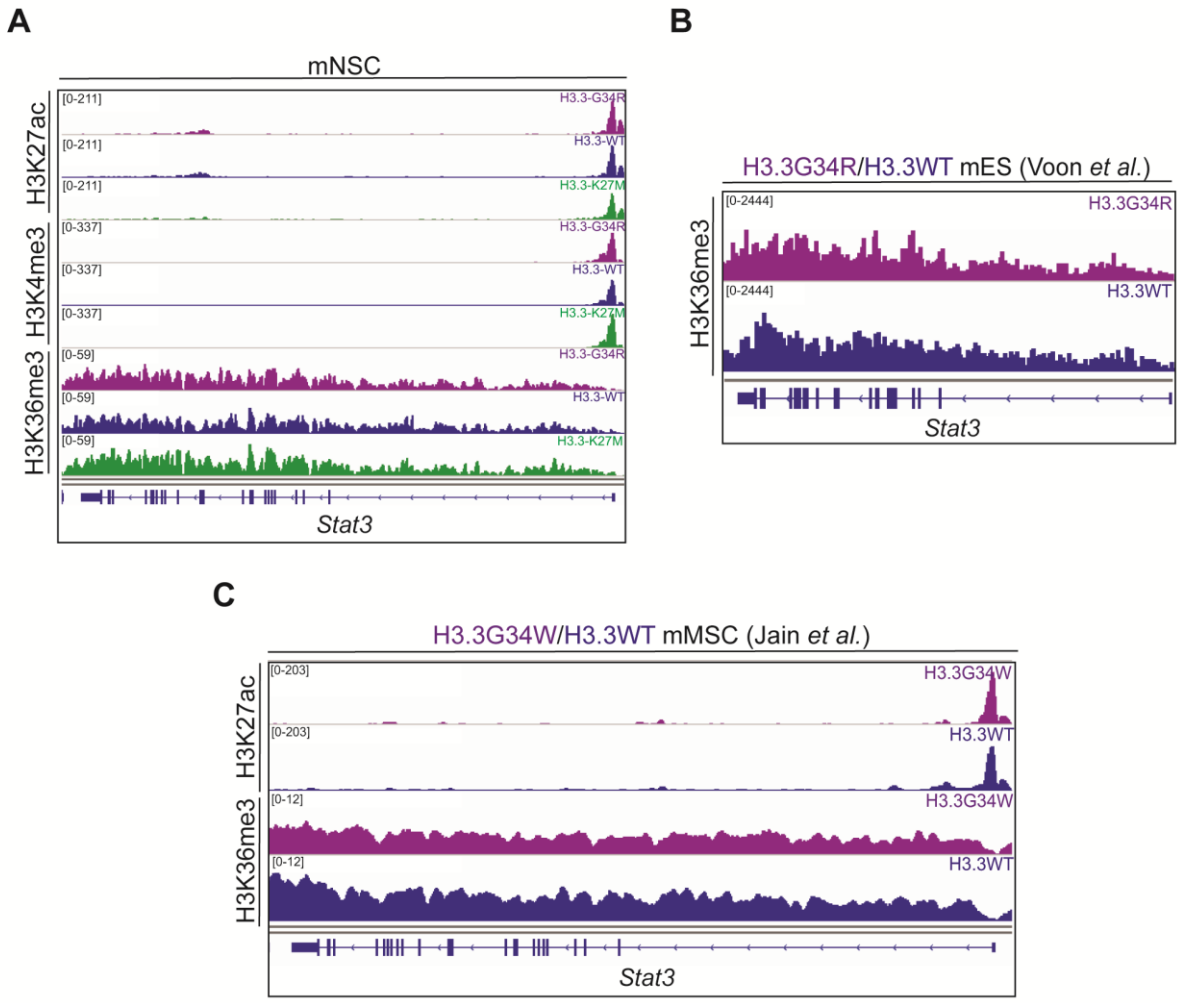

Figure 3.4. Epigenetic modifications at *Stat3* in H3.3G34-mutant cell models.
(A) Integrated Genomics Viewer (IGV) snapshot of H3K27ac, H3K4me3, and H3K36me3 enrichment at *Stat3* in H3.3G34R (*purple*), H3.3WT (*blue*), and H3.3K27M (*green*) mNSC. **(B)** IGV snapshot of H3K36me3 levels at *Stat3* from an endogenous H3.3G34R and H3.3WT mouse cell model established by Voon *et al*. (2018). **(C)** IGV snapshot of H3K36me3 levels at *Stat3* from an endogenous H3.3G34W and H3.3WT mouse cell model established by Jain *et al*. (2020).

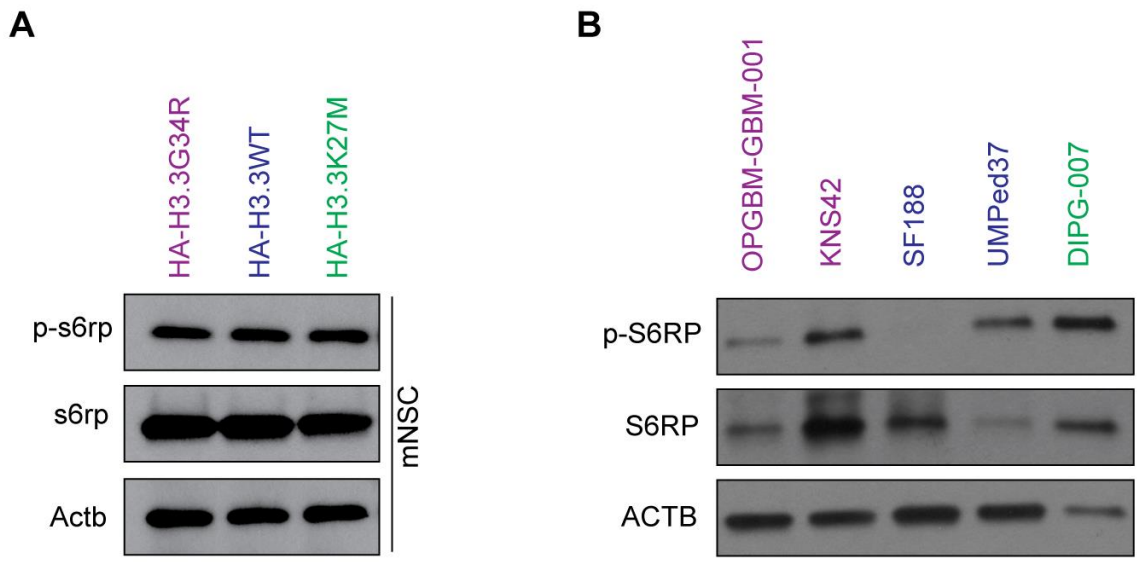

Figure 3.5. Downstream molecular targets of the PI3K/AKT/mTOR pathway are not differentially activated in H3G34R/V cells.
(A) Western blots of cell lysates from mNSCs stably transduced with H3.3G34R, H3.3WT, and H3.3K27M transgenes for phospho-S6 Ribosomal Protein (ps6rp-Ser235/236), total S6 Ribosomal Protein (s6rp), and β-Actin. **(B)** Western blots on cell lysates from pHGG cell lines OPGB-GBM-001 (H3.3G34R), KNS42 (H3.3G34V), SF188 (H3.3WT), UMPed37 (H3.3WT), and HSJD-DIPG-007 (H3.3K27M) for phospho-S6 Ribosomal Protein (pS6RP-Ser235/236), total s6 Ribosomal Protein (S6RP), and β-Actin.

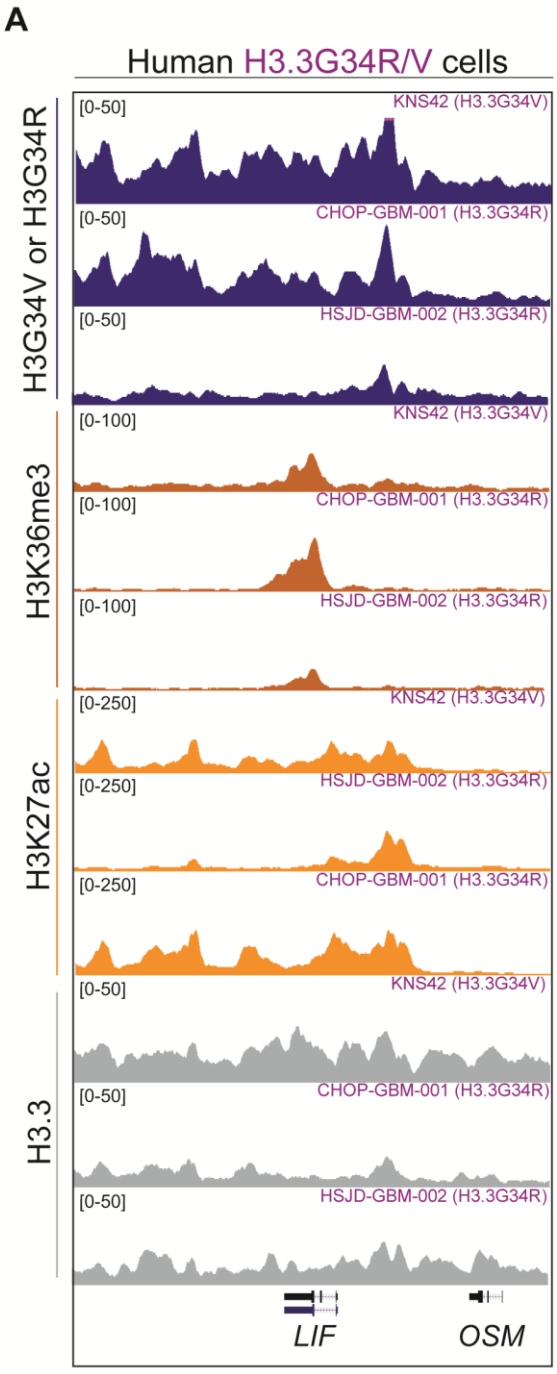

Figure 3.6. Epigenetic modifications at *LIF* in human H3.3G34R/V glioma cells.
(A) IGV snapshot of H3.3G34R or H3.3G34V (*blue*), H3K36me3 (*brown*), H3K27ac (*orange*), and H3.3 (*gray*) enrichment at *LIF* in H3.3G34V (KNS42) and H3.3G34R (CHOP-GBM-001 and HSJD-GBM-002) cells.

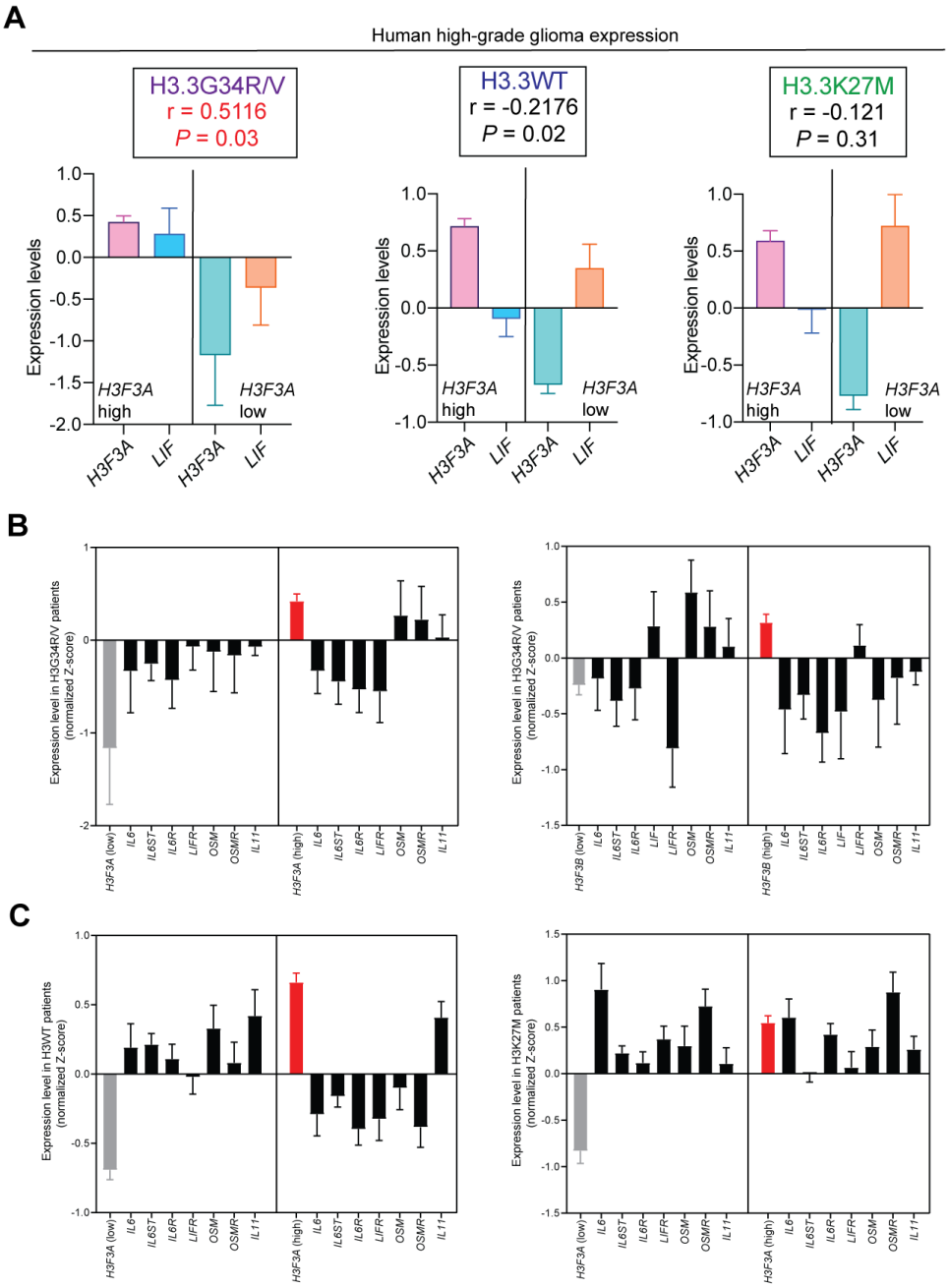

Figure 3.7. *LIF* expression in human pediatric glioma tissues.
(A) Correlation of mutant or wild-type *H3F3A* and *LIF* mRNA transcript levels in H3.3G34R/V (*n*=19), H3.3WT (*n*=101), and H3.3K27M (*n*=71) glioma patients (Pearson's correlation coefficient *r* and *P* values are indicated in boxes above graphs). Note that high expression of *H3F3A* in H3.3G34R/V, but not H3.3WT or H3.3K27M, was associated with increased *LIF* gene expression. **(B)** Bar plots illustrating the relationship between *H3F3A* or *H3F3B* expression and other IL-6 family cytokines in H3WT (*left plot*) or H3K27M (*right plot*) glioma patients. **(C)** Bar plots illustrating the relationship between *H3F3A* (*left plot*) or *H3F3B* (*right plot*) expression and other IL-6 family cytokines in H3G34R/V patients. Data derived from Mackay *et al.* (2017).

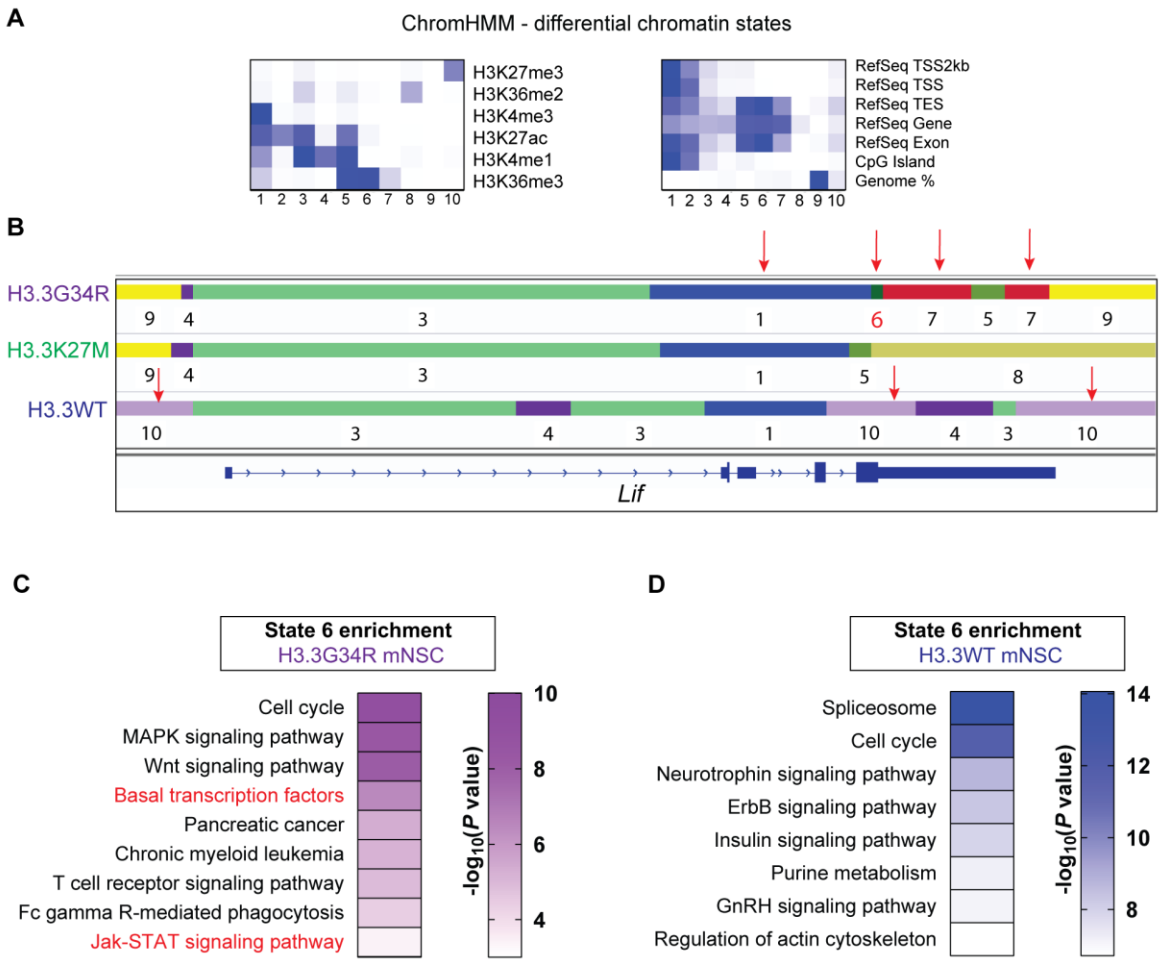

Figure 3.8. ChromHMM analysis of enriched states in mNSC models.
(A) ChromHMM heatmaps illustrating combinatorial patterns of histone epigenetic modifications, H3K36me3, H3K4me1, H3K27ac, H3K4me3, H3K36me2, and H3K27me3, used to assign 10 distinct chromatin states (*left*). Chromatin states are related to each genomic region (CpG islands, exons, transcription start sites) such that each region is associated with its most representative state (*right*). **(B)** Defined chromHMM states assigned to regions of the *Lif* locus in H3.3G34R, H3.3WT, and H3.3K27M 11 mNSCs. Note that State 6 is present only in H3.3G34R cells, State 10 is present exclusively in H3.3WT mNSCs, and State 1 is more widely represented in H3.3G34R mNSC *versus* both H3.3WT and H3.3K27M mNSC. **(C-D)** Pathway analysis for genes demonstrating chromHMM state 6 enrichment in H3.3G34R mNSC *versus* H3.3WT mNSCs **(C)** and H3.3WT *versus* H3.3G34R mNSCs **(D)**.

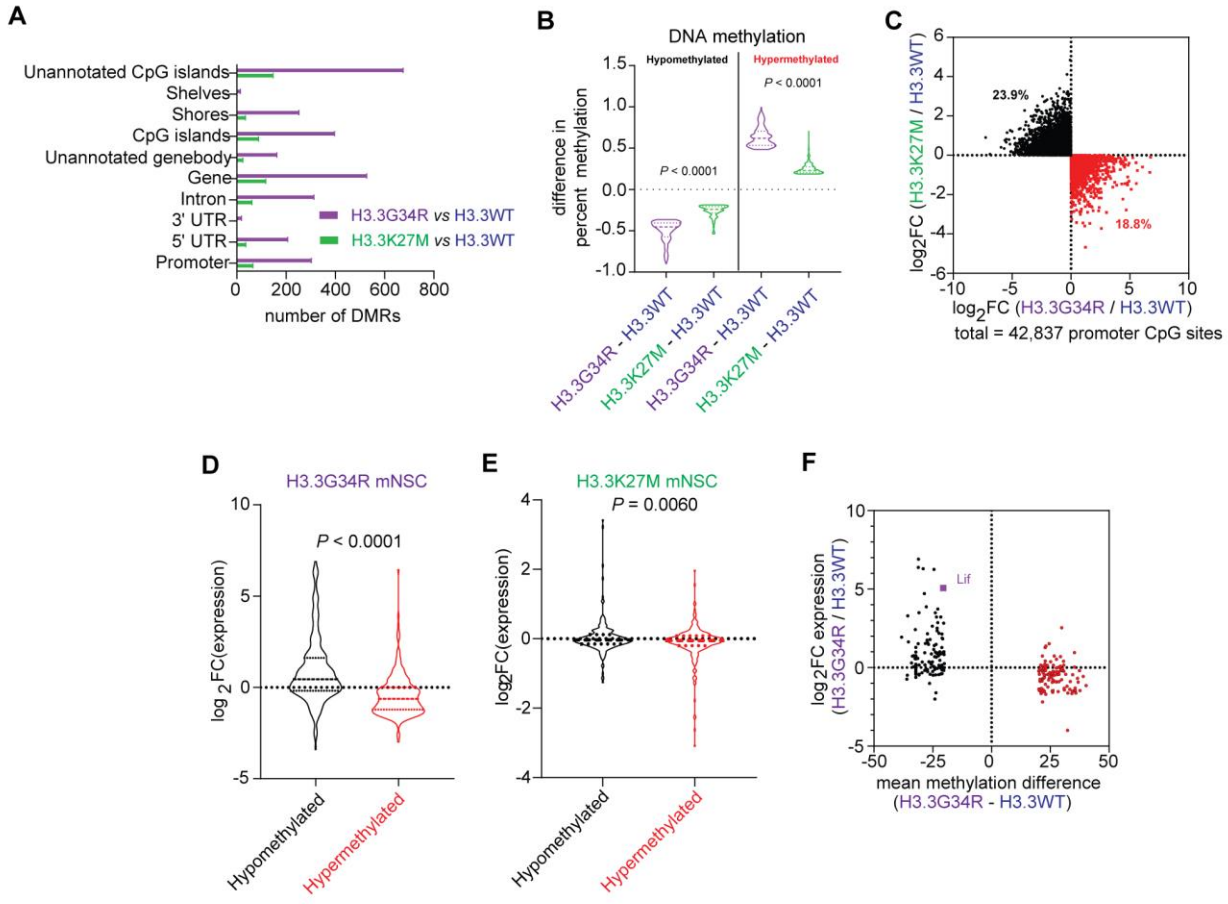

Figure 3.9. DNA methylation changes in isogenic H3.3G34R mNSC correlate with transcription.

(A) Comparison of differentially methylated genomic regions (DMRs) in H3.3G34R *versus* H3.3WT mNSC (*purple*) and H3.3K27M *versus* H3.3WT mNSC (*green*). **(B)** Violin plots depicting the difference in percent methylation for the 500 most hypomethylated or hypermethylated CpG sites within promoters in H3.3G34R (*purple*) *versus* H3.3WT and H3.3K27M (*green*) *versus* H3.3WT mNSC. **(C)** X-Y plot demonstrating $\log_2$ fold-change in methylation for each CpG site within promoters in H3.3K27M/H3.3WT (Y-axis) and H3.3G34R/H3.3WT (X-axis). Black and red indicate hypomethylated and hypermethylated sites, respectively, in H3.3G34R mNSC. **(D)** Violin plot depicting associated $\log_2$ fold-change in mRNA expression of the 500 most hypomethylated and hypermethylated promoter CpG sites in H3.3G34R mNSC. **(E)** Violin plot depicting associated $\log_2$ fold-change in mRNA expression of the 500 most hypomethylated and hypermethylated promoter CpG sites in H3.3K27M mNSC. **(F)** X-Y plot for $\log_2$ fold-change in mRNA expression (Y-axis) and mean methylation difference (X-axis) in H3.3G34R *versus* H3.3WT mNSC. Data in (**B**), (**D**) and (**E**) analyzed by nonparametric, two-sided, unpaired, Student's *t* test.

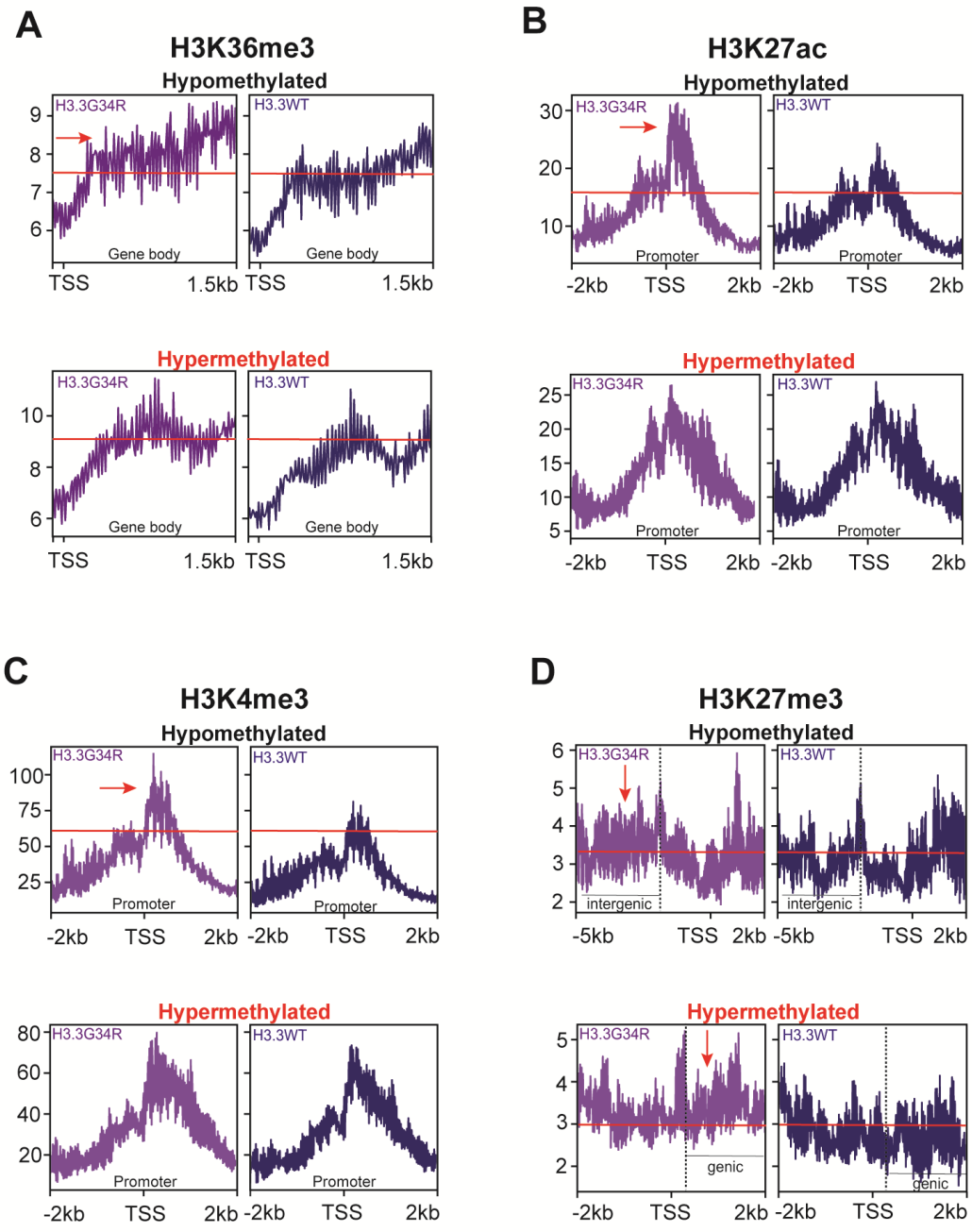

Figure 3.10. Relationship between epigenetic modifications and DNA methylation in H3.3G34R and H3.3WT mNSC models.
(A-D) Average H3K36me3 occupancy at gene bodies **(A)**; H3K27ac **(B)** and H3K4me3 **(C)** enrichment at promoter regions; and H3K27me3 **(D)** occupancy at promoters and flanking regions in H3.3G34R mNSC for gene loci with promoter hypomethylation (*top*) or hypermethylation (*bottom*) in H3.3G34R (*purple*) *versus* H3.3WT (*blue*) mNSC. Red arrows indicate enrichment of the histone modification. Black bars indicate intergenic and genic regions.

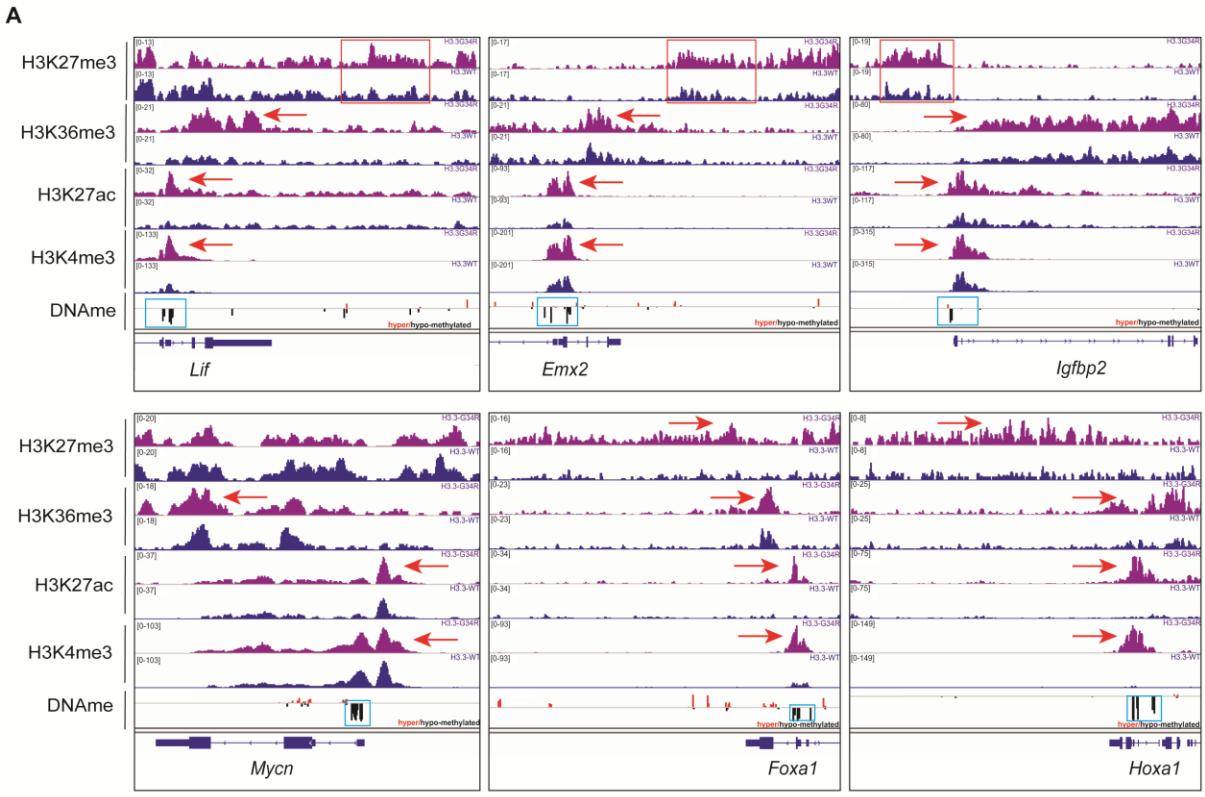

Figure 3.11. Representative loci with DNA hypomethylation and enriched epigenetic activating marks in H3.3G34R mNSCs.

(A) Integrated Genomics Viewer snapshot of H3K27me3, H3K36me3, H3K27ac, and H3K4me3 ChIP-seq signals plotted with DNA methylation (relative to H3.3WT mNSC; black, hypomethylated; red, hypermethylated) at *Lif*, *Emx2*, *Igfbp2*, *Mycn*, *Foxa1*, and *Hoxa1* in H3.3G34R (*purple*) and H3.3WT (*blue*) mNSC. Red boxes indicate gain of H3K27me3 in intergenic regions. Red arrows indicate gain of activating epigenetic marks at gene promoters and gene bodies. Blue boxes indicate DNA hypomethylation at the gene promoter.

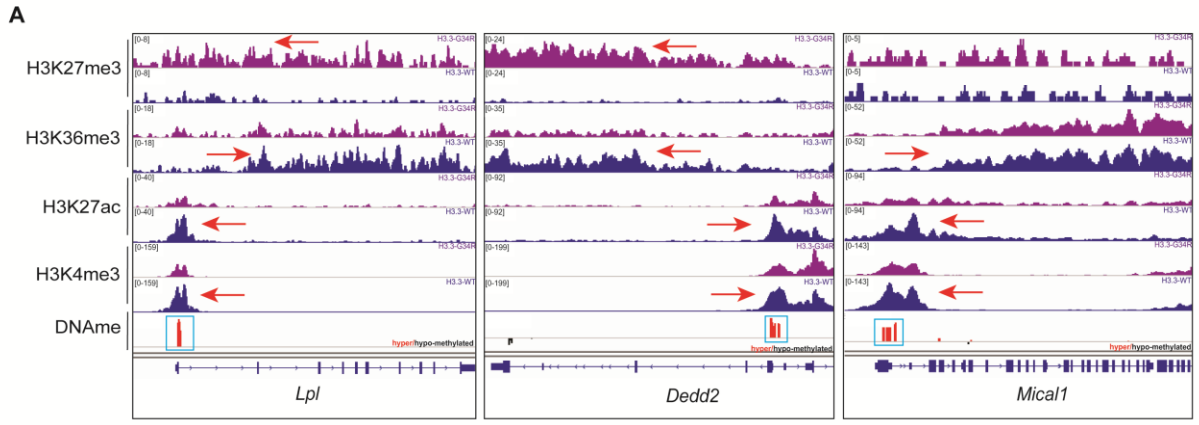

Figure 3.12. Representative loci with DNA hypermethylation and diminished epigenetic activating marks in H3.3G34R mNSCs.
(A) Integrated Genomics Viewer snapshot of H3K27me3, H3K36me3, H3K27ac, and H3K4me3 ChIP-seq signals plotted with DNA methylation (relative to H3.3WT mNSC; black, hypomethylated; red, hypermethylated) at *Lpl*, *Dedd2*, and *Mical1* in H3.3G34R (*purple*) and H3.3WT (*blue*) mNSC. Red arrows indicate gain of activating epigenetic marks at gene promoters and gene bodies. Blue boxes indicate DNA hypermethylation at the gene promoter.

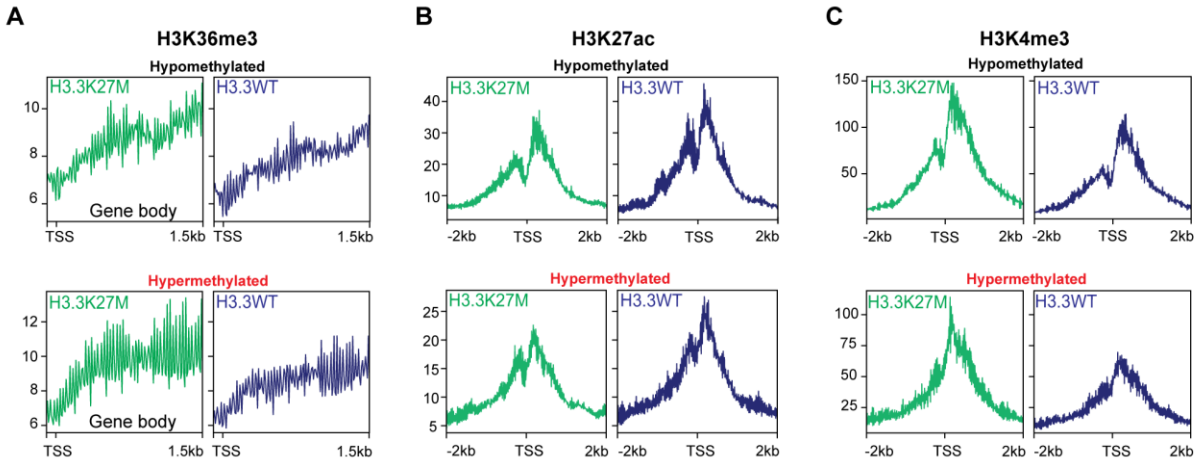

Figure 3.13. Relationship between epigenetic modifications and DNA methylation in H3.3K27M and H3.3WT mNSC models.
(A-C) Average H3K36me3 occupancy at gene bodies **(A)**, and H3K27ac **(B)** and H3K4me3 **(C)** enrichment at promoter regions, for gene loci in H3.3K27M mNSC with promoter hypomethylation (*top*) and hypermethylation (*bottom*) in H3.3K27M (*green*) and H3.3WT (*blue*) mNSC.

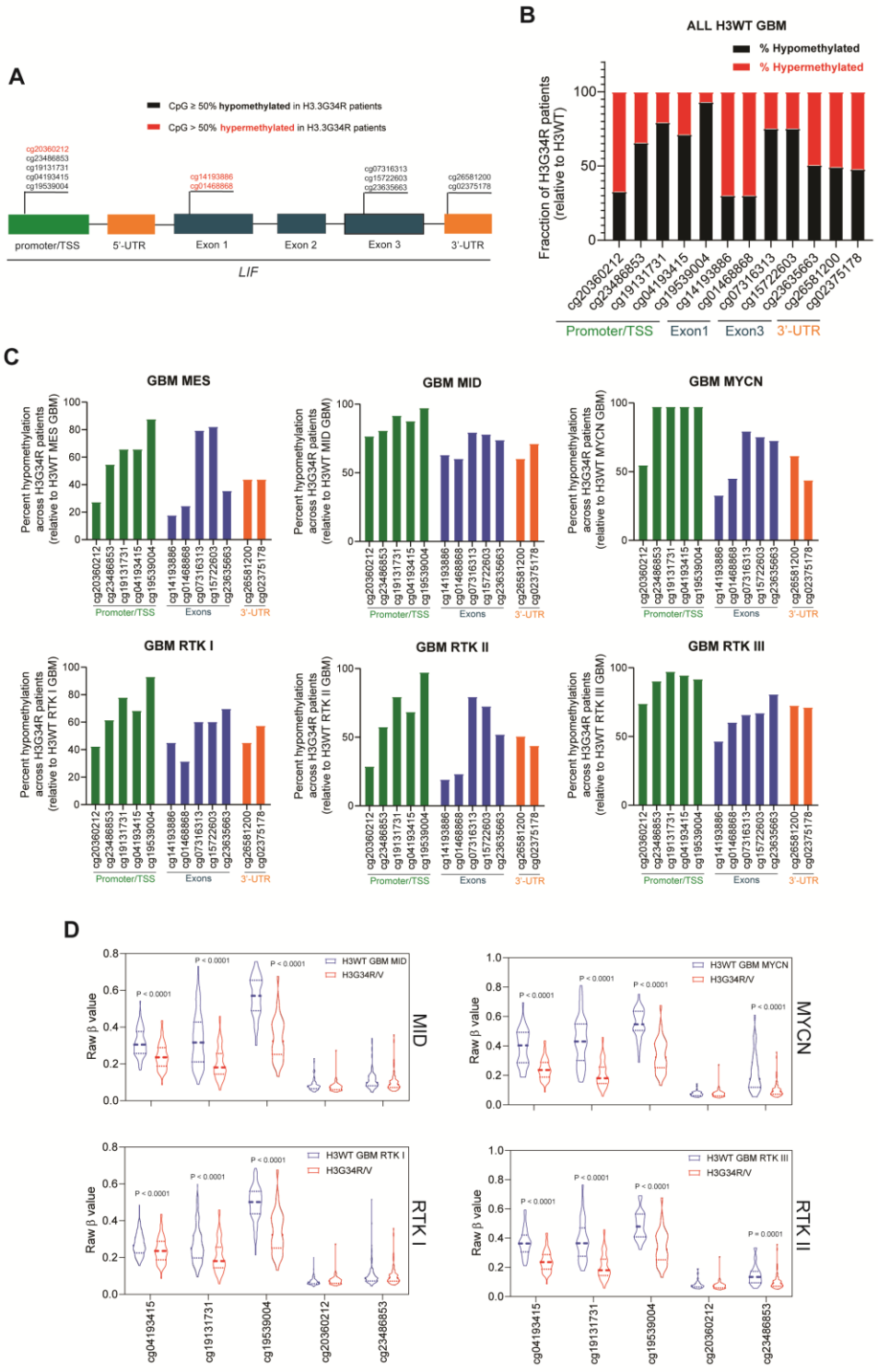

Figure 3.14. DNA methylation at *LIF* gene in glioma patients.
(A) Schematic of human LIF structure indicating CpG site genomic locations. Sites indicated in black and red indicate greater than 50 percent of H3.3G34R patients with hypomethylated or hypermethylation, respectively, of the CpG site relative to all H3.3WT glioma patients. **(B)** Bar graphs showing the proportion of H3.3G34R (*n*=73) glioma patients with hypomethylation (*black*)

or hypermethylation (*red*) of CpG sites within *LIF* relative to H3.3WT (*n*=1306) glioma patients. **(C)** Bar graphs showing the percent hypomethylation of each CpG site in H3.G34R patients compared with each H3.3WT GBM subgroup (MES, MID, MYCN, RTK I, RTK II, and RTK III). **(D)** Violin plots depicting methylation raw beta-value for each *LIF* promoter CpG site in individual H3.3WT subgroups (*blue*) and H3.3G34R (*red*) patients. Data in (**D**) analyzed by parametric, two-sided, unpaired, Student's *t* test.

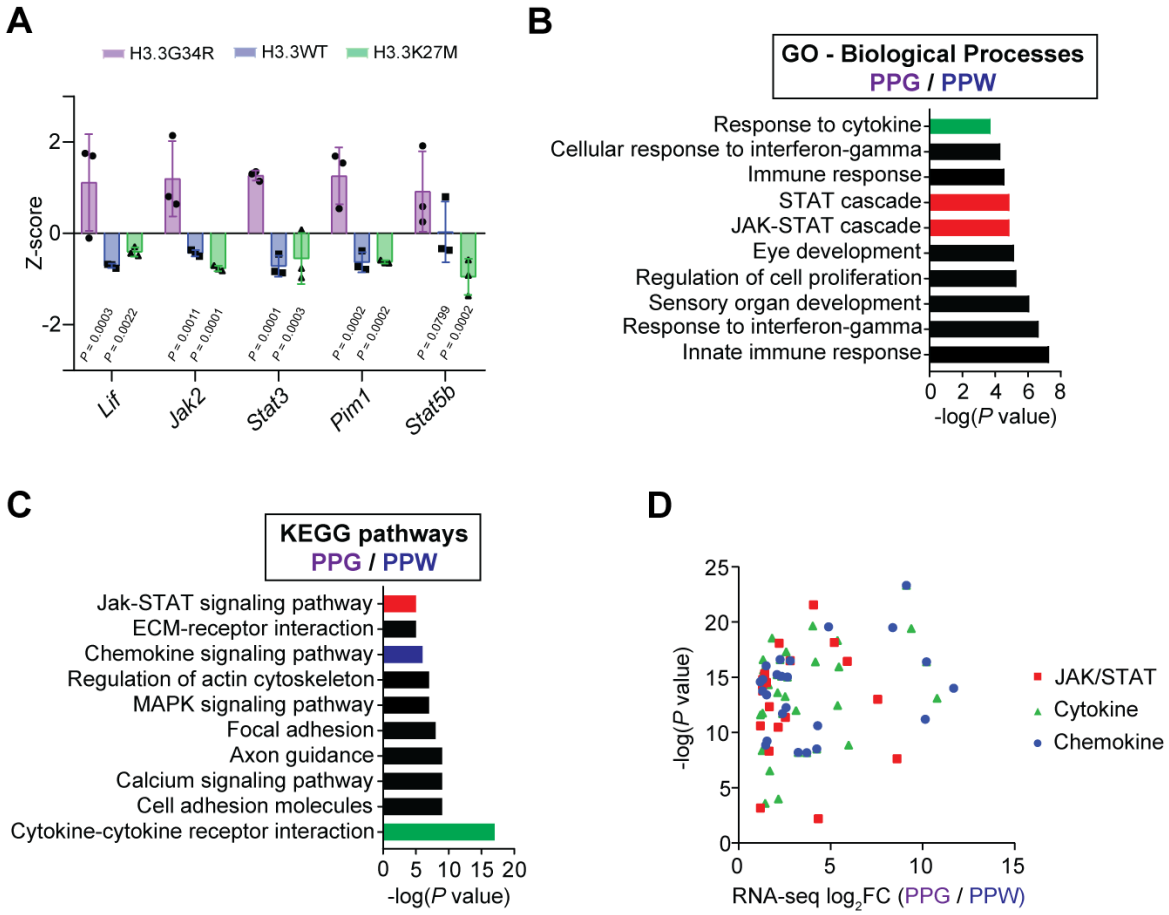

Figure 3.15. Lif/Stat3 pathway transcriptional upregulation in H3.3G34R mouse models. **(A)** Bar plot of differentially expressed genes (Z-score, Y-axis) *Lif*, *Jak2*, *Stat3*, *Pim1*, and *Stat5b* assessed by RNA sequencing in H3.3G34R (*purple*), H3.3WT (*blue*), and H3.3K27M (*green*) mNSC; *n*=3 biological replicates. **(B-C)** GO biological processes **(B)** and KEGG pathways **(C)** of upregulated genes (RNA-*seq*) in H3.3G34R PPG *versus* H3.3WT PPW (in a dominant negative *Tp53* and constitutively active *Pdgfra* background) mouse tumor cells derived from intrauterine electroporation models. *n*=3 biological replicates per cell line. **(D)** Scatter plot of $\log_2$ fold-change in mRNA expression (PPG/PPW; X-axis) *versus* negative $\log_{10}$ p-value (Y-axis) for upregulated genes associated with Jak/Stat (*red*), chemokine (*blue*), and cytokine (*green*) signaling in H3.3G34R PPG *versus* H3.3WT PPW mouse glioma cells from **(B)**. Data in **(A)** are plotted as mean ± S.D. and analyzed by two-way ANOVA with Dunnett's multiple comparisons test.

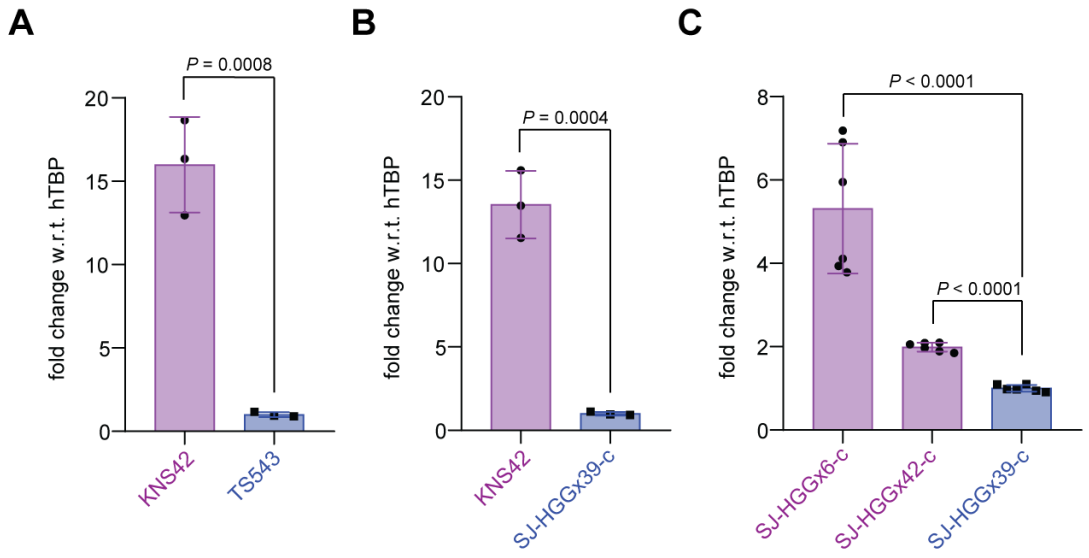

Figure 3.16. *LIF* transcript levels in human glioma cell lines.
(A-B) Bar plot of *LIF* mRNA levels [with respect to (w.r.t) TATA-Box Binding Protein (TBP)] assessed by *q*PCR in H3.3G34V KNS42 *versus* H3.3WT TS543 **(A)** and H3.3WT SJHGGx39-c **(B)**; *n*=3 biological replicates. **(C)** Bar plot of *LIF* mRNA levels [with respect to (w.r.t) TATA-Box Binding Protein (TBP)] assessed by *q*PCR in H3.3G34R SJ-HGGx6-c and H3.3G34R SJ-HGGx42-c *versus* H3.3WT SJ-HGGx39-c; *n*=2 biological replicates, *n*=3 technical replicates each. Data in (**A**), (**B**) and (**C**) analyzed by nonparametric, two-sided, unpaired, Student's *t* test.

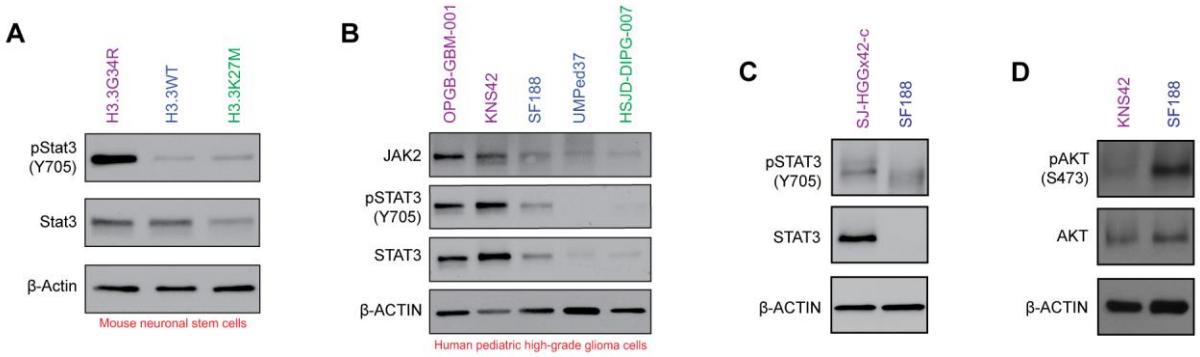

Figure 3.17. LIF/STAT3 signaling upregulation in H3.3G34R/V mouse and human cells.
(A) Western blots of cell lysates from mNSCs stably transduced with H3.3G34R, H3.3WT, and H3.3K27M transgenes for pStat3(Y705), Stat3, and β-Actin. **(B)** Western blots on cell lysates from pHGG cell lines OPGB-GBM-001 (H3.3G34R), KNS42 (H3.3G34V), SF188 (H3.3WT), UMPed37 (H3.3WT), and HSJDDIPG-007 (H3.3K27M) for JAK2, pSTAT3(Y705), STAT3, and β-Actin. **(C)** Western blots of cell lysates from H3.3G34R SJ-HGGx42-c and H3.3WT SF188 cells for pSTAT3(Y705), STAT3, and β-Actin. **(D)** Western blots of H3.3G34V KNS42 and H3.3WT SF188 cells for phospho-AKT(S473), AKT, and β-Actin.

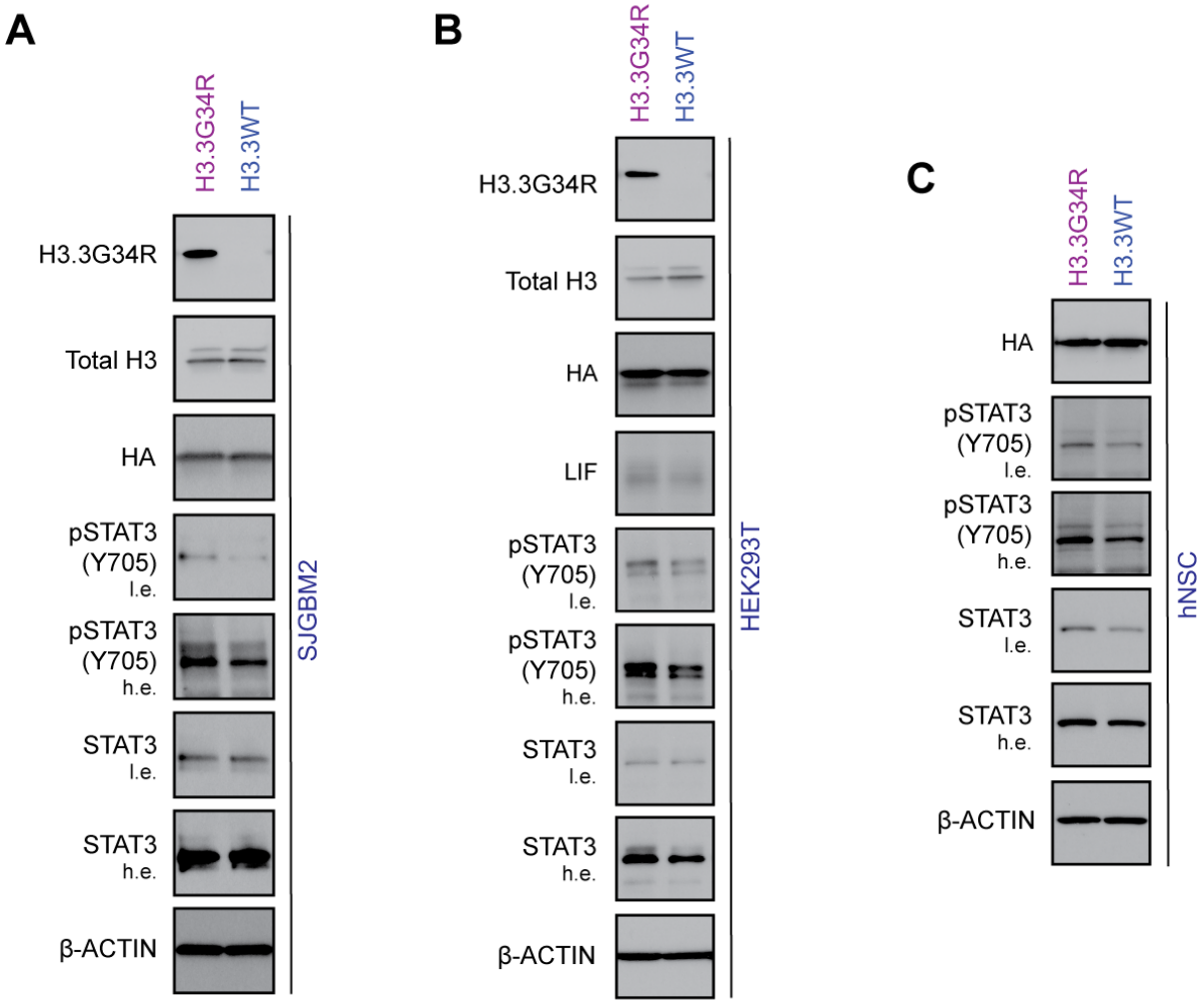

Figure 3.18. LIF/STAT3 signaling upregulation in isogenic H3.3G34R cell models.
(A-C) Western blots of cell lysates from H3.3WT cells SJGBM2 (glioblastoma, **A**), HEK293T (embryonic kidney, **B**), and immortalized human neural stem cells (hNSC, **C**) stably transduced with H3.3G34R or H3.3WT transgenes for H3.3G34R, total H3, HA, LIF, pSTAT3(Y705), STAT3, and β-Actin. *l.e.* = low exposure, *h.e.* = high exposure.

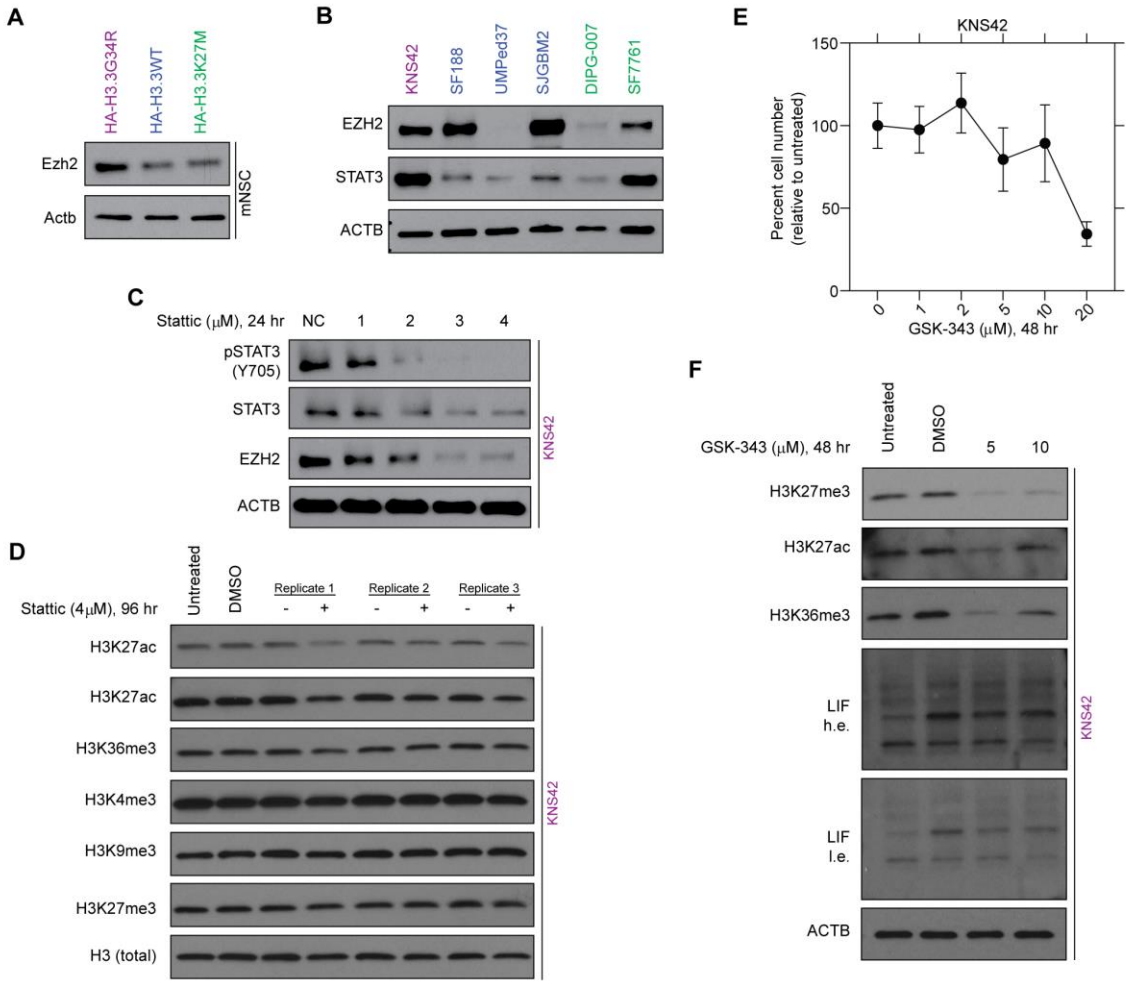

Figure 3.19. EZH2 expression in mNSCs and human glioma cells and cell responses to EZH2 inhibition.

(A) Western blots of cell lysates from mNSCs stably transduced with H3.3G34R, H3.3WT, and H3.3K27M transgenes for Ezh2 and β-Actin. **(B)** Western blots on cell lysates from pHGG cell lines OPGB-GBM-001 (H3.3G34R), KNS42 (H3.3G34V), SF188 (H3.3WT), UMPed37 (H3.3WT), and HSJD-DIPG-007 (H3.3K27M) for EZH2 and β-ACTIN. **(C)** Western blots for pSTAT3(Y705), STAT3, EZH2, and β-Actin on cell lysates from KNS42 cells treated Stattic for 24 hours at indicated concentrations. **(D)** Western blots for H3K27ac, H3K36me3, H3K4me3, H3K9me3, H3K27me3, and total H3 on histone extracts from KNS42 cells treated with Stattic for 96 hours at indicated concentrations. **(E)** Cell counts (percentage of living cells, Y-axis; drug concentrations, X-axis) of H3.3G34V KNS42 cells treated with EZH2 inhibitor GSK-343 for 48 hours at indicated concentrations. *n*=2 biological replicates; *n*=4 technical replicates each. **(F)** Western blots for H3K27me3, H3K27ac, H3K36me3, and total H3 on histone extracts or for LIF on cell lysates from KNS42 cells treated with EZH2 inhibitor GSK-343 for 48 hours at indicated concentrations. *l.e.* = low exposure, *h.e.* = high exposure.

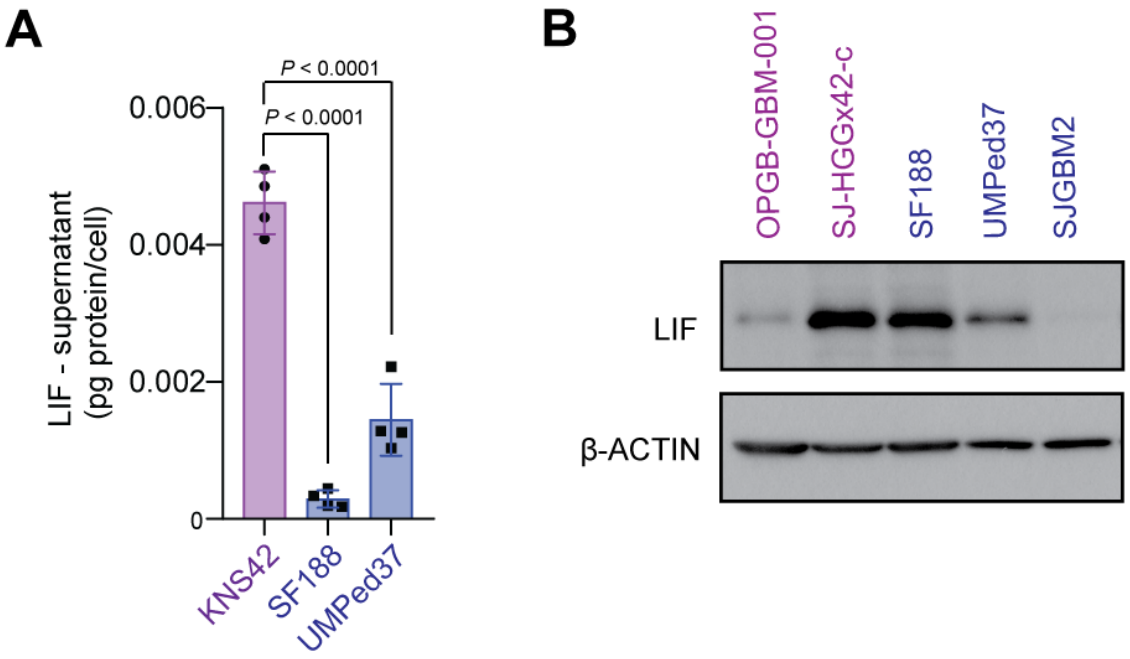

Figure 3.20. LIF extracellular and intracellular levels in human glioma cells.
(A) ELISA for human LIF protein (pg protein/cell, Y-axis) in cell supernatants in H3.3G34V KNS42 cells compared to H3.3WT SF188 and UMPed37 cells after 4 days in culture; *n*=4 biological replicates. **(B)** Western blots for intracellular LIF and β-Actin in H3.3G34R cells (OPGB-GBM-001, SJ-HGGx42-c) and H3.3WT cells (SF188, SJGBM2, UMPed37). Data are plotted as mean ± S.D. Data in (**A**) analyzed by nonparametric, two-sided, unpaired, Student's *t* test.

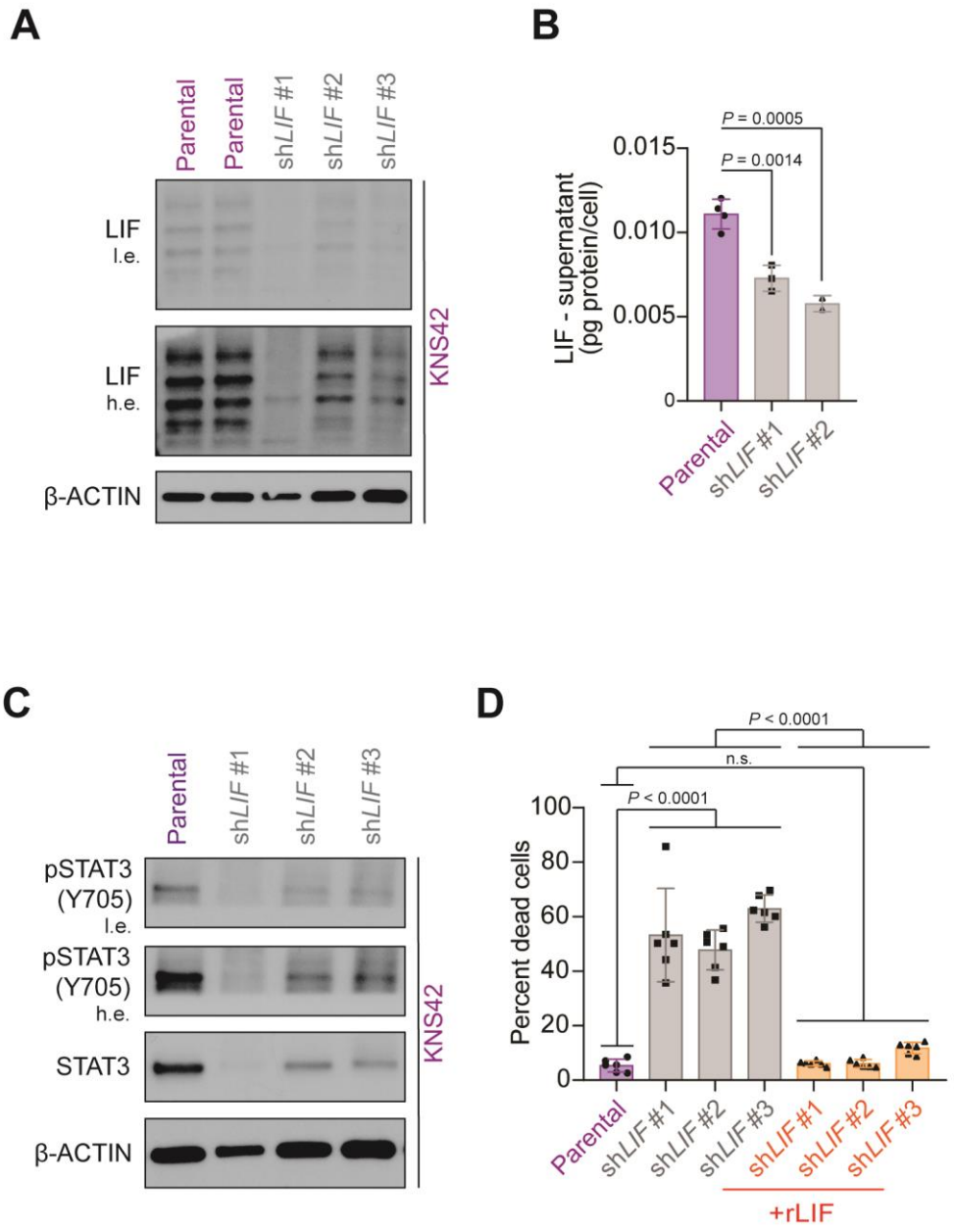

Figure 3.21. LIF regulates STAT3 activation and growth in KNS42 cells.
(A) Representative Western blots for LIF and β-Actin in parental KNS42 cells and cells stably transduced with three independent *LIF* shRNAs. **(B)** ELISA of human LIF protein (pg protein/cell, Y-axis) in cell media supernatants of KNS42 cells from **(A)** with or without *LIF* knockdown; *n*=3-4 biological replicates. **(C)** Western blots of KNS42 cells stably transduced with three independent *LIF* shRNAs for pSTAT3(Y705), STAT3, and β-Actin. **(D)** Percent dead cells (Y-axis) in KNS42 parental cells (*purple bar*), LIF-knockdown cells from (C) (*gray bars*), or knockdown cells in the presence of recombinant human LIF (rLIF, 50 ng/mL, *orange bars*); *n*=6 biological replicates; *n*=4 technical replicates each. Data are plotted as mean ± S.D. and analyzed by two-way ANOVA with Dunnett's multiple comparisons test. *l.e.* = low exposure, *h.e.* = high exposure.

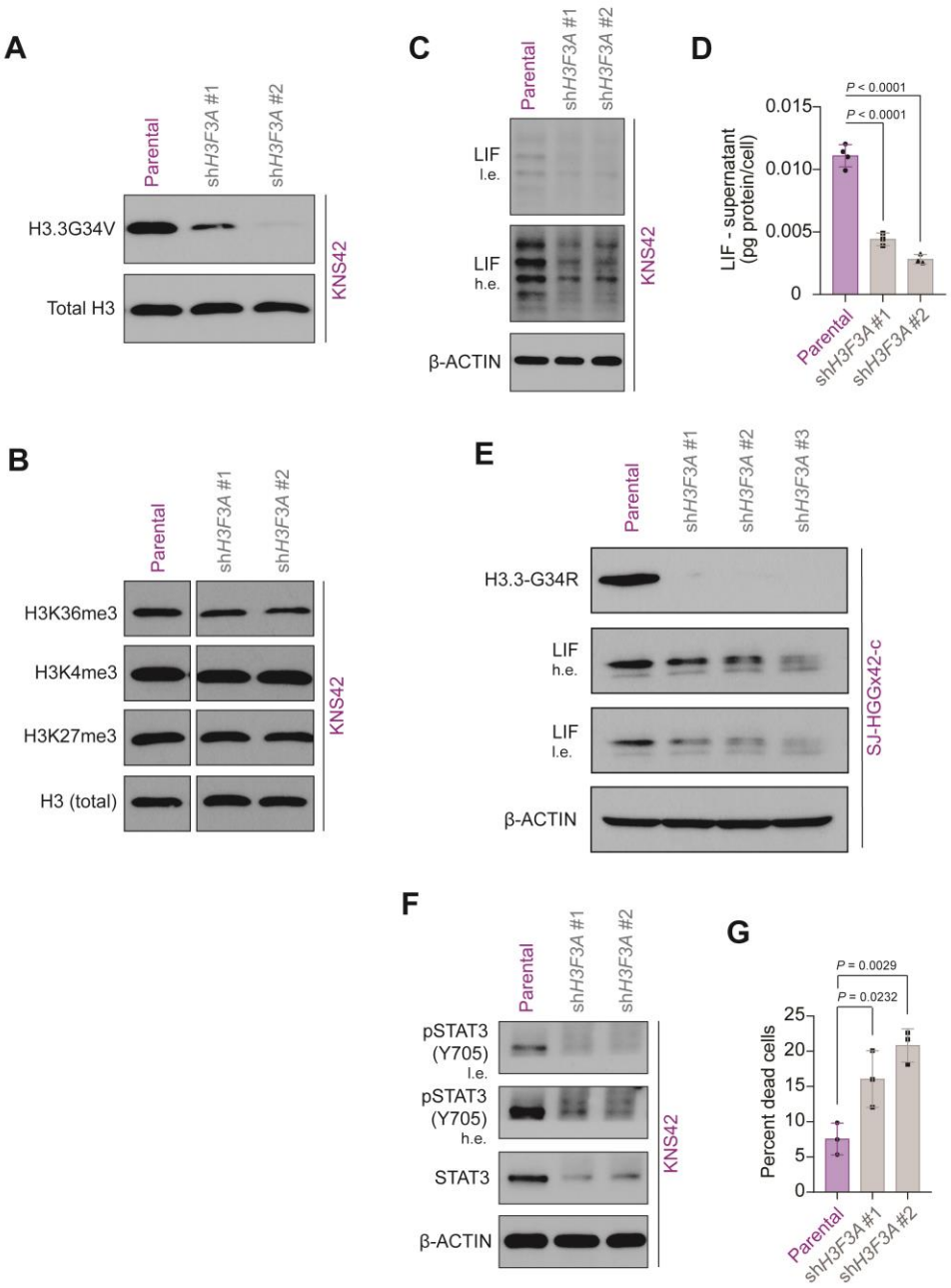

Figure 3.22. Mutant *H3F3A* regulates LIF expression and STAT3 activation in KNS42 cells. **(A)** Western blots for mutant specific-H3.3G34V and total H3 in parental KNS42 cells and cells stably transduced with two independent *H3F3A* shRNAs. **(B)** Western blots for H3K36me3, H3K4me3, H3K27me3, and total H3 in parental KNS42 cells and cells expressing two independent shRNAs targeted to *H3F3A.* **(C)** Western blots for LIF and β-Actin in cells from **(A)**. **(D)** ELISA for human LIF protein (pg protein/cell, Y axis) in cell media supernatants of KNS42 cells from **(C)** with or without *H3F3A* knockdown; *n*=3-4 biological replicates. **(E)** Western blots for mutant specific-H3.3G34R, LIF, and β-Actin in SJHGGx42-c stably transduced with three independent *H3F3A* shRNAs. **(F)** Western blots of KNS42 cells stably transduced with two independent *H3F3A* shRNAs for pSTAT3(Y705), STAT3, and β-Actin. **(G)** Percent dead cells (Y-axis) in KNS42 cells with or without *H3F3A* knockdown from **(A)**; *n*=3 biological replicates; *n*=4

technical replicates each. Data in **(D)** and **(G)** are plotted as mean ± S.D. and analyzed by two-way ANOVA with Dunnett's multiple comparisons test. *l.e.* = low exposure, *h.e.* = high exposure.

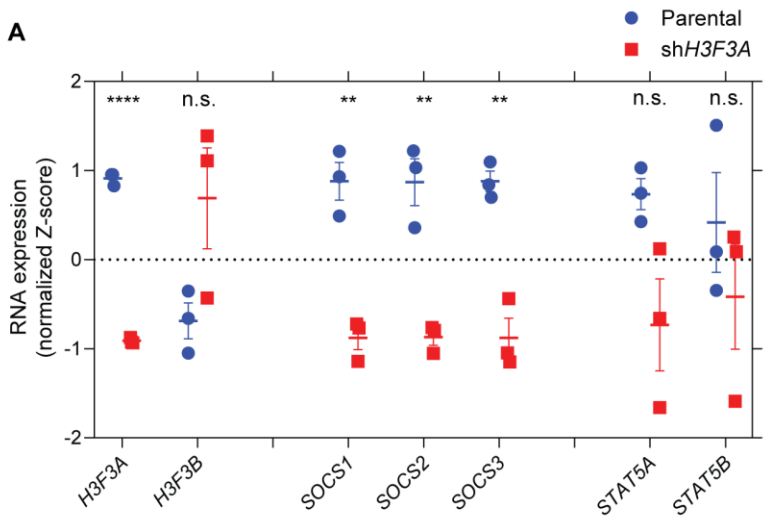

Figure 3.23. H3.3 and STAT3 target gene expression levels in *H3F3A* knockdown cells.
(A) XY-plot demonstrating mRNA expression (normalized Z-score, Y-axis) of *H3F3A*, *H3F3B*, *SOCS1*, *SOCS2*, *SOCS3*, *STAT5A*, and *STAT5B* from parental KNS42 (*blue*) and sh*H3F3A*-expressing cells (*red*). *n*=3 biological replicates per condition. Data are plotted as mean ± S.D. and analyzed by nonparametric, two-sided, unpaired, Student's *t* test. **, *P*<0.01; ****, *P*<0.0001; n.s., not significant.

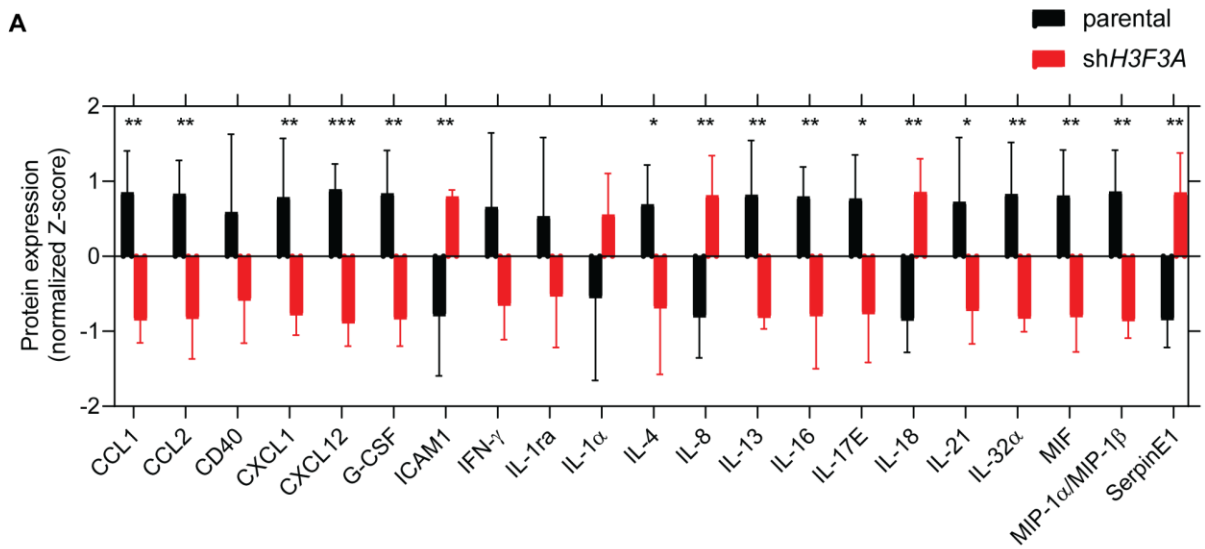

Figure 3.24. Cytokine levels in *H3F3A* knockdown KNS42 cells.
(A) Quantifications of intracellular expression level (normalized Z-score, Y-axis) for human cytokines detected by a human cytokine array in parental KNS42 (*black*) and sh*H3F3A*-expressing cells (*red*). *n*=2 biological replicates; *n*=2 technical replicates each. Data are plotted as mean ± S.D. and analyzed by nonparametric, two-sided, unpaired, Student's *t* test. *, *P*<0.05; **, *P*<0.01; ***, *P*<0.001, ****, *P*<0.0001.

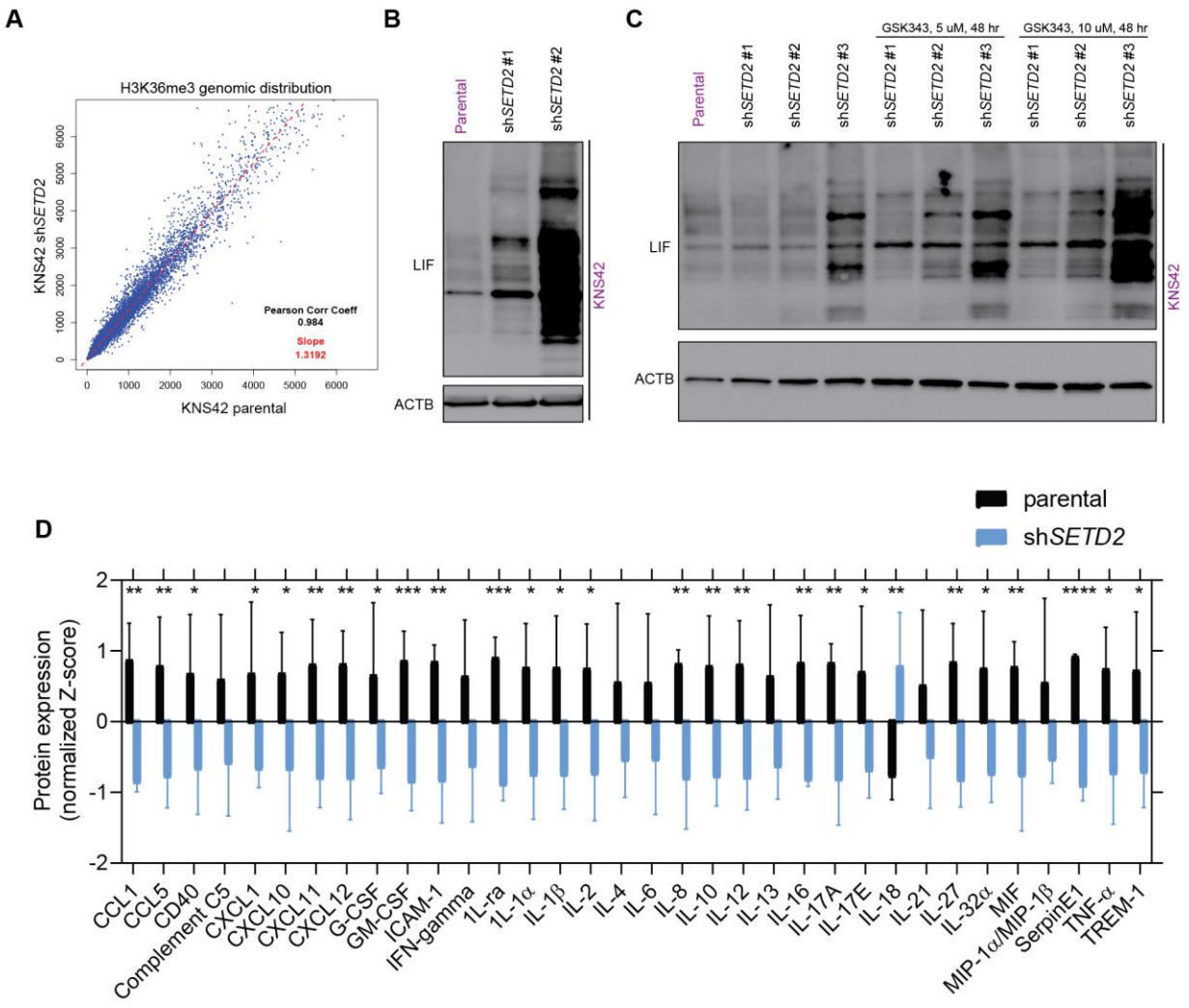

Figure 3.25. *SETD2* knockdown modulates cytokine expression.
(A) XY-plot demonstrating Pearson correlation of genomic H3K36me3 in parental KNS42 (X-axis) and sh*SETD2*-expressing (Y-axis) cells. **(B)** Western blots for LIF and β-Actin in parental KNS42 cells and cells expressing two independent shRNAs targeted to *SETD2*. **(C)** Western blots for LIF and β-Actin in parental KNS42 cells and cells expressing two independent shRNAs targeted to *SETD2* treated with 5 or 10 μM GSK-343 for 48 hours. **(D)** Quantifications of intracellular expression level (normalized Z-score, Y-axis) for human cytokines detected by a human cytokine array in parental KNS42 (*black*) and sh*SETD2*-expressing cells (*blue*). *n*=2 biological replicates; *n*=2 technical replicates each. Data are plotted as mean ± S.D. and analyzed by nonparametric, two-sided, unpaired, Student's *t* test. *, *P*<0.05; **, *P*<0.01; ***, *P*<0.001, ****, *P*<0.0001.

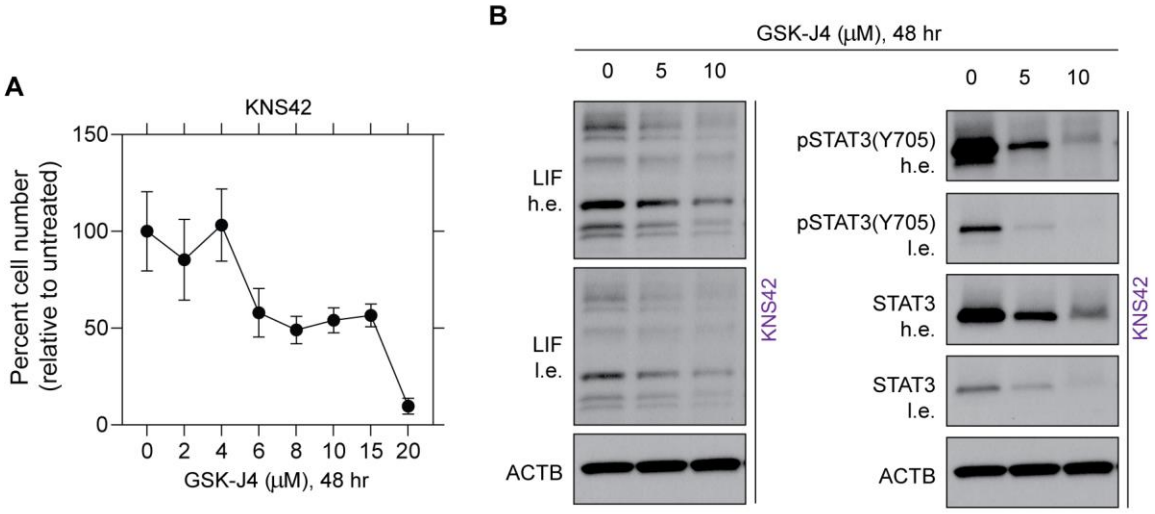

Figure 3.26. KDM6 inhibition affects cell growth and STAT3 activation.
(A) Cell counts (percentage of living cells, Y-axis; drug concentrations, X-axis) of H3.3G34V KNS42 cells treated with KDM6A/6B inhibitor GSK-J4 for 48 hours at indicated concentrations. *n*=2 biological replicates; *n*=4 technical replicates each. **(B)** Western blots for LIF, pSTAT3(Y705), STAT3, and β-Actin on cell lysates from KNS42 cells treated with KDM6A inhibitor GSK-J4 for 48 hours at indicated concentrations. *l.e.* = low exposure, *h.e.* = high exposure.

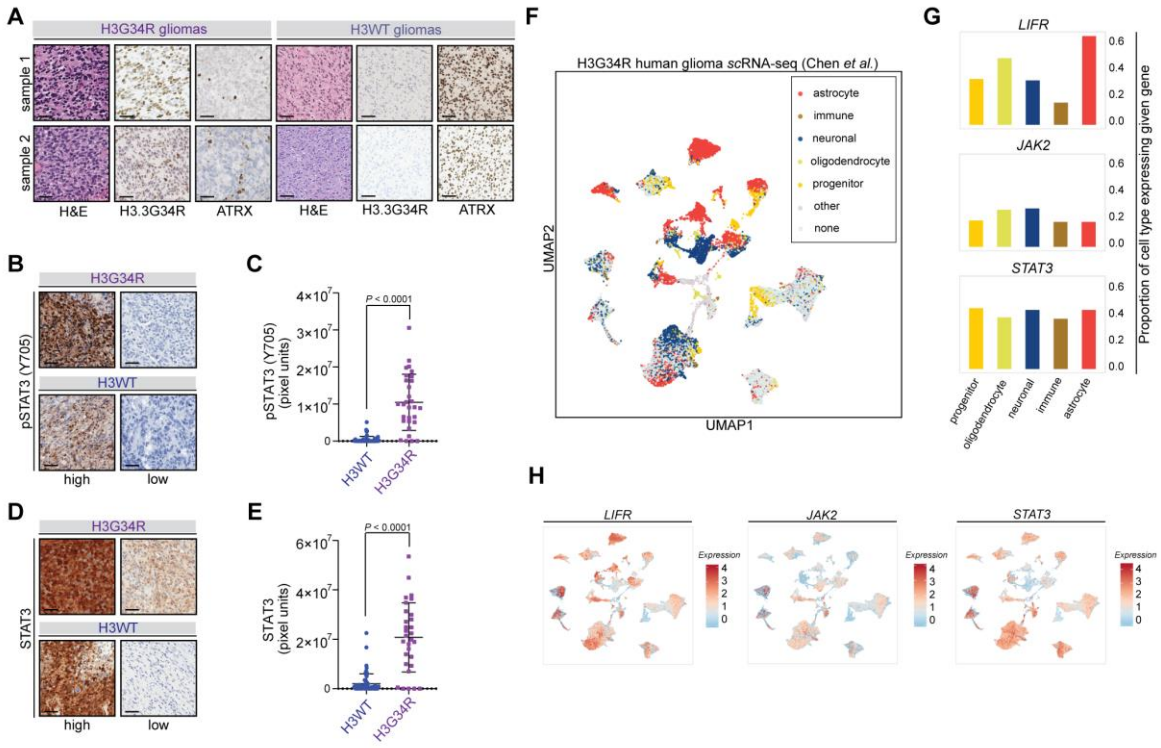

Figure 3.27. Profiling of STAT3 expression and activation in H3WT and H3G34R/V patient-derived tissues and cells.

(A) Representative IHC images of two H3G34R (*purple*, *left*) and two H3WT (*blue*, *right*) human high-grade glioma tumors stained with Hematoxylin & eosin (H&E), mutant-specific H3.3G34R, or ATRX. Scale bar, 60 μm. **(B)** Representative IHC images from human H3G34R (*top*) or H3.3WT (*bottom*) gliomas for pSTAT3(Y705). IHC images demonstrating the highest and lowest pSTAT3(Y705) staining within each cohort were selected. Scale bar, 60 μm. **(C)** Blinded quantification (pixel units, Y-axis) of pSTAT3(Y705) staining in H3.3WT (*blue*) and H3.3G34R (*purple*) human glioma samples. H3G34R, *n*=6 samples; H3.3WT, *n*=12 samples. Five randomly selected regions were imaged per sample. Each dot represents the quantification of a single image from each tumor within each cohort. **(D)** Representative IHC images from human H3.3G34R (*top*) or H3.3WT (*bottom*) gliomas for total STAT3. IHC images demonstrating the highest and lowest STAT3 staining within each cohort were selected. Scale bar, 60 μm. **(E)** Blinded quantification (pixel units, Y-axis) of STAT3 staining in H3.3WT (*blue*) and H3.3G34R (*purple*) human glioma samples. H3.3G34R, *n*=6 samples; H3.3WT, *n*=12 samples. Five randomly selected regions were imaged per sample. Each dot represents the quantification of a single image from each tumor within each cohort. **(F)** Uniform manifold approximation and projection (UMAP) embedding of scRNA-seq data from malignant H3G34R/V cells originating from sixteen patient samples (14 patients, two primary-recurrence pairs) analyzed in Chen *et al.* (2020). Cells are colored by most similar normal brain cell type. **(G)** Bar plots illustrating the proportion of each cell type aggregated from all tumors (progenitor, yellow; oligodendrocyte, green; neuronal, blue; immune, brown; astrocyte, red) expressing the given JAK/STAT pathway genes *LIFR* (*top*), *JAK2* (*center*), and *STAT3* (*bottom*). **(H)** UMAP embedding of *sc*RNA-*seq* data of malignant H3.3G34R/V cells as in **(F)**, with cells colored by expression of *LIFR*, *JAK2*, or *STAT3*. Data in **(C)** and **(E)** are plotted as mean ± S.D. and analyzed by nonparametric, two-sided, unpaired, Student's *t* test.

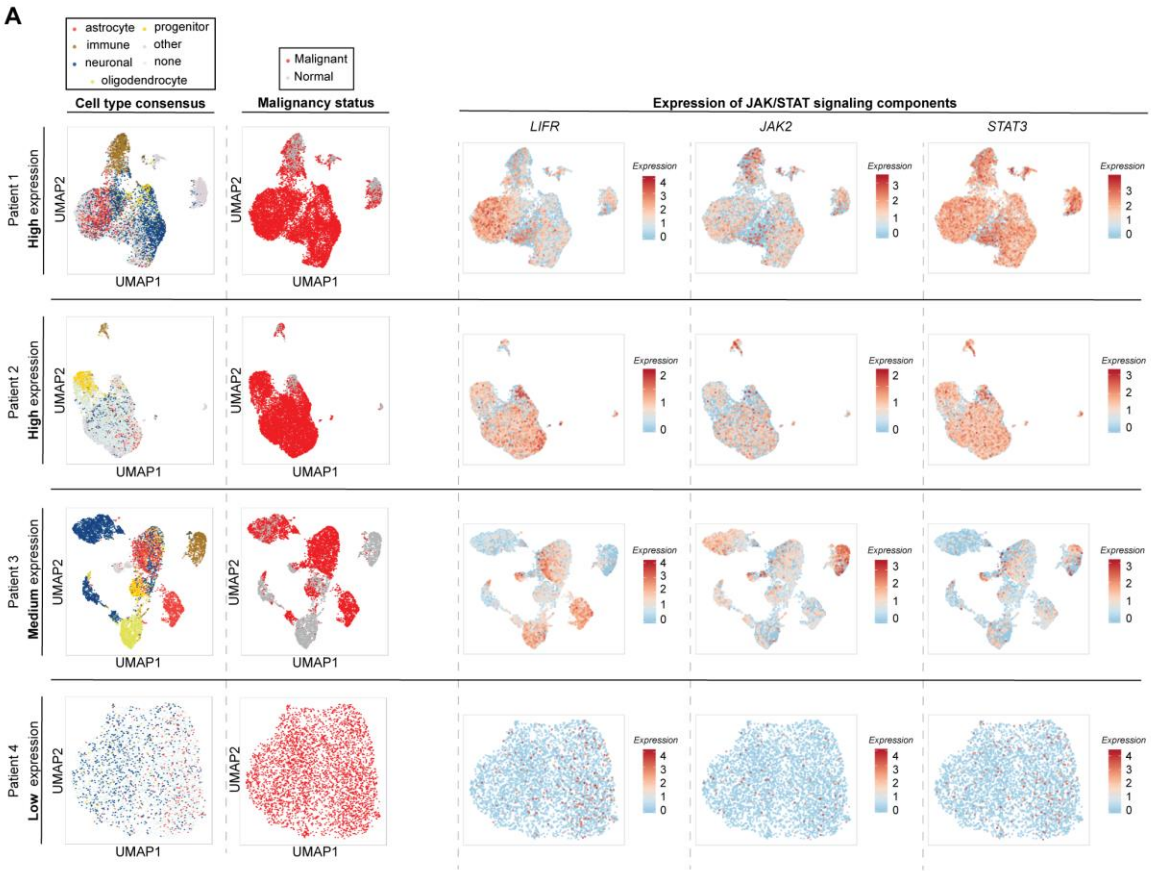

Figure 3.28. Profiling of *LIFR*, *JAK2*, and *STAT3* expression by single cell RNA-seq on patient-derived tumor cells.

(A) Uniform manifold approximation and projection (UMAP) embedding of scRNA-seq for four H3G34R/V patient tumors. Each row represents an individual patient with varying levels of JAK/STAT pathway gene expression (top row, high expression; bottom row; lowest expression). For each patient, UMAP embedding are colored by most normal brain cell type (*leftmost column*); cell assignment as normal or malignant (*second column*); and expression of *LIFR*, *JAK2*, or *STAT3* (*right*).

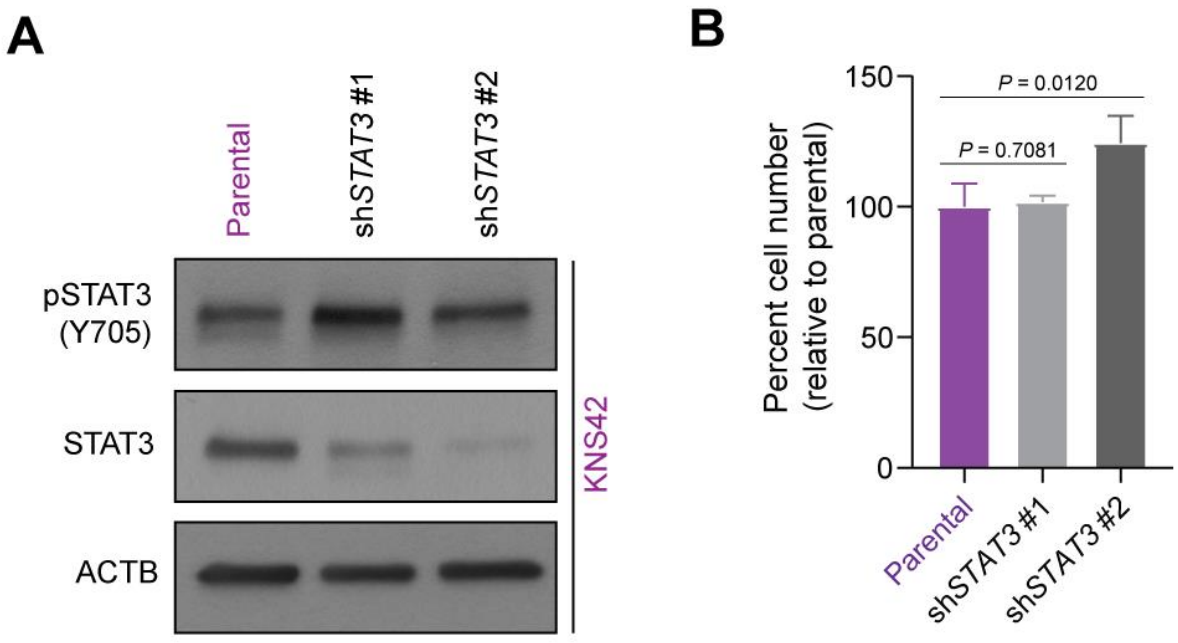

Figure 3.29. *STAT3* knockdown is insufficient to alter growth or activation in KNS42 cells. **(A)** Western blots for pSTAT3(Y705), STAT3, and β-Actin on cell lysates from parental KNS42 cells and cells stably transduced with two independent *STAT3* shRNAs. **(B)** Cell counts (percentage of living cells, Y-axis; cell construct, X-axis) of parental KNS42 cells and cells stably transduced with two independent *STAT3* shRNAs. *n*=4 biological replicates; *n*=4 technical replicates each. Data in **(B)** is plotted as mean ± S.D. and analyzed by nonparametric, two-sided, unpaired, Student's *t* test.

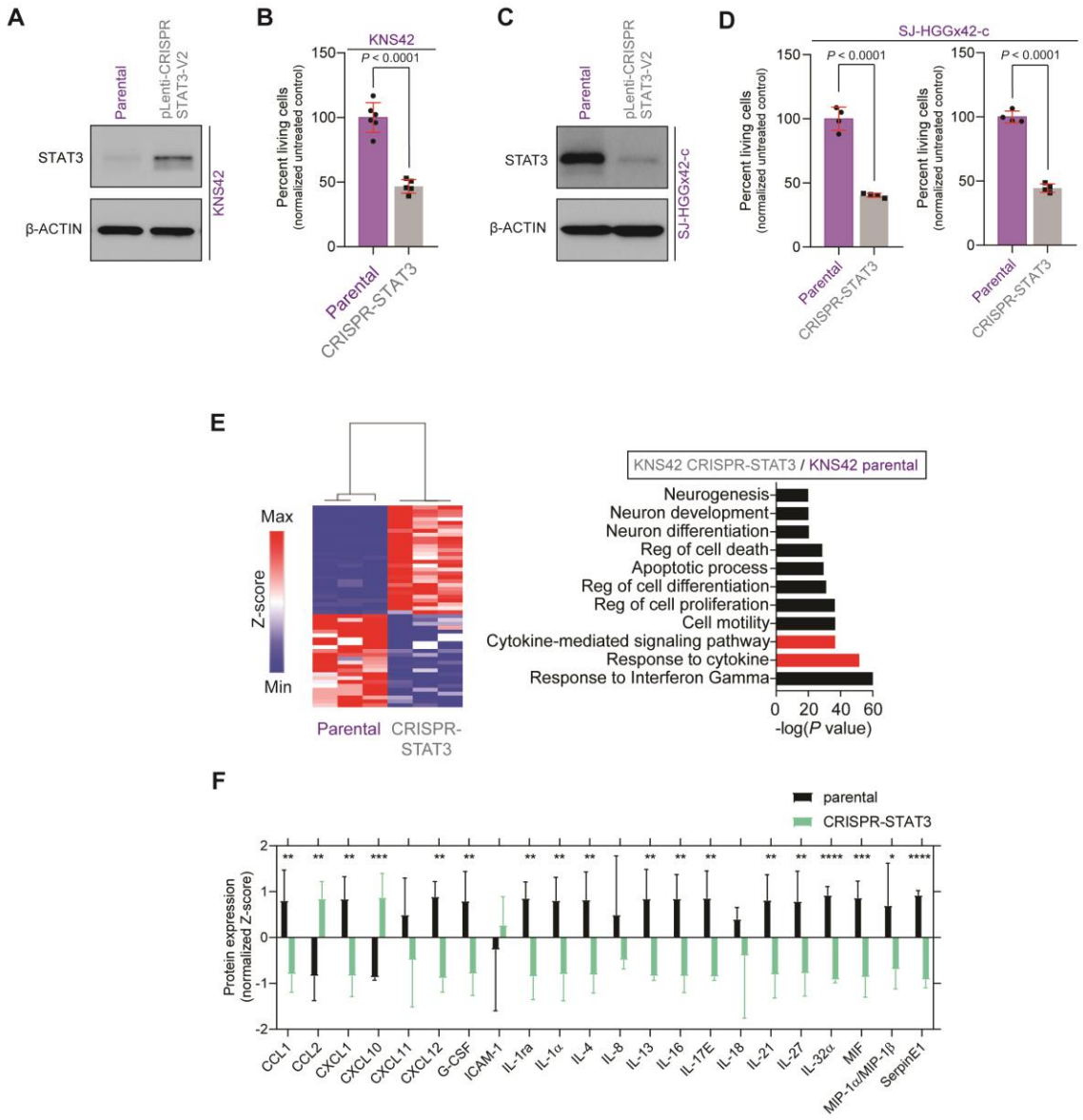

Figure 3.30. STAT3 knockout slows tumor growth in human H3.3G34R/V cells, deregulates differentiation processes, and alters cytokine expression patterns.

(A) Western blots for STAT3 and β-Actin on cell lysates of H3.3G34V KNS42 cells with or without CRISPR-mediated STAT3 knockout. **(B)** Cell counts (percentage of living cells, Y-axis; cell construct, X-axis) in H3.3G34V KNS42 cells with or without STAT3 knockout from **(A)** after 6 days in culture; *n*=6 biological replicates; *n*=4 technical replicates each. **(C)** Western blots for STAT3 and β-Actin on cell lysates of H3.3G34R SJ-HGGx42-c cells with or without CRISPR-mediated STAT3 knockout. **(D)** Cell counts (percentage of living cells, Y-axis; cell construct, X-axis) in H3.3G34R SJ-HGGx42-c cells with or without STAT3 knockout from **(C)** after 3 days in culture at initial seed density of 50,000 cells (left) or 100,000 cells (right); *n*=4 biological replicates; *n*=4 technical replicates each. **(E)** Heatmap and GSEA of differentially expressed genes determined by RNA-seq in H3.3G34V KNS42 cells with or without STAT3 knockout; *n*=3 biological replicates each. **(F)** Quantifications of intracellular expression level (normalized Z-score, Y-axis) for human cytokines detected by a human cytokine array in parental KNS42 (*black*)

and STAT3 knockout cells (*green*). *n*=2 biological replicates; *n*=2 technical replicates each. Data in **(B)**, **(D)**, and **(E)** are plotted as mean ± S.D. and analyzed by parametric, two-sided, unpaired, Student's *t* test. *, *P*<0.05; **, *P*<0.01; ***, *P*<0.001, ****, *P*<0.0001.

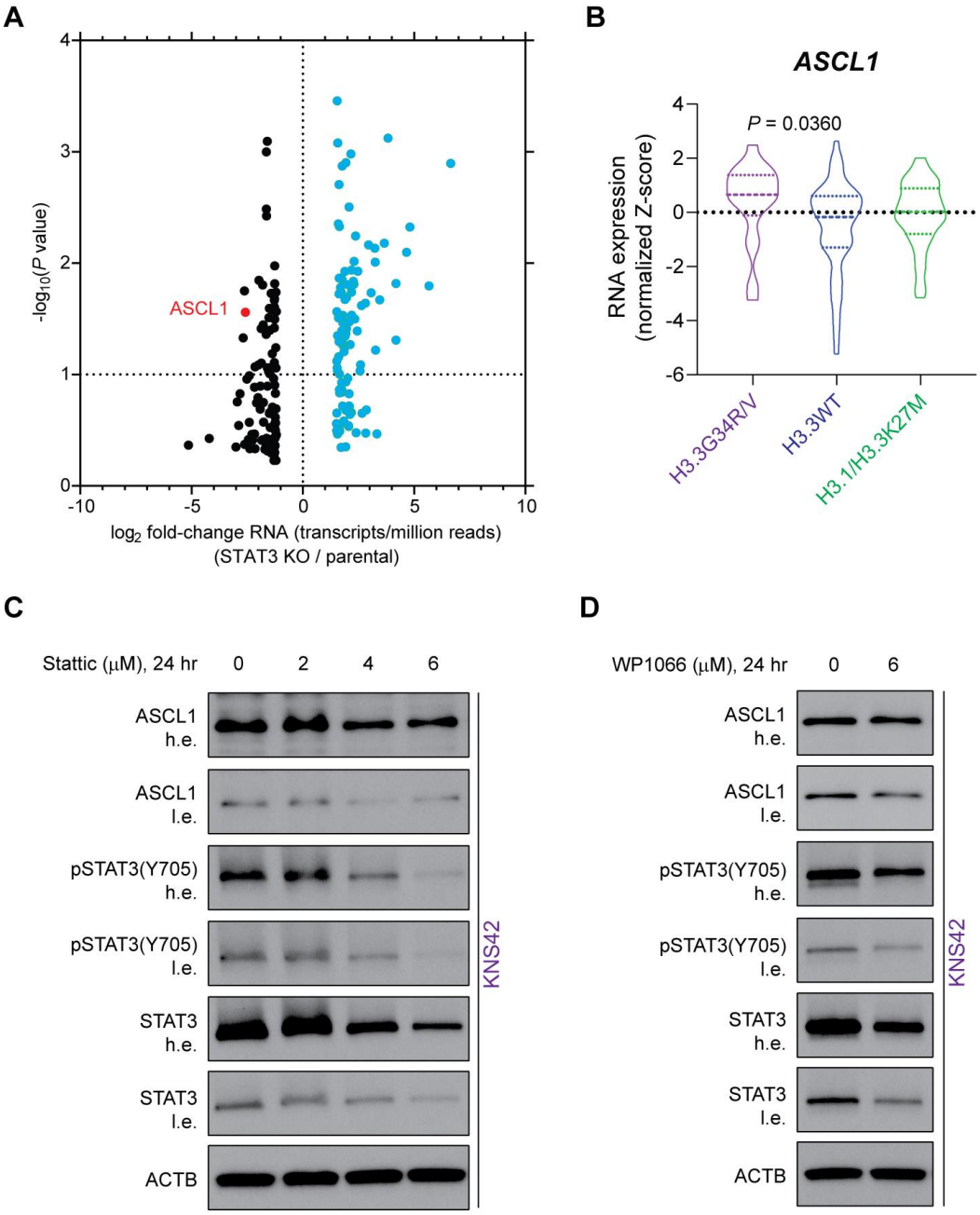

Figure 3.31. STAT3 knockout and pharmacological inhibition reveals ASCL1 as a top deregulated neural progenitor transcription factor.

(A) Scatter plot of $\log_2$ fold-change in RNA expression (KNS42 STAT3 knockout/KNS42 parental; X-axis) *versus* negative $\log_{10}$ *P*-value (Y-axis) for the top 100 upregulated (*blue*) and top 100 downregulated (*black*) genes. **(B)** Violin plot comparing Achaete-Scute Homolog 1 (*ASCL1*) expression in H3.3G34R/V, H3.3WT, and H3.1/3.3K27M glioma patients from Mackay *et al.*

(2017). **(C-D)** Western blots for pSTAT3(Y705), STAT3, ASCL1, and β-Actin on cell lysates from KNS42 cells treated Stattic **(C)** or WP1066 **(D)** for 24 hours at the indicated concentration. Data in **(B)** is analyzed by nonparametric, two-sided, unpaired, Student's *t* test. *l.e.* = low exposure, *h.e.* = high exposure.

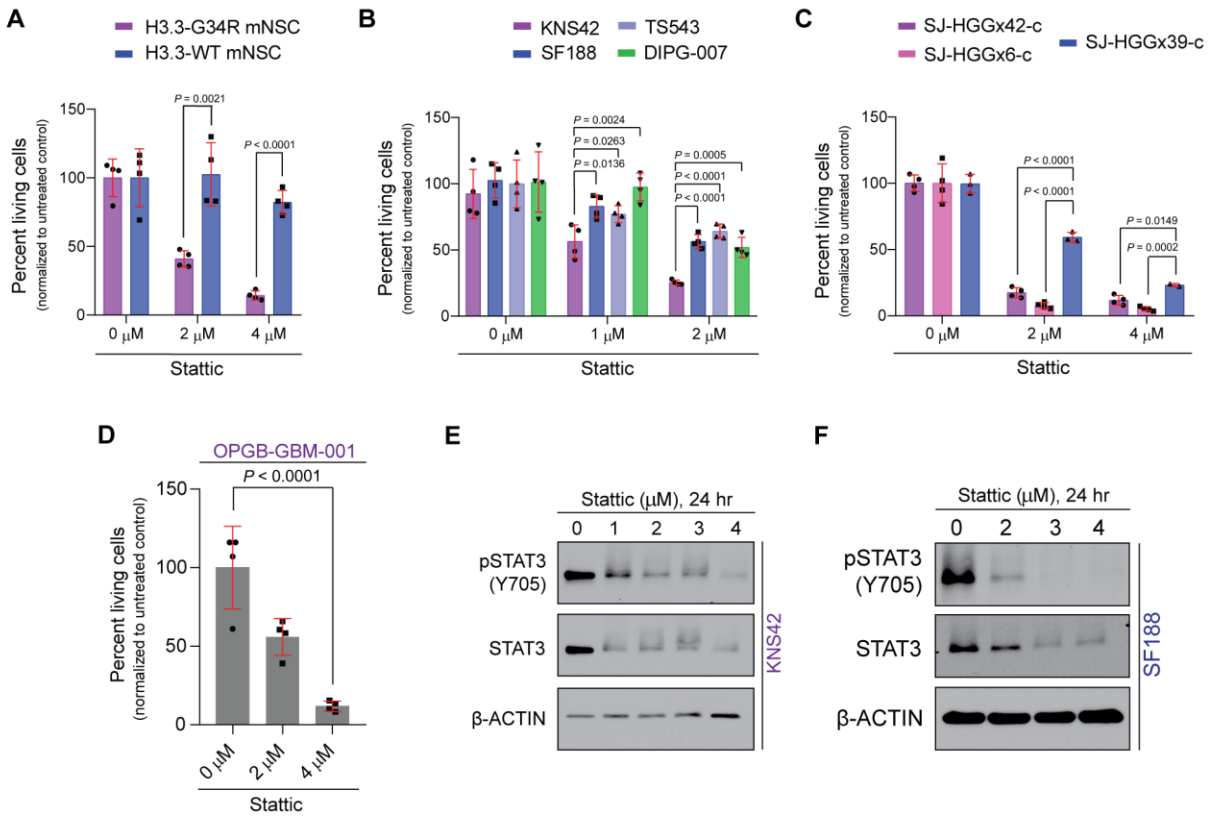

Figure 3.32. Pharmacologic STAT3 inhibition with Stattic demonstrates cytotoxicity in mouse and human H3.3G34R/V glioma cell models.
(A-B) Cell counts (percentage of living cells, Y-axis; drug concentrations, X-axis) of H3.3G34R (*purple*) and H3.3WT (*blue*) mNSCs **(A)**; and H3.3G34V KNS42 (*purple*), 31 H3.3WT SF188 (*blue*), H3.3WT TS543 (*lavender*) and H3.3K27M HSJD-DIPG-007 (*green*) patient-derived pHGG cells **(B)** treated with STAT3 inhibitor, Stattic, for 96 hours at indicated concentrations. *n*=4 technical replicates each. **(C)** Cell counts (percentage of living cells, Y-axis; drug concentrations, X-axis) of H3.3G34R SJ-HGGx42-c (*purple*), H3.3G34R SJ-HGGx6-c (*pink*), and H3.3WT SJHGGx39-c (*blue*) patient-derived pHGG cells treated with Stattic for 96 hours at indicated concentrations. *n*=3-4 technical replicates each. **(D)** Cell counts (percentage of living cells, Y-axis; drug concentrations, X-axis) of H3.3G34R OPGB-GBM-001 cells, grown as neurospheres, treated with Stattic for 96 hours at indicated concentrations. *n*=4 technical replicates each. **(E-F)** Representative Western blots for pSTAT3(Y705), STAT3, and β-Actin in H3.3G34V KNS42 cells **(E)** or H3.3WT SF188 cells **(F)** treated with Stattic for 24 hours at indicated concentrations. Data are plotted as mean ± S.D. and analyzed by nonparametric, two-sided, unpaired, Student's *t* test.

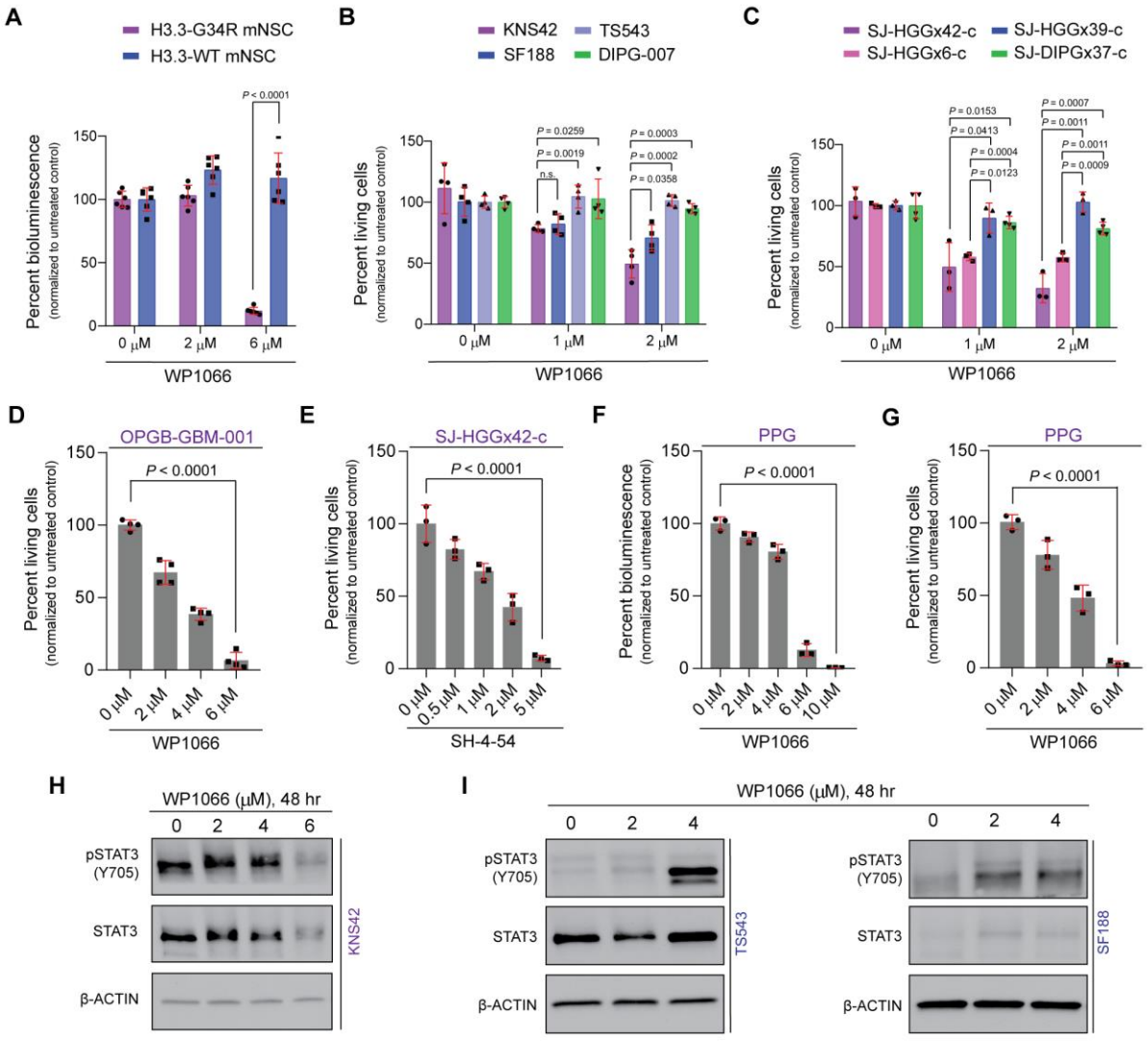

Figure 3.33. Pharmacologic JAK2/STAT3 inhibition with WP1066 demonstrates cytotoxicity in mouse and human H3.3G34R/V glioma cell models.

(A) Cell counts (percentage of bioluminescence signal, Y-axis; drug concentrations, X-axis) of H3.3G34R (*purple*) and H3.3WT (*blue*) mNSCs treated with STAT3 inhibitor, WP1066, for 96 hours at indicated concentrations. *n*=4 technical replicates per condition. **(B)** Cell counts (percentage of living cells, Y-axis; drug concentrations, X-axis) of H3.3G34V KNS42 (*purple*), H3.3WT SF188 (*blue*), H3.3WT TS543 (*lavender*) and H3.3K27M HSJD-DIPG-007 (green) patient-derived pHGG cells treated with STAT3 inhibitor, WP1066, for 96 hours at indicated concentrations. *n*=4 technical replicates each. **(C)** Cell counts (percentage of living cells, Y-axis; drug concentrations, X-axis) of H3.3G34R SJ-HGGx42-c (*purple*), H3.3G34R SJ-HGGx6-c (*pink*), H3.3WT SJ-HGGx39-c (*blue*), and H3.3K27M SJ-DIPGx37-c (green) human patient-derived pHGG cells treated with WP1066 for 96 hours at indicated concentrations; *n*=3-4 technical replicates each. **(D)** Cell counts (percentage of living cells, Y-axis; drug concentrations, X-axis) of H3.3G34R OPGB-GBM-001 cells, grown as neurospheres, treated with WP1066 for 96 hours at indicated concentrations. *n*=4 technical replicates each. **(E)** Cell counts (percentage of living

cells, Y-axis; drug concentrations, X-axis) of H3.3G34R SJ-HGGx42-c cells treated with STAT3 inhibitor SH-4-54 for 72 hours at indicated concentrations. *n*=4 technical replicates each. **(F)** Cell counts (percentage of bioluminescence signal, Y-axis; drug concentrations, X-axis) of IUE model-derived PPG cells, grown as neurospheres, treated with WP1066 for 72 hours at indicated concentrations. *n*=4 technical replicates per condition. **(G)** Cell counts (percentage of living cells, Y-axis; drug concentrations, X-axis) of IUE model-derived PPG cells, grown as neurospheres, treated with WP1066 for 96 hours at indicated concentrations. *n*=4 technical replicates each. **(H-I)** Representative Western blot for pSTAT3(Y705), STAT3, and β-Actin in H3.3G34V KNS42 **(H)** or H3.3WT SF188 and TS543 **(I)** cells treated with WP1066 for 48 hours at indicated concentrations. Data are plotted as mean ± S.D. and analyzed by nonparametric, two-sided, unpaired, Student's *t* test.

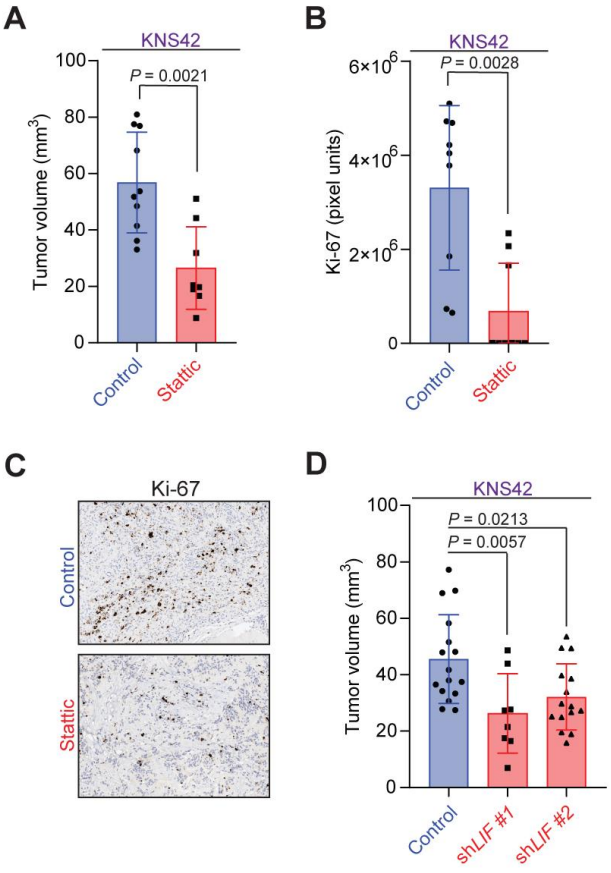

Figure 3.34. KNS42 flank models targeting STAT3 with Stattic or *LIF* knockdown.
(A) Bar plot illustrating tumor volumes (mm^3, Y-axis) from a mouse flank xenograft model of H3.3G34V KNS42 tumors treated with Stattic (10 mg/kg) every three days for 8 total doses. Control, blue, *n*=10; Stattic-treated animals, red, *n*=8. **(B-C)** Blinded quantification **(B)** and representative IHC images **(C)** of Ki-67 staining in H3.3G34R KNS42 xenografts in the flank treated with or without Stattic from **(A)**. Bar plot represents quantification (pixel units, Y-axis) of three randomly selected regions from three independent mice per treatment condition. **(D)** Bar plot illustrating tumor volumes (mm^3, Y-axis) after 10 weeks from mice implanted with H3.3G34V KNS42 flank xenografts with or without two independent *LIF* shRNAs. Control, *blue*, *n*=15; *sh*LIF #1, *red*, *n*=8; *sh*LIF #2, *red*, *n*=15. Data are plotted as mean ± S.D. and analyzed by nonparametric, two-sided, unpaired, Student's *t* test.

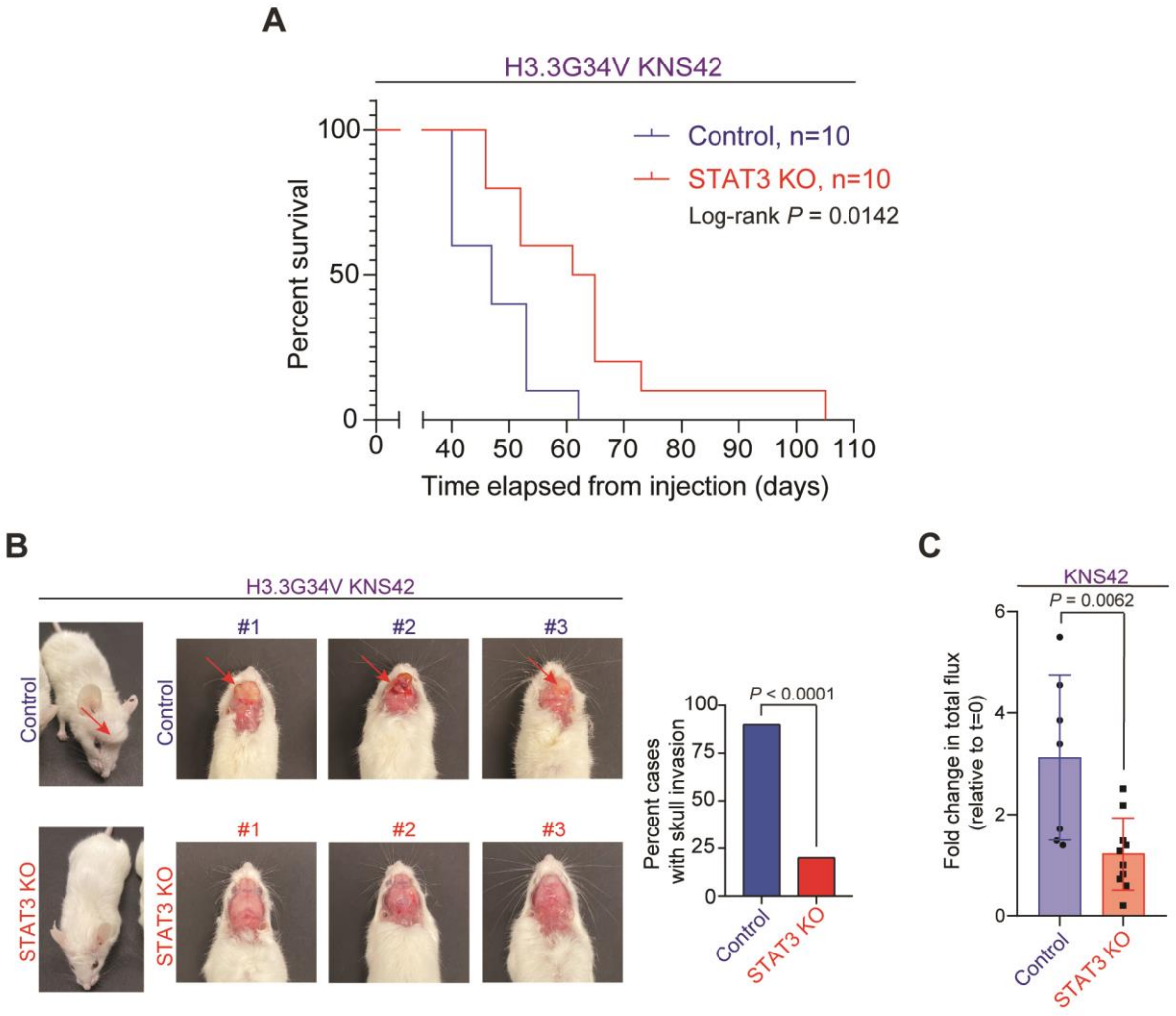

Figure 3.35. STAT3 genetic deletion slows tumor growth in orthotopic KNS42 mouse model. **(A)** Kaplan-Meier analysis of mice harboring H3.3G34V KNS42 tumors with and without *STAT3* genetic knockout (*STAT3* KO) as a function of time post-implantation. Control, *blue*, *n*=10; *STAT3* KO animals, *red*, *n*=10. **(B)** Representative images of tumor invasion into the skull (red arrows) in mice bearing KNS42 tumors with or without *STAT3* genetic knockout (*STAT3* KO) (*left*). Bar graph illustrates percent of mice within control and *STAT3* KO cohorts with observable tumor invasion into the skull (*right*). Control, *blue*, *n*=5; *STAT3* KO, *red*, *n*=10. **(C)** Bioluminescent signal quantification (Y-axis) of animals from **(A)** at week 5 post-implantation. Fold change in total flux was calculated by normalizing bioluminescent signal at the given time point by the corresponding baseline signal for each mouse. Each symbol represents one mouse. Control, *blue*, *n*=7; *STAT3* KO animals, *red*, *n*=10. Data are plotted as mean ± S.D. and analyzed by nonparametric, two-sided, unpaired, Student's *t* test. Log-rank test was utilized for Kaplan-Meier analysis (*P*-values are indicated for comparison with control animals).

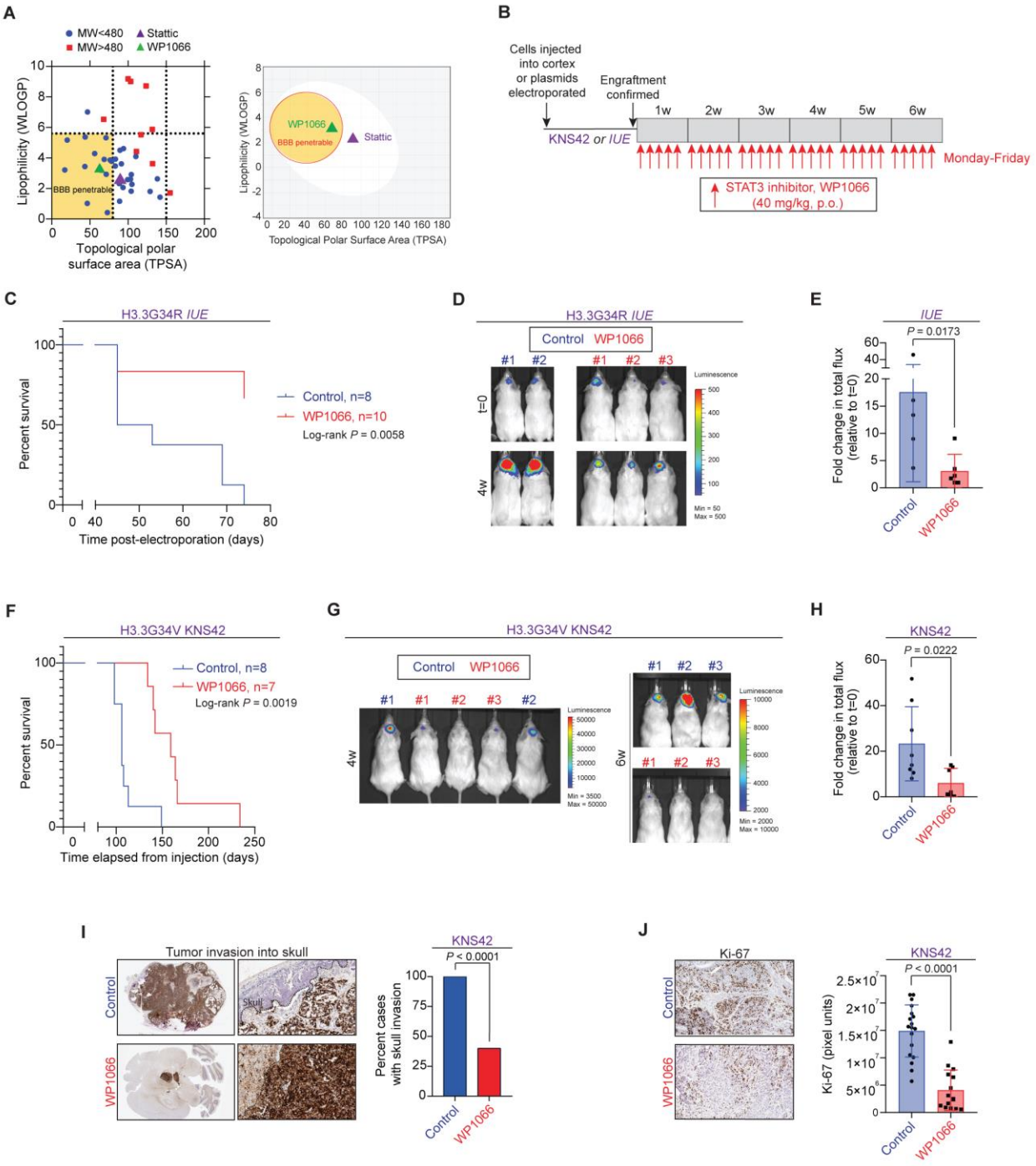

Figure 3.36. STAT3 pharmacologic inhibition with WP1066 slows tumor growth in orthotopic *IUE* and KNS42 mouse models.

(A) XY-plot (*left*) illustrating relative molecular weight (MW < 480 g/mol, blue; MW > 480 g/mol, red), lipophilicity (WLOGP, Y-axis), and topological polar surface area (TPSA, X-axis) characteristics of available STAT3 inhibitors. The SwissADME model developed by the Swiss Institute of Bioinformatics was utilized to generate the pharmacokinetic and ADME properties illustrated on the plot (Daina *et al.*, 2017). Shaded yellow area represents chemical properties associated with predicted BBB penetrability; WP1066 (*green triangle*) and Stattic (*purple*

triangle) are indicated. A BOILED-Egg XY-plot (*right*) demonstrating the lipophilicity (WLOGP, Y-axis) and topological polar surface area (TPSA, X-axis) of STAT3 inhibitors Stattic (*purple triangle*) and WP1066 (*green triangle*). Yellow area defines the range of WLOGP and TPSA properties for inhibitors with predicted BBB penetrability and white area defines the range of WLOGP and TPSA properties associated with predicted gastrointestinal absorption. **(B)** WP1066 treatment paradigm for animals **(1)** orthotopically implanted with H3.3G34V KNS42 cells or **(2)** animals bearing H3.3G34R tumors established via *in utero* electroporation (*IUE*). H3G34R *IUE* tumors are established via *in utero* electroporation in CD-1 mice with expression plasmids for dominant-negative *TP53*, mutant PDGFRA-*D842V*, and mutant H3.3G34R *H3F3A*. Red arrows indicate WP1066 administration via oral gavage over a six-week period. **(C)** Kaplan-Meier analysis of H3.3G34R *IUE*-tumor bearing mice treated with WP1066 as a function of time post-electroporation. Control, *blue*, n=8; WP1066-treated animals, *red*, n=10. **(D)** Representative bioluminescent images from H3.3G34R *IUE* control and WP1066-treated mice before (t=0) and after four weeks (4w) WP1066 treatment. **(E)** Bioluminescent signal quantification of H3.3G34R *IUE*-tumor bearing mice receiving WP1066 or vehicle in **(C)**. Fold change in total flux (Y-axis) is calculated by normalizing bioluminescent signal at treatment time point by corresponding baseline signal before treatment for each mouse. Each symbol represents one mouse. Control, *blue*, n=5; WP1066-treated animals, *red*, n=6. **(F)** Kaplan-Meier analysis of mice harboring H3.3G34V KNS42 tumors treated with WP1066 as a function of time post-implantation. Control, *blue*, n=8; WP1066-treated animals, *red*, n=7. **(G)** Representative bioluminescence images from animals implanted with H3.3G34V KNS42 cells in the cortex following four (4w) and six (6w) weeks of WP1066 treatment. **(H)** Bioluminescent signal quantification (Y-axis) of animals with H3.3G34V KNS42 tumors receiving WP1066 or vehicle in **(F)**. Fold change in total flux is calculated by normalizing bioluminescent signal at treatment time point by the corresponding baseline signal before treatment for each mouse. Each symbol represents one mouse. Control, *blue*, n=8; WP1066-treated animals, *red*, n=7. **(I)** Representative IHC images of KNS42 cranial tumors stained for GFAP illustrating tumor invasion into the skull in mice (assessed in a blinded manner) with orthotopic H3.3G34V KNS42 tumors with or without WP1066 treatment (*left*). Bar graph illustrates percent of mice within control and treatment cohorts with observable tumor invasion into the skull (*right*). Note all control mice exhibit invasion. Control, *blue*, n=8; WP1066-treated animals, *red*, n=7. **(J)** Representative IHC images and blinded quantification of Ki-67 (pixel units, Y-axis) in mice with orthotopic KNS42 tumors with or without WP1066 treatment (*left*). Bar plot represents quantification (pixel units, Y-axis) of three randomly selected regions per mouse, per treatment condition (*right*). Control, *blue*, n=6; WP1066-treated animals, *red*, n=5. Data are plotted as mean ± S.D. and analyzed by nonparametric, two-sided, unpaired, Student's t test. Log-rank test was utilized for Kaplan-Meier analysis (P-values are indicated for comparison with control animals).

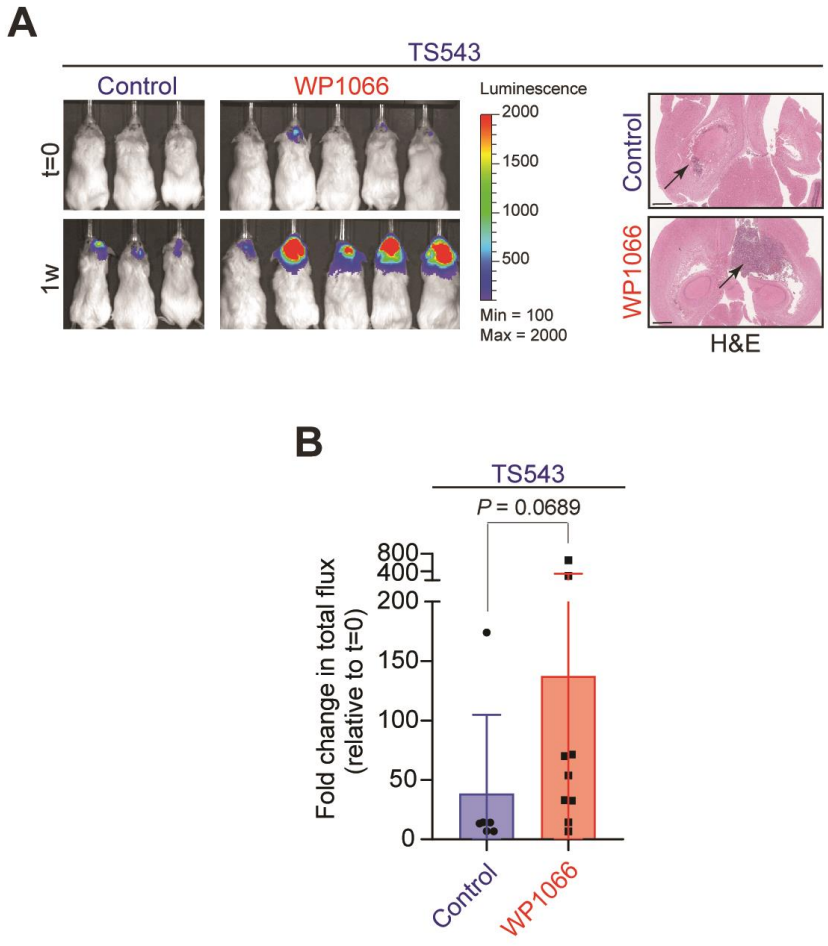

Figure 3.37. WP1066 has no effect on tumor growth in an orthotopic H3WT TS543 model. **(A)** Representative bioluminescence images from animals implanted with H3.3WT TS543 glioblastoma cells in the cortex before (*t*=0) and after one week (1w) of WP1066 treatment (*left*). Hematoxylin & eosin (H&E) staining of cranial TS543 tumors from representative control and WP1066-treated animals (*right*). Scale bar, 1 mm. **(B)** Bioluminescent signal quantification (Y-axis) from control and WP1066-treated mice with TS543 cranial tumors. Fold change in total flux is calculated by normalizing bioluminescent signal at treatment time point with corresponding baseline signal before treatment for each mouse. Each symbol represents one mouse. Control, *blue*, *n*=6; WP1066-treated animals, *red*, *n*=9. Data are plotted as mean ± S.D. and analyzed by nonparametric, two-sided, unpaired, Student's *t* test.

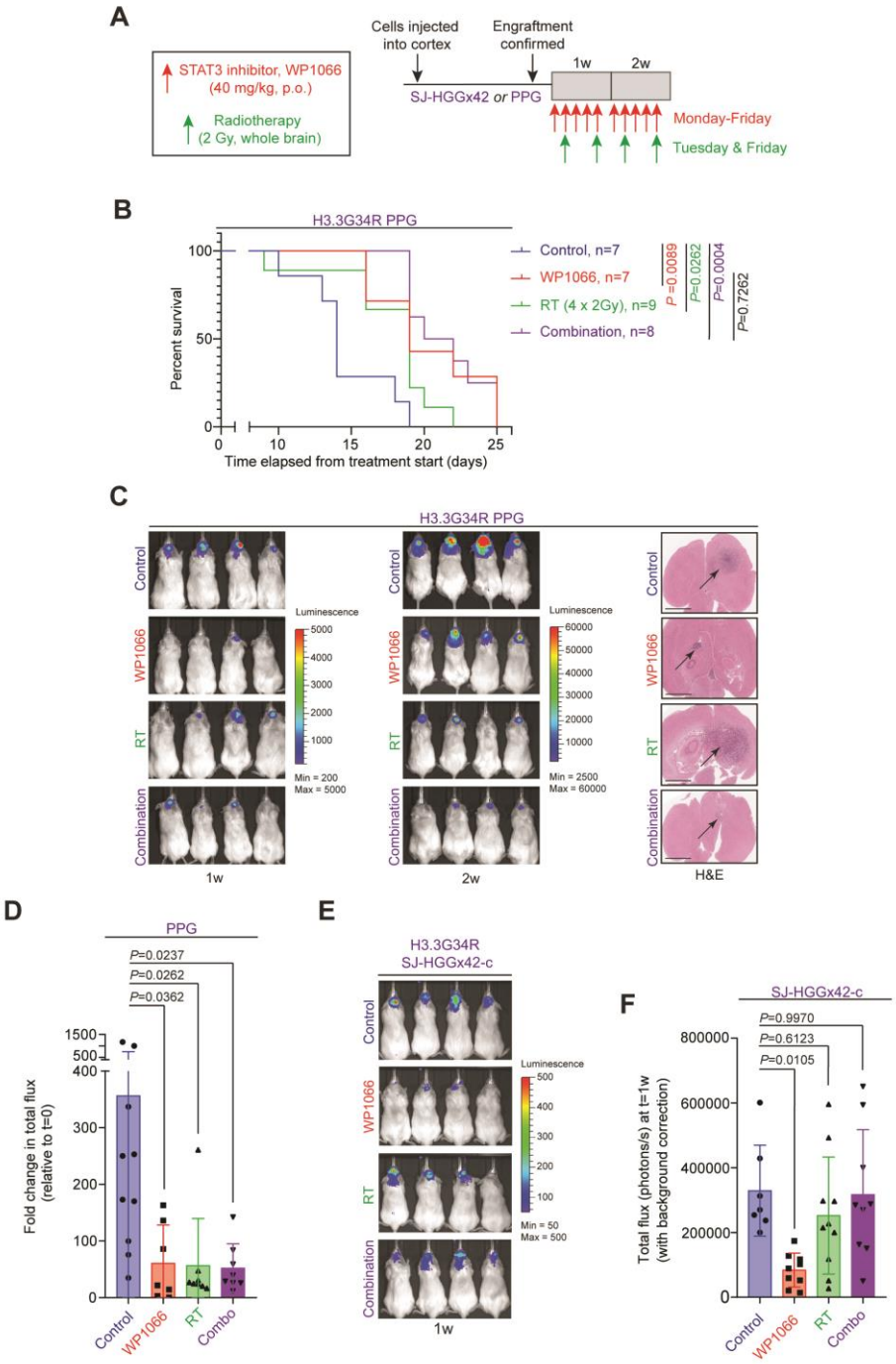

Figure 3.38. WP1066 treatment does not synergize with radiotherapy to reduce tumor burden in H3.3G34R PPG or H3.3G34R SJ-HGGx42 orthotopic models.

(A) WP1066 and radiation therapy (RT) treatment paradigms for animals with H3.3G34R tumors established orthotopically with PPG IUE-derived mouse cells or SJ-HGGx42-c human cells. Red

arrows indicate WP1066 administration. Green arrows indicate RT (cumulative 2 Gy per dose) administration. **(B)** Kaplan-Meier analysis of mice harboring H3.3G34R PPG tumors as a function of time after treatment commences. Control, *blue*, *n*=7; WP1066, *red*, *n*=7; radiation therapy (RT), *green*, *n*=9; Combination, *purple*, *n*=8. **(C)** Representative bioluminescent images from mice orthotopically implanted with PPG cells after one (1w) and two (2w) weeks of treatment with single agent WP1066 (*red*), radiation therapy (RT, *green*), combination therapy (*purple*), or no treatment (*blue*), 43 according to the paradigm outlined in **(A)**. Hematoxylin & eosin (H&E) staining of cranial PPG tumors from representative control and treatment group animals (*right*). Scale bar, 2 mm. **(D)** Bioluminescent signal quantification of H3.3G34R PPG tumor-bearing mice at the end of two weeks of treatment with single agent WP1066 (*red*, *n*=7), radiation therapy (RT, *green*, *n*=8), combination therapy (*purple*, *n*=8), or no treatment (*blue*, *n*=10). Fold change in total flux (Y-axis) is calculated by comparing bioluminescent signal at treatment time point with baseline signal before treatment for each mouse. Each symbol represents one mouse. **(E)** Representative bioluminescent images from mice orthotopically implanted with SJHGGx42-c cells after one week (1w) of treatment with single agent WP1066 (*red*), radiation therapy (RT, *green*), combination therapy (*purple*), or no treatment (*blue*), according to the paradigm outlined in **(A)**. **(F)** Bioluminescent signal quantification of H3.3G34R SJ-HGGx42 tumor-bearing mice after one week of treatment with single agent WP1066 (*red*, *n*=9), radiation therapy (RT, *green*, *n*=10), combination therapy (*purple*, *n*=9), or no treatment (*blue*, *n*=7). Total flux (photons/s, Y-axis) is plotted for each group. Each symbol represents one mouse. Data are plotted as mean ± S.D. and analyzed by nonparametric, two-sided, unpaired, Student's *t* test. Log-rank test was utilized for Kaplan-Meier analysis (*P*-values are indicated for comparison with control animals).

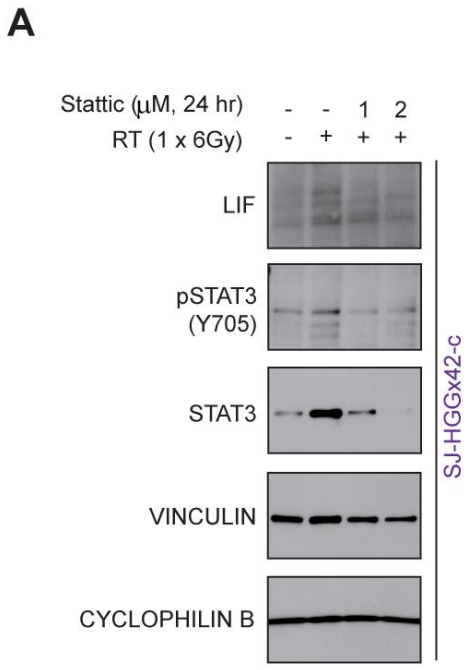

Figure 3.39. Irradiation enhances STAT3 phosphorylation in H3.3G34R SJ-HGGx42 cells. **(A)** Representative Western blots for LIF, pSTAT3(Y705), total STAT3, VINCULIN, and CYCLOPHILIN B in SJ-HGGx42-c cells treated with radiation therapy (a single 6 Gy dose) alone or in combination with Stattic for 24 hours at indicated concentrations.

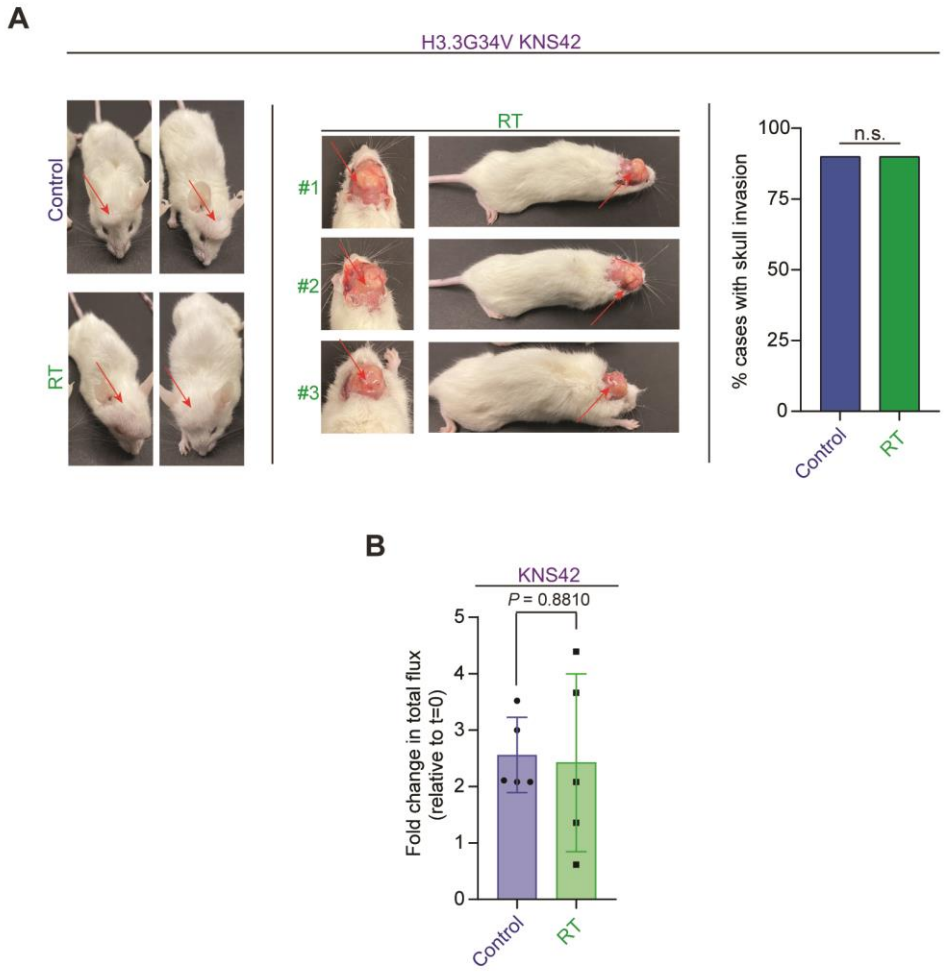

Figure 3.40. Radiotherapy does not slow tumor growth of an orthotopic H3.3G34V KNS42 model.

(A) Representative images of tumor invasion into the skull in mice bearing KNS42 tumors with or without radiation therapy (RT) (*left*). Red arrows indicate evidence of tumor invasion into surrounding skull. Bar graph illustrates percent of mice within control and RT cohorts with observable tumor invasion into the skull (*right*). Control, *blue*, *n*=5; RT-treated animals, *green*, *n*=5. **(B)** Bioluminescent signal quantification (Y-axis) from control and RT-treated mice after treatment following the paradigm in **(A)**. Fold change in total flux is calculated by normalizing bioluminescent signal at treatment time point with corresponding baseline signal before treatment for each mouse. Each symbol represents one mouse. Control, *blue*, *n*=5; RT-treated animals, *green*, *n*=5. Data are plotted as mean ± S.D. and analyzed by nonparametric, two-sided, unpaired, Student's *t* test.

Chapter 4

Conclusion

4.1 Overview

In this dissertation I investigated mechanisms of tumorigenesis in H3K27M diffuse midline gliomas (DMGs)/diffuse intrinsic pontine gliomas (DIPGs) and H3G34R/V high-grade gliomas. Using an isogenic system, I demonstrated that H3K27M cells differentially utilize alpha-ketoglutarate precursors such as glutamine and glutamate to drive cell proliferation. Furthermore, I described epigenetic changes that occur at loci coding for genes involved in glucose and glutamate transport and metabolism. *In vitro* data demonstrated that H3.3K27M-expressing cells and tumors upregulate TCA cycle genes, and these findings are recapitulated by *in silico* gene expression analysis of H3K27M and H3WT tumor tissues. We further probed this finding using metabolomic and proteomic approaches which confirmed elevated import of TCA-cycle related metabolites and expression of key proteins for glucose and glutamine catabolism. I demonstrated that DIPG cells utilize glucose and glutamine heterogeneously to regulate histone lysine 27 methylation and cell growth. Additionally, I show that targeting glutamine and glucose metabolism via targeting hexokinase, glutaminase, and isocitrate dehydrogenase is efficacious *in vitro* and *in vivo* and can therapeutically raise H3K27me3 levels.

A second focus of this thesis was to understand the molecular mechanisms activated through epigenetic reprogramming by H3G34R/V histone mutations. I provide a detailed characterization of the relationship between histone and DNA methylation perturbations in

H3G34R/V mutant cells. I show that the leukemia inhibitory factor/signal transduction and activator of transcription (LIF/STAT3) pathway is activated in H3G34R/V cells and tumor tissues. I also demonstrate that genetic suppression of LIF/STAT3 components can slow growth of H3G34R/V *in vitro.* Importantly, I show that targeting STAT3 activity pharmacologically with small molecule inhibitor, WP1066, is therapeutic in multiple H3G34R/V orthotopic models. In this final chapter, I will discuss interesting questions arising from my results and expand on future directions of study.

4.2 Summary on studies focused on H3K27M mutant glioma

In Chapter 2, I highlighted the importance of alpha-ketoglutarate (α-KG), a critical cofactor for histone lysine demethylases (KDMs), for modulating nuclear H3K27me3 levels in DMG/DIPG cells. Molecules with similar structure to α-KG, such as D-2-hydroxyglutarate (D-2HG) produced by mutant IDH1 (mIDH1) tumors, also play a modulatory role, and can competitively inhibit various DNA and histone demethylases (Dang *et al.,* 2009; Lu *et al.,* 2012; Xu *et al.,* 2011). Prior work in the cancer field has highlighted how H3K27M and H3K36M mutations cause global reduction of methylation on lysine-27 or lysine-36 residues, respectively, in a dominant-negative manner (Lewis *et al.,* 2013; Lu *et al.,* 2016). Much of the early work focused on mapping epigenetic patterns within H3K27M tumors, identifying possible cell-of-origin signatures, and using epigenetic drugs to target enzymes that post-translationally modify H3K27. I sought to build on this work and examine the role of carbon metabolism in regulating the epigenetic state of H3K27M tumors and how we might be able to exploit metabolic processes to design more effective therapies.

Our interest for this work was sparked by previous studies implicating glutamine in regulating histone methylation. One study by Pan *et al.* (2016) set out to understand the interplay between glutamine depletion in tumors, epigenetic changes, and potential therapeutic resistance. Profiling of histone lysine-4, -9, -27, and -36 methylation revealed hypermethylation of these residues, coincident with lowered glutamine and α-KG, in the tumor cores derived from xenograft models relative to methylation state in the tumor periphery. This key finding could be recapitulated *in vitro* using multiple tumor cell lines where specific glutamine deficiency was found to control hypermethylation in a dose-dependent manner which could be abrogated by addition of cell-permeable α-KG to the culture media. Most intriguingly, the study by Pan and colleagues made a parallel between mutant IDH1/2 tumors which have been found to block differentiation and the finding that glutamine deprivation within a tumor core can induce dedifferentiation and treatment resistance. Key experiments with melanoma cells demonstrated a role for EZH2/H3K27me3 in glutamine deprivation where enhanced expression of dedifferentiation genes and suppressed expression of differentiation genes occurs. Knockdown or inhibition of EZH2 activity reversed these phenotypes and sensitized cells to other modes of therapy.

Our work in Chapter 2 revealed that α-KG was elevated in H3K27M cells and blocking metabolism of α-KG precursors could effectively and therapeutically increase H3K27me3. During profiling studies on low grade gliomas, it was discovered that these tumors harbor mutations in *isocitrate dehydrogenase 1* (*IDH1*) (Parsons *et al.,* 2008; Yan *et al.,* 2009). Normally, cytosolic IDH1 functions to perform oxidative decarboxylation of isocitrate to α-KG which can then be utilized in demethylation reactions. Mutations in *IDH1,* often histidine substitutions at arginine 132 (R132H), confer a neomorphic property which allows for the conversion of α-KG to the oncometabolite D-2-hydroxyglutarate (Dang *et al.,* 2009). Prior work in our lab has shown that

H3K27M and IDH1 mutations are mutually exclusive (Chung *et al.*, 2020). Interestingly, treatment of H3K27M-expressing cells with D-2HG *in vitro* and *in vivo* resulted in marked cell death. Moreover, forced expression of mutant IDH1 R132H in DIPG cells caused D-2HG production accompanied by stunted cell growth (Chung *et al.*, 2020). These results suggest the two mutations fail to co-occur because DMG and IDH tumors prefer opposing epigenetic architecture. This works raises additional questions about how α-KG may be affecting methylation at other residues on H3.3 and their consequences for tumorigenesis. Multiple studies have described the importance of targeting regions with H3K27me3 and H3K27ac retention. Although global changes in H3K9me3, H3K4me3, and H3K36me3 have not be reported in H3K27M models, changes in these modifications at genomic regions have not been well characterized to date. Notably, H3K36me3/H3K9me3 demethylases KDM4A/B/C are α-KG dependent (Tran *et al.*, 2018). It is possible that α-KG-mediated reduction of H3K9me3 causes upregulation of dedifferentiation or stem cell lineage genes. Following a similar logic, loss of genomic H3K36me3 loss could cause downregulation of key differentiation genes. An important additional step would be to identify how α-KG may be directly affecting DNA methylation processes which are perturbed in H3K27M mutant tumors. A wider understanding about these epigenetic changes will help uncover deregulated genes that present novel drug targets. This approach assumes that epigenetic perturbations in H3K27M tumors activate target gene expression. However, in-depth profiling of epigenetic changes will allow the identification of genomic regions with H3K27-independent transcriptional deregulation. It is likely that targeting KDMs will be a useful strategy in treating DMG/DIPG and this information will aid in developing therapies with epigenetic drugs building off initial work that focused on targeting K27-modifying enzymes like EZH2. Overall, our observation that α-KG plays an oncogenic role in maintaining low H3K27me3 in DMG/DIPGs

raises questions about other approaches that can therapeutically target metabolism and correct aberrant epigenetic processes.

4.3 Future directions for targeting α-ketoglutarate in H3K27M and mutant IDH gliomas

Several years ago, studies investigated how to therapeutically target and upregulate a key mediator of cellular death called tumor necrosis factor-related apoptosis-inducing ligand, also known as TRAIL (Allen *et al.,* 2013; Allen *et al.,* 2015). TRAIL binds to specific cell surface receptorss, death receptor 4 (DR4) and death receptor 5 (DR5), to exerts it cytotoxic effect (Allen *et al.,* 2013). Clinical trials have attempted to use recombinant TRAIL to selectively induce tumor cell death, however its short-half life and rapid clearance *in vivo* presented challenges (Prabhu *et al.,* 2020). Interestingly, both TP53 and FOXO3a are known transcription factors that can bind to the *TRAIL* promoter and increase its abundance (Ghaffari *et al.,* 2003; Kuribayashi *et al.,* 2008). To find a solution to the clinical shortcomings of recombinant TRAIL and avoid treatments that depend on TP53 (often mutated or inactive in cancers), Allen *et al.* (2015) screened a set of small molecule compounds (NCI Diversity Set II) using an *in vitro* luciferase-reporter assay where luciferase expression was placed under control of the *TRAIL* promoter. This construct was transfected into *TP53*- and *BAX*-null HCT116 cells to find compounds that could induce TRAIL expression on the cell surface in a TP53-independent manner. The screen identified compounds TIC4, TIC8, TIC9, and TIC10 (also known as ONC201) as capable of increasing *TRAIL* mRNA. Further experiments demonstrated that TIC9 and TIC10 were the only compounds that could upregulate TRAIL abundance on the cell surface and induce significant cell death *in vitro.*

Additional studies by Allen and colleagues (2015) confirmed the ability of TIC10 to induce surface TRAIL proteins in various cancer cell lines, found that TRAIL or DR5 knockdown could abrogate cell death, and observed enhanced efficacy of TIC10 to reduce *in vivo* tumor growth in

flank and intracranial xenografts. These reports also provided a molecular mechanism by which TIC10 upregulates TRAIL. TIC10 was found to cause concurrent inhibition of AKT and ERK/MEK phosphorylation which relieved inhibitory phosphorylation of their downstream target FOXO3a and permitted its nuclear translocation to drive TRAIL and its receptor DR5. However, later studies on mantle cell lymphoma (MCL) discovered that TIC10 did not induce TRAIL or DR5 or cause AKT/ERK dephosphorylation, but still exerted cytotoxic effects in these cells (Ishizawa *et al.*, 2016). This finding prompted questions about how TIC10 can still kill cells in a TRAIL-independent manner. One experiment used mouse embryonic fibroblasts without and without *Bax* and *Bak* knockout (proteins controlling intrinsic apoptosis) treated with TIC10 and demonstrated a blockade of apoptosis upon *Bax/Bak* deletion, implicating the role of the intrinsic pathway in TIC10-induced cell death. Another critical experiment compared the responses of TRAIL-resistant lymphoma cells with and without FOXO3a knockdown to TIC10 treatment, noting similar responses in both conditions. Importantly, profiling of these MCL cells treated with TIC10 revealed upregulated genes associated with ER stress, CHOP and ATF4 induction, and the unfolded protein response, suggesting other TRAIL-independent pathways are activated by TIC10 (Ishizawa *et al.*, 2016). This fueled intense interest in understanding other molecular targets of TIC10.

Studies by Graves *et al.* (2019) identified the mitochondrial caseinolytic protease P (ClpP) as a novel interactor with TIC10 and its analogues using mass spectrometry and peptidase assays. Normally, ClpP along with a host of other proteases serve important functions for the elimination of misfolded mitochondrial proteins. Graves and colleagues found that TIC10 activated ClpP proteolytic activity by combining a fluorogenic ClpP substrate and purified ClpP protein in the presence of increasing doses of TIC10. Using a similar *in vitro* approach, the group combined

casein and purified ClpP in the presence and absence of TIC10 and observed significant casein cleavage in the reaction product, indicating ClpP hyperactivity. Biochemical studies by Ishizawa *et al.* (2019) independently discovered TIC10 as a ClpP activator during a screen designed to identify compounds capable of increasing ClpP proteolysis of casein and fluorogenic substrates. Insightful experiments with cells expressing mutant, catalytically-inactive ClpP proteins nicely showed that TIC10 causes degradation of oxidative phosphorylation and mitochondrial translation proteins, and its cytotoxic effect is critically mediated by ClpP.

TIC10 exhibits great clinical potential for oncology as evidenced by its safety and tolerability in preclinical models and ongoing clinical trials. A large range of cancer cell types respond sensitively to TIC10/ONC201 treatment (see Allen *et al.*, 2016; Prahbu *et al.*, 2020 for detailed reviews). Recently, studies have tested the efficacy of ONC201 treatment on human glioblastoma (GBM) cells using *in vitro* assays and *in vivo* orthotopic GBM models. These studies reported therapeutic potential for ONC201 in GBM and observed a synergism with concurrent radiation treatment with little systemic toxicity (He *et al.*, 2021).

The rapid translation potential of ONC201 has led to several informative clinical trials. Arrillaga-Romany *et al.* (2017) discussed results from a Phase II trial comprised of patients with IDH1/2 wild-type glioblastoma who were treated with ONC201 every three weeks. Unlike the neurotoxicity seen with standard-of-care temozolomide and radiation treatments, ONC201 was well tolerated in patients. Surprisingly, one patient presenting with a secondary glioblastoma demonstrated a durable response to therapy and further profiling revealed this patient harbored a H3K27M mutation. A secondary study by Chi *et al.* (2019) provided results from a trial comprised of pediatric and adult H3K27M midline gliomas. Strikingly, one patient presenting with a H3K27M DMG who exhibited tumor rapid progression after radiation/temozolomide treatment

was treated with ONC201. Miraculously, this patient survived their disease and experienced a complete tumor regression. Together, these studies sparked intense interest in ONC201 as a therapeutic agent for DMG/DIPG given its uniformly lethal historical outcome.

Given our recent work on the metabolic-epigenetic axis in DIPG and the ability of ONC201 to compromise oxidative phosphorylation and mitochondrial integrity, our laboratory has been investigating if ONC201 affects epigenetic patterning in DIPG cells. Recent work in our lab has revealed ONC201 treatment of some DIPG cells can effectively reduce the expression of key metabolic enzymes like hexokinase (HK2), glutaminase (GLS), glutamate dehydrogenase (GLUD1/2), and isocitrate dehydrogenase 1/2 (IDH1/2) in a dose-dependent manner (**Figure 4.2A-B**). Unexpectedly, we also observed perturbations in non-mitochondrial protein expression such as for HK2, IDH1, EZH2, KDM6B, KDM4B, KDM5B, and ACLY (**Figure 4.2B** and **Figure 4.3A**). This likely occurs because ONC201 can activate eIF2α phosphorylation which been demonstrated to strongly attenuate protein synthesis (Kline *et al.,* 2016; Graves *et al.,* 2019). We observed robust effects on expression in DIPG-007 and SF7761 while DIPG-XIII exhibited relative resistance to treatment. This raises important questions about mechanisms for ONC201 resistance in a subset of DIPG cells and patients. Indeed, we have performed similar experiments on a cell line (UMPed83) cultured from a patient where ONC201 treatment was largely ineffective. Treatment with ONC201 under similar experimental conditions did not yield robust degradation of metabolic enzymes, highlighting the need to better understand modes of resistance (**Figure 4.4A**). Studies on acute myeloid leukemia and breast cancers have suggested ClpP loss and mutations are key elements of therapy resistance (Prabhu *et al.,* 2020). Low ClpP expression or mutation could explain the lack of clinical response to ONC201 in some patients and requires in-depth study. One future direction for investigation will be to molecularly profile DIPG treatment

candidates to establish information about ClpP expression, deletion, and mutation that will guide decisions about treatment. It is also plausible that H3K27me3 is retained at loci (such as FOXO3a, DR5, TRAIL, or ATF4) that are important for ONC201 cytotoxicity. It will be important to determine if combination therapy with EZH2 inhibitors that can activate these mediators might sensitize such patients to treatment. ONC201 has been shown to deactivate AKT and MEK signaling to activate FOXO3a, and it is possible that therapy resistant patients harbor constitutive activation of the AKT and MEK pathways. Following similar logic, a lack of activation of either pathway could also block the ability of ONC201 to induce FOXO3a. An important next step will be to assess the epigenetic profile and expression of these key proteins in patients to determine which patients are good candidates or could benefit from combination sensitizing therapies.

Our previous studies demonstrated that genetic or pharmacological inhibition of metabolic targets like HK2 and IDH1 can modulate both chromatin accessibility, gene expression, and histone methylation (Chung *et al.,* 2020). Thus, we have also investigated whether these changes induced by ONC201 have consequences for H3K27me3 and H3K27ac. Our initial findings suggest elevated H3K27me3 and reduced H3K27ac, without affecting H3K27M expression, upon ONC201 treatment of H3K27M DIPG-007 and SF7761 cells (**Figure 4.5A-B**). A critical step will be to determine what other epigenetic marks are perturbed by ONC201 and the genomic distribution of these modifications preceeding and following therapy. Interestingly, H3K27M and mutant IDH tumors both utilize α-KG and this has unique downstream consequences in each tumor type, discussed earlier. Work from our lab demonstrated that α-KG plays a role in maintaining a low H3K27me3 state in DIPGs that present a therapeutic vulnerability along this axis. In contrast, mutant IDH1/2 proteins catalyze the conversion of α-KG to D-2HG, an inhibitor of histone demethylases, resulting in a hypermethylator phenotype in mutant tumors (Tahiliani *et al.,* 2009;

Turcan *et al.,* 2012). Early research in the mIDH1/2 glioma field focused on designing inhibitors to target the mutant enzymes, reduce D-2HG production, and reverse hypermethylation (Konteatis *et al.,* 2020; Kopinja *et al.,* 2017; Popovici-Muller *et al.,* 2018; Pusch *et al.,* 2017; Rohle *et al.,* 2013; Turcan *et al.,* 2013). Given our results about ONC201 in the DIPG context, we became interested evaluating the sensitivity of mutant IDH1/2 cells to ONC201. Since ONC201 causes GLS, GDH, IDH1, and IDH2 degradation in DIPG cells, we hypothesized that ONC201 treatment could block glutaminolysis and ultimately decrease both α-KG and 2HG. Experiments on mIDH1 R132H TS603 cells demonstrated little changes in these metabolic enzymes upon treatment (**Figure 4.6A**). Unexpectedly, preliminary experiments suggest that ONC201 causes D-2HG accumulation (data not shown). However, we found that ONC201 treatment decreased cell viability in mIDH1 TS603, mIDH1 JJ012, and mIDH2 CS1 cells (**Figure 4.7A-C**). One future direction of study here would be to understand the effects of ONC201 on α-KG and D-2HG stasis and whether this contributes to epigenetic reprogramming.

4.4 New directions for probing the importance of Isocitrate Dehydrogenase 1 in glioma

Critically, studies in the DIPG and mIDH glioma field have highlighted the important role of IDH1 in tumor biology. One intriguing and unanswered question in the glioma field relates to why IDH mutations preferentially occur in cytosolic IDH1 instead of mitochondrial IDH2. This raises questions about whether IDH1 controls the transport of biomolecules, such as citrate, that are key precursors for α-KG or 2-HG. Recent work in our lab has identified differences in the expression of the mitochondrial citrate carrier (*SLC25A1*) in wild-type (WT) *versus* IDH1 mutant low-grade gliomas using patient TCGA data. Analysis of low-grade glioma datasets revealed that patients with elevated *SLC25A1* had improved survival outcomes (data not shown). To further probe the role of IDH1 in controlling SLC25A1 expression, we expressed wild-type and R132H

IDH1 in normal human astrocytes. We observed SLC25A1 upregulation in both conditions, however SLC25A1 induction was stronger with R132H IDH1 expression (**Figure 4.8**). In their study of R132H-IDH1 effects on α-KG-dependent dioxygenases, Xu *et al.* (2011) elegantly demonstrated that WT-IDH1 overexpression in U-87MG cells caused reduction in the pro-survival transcription factor HIF1α while forced R132H-IDH1 expression or 2HG treatment enhanced HIF1α expression. Interestingly, it has been shown that *SLC25A1* transcription can be controlled by HIF1α (Kolukula *et al.,* 2014). HIF1α is often stabilized under hypoxic conditions, suggesting that the regulation and activity of SLC25A1 may be different in the core and periphery. Recent work has elucidated that glutamine and α-KG deficiency at the tumor core causes increased histone methylation compared to cells in the periphery (Pan *et al.,* 2016). At present, little work has focused on the role of hypoxia in regulating histone methylation in mutant IDH tumors and if and how hypoxia further exacerbates the observed hypermethylator phenotype. Very recent and exciting work has shown that hypoxia affects the catalytic activity of histone lysine demethylases and causes chromatin alterations that block differentiation (Batie *et al.,* 2019; Chakraborty *et al.,* 2019). It is possible that targeting SLC25A1 activity could be therapeutic in the context of hypoxia. Some studies have suggested that reducing D-2HG levels with mutant IDH-specific inhibitors is not sufficient to slow cell growth or reverse histone methylation (Kayabolen *et al.,* 2021). With this in mind, studying the H3K27ac patterning in mIDH cells and whether it can be modulated by SLC25A1 activity can provide critical information about the role of cytosolic citrate in the driving tumor growth. Although mIDH inhibition can reduce 2HG, this may not be sufficient to abrogate HIF1α stability in the hypoxic niche and tumors may be able to maintain SLC25A1 activity and critical histone H3K27ac that drives therapy resistance. Furthermore, additional factors in IDH mutant tumors likely control the H3K27ac landscape. Targeting 2HG under normoxic conditions

may indeed attenuate HIF1α stability and signaling pathways like AKT/mTOR (upregulated in mIDH tumors and indirect drivers of SLC25A1 via SREBP1c), but this may not be sufficient to suppress SLC25A1 expression or activity (Carbonneau *et al.,* 2016; Kolukula *et al.,* 2014). Because others have reported irreversibility of histone methylation with mIDH inhibitors, it will be beneficial to induce mutant IDH1 and IDH2 expression in *SLC25A1*-null cells to determine the role of citrate transport in establishing a distinct H3K27ac profile and tumorgenicity. Work here can potentially answer questions about why IDH1 mutations preferentially occur in glioma while IDH2 mutations often occur in hematological malignancies. Preliminary data from our lab demonstrates elevated SLC25A1 in mIDH1 cells *versus* mIDH2 cells, potentially suggesting that these mIDH2 tumors may have a differential dependence on SLC25A1, distinct H3K27ac profile, and potentially less reliance on processes involving citrate transport like histone acetylation. This presents a unique opportunity to study the mechanisms for how WT-IDH1 and R132H-IDH1 control SLC25A1 expression. Given the survival data, it is also unclear whether SLC25A1 plays a tumor suppressive or promoting role in mutant IDH gliomas. R132H-IDH1 glioma patients exhibit longer overall survival than WT-IDH1 glioma counterparts (Turcan *et al.,* (2012), and SLC25A1 function might play an important role here.

Investigating the function of SLC25A1 in H3K27M DMG/DIPGs, shown to upregulate WT-IDH1, will be informative as well. H3K27M gliomas are thought to arise in cells of oligodendroglial origin and a large fraction of low-grade oligodendrogliomas and astrocytomas harbor IDH1 mutations. On the basis of this knowledge, we queried data Marques *et al.* (2016) who studied transcriptional changes that occur during the stages of oligodendrocyte differentiation. Our preliminary analysis suggests that IDH1 expression is increased during the transition of oligodendrocyte precursors to newly formed oligodendrocytes and subsequently followed by

SLC25A1 expression induction in mature oligodendrocytes. Given the important role of histone acetylation at oligodendroglial genes for DIPG tumorigenesis, investigating the role of SLC25A1 both in the DIPG and mutant IDH contexts could help us further understand how developmental pathways are co-opted for tumor progression. One possibility is that SLC25A1 plays opposing roles in H3K27M and mIDH1 cells. In H3K27M-expressing cells, heightened SLC25A1 activity may allow for increased α-KG and acetyl-CoA production that maintain the reduced H3K27me3 state. In contrast, 2HG production in mIDH1 cells could promote HIF1α stability responsible for SLC25A1 induction which further reinforces 2HG production by supplying cytosolic citrate. Investigating if SLC25A1 perturbs the histone acetylation distribution and localizing such H3K27ac genomic changes in relation to dysregulated H3K27me3/H3K9me3 could clarify if aberrant H3K27ac is tumor suppressive in the mIDH context. Results from this work could provide explanations about why mIDH1 patients have better survival outcomes.

4.5 Overarching questions for future study of H3K27M gliomas

In examining H3K27M tumors, we discovered metabolic vulnerabilities that can leveraged for therapy. Since the initial profiling studies of pediatric glioma (Bender *et al.,* 2013; Mackay *et al.,* 2017; Schwartzentruber *et al.,* 2012; Sturm *et al.,* 2012; Wu *et al.,* 2012), the field has made advances in our knowledge of the epigenetic changes and devised clever therapeutic strategies. We know that K-to-M mutations can occur at lysine 27 in the replication dependent and independent histones, H3.1 and H3.3, respectively, and cause global H3K27me3 loss. H3.1 and H3.2 histone variants are recognized by chaperones distinct from those that deposit H3.3, and their incorporation occurs at distinct locations. However, few studies have extensively profiled the genomic regions where mutant H3.1K27M histones are deposited and epigenetic patterns within these regions. Nagaraja *et al.* (2019) recently reported that H3.1K27M and H3.3K27M DIPG

tumors have different super enhancer landscapes. In addition, the group observed different localization of each mutant histone, unique regions with activating H3K27ac, and differential chromatin accessibility at enhancers implicating specific signaling pathways (p38 MAPK, PI3K, and NF-kB) in H3.1K27M samples. Conclusions from analyses by Nagaraja and colleagues supported the findings from Piunti *et al.* (2017) who reported a strong colocalization between wild-type H3.3 and H3K27M histones. However, they found that H3K27M in H3.1K27M-expressing cells did not behave in this manner and had low abundance in wild-type H3.3-rich regions. This conclusion suggests that H3.3K27M and H3.1K27M inhibit PRC2 to different extents depending on the amount of each mutant localized to a specific region. H3.3 is targeted to regions with high transcriptional activity, and since H3.3K27M deposition closely mirrors wild-type H3.3, it is possible that H3.3K27M deregulates H3K27ac, H3K27me3, and gene expression to a larger extent at these regions. Thus, investigating the differences in H3K27me3 loss (similar to the H3K27ac studies by Nagaraja *et al.,* 2019) can clarify H3.3 region-dependent transcriptional vulnerabilities in H3.3K27M tumors. The observation of differential distribution for H3.1 and H3.3 mutant histones also raises questions about whether their locations in the genome predispose them to aberrantly interact with different chromatin-modifying enzymes. For example, histone H3.1 is incorporated during DNA synthesis and repair, and it is plausible that H3.1 mutations interfere with its recognition by histone chaperones (such as CAF-1) and lead to genomic instability and a specific vulnerability.

On a broader level, more investigation is needed to understand what other proteins might be sequestered or inhibited by H3K27M histones and what consequences these interactions have for chromatin accessibility. Recent studies have demonstrated that H3K27M and other histone mutants can modulate the activity of SWI-SNF chromatin remodeling complexes (Mashtalir *et al.,*

2021). To probe this, different H2A/B, H3, and H4 mononucleosomes substrates were incubated with SWI/SNF complexes. Combinatorial H4 acetylated-H3 methylated mononucleosomes were found to stimulate ncBAF activity but inhibit cBAF activity. Similar analyses on H3 nucleosomes methylated on various residues revealed decreased cBAF activity in the presence of H3K4me3 or H3K27me3 nucleosomes substrates (Mashtalir *et al.*, 2021). This data strongly suggests that H3K27M and its consequential changes on epigenetic modifications like H3K27me3 may modulate SWI/SNF complex activity in tumors. In light of this, it will be important to investigate which SWI/SWF complexes (cBAF, PBAF, or ncBAF) and specific subunits interact with H3K27M mutant histones. It remains unknown if mutant histones can inhibit the ATPase activity of SWI/SNF subunits like SMARCA4 in a cellular context where combinatorial modifications also exist. It will be important to profile differences in genomic localization of BAF complex proteins (such as ARID1A and ARID1B) in H3K27M-mutant and wild-type cells. Several studies have implicated ARID1A/B in modulating enhancer H3K27ac (Chandler *et al.*, 2013; Kelso *et al.*, 2017; Raab *et al.*, 2015). Given the reported colocalization of H3.3K27M and H3K27ac at enhancers in DIPG cells, investigating possible colocalization of ARID1A/B and other SWI/SNF complex subunits at these regions and the mechanisms behind their retention will be insightful. It is also possible that H3K27M-specific inhibition of one of the BAF complexes provides a synthetic lethal dependency on subunits of a different BAF complex that can be exploited for therapy. A recent study on synovial sarcoma and rhabdoid tumors showed that dysfunctional canonical BAF complexes in these cancers led to an essential dependence on the specific components of the non-canonical BAF complex (Michel *et al.*, 2018). Given these findings, the effects of SWI/SNF complex modulation or inhibition on H3K27M tumor growth should be a focus moving forward.

4.6 Future directions for the study of H3G34R/V and H3K27M gliomas

In Chapter 3, I used epigenetic, transcriptomic, and proteomic approaches to study H3.3G34R/V tumors and explore signaling mechanisms activated by mutant histones. I characterized epigenetic patterns using computational methods and found that LIF/STAT3 signaling was upregulated in an epigenetic manner in several H3.3G34R/V cell models. Using genetic approaches, I found that LIF activated STAT3 signaling in these tumors, and I demonstrated that targeting STAT3 is a viable, translational therapy using multiple animal models. Notably, our isogenic model established with mouse neural stem cells recapitulated the reported extensive DNA methylation perturbations in H3.3G34R/V human tumor samples (Sturm *et al.,* 2012; Sangatsuda *et al.,* 2020). DNA methylation changes have also been reported in H3K27M tumors (Bender *et al.,* 2013). These data raise questions as to the different molecular mechanisms responsible for aberrant DNA methylation events. It remains unknown if specific DNA methylation proteins (i.e. DNMT1 and DNMT3A/B) are captured and inhibited by H3K27M or H3G34R/V directly and immunoprecipitation experiments will be insightful here. The ability of DNA methyltransferase DNMT3A to recognize H3K36me3 via a PWWP domain has been described (Dhayalan *et al.,* 2010). Since H3G34R/V has been shown to disrupt K36-residue modifiers such as SETD2, it is possible that H3G34R/V also interferes with DNMT3A-H3K36me3 binding or the catalytic activity of DNMT3A, causing hypomethylation. Similarly, it remains to be investigated if H3K27M exerts direct inhibition on DNMT3A or whether DNA methylation changes are a consequence of H3K27me3 loss. DNA methyltransferases have been shown to directly interact with EZH2 and this interaction is necessary for DNA methylation at PRC2 target genes (Viré *et al.,* 2006). Because ChIP-seq data from Piunti *et al.* (2017) reported an absence of PRC2 subunit proteins from H3.3/H3.3K27M/H3K27ac-rich regions, one interesting possibility is

that DNA methylation is blocked at these regions through a mechanism involving EZH2 exclusion. To dissect these outstanding questions in the H3G34R/V and H3K27M context, additional ChIP-seq assays would clarify the genomic localization of DNA methyltransferases and demethylases in relation to oncohistones. It is also quite possible that the histone mutant themselves do not interact with DNA methylation proteins, and that DNA methylation changes are a secondary effect. In my analysis of the isogenic H3.3G34R cells, I found that promoters with enriched H3K4me3 exhibited DNA hypomethylation. It was recently reported that DNA methylation is modulated by relative levels of H3K4me3 and H3K4me1 (Ooi *et al.*, 2007; Sharifi-Zarchi *et al.*, 2017). This work observed that H3K4me3 antagonized DNA methylation while H3K4me1 permitted it, raising the possibility that H3G34R/V histones perturb H3K4me3 directly and DNA hypomethylation is a consequence of this mechanism. Thus, it will be important to determine if H3G34-mutant histones bind lysine-4 demethylases of the KDM5 family, causing H3K4me3 accumulation via a similar mechanism observed for lysine-36 demethylases (Voon *et al.*, 2018).

Work on H3K27M and H3G34R/V gliomas has uncovered signaling mechanisms upregulated in the distinct tumor types. Chen *et al.* (2020) discovered recurrent *PDGFRA* mutations that activate the MEK/ERK pathway in H3G34R/V cells while Pajovic *et al.* (2020) reported epigenetic activation of RAS/MAPK and MYC signaling and their transcriptional targets in H3.3K27M models. Yet other work by Nagaraja *et al.* (2019) demonstrated selective activation of p38 MAPK signaling in H3.1K27M tumors. Until recently, little work has been performed to understand the interactions between oncogenic signaling pathways, such as MEK/ERK, and the chromatin remodeling process. Groundbreaking work has uncovered that the deposition of histone H3 variants is dynamically controlled by growth factor signaling (Gomes *et al.*, 2019). Strikingly, cells treated with growth factors like TGFβ and TNFα (ERK activators) were observed to modulate

the expression of both H3.1, H3.2, and H3.3, and their respective chaperones responsible for genomic deposition. Growth factor stimulation elicited upregulation of H3.3 and its chaperone HIRA, coincident with downregulation of H3.1/3.2 and their chaperones CHAF1A/1B, resulting in higher expression of pro-metastatic genes. Direct knockdown of CHAF1A/B also made cells more aggressive and resistant to therapy. This study highlighted that elevated ERK activity can reduce CHAF1A/B transcription and protein abundance, permitting increased H3.3 deposition into chromatin and transcriptional reprogramming leading to aggressive tumor properties. This seminal work raises critical questions about whether activated signaling pathways in histone mutant tumors further reshape chromatin accessibility by redirecting or changing the distribution of mutant histones deposited into genomic regions. It has been noted that a large portion of the epigenetic changes in established H3G34R/V cell lines are irreversible upon mutant-allele knockout (Bressan *et al.*, 2021), necessitating the need to understand how ERK/MEK and other signaling may be driving tumor progression via chromatin reprogramming. Overall, more work is needed to delineate additional modes of chromatin regulation uniquely engaged by each histone mutant.

Finally, studies have produced intriguing data regarding inhibition of K36 writer and eraser enzymes by H3.3G34R/V/W histones. This data demonstrates that H3K36me3 can be perturbed in both directions. However, it remains unclear what factors dictate the observed perturbations in discrete genomic regions. This is extremely fascinating and provides ample opportunity for future work. One explanation for H3K36me3 gain and loss at different regions is that the relative amount of SETD2 and KDM4A/B/C differ in these regions, resulting in H3G34R/V-mediated inhibition of the dominant modifiers. For example, if SETD2 abundance is higher than that of KDM4A/B/C and the binding affinities are roughly equal with H3G34R/V histone, the result would be an excess of SETD2 activity and H3K36me3 gain. Conversely, if KDM4A/B/C is the predominant species,

then excess demethylation reactions would occur and H3K36me3 diminishes. The relative affinities of H3G34R/V for each enzyme likely differs, however, and the regulation is probably more complex than these simple cases. More realistically, it might be possible that SETD2 abundance is higher than that of KDM4A/B/C and also exhibits stronger binding affinity with H3G34R/V histones, resulting in stronger SETD2 inhibition and KDM4-mediated H3K36me3 loss. It is likely that the relative presence of each K36-modifier at specific genes dictates the direction for H3K36me3 changes because a simple dependence on binding affinity cannot explain the bidirectional nature of the changes. Additionally, the observations of H3K36me3 gain and losses in G34R, G34V, and G34W-mutants, which likely each exhibit different relative affinities for the K36-modifying enzymes, suggest that there are other contributing factors.

One intriguing possibility is that H3G34 mutant-mediated perturbations of DNA methylation itself cause differential targeting of SETD2 and KDM4 to specific genes. Similar to our rationale for the K36-modifiers, it is possible that loci with different intrinsic abundances of DNA methylation enzymes experience H3G34R/V/W-mediated DNA methylation gains or losses depending on the residual activity of the less inhibited DNA methylation enzyme. The resulting DNA methylation patterning might then dictate whether SETD2 or KDM4 enzymes are recruited to a locus and consequently determine the H3K36me3 pattern established. Unfortunately, the lack of a robust SETD2 ChIP-grade antibody has precluded interrogation of these questions to date. When possible, it will be useful to analyze the relative distribution of K36-modifying enzymes and DNA methylating enzymes together with the H3.3G34R/V distribution to answer these questions rigorously.

4.7 Concluding remarks

Pediatric high-grade gliomas are devastating malignancies with poor outcomes and few treatments available. Although these cancers have been deeply molecularly profiled and analyzed, our understanding of the chromatin dynamics in these tumors is still in the early stages. Mutant histones have importance consequences for cell signaling, gene silencing, enhancer activation and hijacking, redistribution of histone and DNA methylation, transcription factor recruitment, and metabolic reprogramming. Further understanding aberrant interactions between each mutant histone and other chromatin-binding enzymes, such as the SWI/SNF complex, and how this affects epigenetic remodeling will be critical to find dependencies that can be specifically targeted. In this thesis, I examined effects of H3K27M on cellular metabolism and uncovered the ability to target energy pathways to raise H3K27me3. Furthermore, I provided a detailed characterization of cell signaling mechanisms epigenetically activated by H3G34R/V and demonstrated the efficacy of targeting the STAT3 axis in H3G34R/V tumors. I hope the work and ideas described in this thesis will contribute to further therapeutic development that will benefit patients and their families.

4.8 References

Allen JE, Kline CL, Prabhu VV, Wagner J, Ishizawa J, Madhukar N, Lev A, Baumeister M, Zhou L, Lulla A, Stogniew M, Schalop L, Benes C, Kaufman HL, Pottorf RS, Nallaganchu BR, Olson GL, Al-Mulla F, Duvic M, Wu GS, Dicker DT, Talekar MK, Lim B, Elemento O, Oster W, Bertino J, Flaherty K, Wang ML, Borthakur G, Andreeff M, Stein M, El-Deiry WS. Discovery and clinical introduction of first-in-class imipridone ONC201. *Oncotarget*. 2016 Nov 8;7(45):74380-74392. doi: 10.18632/oncotarget.11814.

Allen JE, Krigsfeld G, Mayes PA, Patel L, Dicker DT, Patel AS, Dolloff NG, Messaris E, Scata KA, Wang W, Zhou JY, Wu GS, El-Deiry WS. Dual inactivation of Akt and ERK by TIC10 signals Foxo3a nuclear translocation, TRAIL gene induction, and potent antitumor effects. *Sci Transl Med*. 2013 Feb 6;5(171):171ra17. doi: 10.1126/scitranslmed.3004828.

Allen JE, Krigsfeld G, Patel L, Mayes PA, Dicker DT, Wu GS, El-Deiry WS. Identification of TRAIL-inducing compounds highlights small molecule ONC201/TIC10 as a unique anti-cancer agent that activates the TRAIL pathway. *Mol Cancer*. 2015 May 1;14:99. doi: 10.1186/s12943-015-0346-9.

Arrillaga-Romany I, Chi AS, Allen JE, Oster W, Wen PY, Batchelor TT. A phase 2 study of the first imipridone ONC201, a selective DRD2 antagonist for oncology, administered every three weeks in recurrent glioblastoma. *Oncotarget*. 2017 May 12;8(45):79298-79304. doi: 10.18632/oncotarget.17837.

Batie M, Frost J, Frost M, Wilson JW, Schofield P, Rocha S. Hypoxia induces rapid changes to histone methylation and reprograms chromatin. *Science*. 2019 Mar 15;363(6432):1222-1226. doi: 10.1126/science.aau5870.

Bender S, Tang Y, Lindroth AM, Hovestadt V, Jones DT, Kool M, Zapatka M, Northcott PA, Sturm D, Wang W, Radlwimmer B, Højfeldt JW, Truffaux N, Castel D, Schubert S, Ryzhova M, Seker-Cin H, Gronych J, Johann PD, Stark S, Meyer J, Milde T, Schuhmann M, Ebinger M, Monoranu CM, Ponnuswami A, Chen S, Jones C, Witt O, Collins VP, von Deimling A, Jabado N, Puget S, Grill J, Helin K, Korshunov A, Lichter P, Monje M, Plass C, Cho YJ, Pfister SM. Reduced H3K27me3 and DNA hypomethylation are major drivers of gene expression in K27M mutant pediatric high-grade gliomas. *Cancer Cell*. 2013 Nov 11;24(5):660-72. doi: 10.1016/j.ccr.2013.10.006.

Bressan RB, Southgate B, Ferguson KM, Blin C, Grant V, Alfazema N, Wills JC, Marques-Torrejon MA, Morrison GM, Ashmore J, Robertson F, Williams CAC, Bradley L, von Kriegsheim A, Anderson RA, Tomlinson SR, Pollard SM. Regional identity of human neural stem cells determines oncogenic responses to histone H3.3 mutants. *Cell Stem Cell*. 2021 May 6;28(5):877-893.e9. doi: 10.1016/j.stem.2021.01.016.

Carbonneau M, M Gagné L, Lalonde ME, Germain MA, Motorina A, Guiot MC, Secco B, Vincent EE, Tumber A, Hulea L, Bergeman J, Oppermann U, Jones RG, Laplante M, Topisirovic I,

Petrecca K, Huot MÉ, Mallette FA. The oncometabolite 2-hydroxyglutarate activates the mTOR signalling pathway. *Nat Commun*. 2016 Sep 14;7:12700. doi: 10.1038/ncomms12700.

Chakraborty AA, Laukka T, Myllykoski M, Ringel AE, Booker MA, Tolstorukov MY, Meng YJ, Meier SR, Jennings RB, Creech AL, Herbert ZT, McBrayer SK, Olenchock BA, Jaffe JD, Haigis MC, Beroukhim R, Signoretti S, Koivunen P, Kaelin WG Jr. Histone demethylase KDM6A directly senses oxygen to control chromatin and cell fate. *Science*. 2019 Mar 15;363(6432):1217-1222. doi: 10.1126/science.aaw1026.

Chandler RL, Brennan J, Schisler JC, Serber D, Patterson C, Magnuson T. ARID1a-DNA interactions are required for promoter occupancy by SWI/SNF. *Mol Cell Biol*. 2013 Jan;33(2):265-80. doi: 10.1128/MCB.01008-12.

Chen CCL, Deshmukh S, Jessa S, Hadjadj D, Lisi V, Andrade AF, Faury D, Jawhar W, Dali R, Suzuki H, Pathania M, A D, Dubois F, Woodward E, Hébert S, Coutelier M, Karamchandani J, Albrecht S, Brandner S, De Jay N, Gayden T, Bajic A, Harutyunyan AS, Marchione DM, Mikael LG, Juretic N, Zeinieh M, Russo C, Maestro N, Bassenden AV, Hauser P, Virga J, Bognar L, Klekner A, Zapotocky M, Vicha A, Krskova L, Vanova K, Zamecnik J, Sumerauer D, Ekert PG, Ziegler DS, Ellezam B, Filbin MG, Blanchette M, Hansford JR, Khuong-Quang DA, Berghuis AM, Weil AG, Garcia BA, Garzia L, Mack SC, Beroukhim R, Ligon KL, Taylor MD, Bandopadhayay P, Kramm C, Pfister SM, Korshunov A, Sturm D, Jones DTW, Salomoni P, Kleinman CL, Jabado N. Histone H3.3G34-Mutant Interneuron Progenitors Co-opt PDGFRA for Gliomagenesis. *Cell*. 2020 Dec 10;183(6):1617-1633.e22. doi: 10.1016/j.cell.2020.11.012.

Chi AS, Tarapore RS, Hall MD, Shonka N, Gardner S, Umemura Y, Sumrall A, Khatib Z, Mueller S, Kline C, Zaky W, Khatua S, Weathers SP, Odia Y, Niazi TN, Daghistani D, Cherrick I, Korones D, Karajannis MA, Kong XT, Minturn J, Waanders A, Arillaga-Romany I, Batchelor T, Wen PY, Merdinger K, Schalop L, Stogniew M, Allen JE, Oster W, Mehta MP. Pediatric and adult H3 K27M-mutant diffuse midline glioma treated with the selective DRD2 antagonist ONC201. *J Neurooncol*. 2019 Oct;145(1):97-105. doi: 10.1007/s11060-019-03271-3.

Chung C, Sweha SR, Pratt D, Tamrazi B, Panwalkar P, Banda A, Bayliss J, Hawes D, Yang F, Lee HJ, Shan M, Cieslik M, Qin T, Werner CK, Wahl DR, Lyssiotis CA, Bian Z, Shotwell JB, Yadav VN, Koschmann C, Chinnaiyan AM, Blüml S, Judkins AR, Venneti S. Integrated Metabolic and Epigenomic Reprograming by H3K27M Mutations in Diffuse Intrinsic Pontine Gliomas. *Cancer Cell*. 2020 Sep 14;38(3):334-349.e9. doi: 10.1016/j.ccell.2020.07.008.

Dang L, White DW, Gross S, Bennett BD, Bittinger MA, Driggers EM, Fantin VR, Jang HG, Jin S, Keenan MC, Marks KM, Prins RM, Ward PS, Yen KE, Liau LM, Rabinowitz JD, Cantley LC, Thompson CB, Vander Heiden MG, Su SM. Cancer-associated IDH1 mutations produce 2-hydroxyglutarate. *Nature*. 2009 Dec 10;462(7274):739-44. doi: 10.1038/nature08617.

Ghaffari S, Jagani Z, Kitidis C, Lodish HF, Khosravi-Far R. Cytokines and BCR-ABL mediate suppression of TRAIL-induced apoptosis through inhibition of forkhead FOXO3a transcription factor. *Proc Natl Acad Sci USA*. 2003 May 27;100(11):6523-8. doi: 10.1073/pnas.0731871100.

Gomes AP, Ilter D, Low V, Rosenzweig A, Shen ZJ, Schild T, Rivas MA, Er EE, McNally DR, Mutvei AP, Han J, Ou YH, Cavaliere P, Mullarky E, Nagiec M, Shin S, Yoon SO, Dephoure N, Massagué J, Melnick AM, Cantley LC, Tyler JK, Blenis J. Dynamic Incorporation of Histone H3 Variants into Chromatin Is Essential for Acquisition of Aggressive Traits and Metastatic Colonization. *Cancer Cell*. 2019 Oct 14;36(4):402-417.e13. doi: 10.1016/j.ccell.2019.08.006.

Graves PR, Aponte-Collazo LJ, Fennell EMJ, Graves AC, Hale AE, Dicheva N, Herring LE, Gilbert TSK, East MP, McDonald IM, Lockett MR, Ashamalla H, Moorman NJ, Karanewsky DS, Iwanowicz EJ, Holmuhamedov E, Graves LM. Mitochondrial Protease ClpP is a Target for the Anticancer Compounds ONC201 and Related Analogues. *ACS Chem Biol*. 2019 May 17;14(5):1020-1029. doi: 10.1021/acschembio.9b00222.

He L, Bhat K, Ioannidis A, Zhang L, Nguyen NT, Allen JE, Nghiemphu PL, Cloughesy TF, Liau LM, Kornblum HI, Pajonk F. Effects of the DRD2/3 antagonist ONC201 and radiation in glioblastoma. *Radiother Oncol*. 2021 Aug;161:140-147. doi: 10.1016/j.radonc.2021.05.027.

Ishizawa J, Kojima K, Chachad D, Ruvolo P, Ruvolo V, Jacamo RO, Borthakur G, Mu H, Zeng Z, Tabe Y, Allen JE, Wang Z, Ma W, Lee HC, Orlowski R, Sarbassov dos D, Lorenzi PL, Huang X, Neelapu SS, McDonnell T, Miranda RN, Wang M, Kantarjian H, Konopleva M, Davis RE, Andreeff M. ATF4 induction through an atypical integrated stress response to ONC201 triggers p53-independent apoptosis in hematological malignancies. *Sci Signal*. 2016 Feb 16;9(415):ra17. doi: 10.1126/scisignal.aac4380.

Ishizawa J, Zarabi SF, Davis RE, Halgas O, Nii T, Jitkova Y, Zhao R, St-Germain J, Heese LE, Egan G, Ruvolo VR, Barghout SH, Nishida Y, Hurren R, Ma W, Gronda M, Link T, Wong K, Mabanglo M, Kojima K, Borthakur G, MacLean N, Ma MCJ, Leber AB, Minden MD, Houry W, Kantarjian H, Stogniew M, Raught B, Pai EF, Schimmer AD, Andreeff M. Mitochondrial ClpP-Mediated Proteolysis Induces Selective Cancer Cell Lethality. *Cancer Cell*. 2019 May 13;35(5):721-737.e9. doi: 10.1016/j.ccell.2019.03.014.

Kayabolen A, Yilmaz E, Bagci-Onder T. *IDH* Mutations in Glioma: Double-Edged Sword in Clinical Applications? Biomedicines. 2021 Jul 10;9(7):799. doi: 10.3390/biomedicines9070799.

Kelso TWR, Porter DK, Amaral ML, Shokhirev MN, Benner C, Hargreaves DC. Chromatin accessibility underlies synthetic lethality of SWI/SNF subunits in ARID1A-mutant cancers. *Elife*. 2017 Oct 2;6:e30506. doi: 10.7554/eLife.30506.

Kline CL, Van den Heuvel AP, Allen JE, Prabhu VV, Dicker DT, El-Deiry WS. ONC201 kills solid tumor cells by triggering an integrated stress response dependent on ATF4 activation by specific eIF2α kinases. *Sci Signal*. 2016 Feb 16;9(415):ra18. doi: 10.1126/scisignal.aac4374.

Kolukula VK, Sahu G, Wellstein A, Rodriguez OC, Preet A, Iacobazzi V, D'Orazi G, Albanese C, Palmieri F, Avantaggiati ML. SLC25A1, or CIC, is a novel transcriptional target of mutant p53 and a negative tumor prognostic marker. *Oncotarget*. 2014 Mar 15;5(5):1212-25. doi: 10.18632/oncotarget.1831.

Konteatis Z, Artin E, Nicolay B, Straley K, Padyana AK, Jin L, Chen Y, Narayaraswamy R, Tong S, Wang F, Zhou D, Cui D, Cai Z, Luo Z, Fang C, Tang H, Lv X, Nagaraja R, Yang H, Su SM, Sui Z, Dang L, Yen K, Popovici-Muller J, Codega P, Campos C, Mellinghoff IK, Biller SA. Vorasidenib (AG-881): A First-in-Class, Brain-Penetrant Dual Inhibitor of Mutant IDH1 and 2 for Treatment of Glioma. *ACS Med Chem Lett*. 2020 Jan 22;11(2):101-107. doi: 10.1021/acsmedchemlett.9b00509.

Kopinja J, Sevilla RS, Levitan D, Dai D, Vanko A, Spooner E, Ware C, Forget R, Hu K, Kral A, Spacciapoli P, Kennan R, Jayaraman L, Pucci V, Perera S, Zhang W, Fischer C, Lam MH. A Brain Penetrant Mutant IDH1 Inhibitor Provides In Vivo Survival Benefit. *Sci Rep*. 2017 Oct 23;7(1):13853. doi: 10.1038/s41598-017-14065-w.

Kuribayashi K, Krigsfeld G, Wang W, Xu J, Mayes PA, Dicker DT, Wu GS, El-Deiry WS. TNFSF10 (TRAIL), a p53 target gene that mediates p53-dependent cell death. *Cancer Biol Ther*. 2008 Dec;7(12):2034-8. doi: 10.4161/cbt.7.12.7460.

Lewis PW, Müller MM, Koletsky MS, Cordero F, Lin S, Banaszynski LA, Garcia BA, Muir TW, Becher OJ, Allis CD. Inhibition of PRC2 activity by a gain-of-function H3 mutation found in pediatric glioblastoma. *Science*. 2013 May 17;340(6134):857-61. doi: 10.1126/science.1232245.

Lu C, Jain SU, Hoelper D, Bechet D, Molden RC, Ran L, Murphy D, Venneti S, Hameed M, Pawel BR, Wunder JS, Dickson BC, Lundgren SM, Jani KS, De Jay N, Papillon-Cavanagh S, Andrulis IL, Sawyer SL, Grynspan D, Turcotte RE, Nadaf J, Fahiminiyah S, Muir TW, Majewski J, Thompson CB, Chi P, Garcia BA, Allis CD, Jabado N, Lewis PW. Histone H3K36 mutations promote sarcomagenesis through altered histone methylation landscape. *Science*. 2016 May 13;352(6287):844-9. doi: 10.1126/science.aac7272.

Lu C, Ward PS, Kapoor GS, Rohle D, Turcan S, Abdel-Wahab O, Edwards CR, Khanin R, Figueroa ME, Melnick A, Wellen KE, O'Rourke DM, Berger SL, Chan TA, Levine RL, Mellinghoff IK, Thompson CB. IDH mutation impairs histone demethylation and results in a block to cell differentiation. *Nature*. 2012 Feb 15;483(7390):474-8. doi: 10.1038/nature10860.

Mackay A, Burford A, Carvalho D, Izquierdo E, Fazal-Salom J, Taylor KR, Bjerke L, Clarke M, Vinci M, Nandhabalan M, Temelso S, Popov S, Molinari V, Raman P, Waanders AJ, Han HJ, Gupta S, Marshall L, Zacharoulis S, Vaidya S, Mandeville HC, Bridges LR, Martin AJ, Al-Sarraj S, Chandler C, Ng HK, Li X, Mu K, Trabelsi S, Brahim DH, Kisljakov AN, Konovalov DM, Moore AS, Carcaboso AM, Sunol M, de Torres C, Cruz O, Mora J, Shats LI, Stavale JN, Bidinotto LT, Reis RM, Entz-Werle N, Farrell M, Cryan J, Crimmins D, Caird J, Pears J, Monje M, Debily MA, Castel D, Grill J, Hawkins C, Nikbakht H, Jabado N, Baker SJ, Pfister SM, Jones DTW, Fouladi M, von Bueren AO, Baudis M, Resnick A, Jones C. Integrated Molecular Meta-Analysis of 1,000 Pediatric High-Grade and Diffuse Intrinsic Pontine Glioma. *Cancer Cell*. 2017 Oct 9;32(4):520-537.e5. doi: 10.1016/j.ccell.2017.08.017.

Marques S, Zeisel A, Codeluppi S, van Bruggen D, Mendanha Falcão A, Xiao L, Li H, Häring M, Hochgerner H, Romanov RA, Gyllborg D, Muñoz Manchado A, La Manno G, Lönnerberg P, Floriddia EM, Rezayee F, Ernfors P, Arenas E, Hjerling-Leffler J, Harkany T, Richardson WD,

Linnarsson S, Castelo-Branco G. Oligodendrocyte heterogeneity in the mouse juvenile and adult central nervous system. *Science*. 2016 Jun 10;352(6291):1326-1329. doi: 10.1126/science.aaf6463.

Mashtalir N, Dao HT, Sankar A, Liu H, Corin AJ, Bagert JD, Ge EJ, D'Avino AR, Filipovski M, Michel BC, Dann GP, Muir TW, Kadoch C. Chromatin landscape signals differentially dictate the activities of mSWI/SNF family complexes. *Science*. 2021 Jul 16;373(6552):306-315. doi: 10.1126/science.abf8705.

Michel BC, D'Avino AR, Cassel SH, Mashtalir N, McKenzie ZM, McBride MJ, Valencia AM, Zhou Q, Bocker M, Soares LMM, Pan J, Remillard DI, Lareau CA, Zullow HJ, Fortoul N, Gray NS, Bradner JE, Chan HM, Kadoch C. A non-canonical SWI/SNF complex is a synthetic lethal target in cancers driven by BAF complex perturbation. Nat Cell Biol. 2018 Dec;20(12):1410-1420. doi: 10.1038/s41556-018-0221-1.

Nagaraja S, Quezada MA, Gillespie SM, Arzt M, Lennon JJ, Woo PJ, Hovestadt V, Kambhampati M, Filbin MG, Suva ML, Nazarian J, Monje M. Histone Variant and Cell Context Determine H3K27M Reprogramming of the Enhancer Landscape and Oncogenic State. *Mol Cell*. 2019 Dec 19;76(6):965-980.e12. doi: 10.1016/j.molcel.2019.08.030.

Ooi SK, Qiu C, Bernstein E, Li K, Jia D, Yang Z, Erdjument-Bromage H, Tempst P, Lin SP, Allis CD, Cheng X, Bestor TH. DNMT3L connects unmethylated lysine 4 of histone H3 to de novo methylation of DNA. *Nature*. 2007 Aug 9;448(7154):714-7. doi: 10.1038/nature05987.

Pajovic S, Siddaway R, Bridge T, Sheth J, Rakopoulos P, Kim B, Ryall S, Agnihotri S, Phillips L, Yu M, Li C, Milos S, Patel P, Srikanthan D, Huang A, Hawkins C. Epigenetic activation of a RAS/MYC axis in H3.3K27M-driven cancer. *Nat Commun*. 2020 Dec 4;11(1):6216. doi: 10.1038/s41467-020-19972-7.

Pan M, Reid MA, Lowman XH, Kulkarni RP, Tran TQ, Liu X, Yang Y, Hernandez-Davies JE, Rosales KK, Li H, Hugo W, Song C, Xu X, Schones DE, Ann DK, Gradinaru V, Lo RS, Locasale JW, Kong M. Regional glutamine deficiency in tumours promotes dedifferentiation through inhibition of histone demethylation. *Nat Cell Biol*. 2016 Oct;18(10):1090-101. doi: 10.1038/ncb3410.

Parsons DW, Jones S, Zhang X, Lin JC, Leary RJ, Angenendt P, Mankoo P, Carter H, Siu IM, Gallia GL, Olivi A, McLendon R, Rasheed BA, Keir S, Nikolskaya T, Nikolsky Y, Busam DA, Tekleab H, Diaz LA Jr, Hartigan J, Smith DR, Strausberg RL, Marie SK, Shinjo SM, Yan H, Riggins GJ, Bigner DD, Karchin R, Papadopoulos N, Parmigiani G, Vogelstein B, Velculescu VE, Kinzler KW. An integrated genomic analysis of human glioblastoma multiforme. *Science*. 2008 Sep 26;321(5897):1807-12. doi: 10.1126/science.1164382.

Piunti A, Hashizume R, Morgan MA, Bartom ET, Horbinski CM, Marshall SA, Rendleman EJ, Ma Q, Takahashi YH, Woodfin AR, Misharin AV, Abshiru NA, Lulla RR, Saratsis AM, Kelleher NL, James CD, Shilatifard A. Therapeutic targeting of polycomb and BET bromodomain proteins in diffuse intrinsic pontine gliomas. *Nat Med*. 2017 Apr;23(4):493-500. doi: 10.1038/nm.4296.

Popovici-Muller J, Lemieux RM, Artin E, Saunders JO, Salituro FG, Travins J, Cianchetta G, Cai Z, Zhou D, Cui D, Chen P, Straley K, Tobin E, Wang F, David MD, Penard-Lacronique V, Quivoron C, Saada V, de Botton S, Gross S, Dang L, Yang H, Utley L, Chen Y, Kim H, Jin S, Gu Z, Yao G, Luo Z, Lv X, Fang C, Yan L, Olaharski A, Silverman L, Biller S, Su SM, Yen K. Discovery of AG-120 (Ivosidenib): A First-in-Class Mutant IDH1 Inhibitor for the Treatment of IDH1 Mutant Cancers. *ACS Med Chem Lett*. 2018 Jan 19;9(4):300-305. doi: 10.1021/acsmedchemlett.7b00421.

Prabhu VV, Morrow S, Rahman Kawakibi A, Zhou L, Ralff M, Ray J, Jhaveri A, Ferrarini I, Lee Y, Parker C, Zhang Y, Borsuk R, Chang WI, Honeyman JN, Tavora F, Carneiro B, Raufi A, Huntington K, Carlsen L, Louie A, Safran H, Seyhan AA, Tarapore RS, Schalop L, Stogniew M, Allen JE, Oster W, El-Deiry WS. ONC201 and imipridones: Anti-cancer compounds with clinical efficacy. *Neoplasia*. 2020 Dec;22(12):725-744. doi: 10.1016/j.neo.2020.09.005.

Pusch S, Krausert S, Fischer V, Balss J, Ott M, Schrimpf D, Capper D, Sahm F, Eisel J, Beck AC, Jugold M, Eichwald V, Kaulfuss S, Panknin O, Rehwinkel H, Zimmermann K, Hillig RC, Guenther J, Toschi L, Neuhaus R, Haegebart A, Hess-Stumpp H, Bauser M, Wick W, Unterberg A, Herold-Mende C, Platten M, von Deimling A. Pan-mutant IDH1 inhibitor BAY 1436032 for effective treatment of IDH1 mutant astrocytoma in vivo. *Acta Neuropathol*. 2017 Apr;133(4):629-644. doi: 10.1007/s00401-017-1677-y.

Raab JR, Resnick S, Magnuson T. Genome-Wide Transcriptional Regulation Mediated by Biochemically Distinct SWI/SNF Complexes. *PLoS Genet*. 2015 Dec 30;11(12):e1005748. doi: 10.1371/journal.pgen.1005748.

Rohle D, Popovici-Muller J, Palaskas N, Turcan S, Grommes C, Campos C, Tsoi J, Clark O, Oldrini B, Komisopoulou E, Kunii K, Pedraza A, Schalm S, Silverman L, Miller A, Wang F, Yang H, Chen Y, Kernytsky A, Rosenblum MK, Liu W, Biller SA, Su SM, Brennan CW, Chan TA, Graeber TG, Yen KE, Mellinghoff IK. An inhibitor of mutant IDH1 delays growth and promotes differentiation of glioma cells. *Science*. 2013 May 3;340(6132):626-30. doi: 10.1126/science.1236062.

Schwartzentruber J, Korshunov A, Liu XY, Jones DT, Pfaff E, Jacob K, Sturm D, Fontebasso AM, Quang DA, Tönjes M, Hovestadt V, Albrecht S, Kool M, Nantel A, Konermann C, Lindroth A, Jäger N, Rausch T, Ryzhova M, Korbel JO, Hielscher T, Hauser P, Garami M, Klekner A, Bognar L, Ebinger M, Schuhmann MU, Scheurlen W, Pekrun A, Frühwald MC, Roggendorf W, Kramm C, Dürken M, Atkinson J, Lepage P, Montpetit A, Zakrzewska M, Zakrzewski K, Liberski PP, Dong Z, Siegel P, Kulozik AE, Zapatka M, Guha A, Malkin D, Felsberg J, Reifenberger G, von Deimling A, Ichimura K, Collins VP, Witt H, Milde T, Witt O, Zhang C, Castelo-Branco P, Lichter P, Faury D, Tabori U, Plass C, Majewski J, Pfister SM, Jabado N. Driver mutations in histone H3.3 and chromatin remodelling genes in paediatric glioblastoma. *Nature*. 2012 Jan 29;482(7384):226-31. doi: 10.1038/nature10833.

Sharifi-Zarchi A, Gerovska D, Adachi K, Totonchi M, Pezeshk H, Taft RJ, Schöler HR, Chitsaz H, Sadeghi M, Baharvand H, Araúzo-Bravo MJ. DNA methylation regulates discrimination of

enhancers from promoters through a H3K4me1-H3K4me3 seesaw mechanism. *BMC Genomics*. 2017 Dec 12;18(1):964. doi: 10.1186/s12864-017-4353-7.

Sturm D, Witt H, Hovestadt V, Khuong-Quang DA, Jones DT, Konermann C, Pfaff E, Tönjes M, Sill M, Bender S, Kool M, Zapatka M, Becker N, Zucknick M, Hielscher T, Liu XY, Fontebasso AM, Ryzhova M, Albrecht S, Jacob K, Wolter M, Ebinger M, Schuhmann MU, van Meter T, Frühwald MC, Hauch H, Pekrun A, Radlwimmer B, Niehues T, von Komorowski G, Dürken M, Kulozik AE, Madden J, Donson A, Foreman NK, Drissi R, Fouladi M, Scheurlen W, von Deimling A, Monoranu C, Roggendorf W, Herold-Mende C, Unterberg A, Kramm CM, Felsberg J, Hartmann C, Wiestler B, Wick W, Milde T, Witt O, Lindroth AM, Schwartzentruber J, Faury D, Fleming A, Zakrzewska M, Liberski PP, Zakrzewski K, Hauser P, Garami M, Klekner A, Bognar L, Morrissy S, Cavalli F, Taylor MD, van Sluis P, Koster J, Versteeg R, Volckmann R, Mikkelsen T, Aldape K, Reifenberger G, Collins VP, Majewski J, Korshunov A, Lichter P, Plass C, Jabado N, Pfister SM. Hotspot mutations in H3F3A and IDH1 define distinct epigenetic and biological subgroups of glioblastoma. *Cancer Cell*. 2012 Oct 16;22(4):425-37. doi: 10.1016/j.ccr.2012.08.024.

Tahiliani M, Koh KP, Shen Y, Pastor WA, Bandukwala H, Brudno Y, Agarwal S, Iyer LM, Liu DR, Aravind L, Rao A. Conversion of 5-methylcytosine to 5-hydroxymethylcytosine in mammalian DNA by MLL partner TET1. Science. 2009 May 15;324(5929):930-5. doi: 10.1126/science.1170116.

Tran KA, Dillingham CM, Sridharan R. The role of α-ketoglutarate-dependent proteins in pluripotency acquisition and maintenance. *J Biol Chem*. 2019 Apr 5;294(14):5408-5419. doi: 10.1074/jbc.TM118.000831.

Turcan S, Fabius AW, Borodovsky A, Pedraza A, Brennan C, Huse J, Viale A, Riggins GJ, Chan TA. Efficient induction of differentiation and growth inhibition in IDH1 mutant glioma cells by the DNMT Inhibitor Decitabine. *Oncotarget*. 2013 Oct;4(10):1729-36. doi: 10.18632/oncotarget.1412.

Turcan S, Rohle D, Goenka A, Walsh LA, Fang F, Yilmaz E, Campos C, Fabius AW, Lu C, Ward PS, Thompson CB, Kaufman A, Guryanova O, Levine R, Heguy A, Viale A, Morris LG, Huse JT, Mellinghoff IK, Chan TA. IDH1 mutation is sufficient to establish the glioma hypermethylator phenotype. *Nature*. 2012 Feb 15;483(7390):479-83. doi: 10.1038/nature10866.

Viré E, Brenner C, Deplus R, Blanchon L, Fraga M, Didelot C, Morey L, Van Eynde A, Bernard D, Vanderwinden JM, Bollen M, Esteller M, Di Croce L, de Launoit Y, Fuks F. The Polycomb group protein EZH2 directly controls DNA methylation. *Nature*. 2006 Feb 16;439(7078):871-4. doi: 10.1038/nature04431.

Voon HPJ, Udugama M, Lin W, Hii L, Law RHP, Steer DL, Das PP, Mann JR, Wong LH. Inhibition of a K9/K36 demethylase by an H3.3 point mutation found in paediatric glioblastoma. *Nat Commun*. 2018 Aug 7;9(1):3142. doi: 10.1038/s41467-018-05607-5.

Wu G, Broniscer A, McEachron TA, Lu C, Paugh BS, Becksfort J, Qu C, Ding L, Huether R, Parker M, Zhang J, Gajjar A, Dyer MA, Mullighan CG, Gilbertson RJ, Mardis ER, Wilson RK, Downing JR, Ellison DW, Zhang J, Baker SJ; St. Jude Children's Research Hospital–Washington University Pediatric Cancer Genome Project. Somatic histone H3 alterations in pediatric diffuse intrinsic pontine gliomas and non-brainstem glioblastomas. *Nat Genet*. 2012 Jan 29;44(3):251-3. doi: 10.1038/ng.1102.

Xu W, Yang H, Liu Y, Yang Y, Wang P, Kim SH, Ito S, Yang C, Wang P, Xiao MT, Liu LX, Jiang WQ, Liu J, Zhang JY, Wang B, Frye S, Zhang Y, Xu YH, Lei QY, Guan KL, Zhao SM, Xiong Y. Oncometabolite 2-hydroxyglutarate is a competitive inhibitor of α-ketoglutarate-dependent dioxygenases. *Cancer Cell*. 2011 Jan 18;19(1):17-30. doi: 10.1016/j.ccr.2010.12.014.

Yan H, Parsons DW, Jin G, McLendon R, Rasheed BA, Yuan W, Kos I, Batinic-Haberle I, Jones S, Riggins GJ, Friedman H, Friedman A, Reardon D, Herndon J, Kinzler KW, Velculescu VE, Vogelstein B, Bigner DD. IDH1 and IDH2 mutations in gliomas. *N Engl J Med*. 2009 Feb 19;360(8):765-73. doi: 10.1056/NEJMoa0808710.

4.9 Figures & Figure Legends

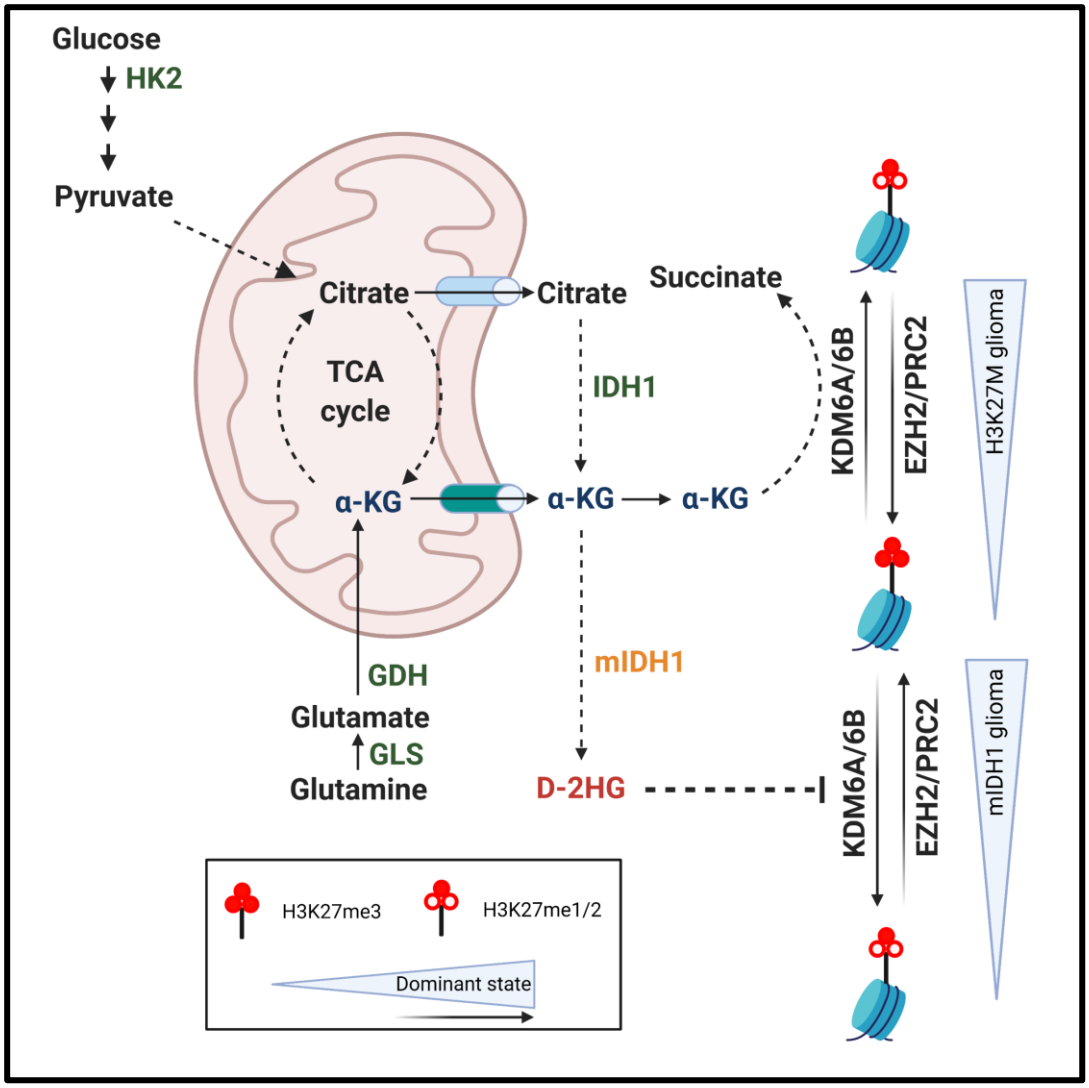

Figure 4.1. Metabolic pathways modulate the catalytic activity of histone lysine-27 modifying enzymes. Alpha-ketoglutarate (α-KG) is derived from citrate in the mitochondrial tricarboxylic acid (TCA) cycle. α-KG is a cofactor for H3K27-demethylation reactions catalyzed by KDM6A/B. H3K27M tumors exhibit loss of H3K27me3 due to EZH2 inhibition and elevated α-KG levels which favor the demethylation reaction. Contrastingly, tumors with mutant IDH1 protein gain the ability to convert α-KG into D-2HG. This oncometabolite competitively inhibits KDM6A/B, raising H3K27me3. Figure constructed with BioRender.com.

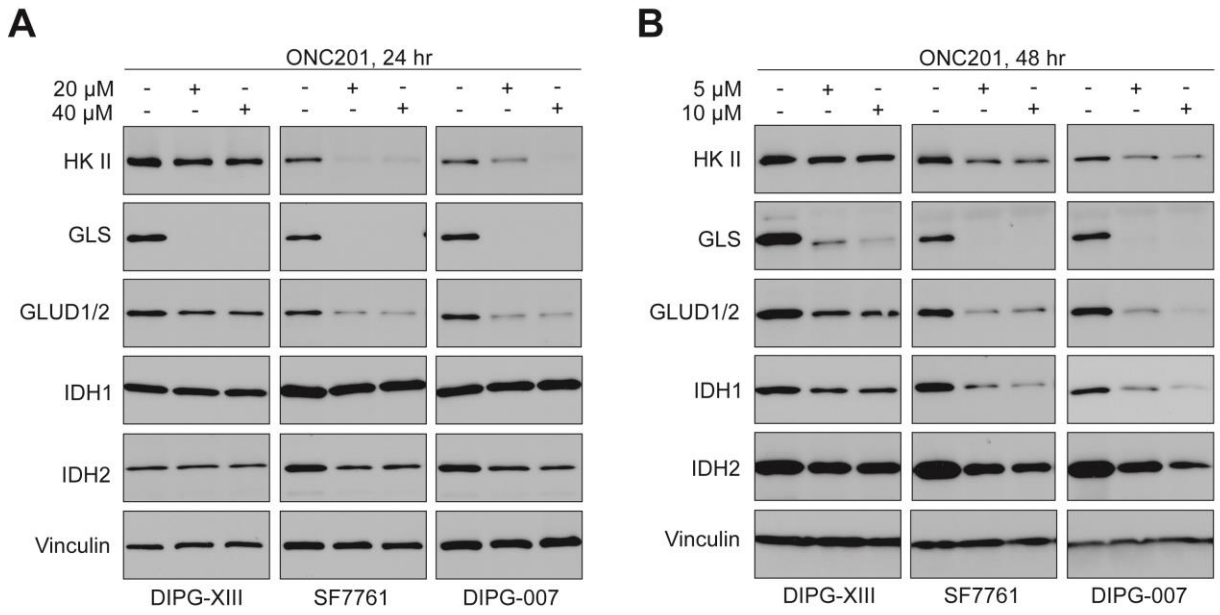

Figure 4.2. ONC201 modulates metabolic enzyme expression in H3.3K27M DIPG cells. **(A)** Immunoblots of cell lysates from H3.3K27M DIPG-XIII, SF7761, and DIPG-007 cells after treatment with ONC201 for 24 hours at indicate concentrations. Expression for hexokinase II (HKII), glutaminase (GLS), glutamate dehydrogenase 1/2 (GLUD1/2), isocitrate dehydrogenase 1/2 (IDH1/2), and vinculin was probed. **(B)** Same experiment as in **(A)** at 48 hours at indicated concentrations.

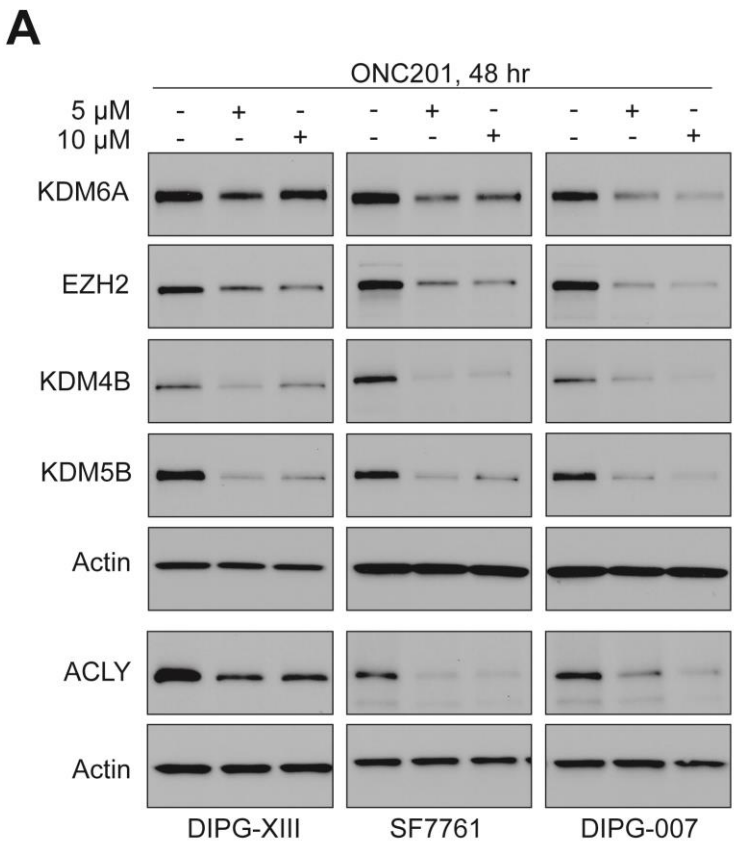

Figure 4.3. ONC201-treated DIPG cells exhibit changes in epigenetic-modifying enzymes. **(A)** Immunoblots of cell lysates from H3.3K27M DIPG-XIII, SF7761, and DIPG-007 cells after treatment with ONC201 for 48 hours at indicate concentrations. Expression for lysine demethylase 6A (KDM6A), enhancer of zeste homolog 2 (EZH2), lysine demethylase 4B and 5B (KDM4B/KDM5B), ATP citrate lyase (ACLY), and β-Actin was probed.

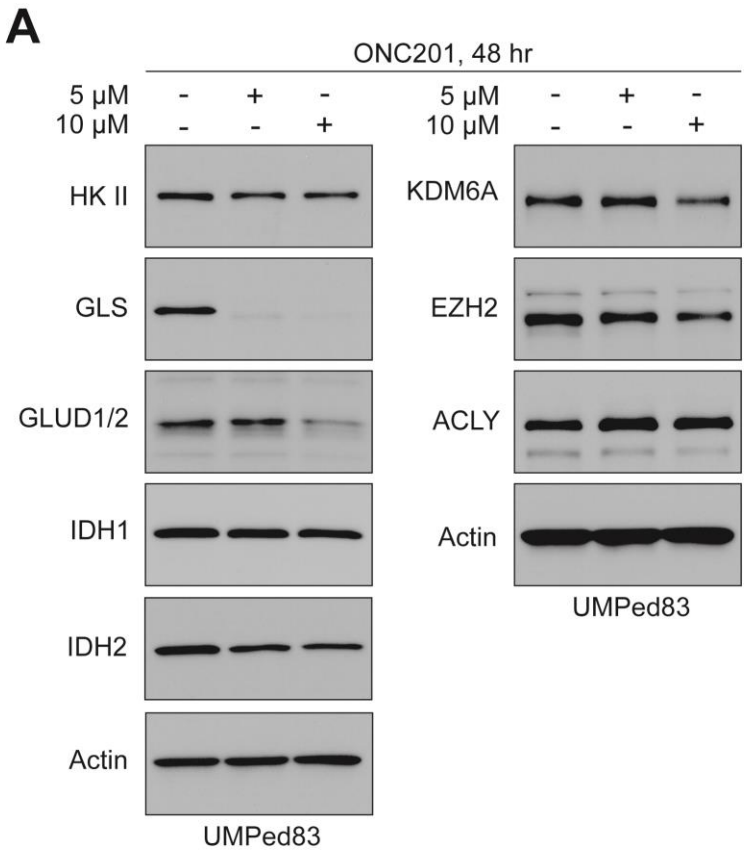

Figure 4.4. Patient-derived H3.3K27M UMPed83 cells exhibit resistance to ONC201-induced degradation of metabolic and epigenetic modifier enzymes.
(A) Immunoblots of cell lysates from UMPed83 cells treated with ONC201 for 48 hours at the indicated concentrations. Expression for hexokinase II (HKII), glutaminase (GLS), glutamate dehydrogenase 1/2 (GLUD1/2), isocitrate dehydrogenase 1/2 (IDH1/2), lysine demethylase 6A (KDM6A), enhancer of zeste homolog 2 (EZH2), ATP citrate lyase (ACLY), and β-Actin was probed.

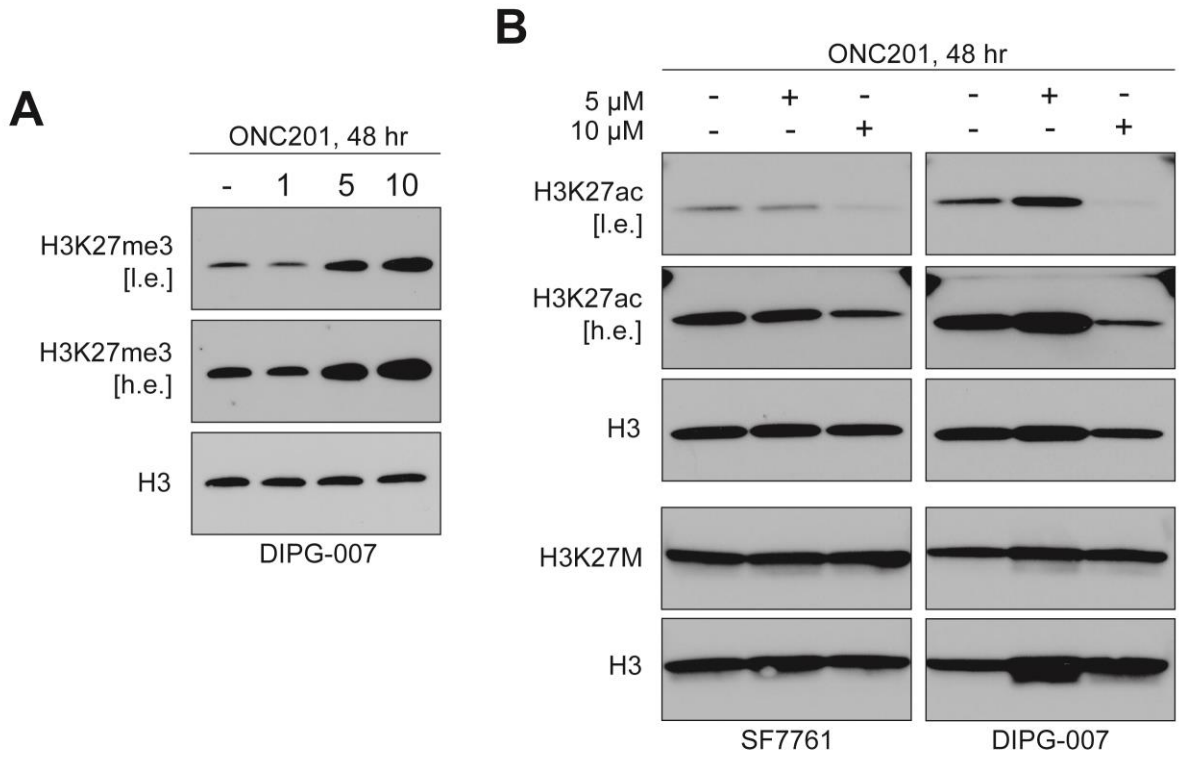

Figure 4.5. ONC201 treatment raises H3K27me3 and suppresses H3K27ac in DIPG cells. **(A)** Immunoblots for H3K27me3 and total H3 on histone extracts from DIPG-007 cells treated with increasing concentrations of ONC201 for 48 hours. **(B)** Immunoblots for H3K27ac, H3K27M, and total H3 on histone extracts from SF7761 and DIPG-007 cells treated with ONC201 for 48 hours at the indicated concentrations. *l.e.* = low exposure; *h.e.* = high exposure.

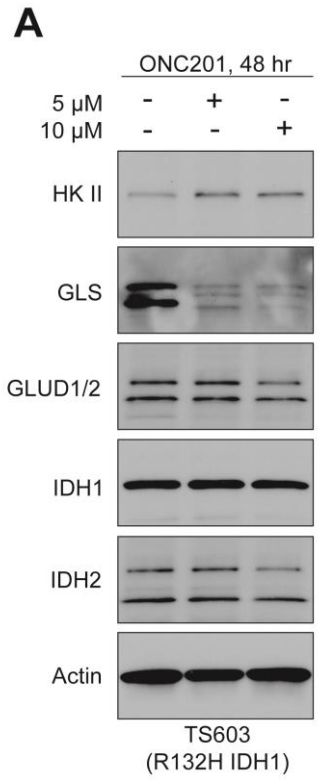

Figure 4.6. ONC201 treatment does not affect IDH1 or IDH2 expression in mIDH1 cells.
(A) Immunoblots of cell lysates from R132H IDH1 TS603 cells treated with ONC201 for 48 hours at the indicated concentrations. Expression for hexokinase II (HKII), glutaminase (GLS), glutamate dehydrogenase 1/2 (GLUD1/2), isocitrate dehydrogenase 1/2 (IDH1/2) and β-Actin was probed.

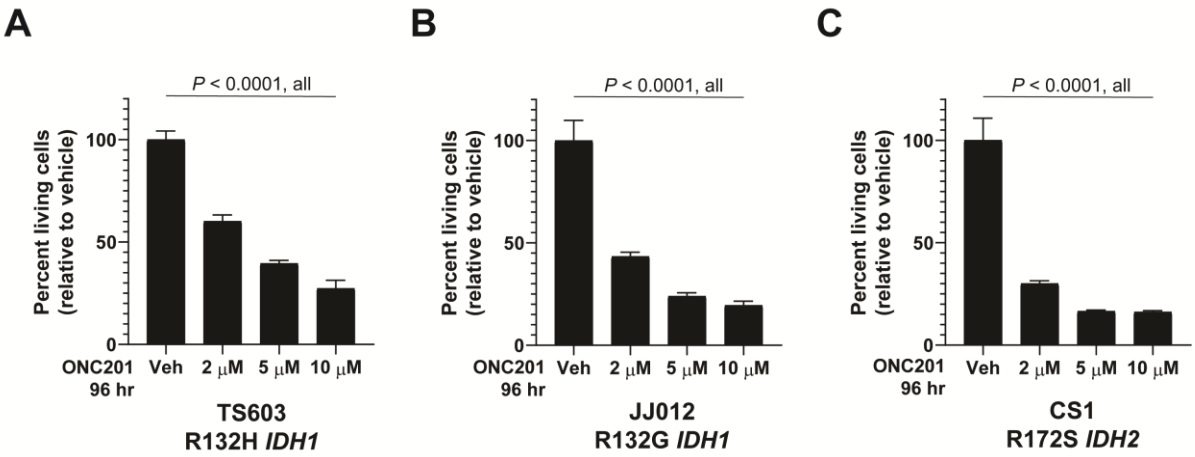

Figure 4.7. ONC201 shows toxicity in mutant IDH1 and IDH2 cells.
(A-C) Cell viability of TS603 **(A)**, JJ012 **(B)**, and CS1 **(C)** mutant IDH cells after treatment with ONC201 for 96 hours at indicated concentrations. *n*=4 technical replicates per condition.

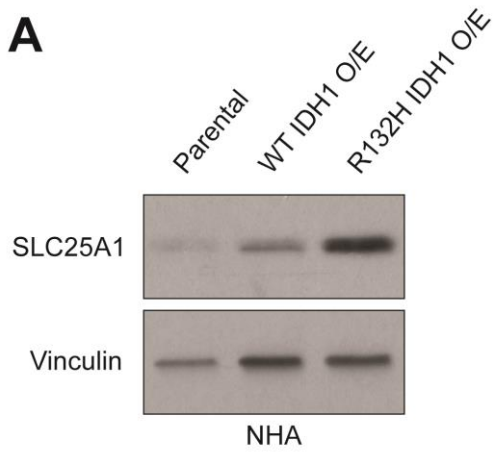

Figure 4.8. Wild-type and R132H IDH1 induces citrate transporter SLC25A1 expression in normal human astrocytes.
(A) Immunoblots of cell lysates from normal human astrocytes (NHA), stably transduced with wild-type IDH1 or R132H IDH1 overexpression (O/E) constructs, for mitochondrial citrate transporter SLC25A1 and vinculin. Data provided by Dr. Chan Chung.